

# Quantum Diffusion of Hydrogen and Deuterium on Nickel

Aaron Russell Hopkinson

Doctor of Philosophy

University of York  
Physics

January 2017

# Abstract

The quantum nature of hydrogen has long been observed to play an important role on its diffusion within metals.

Motivated by recent experimental work, diffusion rates were calculated for both hydrogen and deuterium on the nickel (111) surface across a range of temperatures (75 K to 250 K), taking into account quantum nuclear effects. This was achieved through the method of partially adiabatic centroid molecular dynamics, which places the Feynman path integral in a central role. This method makes the calculation of quantum time correlation functions possible through an extension to classical molecular dynamics.

The ab initio calculation of the quantum diffusion of hydrogen/deuterium on the nickel surface is computationally demanding, and a method for approximating these interactions, in the form of a static potential energy surface is presented. Implicit in this method is that there is an adiabatic separation between motion of the surface ions and the adsorbate, due to their large mass differences. The resulting potential energy surface allows for the accurate determination of the energies and forces acting on the adsorbate, at all positions along the static surface, with a significantly reduced cost when compared with density functional theory.

The quantum dynamics calculations showed that, for the temperature range studied, the inclusion of quantum nuclear effects acted to increase the diffusion rate of both adsorbates. At 250 K, the quantum diffusion coefficients were found to be  $\sim 34$  times larger than the classical result. At 75 K, the quantum contribution is significantly increased, and the diffusion coefficient is  $\sim 4 \times 10^6$  times larger for deuterium and  $\sim 1 \times 10^7$  times larger for hydrogen. The classical and quantum treatments also give rise to qualitatively different diffusion profiles on an Arrhenius plot, especially in the low temperature regime, where there is a transition from classical (thermally activated) to quantum (tunnelling) diffusion.

# Contents

<b>Abstract</b>	<b>2</b>
<b>Contents</b>	<b>3</b>
<b>List of Tables</b>	<b>9</b>
<b>List of Figures</b>	<b>11</b>
<b>Acknowledgements</b>	<b>17</b>
<b>Declaration</b>	<b>18</b>
<b>1 Introduction</b>	<b>19</b>
1.1 Motivation . . . . .	19
1.2 Software development . . . . .	20
1.3 Outline of the thesis . . . . .	20
<b>2 Hydrogen and Metals</b>	<b>21</b>
2.1 Introduction . . . . .	21
2.2 Why study surfaces? . . . . .	22
2.3 H/D diffusion on the (111) Ni surface . . . . .	23
2.3.1 Related work . . . . .	26
2.4 Summary . . . . .	27

---

<b>3</b>	<b>Diffusion</b>	<b>28</b>
3.1	Introduction . . . . .	28
3.2	Fick's laws of diffusion . . . . .	29
3.2.1	Derivation of Fick's first law . . . . .	29
3.2.2	Derivation of Fick's second law . . . . .	30
3.3	Einstein's theory of Brownian motion . . . . .	31
3.4	The Langevin equation . . . . .	32
3.5	Diffusion and entropy . . . . .	32
3.6	Classical and quantum diffusion . . . . .	33
3.7	Summary . . . . .	34
<b>4</b>	<b>Hydrogen-Nickel Interactions</b>	<b>36</b>
4.1	Introduction . . . . .	36
4.2	Ab initio materials modelling . . . . .	37
4.2.1	The many-body problem . . . . .	37
4.2.2	Born-Oppenheimer approximation . . . . .	37
4.2.3	The variational method . . . . .	38
4.2.4	Density Functional Theory: The Hohenberg-Kohn theorems . . . . .	39
4.2.5	Density Functional Theory: The Kohn-Sham equations . . . . .	39
4.2.6	Exchange-Correlation functionals . . . . .	42
4.2.7	Periodicity and Bloch's theorem . . . . .	43
4.2.8	The Pseudopotential Approximation . . . . .	44
4.2.9	Calculating forces: The Hellmann-Feynman theorem . . . . .	44
4.2.10	The CASTEP software package . . . . .	45
4.3	The Ni (111) surface . . . . .	45
4.3.1	Convergence testing . . . . .	47

---

4.3.1.1	Convergence of basis set size . . . . .	48
4.3.1.2	Convergence of Brillouin zone sampling . . . . .	49
4.3.1.3	Preparing surface calculations: Bulk geometry optimization . . . . .	50
4.3.1.4	Surface calculations: Convergence of vacuum gap size . . . . .	51
4.3.1.5	Surface calculations: Convergence of slab thickness . . . . .	52
4.3.1.6	Surface calculations: Concentration of H on surface . . . . .	53
4.3.1.7	Summary of CASTEP calculation parameters . . . . .	54
4.4	Embedded Atom Method . . . . .	55
4.4.1	Notes on EAM5 . . . . .	58
4.4.2	Finite size effects . . . . .	59
4.4.2.1	Converging supercell size/number of layers . . . . .	60
4.4.2.2	Minimizing image interactions . . . . .	61
4.4.2.3	Bulk nickel lattice constant using EAM5 . . . . .	61
4.4.2.4	Determination of the (111) surface . . . . .	62
4.5	Summary . . . . .	62
<b>5</b>	<b>Potential Energy Surfaces</b>	<b>64</b>
5.1	Introduction . . . . .	64
5.2	The adiabatic approximation . . . . .	64
5.3	Determining the potential energy surface . . . . .	65
5.4	Fourier interpolation . . . . .	66
5.5	Fourier interpolation potential energy surfaces . . . . .	68
5.5.1	Calculating spring constants . . . . .	69
5.5.1.1	Determining the quality of a least squares fit . . . . .	70
5.6	Results: Calculated potential energy surfaces . . . . .	71
5.6.1	DFT (CASTEP) determined PES . . . . .	72

---

5.6.1.1	Computational details . . . . .	72
5.6.1.2	Interpolation of energies . . . . .	72
5.6.1.3	Interpolation of heights . . . . .	73
5.6.1.4	Interpolation of spring constants . . . . .	74
5.6.2	EAM5 determined PES . . . . .	76
5.6.2.1	Computational details . . . . .	76
5.6.2.2	Interpolation of energies . . . . .	77
5.6.2.3	Interpolation of heights . . . . .	78
5.6.2.4	Interpolation of spring constants . . . . .	79
5.7	Summary . . . . .	81
<b>6</b>	<b>Molecular Dynamics</b>	<b>82</b>
6.1	Introduction . . . . .	82
6.2	Classical mechanics: Hamiltonian formalism . . . . .	83
6.3	Integrating the equations of motion: Velocity Verlet . . . . .	84
6.4	The ergodic hypothesis . . . . .	86
6.5	Ensemble sampling and the thermodynamic limit . . . . .	87
6.6	The canonical ensemble: Thermostatting . . . . .	88
6.6.1	Temperature fluctuations in the canonical ensemble . . . . .	88
6.7	Thermostatting methods . . . . .	90
6.7.1	The Nosé-Hoover thermostat . . . . .	90
6.7.1.1	Non-ergodic behaviour and Nosé-Hoover chains . . . . .	92
6.7.2	The Langevin thermostat . . . . .	92
6.8	Initialization and equilibration . . . . .	94
6.9	Periodic boundary conditions . . . . .	95
6.9.1	Minimum image convention . . . . .	96
6.10	Centre of mass constraint . . . . .	97
6.11	Correlation functions . . . . .	97
6.12	Calculation of the diffusion coefficient . . . . .	99
6.13	Summary . . . . .	100

---

<b>7</b>	<b>Path Integrals in Molecular Dynamics</b>	<b>102</b>
7.1	Introduction . . . . .	102
7.2	From classical to quantum mechanics . . . . .	103
7.2.1	The principle of least action and classical mechanics . . . . .	103
7.2.2	Extension to quantum mechanics . . . . .	104
7.3	The path integral . . . . .	105
7.3.1	Path integrals with variable starting points . . . . .	106
7.3.2	Imaginary time propagators and statistical mechanics . . . . .	107
7.3.3	The free particle density matrix . . . . .	109
7.4	A classical isomorphism – beads and springs . . . . .	110
7.4.1	Capturing quantum effects with ring polymers . . . . .	112
7.5	Path integral molecular dynamics . . . . .	113
7.5.1	Computational details . . . . .	115
7.6	Quantum dynamics . . . . .	115
7.7	Centroid molecular dynamics . . . . .	116
7.7.1	Fundamentals . . . . .	116
7.7.2	Centroid constrained molecular dynamics . . . . .	119
7.7.3	Partially adiabatic centroid molecular dynamics . . . . .	121
7.7.3.1	Normal mode transformation . . . . .	122
7.7.3.2	Enforcing the adiabatic separation . . . . .	124
7.8	Common path integral measurements . . . . .	124
7.8.1	Measuring delocalization: the gyration tensor and radius of gyration . . . . .	124
7.8.2	Thermodynamic energy estimators . . . . .	125
7.9	Summary . . . . .	126

---

<b>8</b>	<b>Diffusion of H/D on the (111) Ni surface</b>	<b>128</b>
8.1	Introduction . . . . .	128
8.2	Classical simulations . . . . .	128
8.2.1	Determination of the timestep . . . . .	128
8.2.2	Determination of Langevin damping time . . . . .	130
8.2.2.1	Computational details . . . . .	132
8.2.2.2	Diffusion coefficients as a function of damping time . . . . .	133
8.2.3	Temperature dependence of the diffusion rate . . . . .	135
8.2.4	Classical trajectories . . . . .	139
8.3	Quantum diffusion . . . . .	141
8.3.1	Convergence of number of beads . . . . .	142
8.3.1.1	Determining the timestep in PIMD simulations . . . . .	142
8.3.1.2	Bead convergence . . . . .	144
8.3.2	Convergence of the adiabaticity parameter . . . . .	146
8.3.3	Temperature dependence of diffusion rate . . . . .	154
8.3.4	Radius of gyration as a function of temperature . . . . .	159
8.3.5	Quantum trajectories . . . . .	161
8.3.6	Ratio of classical and quantum diffusion coefficients . . . . .	165
8.4	Summary . . . . .	167
<b>9</b>	<b>Conclusions</b>	<b>169</b>
9.1	Further work: Improving on the adiabatic approximation . . . . .	170
<b>A</b>	<b>Geometry Optimization</b>	<b>171</b>
	<b>Bibliography</b>	<b>174</b>

# List of Tables

4.3.1	Binding energies for a hydrogen atom placed above a 10 layer thick (111) nickel surface (with a 10Å interslab spacing), as a function of the supercell size (concentration of hydrogen). . . . .	54
4.4.1	Parameters used for calculation of the atomic density of Ni atoms, reproduced from Clementi and Roetti (1974) . . . . .	57
4.4.2	EAM5 parameter set, reproduced from Wonchoba et al. (1995) . . . .	58
4.4.3	Convergence of change in binding energy and maximum force components (for Ni-only and Ni-H systems), relative to an 8x8 supercell, as a function of supercell size (number of repeats along the <b>a</b> and <b>b</b> directions). The results shown are for 7 layers, with an interslab spacing of 15Å, and with a H atom placed 1.5Å above the surface (for the Ni-H systems). All results are presented to 3 significant figures. . . . .	60
5.6.1	The statistics of the energy difference between the interpolated values and the validation set, calculated using DFT. The mean energy difference reduces to meV level for the 8x8 grid, and is reduced to the sub-meV level for the 16x16 grid (with a sub-meV standard deviation).	73
5.6.2	The statistics of the difference in equilibrium hydrogen height between the interpolated values and the validation set, calculated using DFT.	74
5.6.3	The statistics of the difference in spring constant between the interpolated values and the validation set, calculated using DFT. The mean difference in spring constant drops by two orders of magnitude as the grid dimensions increase from 8x8 to 16x16. Note the large standard deviations and maximum differences for grid sizes smaller than the 8x8.	75
5.6.4	The statistics associated with the coefficient of determination (a measure of the quality of the harmonic approximation used for the <b>c</b> dependence of the potential) as a function of the number of grid points. These calculations were based on a least squares fit to the results of geometry optimizations carried out using DFT. . . . .	76

5.6.5	The statistics of the energy difference between the interpolated values and the validation set, calculated using the EAM5 potential. By the 4x4 grid, the mean energy difference is at the sub-meV level, but the maximum energy difference does not decrease to the sub-meV level until the 8x8 grid. . . . .	78
5.6.6	The statistics of the difference in equilibrium hydrogen height between the interpolated values and the validation set, calculated using the EAM5 potential. The 8x8 grid calculated using EAM5 shows similar agreement its validation set as the 16x16 grid calculated using DFT. .	79
5.6.7	The statistics of the difference in spring constant between the interpolated values and the validation set, calculated using the EAM5 potential. There is very little to gain in going from the 8x8 to the 16x16 grid. The 8x8 grid calculated with the EAM5 potential has a similar mean, and a better minimum, maximum and standard deviation than the 16x16 grid generated using DFT. . . . .	80
5.6.8	The statistics associated with the coefficient of determination (a measure of the quality of the harmonic approximation used for the $\mathbf{c}$ dependence of the potential) as a function of the number of grid points. These calculations were based on a least squares fit to the results of geometry optimizations carried out using the EAM5 potential. . . . .	80
8.2.1	Frequency factors and activation energies from the Arrhenius law, for classical H and D on the (111) Ni surface. . . . .	138
8.3.1	Frequency factors and activation energies (given to 3 significant figures) from the Arrhenius law fitted across the entire temperature range, for quantum H and D (16 beads) on the (111) Ni surface. . . .	157
8.3.2	Frequency factors and activation energies (given to 3 significant figures) from the Arrhenius law, for quantum H and D (16 beads) on the (111) Ni surface. In this case, these values are calculated separately for the high and low temperature regions. . . . .	159

# List of Figures

2.3.1	Diffusion rates as a function of temperature for H (left) and D (right) on (111) Ni at a variety of different adsorbate coverages, measured by field emission fluctuation experiments, carried out by Lin and Gomer (1991). Note that we see that there is no obvious correlation between adsorbate concentration and diffusion rate (possibly suggesting uncertainty in the diffusion coefficients). . . . .	24
2.3.2	Diffusion rates as a function of temperature for H and D on (111) Ni, at a coverage of 0.3 ML, measured using laser optical diffraction experiments, carried out by Lee et al. (1993). . . . .	25
2.3.3	Diffusion rates as a function of temperature for H and D on (111) Ni, at a coverage of 0.3 ML, measured using laser optical diffraction experiments, carried out by Cao et al. (1997). These results suggest that the diffusion coefficient varies over several orders of magnitude, and while there is a deviation from Arrhenius behaviour, there appears to be a further significant decrease in the diffusion rates as the temperature decreases past the classical to quantum transition temperature. . . . .	25
4.3.1	The simulation cell for nickel, which exposes the (111) surface to the vacuum. Because Ni is an FCC material, it has ABCA stacking. . . . .	45
4.3.2	Change in binding energy for a hydrogen atom placed in a bulk nickel system (with a 3x3x3 k-point grid) as a function of cut-off energy. The energy change drops to 0.6 meV at a cut-off energy of 725 eV with all energies presented relative to the 750 eV result. . . . .	49
4.3.3	Change in binding energy for a hydrogen atom placed in a bulk nickel system (with a 400 eV cut-off energy) as a function of k-point grid size. The convergence of binding energy is not monotonic as k-point grid dimensions are increased: the zero of energy is defined for 12x12x12 k-point grid. For a 7x7x7 grid, the energy difference is 2.7 meV. . . . .	50

4.3.4	Convergence of binding energy for a hydrogen atom placed 1.5Å above a 4 layer thick (111) nickel surface as a function of interslab spacing. The zero of energy is defined for a 15Å spacing between neighbouring slabs. At 10Å, the change in energy is less than 0.04 meV - this corresponds to a vacuum gap of 8.5Å above the H atom. . . . .	52
4.3.5	Convergence of binding energy as a function of number of layers, for a hydrogen atom placed 1.5Å above a nickel (111) surface, with an interslab spacing of 6Å (4.5Å of vacuum above the H). The cut-off energy was 725 eV, and the k-point grid was 7x7x1. For 10 layers, the change in binding energy reduces to 1.8 meV. . . . .	53
4.4.1	Variation of energy per atom as a function of lattice constant for the EAM potential (5x5 supercell with 6 layers). The lattice parameter is shown to be 3.5208Å. . . . .	61
5.3.1	Top (left) and side (right) view of the nickel slab used for the DFT PES calculations. Due to the symmetry of the slab, the H atom is only scanned along sites in the bottom left quadrant of the (111) surface. .	66
5.6.1	Relative potential energies of a single H atom, interacting with a 2x2 (111) Ni surface, calculated using DFT. The raw data (left), along with the interpolated surface (right), for a 16x16 grid are presented. All energies are shown relative to the global minimum. . . . .	73
5.6.2	Relative binding heights of a single H atom, interacting with a 2x2 (111) Ni surface, calculated using DFT. The raw data (left), along with the interpolated surface (right), for a 16x16 grid are presented. All heights are shown relative to the global minimum. . . . .	74
5.6.3	Effective spring constants approximating the $\mathbf{c}$ dependent harmonic interaction for a single H atom, interacting with a 2x2 (111) Ni surface, calculated using DFT. The raw data (left), along with the interpolated surface (right), for a 16x16 grid are presented. . . . .	75
5.6.4	The position dependence of the coefficient of determination, which was used as a measure of quantifying the quality of the $\mathbf{c}$ dependent harmonic interaction. Calculations modelled a single H atom interacting with a 2x2 (111) Ni surface using DFT. (A 16x16 grid of points was used). . . . .	76
5.6.5	Relative potential energies of a single H atom, interacting with a 5x5 (111) Ni surface, calculated using the EAM5 potential. The raw data (left), along with the interpolated surface (right), for an 8x8 grid are presented. All energies are shown relative to the global minimum. . .	77

5.6.6	Relative binding heights of a single H atom, interacting with a 5x5 (111) Ni surface, calculated using the EAM5 potential. The raw data (left), along with the interpolated surface (right), for an 8x8 grid are presented. All heights are shown relative to the global minimum. . . .	78
5.6.7	Effective spring constants approximating the $\mathbf{c}$ dependent harmonic interaction for a single H atom, interacting with a 5x5 (111) Ni surface, calculated using the EAM5 potential. The raw data (left), along with the interpolated surface (right), for an 8x8 grid are presented. . . .	79
5.6.8	The position dependence of the coefficient of determination, which was used as a measure of quantifying the quality of the $\mathbf{c}$ dependent harmonic interaction. Calculations modelled a single H atom interacting with a 5x5 (111) Ni surface using the EAM5 potential. (An 8x8 grid of points was used). . . .	80
8.2.1	RMS fluctuations of the total energy for H on the (111) Ni PES under the NVE ensemble (with an initial temperature of 250 K), from (1 ns) classical MD trajectories as a function of timestep size. . . .	129
8.2.2	Long time total energy drift of H on the (111) Ni PES under the NVE ensemble (with an initial temperature of 250 K) when the timestep is 2 fs. The red line is a running average taken over a 50 ps interval. . .	130
8.2.3	Diffusion coefficients of classical H and D on the (111) Ni surface, as a function of the Langevin damping time, at a temperature of 75 K. .	133
8.2.4	Diffusion coefficients of classical H and D on the (111) Ni surface, as a function of the Langevin damping time, at a temperature of 250 K.	134
8.2.5	Diffusion coefficients of classical H and D on the (111) Ni surface, as a function of the Langevin damping time, at temperatures of 75 K and 250 K. . . .	135
8.2.6	Mean squared displacements from the classical simulations of H (top) and D (bottom) on (111) Ni, at a range of temperatures. The MSDs pictured were obtained through averaging over MSDs resulting from 20 independent trajectories at each temperature. . . .	136
8.2.7	Diffusion coefficients as a function of temperature for classical simulations of H and D on the (111) Ni surface. . . .	137
8.2.8	Arrhenius plot of the diffusion coefficient as a function of inverse temperature, for classical simulations of H and D on the (111) Ni surface (shown with lines of best fit). . . .	138

8.2.9	The trajectories of H (top, blue) and D (bottom, red) along the Ni (111) PES at a temperature of 75 K. For visualization purposes, these trajectories were plotted from a short 500 ps simulation, with the adsorbate position written out to disk every 10 fs. All other simulation parameters were kept the same as in the calculations which were used to calculate the diffusion coefficients (i.e: a Langevin damping time of 500 fs, and a timestep of 1 fs). . . . .	140
8.2.10	The trajectories of H (top, blue) and D (bottom, red) along the Ni (111) PES at a temperature of 250 K. For visualization purposes, these trajectories were plotted from a short 500 ps simulation, with the adsorbate position written out to disk every 10 fs. All other simulation parameters were kept the same as in the calculations which were used to calculate the diffusion coefficients (i.e: a Langevin damping time of 500 fs, and a timestep of 1 fs). . . . .	141
8.3.1	The mean (top) and RMS fluctuation/standard deviation (bottom) of the virial total energy for H/D on (111) Ni at 75/250 K as a function of timestep size. The PIMD calculations were carried under the normal mode transformation, with 64 beads. . . . .	143
8.3.2	Convergence behaviour of the mean radius of gyration (top) and virial total energy (bottom) as a function of the number of beads, for H/D on (111) Ni at 75/250 K. . . . .	145
8.3.3	Effect of the adiabaticity parameter on the diffusion coefficients for H/D (16 beads) on the (111) Ni surface, at 75 K (top) and 250 K (bottom). Note that only a single short run for each value of adiabatic separation was carried out, and so diffusion coefficients will be a poor estimate to the true value. . . . .	148
8.3.4	The mean radius of gyration of H (top) and D (bottom) on the (111) Ni surface (at 75 K) at varying degrees of adiabatic separation between the centroid and non-centroid modes (16 beads). . . . .	149
8.3.5	The mean radius of gyration of H (top) and D (bottom) on the (111) Ni surface (at 250 K) at varying degrees of adiabatic separation between the centroid and non-centroid modes (16 beads). . . . .	150
8.3.6	The root mean squared fluctuation of the radius of gyration of H (top) and D (bottom) on the (111) Ni surface, at 75 K and 250 K, for varying amounts of adiabatic separation between the centroid and non-centroid modes (16 beads). . . . .	151
8.3.7	Mean virial total energies of H and D on the (111) Ni surface, at 75 K (top) and 250 K (bottom), as a function of the adiabaticity parameter (16 beads). . . . .	152

---

8.3.8	The root mean squared fluctuation of the virial total energy estimator for H and D on the (111) Ni surface, at 75 K and 250 K, as a function of the adiabaticity parameter (16 beads). . . . .	153
8.3.9	Mean squared displacements obtained through quantum (PACMD) simulations of H (top) and D (bottom) on (111) Ni (using 16 beads). These MSDs were taken by averaging over the resulting MSDs from 12 independent trajectories at each temperature. . . . .	155
8.3.10	Diffusion coefficients as a function of temperature for quantum (PACMD) simulations of H and D on the (111) Ni surface (using 16 beads). . . .	156
8.3.11	Arrhenius plot of diffusion rates against inverse temperature from quantum (PACMD) simulations of H and D on the (111) Ni surface (using 16 beads). Presented with a single line of best fit across the whole temperature range. . . . .	157
8.3.12	Arrhenius plot of diffusion rates against inverse temperature from quantum (PACMD) simulations of H and D on the (111) Ni surface (using 16 beads). Presented with a two lines of best fit, this time with one line fitted at high temperatures (from 250 K to 100 K), and another at low temperatures (100 K to 75 K). A sharp break in the gradient between the two lines indicates a possible transition from thermally activated (classical) diffusion to diffusion mediated by tunnelling (quantum diffusion). . . . .	158
8.3.13	The temperature dependence of the mean (top) and RMS fluctuations (bottom) of the radius of gyration for H and D on the (111) Ni surface (using 16 beads). . . . .	160
8.3.14	The ratio of the H to D mean radius of gyration from quantum (PACMD, 16 beads) simulations on the (111) Ni surface as a function of temperature. . . . .	161
8.3.15	Quantum trajectories of the H (top, blue) and D (bottom, red), both represented by a ring polymer (of 16 beads), along the Ni (111) PES at a temperature of 75 K. These plots were generated from a short PACMD trajectory of 200 ps, with the centroid position and radius of gyration outputted to disk every 10 fs. All other simulation parameters were kept identical to those used for the calculation of the diffusion coefficients (16 beads, Langevin damping time of 500 fs and an adiabaticity parameter of 0.01). Here the (darker) points represent the centroid position, with the (lighter) circles representing the radius of gyration of the ring polymer at that point. . . . .	162

- 
- 8.3.16 Quantum trajectories of the H (top, blue) and D (bottom, red), both represented by a ring polymer (of 16 beads), along the Ni (111) PES at a temperature of 250 K. These plots were generated from a short PACMD trajectory of 200 ps, with the centroid position and radius of gyration outputted to disk every 10 fs. All other simulation parameters were kept identical to those used for the calculation of the diffusion coefficients (16 beads, Langevin damping time of 500 fs and an adiabaticity parameter of 0.01). Here the (darker) points represent the centroid position, with the (lighter) circles representing the radius of gyration of the ring polymer at that point. . . . . 163
- 8.3.17 A subset of the quantum trajectories shown in Figure 8.3.16 for H (top, blue) and D (bottom, red) moving along the Ni PES at 250 K. . 164
- 8.3.18 The ratio of H to D diffusion coefficients for classical and quantum (PACMD, 16 beads) simulations on the (111) Ni surface as a function of temperature.  
165
- 8.3.19 The ratio of quantum (PACMD, 16 beads) to classical diffusion coefficients for H and D on the (111) Ni surface as a function of temperature. 166
- 8.4.1 Arrhenius plots of the diffusion coefficient as a function of inverse temperature for classical and quantum (PACMD, 16 beads) of H and D on the (111) Ni surface. Presented with lines of best fit (1 line for classical results, 2 lines for quantum results). . . . . 167

# Acknowledgements

I would like to take this opportunity to thank my supervisor, Professor Matt Probert, for all of the guidance and support he has shown me throughout the years. No matter how difficult a problem I faced, I was always confident that a discussion with him would resolve it.

In addition, my thanks go to Dr Phil Hasnip, whose insight was invaluable and whose reassurance I greatly appreciated.

Over the last few years I have been incredibly privileged to share an office with some very bright and talented people, who I am also fortunate to call my friends. When I started this project, there were often times when I felt out of my depth — were it not for the advice of Jolyon Aarons, early on in this project, I am not sure that I would have ever recovered from this feeling. In addition, I would like to thank Ed Higgins for providing me with countless interesting ideas, as well as his coding know-how — it has helped me learn a lot. Jack Shepherd has been a constant source of amusing tales, late night conversation and strong political opinions. Finally, Jacob Wilkins should be thanked for his interesting trivia and for being a willing participant in many programming related competitions.

In addition to my friends in the office, Rocío Cid Lahoz has also provided me with her friendship and emotional support, especially during the difficult times when I needed it the most. I would also like to thank Karielle for her support and patience, especially during these last few months when I have not been as attentive as I should have been.

The last few years have provided me with some incredibly difficult times — I would like to thank my two cats, Walt and Jesse, for the love and affection that they shared with me. Jesse’s “help” during the writing of this thesis has been greatly entertaining. In particular, I would like to thank Walt for the times that we shared, and for hanging on as long as he possibly could — I’ll miss you.

Finally, I want to thank my family for providing me with all of their support and faith in me over the years — I couldn’t have made it this far without you. I should especially thank my mum for all of the times that she listened to me complain when things didn’t go to plan.

# Declaration

I declare that this thesis is a presentation of original work and I am the sole author. This work has not previously been presented for an award at this, or any other, university. All sources are acknowledged as references.

Signed,

Aaron Russell Hopkinson

# Chapter 1

## Introduction

Computational physics plays an increasingly important role in modern physics. The tremendous increase in computational power, coupled with the decreasing cost, has allowed “computer experiments” to provide a “third way” of probing the behaviour of nature, alongside theory and traditional experiments (Ceperley, 1999).

One of the particular advantages of computer simulations, are that we may often probe length and timescales which may be inaccessible to the experiments of the day. Furthermore, by designing a computational experiment in a careful manner, it is often possible to “switch on” or “off” various physical effects, or levels of approximation, in order to learn more about the relative effects that the approximations may have on the behaviour of the system as a whole — something which would be difficult to do in the real world.

### 1.1 Motivation

It has been observed by many people (Wipf, 1997; Gillan, 1988) that quantum nuclear effects play a particularly important role in the dynamics of systems containing hydrogen, due to its light mass. Failure to properly take account of the quantum effects possessed by hydrogen when determining its dynamics can lead to results which are wildly inaccurate.

Motivated by new experimental techniques (Jardine et al., 2009b,a), which have allowed for the resolution of hydrogen dynamics on time and length scales which were previously inaccessible, the focus of this thesis is to show how quantum nuclear effects play a role in the temperature dependence of the diffusion of hydrogen and deuterium across the (111) nickel surface. This study is made possible through the combination of widely used extension to the molecular dynamics method which allows for the quantum dynamics to be calculated, and a parameterized potential energy surface approach.

## 1.2 Software development

With the exception of the density functional theory calculations which were completed using the CASTEP software package (Clark et al., 2005), all of the results presented in this work were carried out using software developed by the author.

The aforementioned software required a substantial amount of development time, and provides a range of functionality: classical molecular dynamics, centroid/path integral molecular dynamics, geometry optimization, and potential energy surface generation are all possible using this code. In addition to this, the software also contains a preliminary implementation of lattice dynamics functionality, although the work which relates to this functionality did not make it into this thesis.

## 1.3 Outline of the thesis

In Chapter 2, we discuss in more detail the motivation behind this project, as well as the importance of the study of hydrogen/metal systems to materials science. Chapter 3 is concerned with some of the theories used to describe diffusion, and the importance that quantum mechanics has on the diffusion of light objects at low temperatures. Chapter 4 describes two of the methods, density functional theory, and the embedded atom method, which may be used to model hydrogen-nickel interactions (amongst other things). This is followed by Chapter 5 which shows how the methods detailed in the previous chapter may be used to parameterize potential energy surfaces, upon which we can perform our simulations. Chapters 6 and 7 then discuss the molecular dynamics and path integral based molecular dynamics methods, including their background theory and implementation details. Chapter 8 then presents the results of this work, while Chapter 9 concludes the thesis, giving possible avenues for future work.

## Chapter 2

# Hydrogen and Metals

### 2.1 Introduction

The diffusion of hydrogen in metals have been studied for a long time, perhaps beginning with Graham (1866), who, when determining the relative diffusibility of various gases through metals, discovered that hydrogen rapidly diffused through palladium. Since his work, many others have followed, and determined the diffusive properties of hydrogen through a wide variety of metal systems (Wipf, 1997).

This study is more than just an intellectual curiosity, however. It was observed by Johnson (1875) that hydrogen diffusion plays an important role in the embrittlement of metals (particularly steel) — causing it to fail. Since this discovery, the hydrogen embrittlement problem has been the focus of many people, with Bhadeshia (2016) estimating that 38,000 papers have been published on this problem.

The number of studies on hydrogen embrittlement can likely be attributed to the pervasiveness of steel in engineering applications, and the associated risks/costs associated with mechanical failure. One prominent example of structure failure, which was attributed to environmental hydrogen embrittlement, was the failure of a number of anchor rods used to support part of the San Francisco-Oakland bay bridge, only 2 weeks after installation, in 2013 (Chung, 2014).

Given the implications of mechanical failure due to hydrogen embrittlement, it has long been the goal to try and minimize this effect. To this end, a number of proposals have been made: the diffusing hydrogen may be trapped (through the presence of grain boundaries and/or dislocations in the material, or at interfaces between different alloys), or the metal may be coated as a means of preventing the hydrogen from entering (Bhadeshia, 2016).

The rapid diffusion of hydrogen through metals occurs through two distinct mechanisms: there is the classical “hopping” between interstitial sites, due to thermal energy,

and then there is quantum mechanical tunnelling, which plays a significant role due to its light mass.

Although this work does not focus on the study of hydrogen in bulk-metals, it is clear that diffusive processes play an important role in hydrogen interactions with metals, and the study of surface diffusion is a part of a much bigger picture.

## 2.2 Why study surfaces?

Surface science has played an important role in many of the technological developments of the last century; advances in this field have led to the development of many modern semi-conductor based devices, such as integrated circuits, solar cells and thin film transistors.

Although it would be unjust to reduce the field of surface science down to only a handful of papers, it is worthwhile to highlight a handful of important moments in the recent history of this field. One of the key developments was the scanning tunnelling microscope (STM) (Binnig et al., 1982), a device which allowed for the imaging of (typically conductive) surfaces with previously unseen precision, and which gave researchers valuable insight into structure at the atomic scale (far beyond the capabilities of older technologies such as the scanning electron microscope). Beyond simply producing images, the STM was later put to use to show that it was also possible to manipulate individual atoms at the nanoscale, creating nanostructures by design: a noteworthy example of this was the work of Eigler and Schweizer (1990), who placed individual xenon atoms on a nickel surface and were able to spell out their company name, “IBM” — this is perhaps one of the most well known early examples of constructing a nanostructure from individual atoms, rather than etching away surface atoms through lithographic processes, or depositing entire layers of atoms (though, e.g: chemical vapour deposition).

The development of the STM was an important breakthrough, and later led to the creation of the atomic force microscope (AFM) (Binnig et al., 1986), which, in addition to allowing for the imaging of non-conductive materials, is also noted for its ability to measure forces as small as  $10^{-18}$  N. Due to its success in imaging non-conductive materials, the AFM has been used to study a range of systems, including biological ones (e.g: DNA, (Lindsay et al., 1989)) — giving deeper insight into the structure and properties of the biological building blocks of nature. In addition, the AFM has also been used for the study of atomic scale friction (Germann et al., 1993; Krim, 2002; Hirano, 2006) (although as we shall see, this apparatus is not particularly well suited to the study of friction for H/D on Ni(111)).

As well as being a testing ground for nanofabrication techniques, surfaces also often play a fundamental role in chemical catalysis. Many catalytic reactions take place between a

solid catalyst and reactants in the liquid/gas phase (heterogenous catalysis). Here, the surface of the catalyst provides adsorption sites for the reactants, acting to increase the reaction rate through a lowering of the activation energy. Catalysts are both widely used in industry, as well as biologically, where they take the form of enzymes. Two examples of widely known uses of catalysts are: the Haber-Bosch process, which uses an iron catalyst to increase the reaction rate of nitrogen and hydrogen to produce ammonia (commonly used as a fertilizer), and the use of (commonly) platinum as a catalyst in the catalytic converter of a car exhaust, which acts to reduce some of the more harmful emissions leaving the vehicle (Burton et al., 2000). Therefore, the study of surfaces (in particular, metals, which are often catalysts), are important as they may have a direct impact on future industrial processes.

Fundamentally, surface science arises out of the desire to understand the physical processes which take place at surfaces — these can be very different from the bulk, due to the abrupt change in the local environment. Since all physical systems are finite in size, surfaces are an inescapable fact of nature, and must be studied if we seek a complete description of reality.

### 2.3 H/D diffusion on the (111) Ni surface

As we have already seen, the quantum nuclear effects play a large role of the diffusion of hydrogen *within* metals, this is also true of hydrogen *on* metals. The light mass of hydrogen means that its surface dynamics are heavily influenced by quantum nuclear effects. It has been experimentally observed that there is evidence of quantum diffusion on the surface of nickel even at relatively high temperatures (with transitions reported at around 100 K to 125 K) (Lin and Gomer, 1991; Lee et al., 1993; Cao et al., 1997). One experimental group in particular (Cao et al., 1997) have reported that the diffusion rate of hydrogen on nickel may vary by as many as 8 orders of magnitude over a relatively small temperature range (65 K to 240 K), with a decrease of around 3 orders of magnitude after the transition temperature (to quantum tunnelling mediated diffusion) reported by other groups (see Figure 2.3.3).

Figures 2.3.1, 2.3.2 and 2.3.3 show the temperature dependence of the diffusion rate of both hydrogen and deuterium along the (111) Ni surface, from three different experimental groups. By comparing the differences between these sets of experimental results, we are able to gain an appreciation of the difficulty faced in the measurement of accurate diffusion rates.

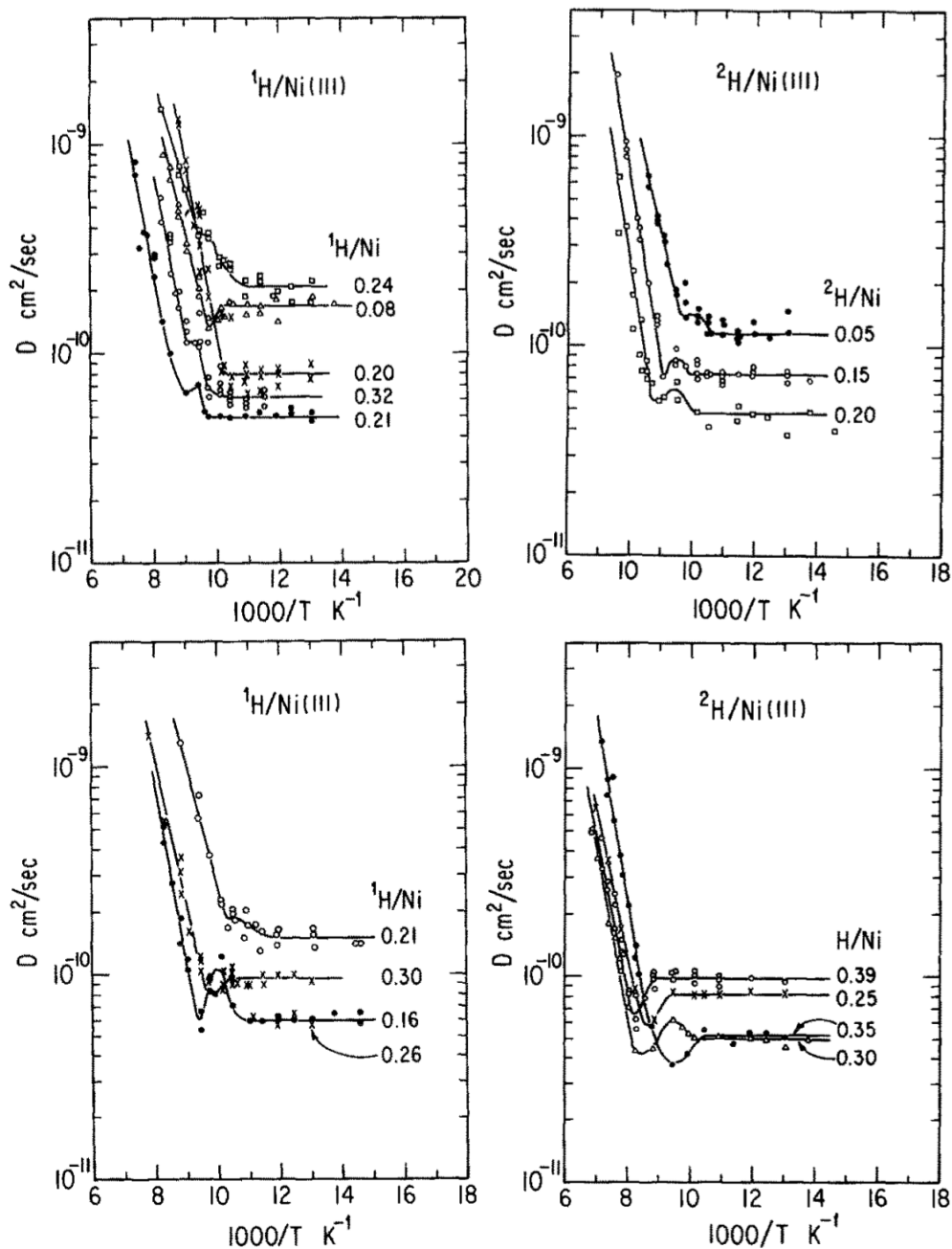


Figure 2.3.1: Diffusion rates as a function of temperature for H (left) and D (right) on (111) Ni at a variety of different adsorbate coverages, measured by field emission fluctuation experiments, carried out by Lin and Gomer (1991). Note that we see that there is no obvious correlation between adsorbate concentration and diffusion rate (possibly suggesting uncertainty in the diffusion coefficients).

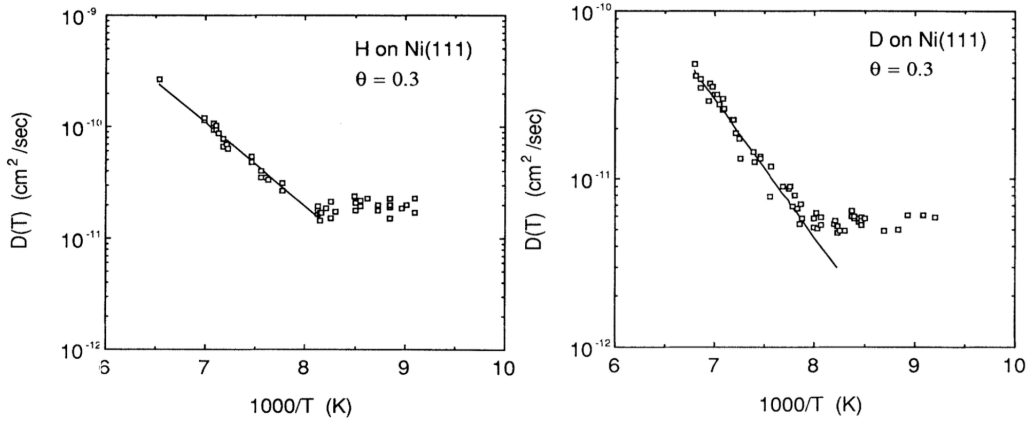


Figure 2.3.2: Diffusion rates as a function of temperature for H and D on (111) Ni, at a coverage of 0.3 ML, measured using laser optical diffraction experiments, carried out by Lee et al. (1993).

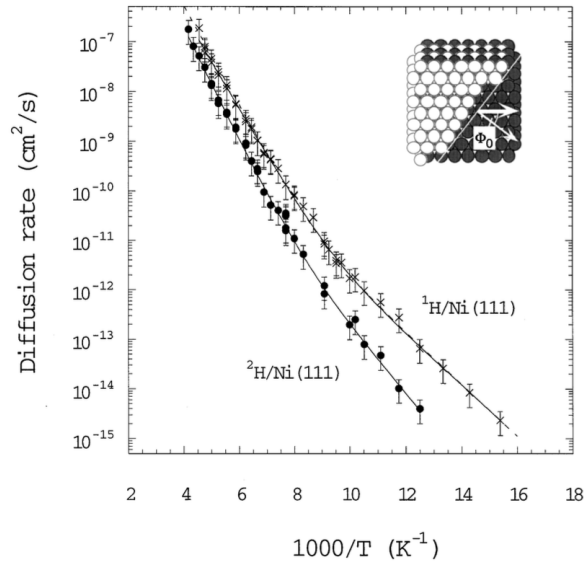


Figure 2.3.3: Diffusion rates as a function of temperature for H and D on (111) Ni, at a coverage of 0.3 ML, measured using laser optical diffraction experiments, carried out by Cao et al. (1997). These results suggest that the diffusion coefficient varies over several orders of magnitude, and while there is a deviation from Arrhenius behaviour, there appears to be a further significant decrease in the diffusion rates as the temperature decreases past the classical to quantum transition temperature.

As we have already seen, the study of the diffusion of H/D on (111) Ni is interesting because there has been a degree of discrepancy between the diffusion rates reported by several experimental groups, even when comparing results across an identical temperature range.

In recent years, a promising new experimental technique, based on the method of helium spin-echo interferometry, has been developed (Jardine et al., 2009b,a). This technique allows for the accurate measurement of fast diffusive dynamics across surfaces at previously inaccessible length and time scales (beyond the capabilities of e.g: STM/AFM,

which operates on much longer timescales), and has already been successfully used to characterise the diffusion of hydrogen across Pt and Ru surfaces (Jardine et al., 2010; McIntosh et al., 2013). In addition to these studies, the same experimental group have also gathered data on the diffusion of both hydrogen and deuterium along the (111) nickel surface — these results have suggested diffusion rates which are significantly faster than previously reported (preliminary results suggesting diffusion rates of  $\sim 10^{-6}$  to  $10^{-7}$  cm<sup>2</sup>/s across a temperature range of 250 K to 125 K, and transition temperatures of approximately 170 K) (Zhu and Ward, 2013).

The difference between the newer helium spin-echo experimental results, and the older ones shown above, are suspected to be a consequence of the older experimental apparatus being unable to track the fast adsorbate at the time scales required in order to accurately determine the diffusion rates (Zhu and Ward, 2013).

In addition to the new experimental results mentioned above, theoretical studies within the same group, based on the application of combined band structure/transition state theory calculations have also shown that the diffusion of deuterium is unable to be explained by a simple mass rescaling of their hydrogen calculations — suggesting that a full quantum nuclear treatment of the adsorbates is required in order to accurately model the diffusive behaviour.

The desire of this project is therefore to shed light on this apparently anomalous behaviour, and determine whether the widely used path integral based molecular dynamics based methods (Berne and Thirumalai 1986; Tuckerman et al. 1993; Cao and Voth 1993) are able to correctly predict the diffusion of hydrogen and deuterium on this surface. Ideally, we would like to do this in an *ab initio* manner, but the calculation of magnetic materials is computationally demanding — making the dynamics calculations prohibitively expensive to tackle using a “brute force” application of density functional theory. Therefore, in order to improve the feasibility of these calculations, a potential energy surface based approach has been used which vastly reduces the computational resources required to study this problem.

### 2.3.1 Related work

In collaboration with the surface science group at the University of Cambridge (McIntosh et al., 2013), a previous project within the group at York (Aarons, 2013) tackled the problem of describing the quantum dynamics of hydrogen on a ruthenium surface in order to theoretically describe the some of aforementioned experimental results. This previous project shares many similarities with this current work, but also some key differences.

The approach of the previous project was, like this one, to model the metal surface using a simple model potential (parameterized to density functional theory calculations), and

then to use this model potential to calculate the quantum dynamics of the hydrogen adsorbate, though the method of partially adiabatic centroid molecular dynamics.

This project differs in two key areas however — in the previous project, the objective was to use a Langevin thermostat as a simple model for atomic scale friction, and to specifically tune the parameters of that thermostat so that the dynamics could give quantitative agreement to experiment — essentially, treating the damping time of the thermostat as a physical parameter, giving interpretation to the experimental results.

In this project, the goal is not to reproduce the experimental results by adjusting the thermostat so as to match the experimental data, but to try and predict the adsorbate dynamics based on a few simple assumptions, in order to determine which of the ingredients are missing from our model. It is hoped that, even if our predictions do not turn out to agree with experiment, we may gradually refine our model, through a reduction in the number of approximations, in order to learn more about the underlying processes which affect the dynamics of adsorbates on surfaces.

Because we wish to describe the adsorbate-metal interaction as accurately as possible, the model potential which is used for this study also differs from that used in the previous study, as it has been designed to allow for a more accurate representation of the true potential energy surface, rather than being a minimal model.

The second key difference is that the previous study considered only the dynamics of hydrogen, whereas this project involves the determination of the dynamics of both hydrogen and deuterium, allowing us to quantify the different effects which result in the variation of the diffusion rates of the two adsorbates. This is a particularly interesting problem because hydrogen and deuterium are chemically identical, and they should therefore should bind to the surface in the same manner — any difference which arises in the diffusion must be related to the quantum nuclear effects of the adsorbate, especially if the change in diffusion is not simply explained by rescaling the mass of a classical hydrogen atom.

## 2.4 Summary

In this section we described the motivation behind this project, surveyed some of the existing experimental data, and mentioned how the development of new experimental equipment has necessitated further study into this system. We then drew comparisons between this work and previous work which was carried out within the group, describing the key similarities and differences between the projects. In the following chapter we will give a brief explanation of what is meant by diffusion, describe some of the different theoretical descriptions of diffusion, and we shall state how quantum diffusion differs from classical diffusion.

## Chapter 3

# Diffusion

### 3.1 Introduction

Diffusive processes are all around us, playing important roles in chemistry and biology — it is no exaggeration say that we depend on them to live: within the body, the transport of materials across capillary walls, into and out of blood, occurs mainly by diffusion (Sherwood, 2007). We do not only see examples of diffusion when we look down the microscope: tea spreading out to fill a cup of water, and a cloud of smoke expanding to fill a room are both everyday examples of diffusion which can be seen with the naked eye.

There have been several equally powerful descriptions of diffusion over the years. From the macroscopic viewpoint of Fick (1855), who showed how diffusion could be understood by considering concentrations of substance, through to the microscopic approaches of Einstein (1905) and Langevin (1908), who concerned themselves with the motion of individual atoms/molecules, the study of diffusion has told us a lot about the world. The studies of Einstein in particular, originally motivated by the observations of Brown (1828), helped to guide experiment to some of the first experimental evidence confirming the existence of atoms.

Most generally, diffusion refers to the tendency of matter to move from regions of high concentration to regions of low concentration — this is the intuitive picture that we have when we consider how smoke clouds fill a room. In the microscopic world, kinetic theory tells us that this behaviour actually emerges out of the collisions with nearby particles, but on the macroscopic system, we do not see these collisions, only their effects. Due to the large number of degrees of freedom involved in modelling microscopic scale diffusion, Langevin showed that these collisions can often be modelled through the use of random variables – for this reason, the motion of diffusing particles is often described as “random”.

In this chapter, we shall give a very brief summary of the results of Fick, Einstein and Langevin, who each contributed a different way of viewing diffusive processes. This

is then followed by an explanation of the difference between classical and quantum diffusion, and how this can lead to (approximately) temperature independent diffusion.

## 3.2 Fick's laws of diffusion

The macroscopic theory of diffusion is succinctly captured Fick's laws (1855; 1995). These laws show us that concentration gradients in an amount of substance gives rise to diffusive fluxes, and that by considering these diffusive fluxes, we are able to determine the concentration profile at all instances of time.

We begin with the first of Fick's laws, which states that the diffusion flux,  $\mathbf{J}$ , which is the amount of substance flowing per unit area per unit time, is caused by the presence of a gradient in the concentration,  $\varphi$ , which acts to reduce it:

$$\mathbf{J}(\mathbf{r}, t) = -D\nabla\varphi(\mathbf{r}, t) \quad (3.2.1)$$

i.e. there is a diffusive flux which acts to cause substance to flow from regions of high concentration to regions of low concentration (with a rate proportional to how sharp the concentration gradient is). The constant of proportionality in this equation,  $D$ , is known as the diffusion constant.

We note that, while for a system at thermal equilibrium, there may be no *net* flux because the concentration is macroscopically equal everywhere, locally there will still be diffusive motion.

The second of Fick's laws explains how the concentration of a substance undergoing diffusion changes over time. This is more commonly known as the diffusion equation:

$$\frac{\partial\varphi(\mathbf{r}, t)}{\partial t} = D\nabla^2\varphi(\mathbf{r}, t). \quad (3.2.2)$$

In the following two subsections we attempt to show how these two results are true.

### 3.2.1 Derivation of Fick's first law

In order to see how Fick's first law arises, we reproduce the excellent derivation of Berg (1993).

We assume that, there are initially a collection of particles, with  $N(x)$  particles at  $x$  and  $N(x + \delta x)$  particles at  $x + \delta x$ . As we evolve the system through time, we assume that each particle has an equal probability of moving to either the left, or the right.

If there is a surface/barrier at the mid-point between  $x$  and  $x + \delta x$ , which allows particles to move freely, then, at the next timestep ( $t + \delta t$ ), we expect  $N(x)/2$  particles to move across a barrier, from left to right — and  $N(x + \delta x)/2$  particles will move across from right to left.

Therefore, the net number of particles which flow through the barrier, from left to right, is

$$\frac{1}{2}N(x) - \frac{1}{2}N(x + \delta x). \quad (3.2.3)$$

The flux,  $J_x$ , is the flow of this number of particles flowing through an area  $A$  in the time period,  $\delta t$ :

$$J_x = \frac{N(x) - N(x + \delta x)}{2A\delta t}. \quad (3.2.4)$$

Recognising that  $A\delta x = V$  (where  $V$  is the volume), and that  $\varphi = N/V$  (i.e. a concentration), we can rewrite Equation 3.2.4 as

$$J_x = -\frac{(\delta x)^2}{2(\delta t)} \frac{[\varphi(x + \delta x) - \varphi(x)]}{\delta x}, \quad (3.2.5)$$

which, if we replace  $(\delta x)^2/2(\delta t) = D$ , for reasons which will be clear shortly, we arrive at

$$J_x = -D \frac{[\varphi(x + \delta x) - \varphi(x)]}{\delta x}. \quad (3.2.6)$$

The 1-dimensional form of Fick's first law, may then be found by taking the limit as  $\delta x \rightarrow 0$ :

$$J_x = -D \frac{\partial \varphi}{\partial x}. \quad (3.2.7)$$

Hence, the tendency of particles to move from regions of high concentration to low concentration arises as emergent behaviour from the equal probability of a particle being able to move along each spatial direction.

### 3.2.2 Derivation of Fick's second law

Fick's second law can be shown to form as a consequence of the first law (arising from the equal probability of a particle moving along each direction), and the continuity equation, which conserves the amount of substance.

To show this, if we enforce that the flux out of a closed surface is equal to the rate of change of amount of substance (there are no sinks or sources of particles), then the continuity equation is

$$\frac{dN}{dt} + \oint_S \mathbf{J} \cdot d\mathbf{S} = 0, \quad (3.2.8)$$

where  $\mathbf{J}$  is the flux of particles,  $d\mathbf{S}$  is an infinitesimal vector which is normal to the surface, and  $N = \iiint \varphi dV$ , which is the amount of substance contained within the volume enclosed by the surface.

By making use of the divergence theorem:

$$\iiint_V (\nabla \cdot \mathbf{J}) dV = \oint_{S(V)} \mathbf{J} \cdot d\mathbf{S}, \quad (3.2.9)$$

we may transform into into the differential form of the continuity equation:

$$\frac{\partial \varphi(\mathbf{r}, t)}{\partial t} + \nabla \cdot \mathbf{J}(\mathbf{r}, t) = 0. \quad (3.2.10)$$

Assuming Fick's first law (Equation 3.2.1) to be true, we can substitute into the differential form of the continuity equation (3.2.10) to arrive at Fick's second law (Equation 3.2.2).

### 3.3 Einstein's theory of Brownian motion

When considering the motion of particles which was observed by Brown (1828), Einstein (1905; 1926) was able to determine their distribution functions — the results of his work showed the relationship between the motion of Brownian particles, and the diffusion laws of Fick.

While we do not reproduce the derivation, one of the key results that Einstein determined, was that the mean displacement of Brownian particles was proportional to the square root of the time (between observations) — furthermore, this constant of proportionality is related to the diffusion coefficient. The central result of Einstein, can be summarised in Equation 3.3.1:

$$\frac{d\langle r^2(t) \rangle}{dt} = 2\nu D, \quad (3.3.1)$$

where  $r^2(t)$  is the squared displacement of the particle from its starting position,  $\nu$  represents the dimensionality of the system (3 in our case), and  $D$  is the diffusion coefficient identified in Fick's laws.

This proves to be an important result, because, as we shall see (Section 6.12), the mean squared displacement of particles is straightforwardly measured in a molecular dynamics simulation, allowing for the diffusion rate to be determined through computer simulation.

### 3.4 The Langevin equation

Following the work of Einstein, Langevin (1908) later derived an entirely new method for modelling Brownian motion, based on stochastic variables. While Einstein's work focused on describing the distribution function of Brownian particles, Langevin took a different route, and was able to derive the equations of motion of the particles. He did so by considering that the force on Brownian particles could be described as having a balance between a viscous drag term (proportional to the particle's velocity, with a constant of proportionality,  $\gamma$ , which depends on the viscosity of the suspending fluid), and a stochastic "complementary force",  $\eta$ , which represents the buffeting of the particle by other particles. This is expressed mathematically as:

$$m \frac{d^2 \mathbf{r}}{dt^2} = -\gamma \frac{d\mathbf{r}}{dt} + \eta(t). \quad (3.4.1)$$

In a later section (6.7.2), we shall use the Langevin equation of Equation 3.4.1 as a means of providing temperature control in molecular dynamics systems, but we note that its original purpose was to describe the motion of diffusing Brownian particles.

The success of Langevin's approach led to his work being described as providing "the 'F = ma' of stochastic physics" (Lemons and Gythiel, 1997).

### 3.5 Diffusion and entropy

Diffusion can be thought of as arising as a natural consequence of the second law of thermodynamics: i.e: diffusive motion increases the entropy (disorder) of a system. For example, when a drop of ink diffuses throughout a glass of water, the dispersion of the ink throughout the water occurs as the system goes from a highly ordered, to a more disordered state.

It can be shown that the Einstein relationship of Brownian motion can also be derived from entropic considerations: by starting with Boltzmann's equation, and considering the balance between a radial diffusional driving force which acts to increase the distance of a Brownian particle as a function of time, and a viscous drag force which acts against the motion of the particle, Neumann (1980) was able to show that the Einstein relationship is able to be derived exclusively from the consideration of the entropy of the Brownian system.

Since the Langevin equation is known to be equally valid to the Einstein relationship in the description of Brownian motion, we are justified in assuming that the Langevin equation should also give rise to an increase in entropy. This should not be surprising, because Neumann's assumption that there is a balance between the diffusional driving force and the viscous drag force (whose ensemble averages are equal) is a similar argument to that of Langevin, who balanced the viscous drag against the complementary force in his equation.

### 3.6 Classical and quantum diffusion

In order to appreciate how the motion of hydrogen/deuterium moving across the nickel surface differs at low temperatures to how it behaves at high temperatures, we should take a moment to consider the mechanism behind quantum diffusion.

We know that, at higher temperatures, (the classical regime) the kinetic theory approach involving collisions with other particles works well to describe diffusion at the microscopic level — we can also see through the laws of Einstein and Langevin how these collisions lead to the macroscopic properties described by Fick. When considering the motion of an atom moving along a surface, the diffusive process occurs through a thermal “hopping” between sites. That is, the kinetic energy of the atom is sufficiently high that it is able to overcome potential energy barriers, and move between different energy minima — while there may be periods where an atom is trapped inside a potential well for a short period of time, it is not long before it either gains kinetic energy due to a collision, or the vibrational modes of the underlying surface lead to the creation of a new low energy pathway (with the exact mechanism depending on the system of interest).

As the temperature of the system decreases, we know that the thermal motion of particles becomes “frozen out”, and classically the adsorbate no longer possesses enough kinetic energy to move over an energy barrier. Fortunately, at low temperatures, where the quantum mechanical zero point energy becomes comparable with the size of the energy barrier, and the delocalization of the particle becomes apparent, the particle is able to tunnel through the energy barrier rather than going “over” it.

This means that there will be certain temperatures for which the diffusive motion will be correctly described by classical mechanics, and there will be certain temperatures where only quantum mechanics is able to provide an accurate description of the motion. This change in diffusive regimes leads to a change in the temperature dependence of the diffusion rate.

The diffusion rate is commonly related to the temperature,  $T$ , through the empirical Arrhenius equation (Atkins and de Paula, 2006):

$$D = A \exp\left(\frac{-E_a}{k_B T}\right), \quad (3.6.1)$$

where  $A$  is a constant, often known as the frequency factor, and  $E_a$  is the activation energy associated with an energy barrier ( $k_B$  is the usual Boltzmann constant).

When quantum motion becomes important, as previously stated, there becomes a change in the temperature dependence of the diffusion rate — this may be interpreted as a change in the activation energy required for a particle to move over a barrier. This can easily be demonstrated by plotting what is known as the Arrhenius plot.

The Arrhenius plot can be created through plotting the logarithm of the diffusion rate against the inverse temperature (Equation 3.6.2):

$$\ln(D) = \ln(A) + \left(\frac{-E_a}{k_B}\right) \left(\frac{1}{T}\right). \quad (3.6.2)$$

If there is a quantum mechanical change in the activation energy, then we would see that there is no longer a single gradient which spans the whole temperature range. This deviation from the Arrhenius equation is known as non-Arrhenius behaviour.

In order to determine at what point quantum effects may play a role, we may consider the calculation of the thermal de Broglie wavelength,  $\lambda$  (Atkins and de Paula, 2006):

$$\lambda = \frac{h}{\sqrt{2\pi m k_B T}}. \quad (3.6.3)$$

Note that there is a dependence of both the temperature, as well as the mass ( $m$ ) of the particle on the de Broglie wavelength — this means that a decrease in either quantity will increase the wavelength, and therefore increase the degree of delocalization of the particle.

More specifically, in a bulk, if the thermal de Broglie wavelength becomes comparable to the separation between neighbouring sites, then it is clear that quantum nuclear effects need to be considered, because the particle will likely be sufficiently delocalized for there to be a non-zero probability of tunnelling into this site.

### 3.7 Summary

In this chapter we have summarized how the works of Fick, Einstein and Langevin have led to the development of the equations associated with diffusive processes. We note that the Einstein relationship will play a particularly important role in the calculation of diffusion coefficients from molecular dynamics simulations. Finally, we ended this

chapter with a discussion of the role of quantum mechanics on low temperature diffusion, as well as how this process can lead to a deviation from the empirical Arrhenius equation.

In the following chapter we shall explain how the interactions between hydrogen (or deuterium) can be modelled, in order to calculate their energies of interaction, or the forces interacting between them, in order to perform the dynamics calculations which will allow us to calculate the diffusion.

## Chapter 4

# Hydrogen-Nickel Interactions

### 4.1 Introduction

The diffusion of an adsorbate is sensitive to the energy barriers which are encountered as it moves along the surface. It is therefore crucially important that the underlying interactions between the atoms of the surface and the adsorbate are described as accurately as possible. Unfortunately, the most accurate methods often prove to be the most demanding, and compromises sometimes have to be made based on the resources which are available at the time.

This chapter provides a brief overview of two methods which may be used to model the interactions of hydrogen/deuterium adsorbates on nickel surfaces — density functional theory, and the embedded atom method. While density functional theory provides an incredibly accurate (*ab initio*) description of the underlying interactions, it is also computationally demanding, which makes the calculation of diffusion constants using molecular dynamics incredibly time consuming. The embedded atom method is a semi-empirical method, which proves to be the least accurate of the two methods, but is significantly less demanding than density functional theory.

The interaction schemes described in this chapter are ultimately used to calculate approximate potential energy surfaces (described in Chapter 5). These potential energy surfaces may then be used to perform molecular dynamics studies with similar accuracy as direct application of the methods discussed in this section, albeit with significantly reduced computational costs.

Throughout this chapter, no distinction shall be made between hydrogen and deuterium, as they share identical chemical properties.

## 4.2 Ab initio materials modelling

### 4.2.1 The many-body problem

The properties of materials are (neglecting relativistic effects) determined by the Schrödinger equation:

$$i\hbar \frac{\partial \Psi}{\partial t} = \hat{H} \Psi. \quad (4.2.1)$$

The most obvious way of calculating atomic interactions, would therefore be to solve the Schrödinger equation to find the many-body wavefunction,  $\Psi = \Psi(\{\mathbf{r}_i, i = 1, \dots, N\}, \{R_I, I = 1, \dots, M\}, t)$ . In this case, the system being studied is composed of  $N$  electrons and  $M$  nuclei.

For our system of interest, the many-body Hamiltonian can be written as

$$\hat{H} = -\frac{\hbar^2}{2} \left( \sum_{i=1}^N \frac{1}{m_e} \nabla_i^2 + \sum_{I=1}^M \frac{1}{m_I} \nabla_I^2 \right) + \frac{e^2}{4\pi\epsilon_0} \left( -\sum_{i=1}^N \sum_{I=1}^M \frac{z_I}{r_{iI}} + \sum_{i=1}^N \sum_{j>i}^N \frac{1}{r_{ij}} + \sum_{I=1}^M \sum_{J>I}^M \frac{z_I z_J}{R_{IJ}} \right). \quad (4.2.2)$$

For all but the smallest systems, direct solution of the Schrödinger equation is impossible, owing to the large memory and computation requirements. In order to make calculating properties of large systems from first principles computationally viable, there are a number of approximations that can help to simplify the problem. Let us start by describing one such approximation, the Born-Oppenheimer approximation, which allows us to reduce the complexity of the problem significantly.

Henceforth, in order to simplify the equations, we make use of a system of units (atomic units), such that  $e = m_e = \hbar = 1/(4\pi\epsilon_0) = 1$ .

### 4.2.2 Born-Oppenheimer approximation

The Born-Oppenheimer approximation (Born and Oppenheimer, 1927) states that, since the electrons are much less massive than the nuclei, the many-body problem can be decoupled into separate Schrödinger equations for the electrons and the nuclei. From the point of view of the electrons, the nuclei can be considered a collection of static charges, and hence enter into the electronic Hamiltonian in the form of an external potential. The resulting Born-Oppenheimer Hamiltonian (for the electrons) is given as

$$\hat{H} = \sum_i \left[ -\frac{1}{2} \nabla_i^2 + V_{\text{ext}}(\mathbf{r}_i) \right] + \frac{1}{2} \sum_{i,j,i \neq j} \frac{1}{|\mathbf{r}_i - \mathbf{r}_j|}. \quad (4.2.3)$$

The external potential,  $V_{\text{ext}}(\mathbf{r}_i)$  is simply the Coulomb interaction between the electrons and nuclei. For such a collection of static nuclei, the nuclear Coulomb interaction is simply a constant shift in energy and is therefore not included in the electronic Hamiltonian above.

In the type of calculations we are considering, we concern ourselves with only the electronic ground state (which governs many material properties), and until path integral molecular dynamics based methods are considered (Chapter 7), the nuclei are treated classically. Such nuclei, when their dynamics are considered, will move under the influence of a potential which is generated by an electronic configuration which responds instantaneously to a change in the nuclear configuration. This instantaneous response of the electrons means that the solution of the time independent form of the Schrödinger equation, rather than the time dependent form, can be sought. This is the basis of what is known as Born-Oppenheimer molecular dynamics: for a given nuclear configuration, a Schrödinger-like equation is solved to find the electronic ground state, the forces acting on the nuclei due to such a configuration are calculated, and the positions of the nuclei are evolved, the process then being repeated as necessary.

Because the Born-Oppenheimer approximation allows us to reduce the problem of solving the time dependent Schrödinger equation for both the nuclei and the electrons, into one of solving the time independent Schrödinger equation for only the electrons, henceforth we shall replace  $\Psi(\{\mathbf{r}_i\} \{\mathbf{R}_I\}, t)$  with  $\psi(\{\mathbf{r}_i\})$  to make clear this reduction in complexity.

### 4.2.3 The variational method

The variational method (described in Springborg (2000); Thijssen (2007)) provides a computationally convenient way of calculating energies which are consistent with the Schrödinger equation (particularly the ground state). By recasting the problem as a minimization problem, the variational method allows for a wide variety of computational algorithms to be employed, improving the efficiency of quantum mechanical calculations.

We note that the expectation value of the energy can be considered a functional of the wavefunction,  $E[\psi]$ . Because the ground state energy is, by definition, the lowest possible energy state of the system, *any* trial wavefunction can be chosen, and minimized with respect to the free parameters of the wavefunction in order to calculate an upper bound on the ground state energy,  $E_0$ , provided that the constraint of orthonormality is satisfied:

$$E[\psi] = \min_{\psi} \langle \psi | \hat{H} | \psi \rangle \geq E_0. \quad (4.2.4)$$

When the wavefunction is represented by a linear expansion of basis functions and the size of basis sets increases, the wavefunction has greater freedom to accurately

represent the true ground state wavefunction, and so the upper bound for the ground state energy decreases. In the limit of the complete basis set, the minimization of the energy functional gives the true ground state energy.

The variational method allows for the determination of reasonable ground state energies, even when the underlying wavefunction may be a poor approximation to the true wavefunction.

#### 4.2.4 Density Functional Theory: The Hohenberg-Kohn theorems

The Born-Oppenheimer approximation has justified the simplification of the nuclear and electronic many-body problem to that of only the electrons. Unfortunately the direct solution of the Schrödinger equation (to find the many-body wavefunction), even for many electrons moving under the influence of an external potential, still proves to be intractable due to the large number of degrees of freedom involved in the electron-electron interactions. By seeking only the ground state, and making use of the work of Hohenberg and Kohn (1964), the problem can be simplified further still.

The Hohenberg-Kohn theorems state that:

1. The ground state energy of a system of electrons is uniquely determined by the ground state electron density.
2. The ground state electron density can be found by minimizing some energy functional,  $E[n]$ , with respect to the electron density.

In principle, this means that the calculation of the many-body wavefunction is unnecessary, and our efforts should instead be focused on finding the ground state electron density,  $n(\mathbf{r})$ . This concept underpins the method known as *density functional theory*. The reduction of the problem of finding a  $3N$ -dimensional wavefunction into one of finding a 3-dimensional electron density, with no loss of accuracy, is what makes density functional theory so remarkable.

#### 4.2.5 Density Functional Theory: The Kohn-Sham equations

While Hohenberg and Kohn laid the foundations for density functional theory by stating that the ground state energy could be uniquely determined by the minimization of some energy functional,  $E[n]$ , it was not until the later work by Kohn and Sham (1965) that the form of  $E[n]$  was determined and density functional theory could be applied as a computational scheme. A brief overview of the method of Kohn and Sham is reproduced below.

Under the Born-Oppenheimer approximation, the energy functional,  $E[n]$ , is separated out into two parts:

$$E[n] = F[n] + \int V_{\text{ext}}(\mathbf{r}) n(\mathbf{r}) d^3r, \quad (4.2.5)$$

where the first part of the energy functional,  $F[n]$ , is a functional that depends only on the electron-electron contributions to the energy, and the second term contains the electron-ion interactions (which are in the form of a static external potential).

The electron-electron contribution (of Equation 4.2.5) is then further divided into three parts:

$$F[n] = T[n] + \frac{1}{2} \int \int n(\mathbf{r}') \frac{1}{|\mathbf{r} - \mathbf{r}'|} n(\mathbf{r}) d^3r d^3r' + E_{\text{xc}}[n], \quad (4.2.6)$$

$T[n]$  is the kinetic energy contribution to the functional, the second term is the Hartree potential (the potential generated by a collection of static charges), and  $E_{\text{xc}}[n]$  is the so-called exchange-correlation functional. This exchange-correlation functional contains all of the many-body effects which are not accounted for in the rest of the functional. Exchange arises due to the Pauli exclusion principle, and the requirement that any wavefunction is anti-symmetric on the exchange of two electrons, while correlation includes effects due to their correlated nature — that is to say, the effect that the position of electrons will have on the other electrons in the system.

Unfortunately, although the work of Hohenberg and Kohn removes the need to calculate the wavefunction *in principle*, the determination of the kinetic energy,  $T[n]$ , proves to be impossible without requiring some wavefunction-like objects. These wavefunction-like objects ( $\psi_i$ ) are known as the Kohn-Sham orbitals, which are fictitious, non-interacting, single electron wavefunctions, and are constructed to be consistent with the ground state electron density,  $n(\mathbf{r})$ :

$$n(\mathbf{r}) = \sum_{i=1}^N |\psi_i(\mathbf{r})|^2. \quad (4.2.7)$$

After the introduction of these fictitious wavefunctions, the kinetic energy,  $T$ , can be calculated in the usual way:

$$T = -\frac{1}{2} \sum_{i=1}^N \nabla^2 \psi_i. \quad (4.2.8)$$

This leads to a (semi-)complete description of the energy functional we seek to minimize, where all of the unknown contributions to the energy functional are now packaged together inside the exchange-correlation functional,  $E_{\text{xc}}[n]$ :

$$E[n] = T + \frac{1}{2} \int \int n(\mathbf{r}') \frac{1}{|\mathbf{r} - \mathbf{r}'|} n(\mathbf{r}) d^3r d^3r' + E_{\text{xc}}[n] + \int V_{\text{ext}}(\mathbf{r}) n(\mathbf{r}) d^3r. \quad (4.2.9)$$

Of course, there will be a difference between the kinetic energy of the true many-body wavefunction, and the kinetic energy of the non-interacting Kohn-Sham orbitals — this contribution to the energy has also been placed into the exchange-correlation functional.

It is important to note that both Hohenberg-Kohn theorems, and the Kohn-Sham method are essentially exact. If the exchange-correlation functional were known exactly, then density functional theory would give results (for the ground state) in complete agreement with the solution of the Schrödinger equation. Unfortunately, the exchange-correlation function is not known, and must instead be approximated.

With the energy functional known (and a suitable approximation for  $E_{\text{xc}}$  chosen), the ground state energy can be calculated by making use of the variational method, and solving the Kohn-Sham equations (minimizing the energy functional):

$$\left[ -\frac{1}{2}\nabla^2 + V_{\text{eff}} \right] \psi_i = \varepsilon_i \psi_i. \quad (4.2.10)$$

Equation 4.2.10 introduces an effective potential,  $V_{\text{eff}}$ , which has the form:

$$V_{\text{eff}}(\mathbf{r}) = \int n(\mathbf{r}') \frac{1}{|\mathbf{r} - \mathbf{r}'|} d^3r' + V_{\text{xc}}[n(\mathbf{r})] + V_{\text{ext}}(\mathbf{r}). \quad (4.2.11)$$

Before proceeding, we note that the minimization which solves the Kohn-Sham equations must take place under the constraint of orthonormality. i.e: the Kohn-Sham orbitals must satisfy the condition

$$\int \psi_i^*(\mathbf{r}) \psi_j(\mathbf{r}) d^3r = \delta_{ij}. \quad (4.2.12)$$

This means that the electron density must also conserve the number of electrons (and therefore total charge of the system),

$$\int n(\mathbf{r}) d^3r = N. \quad (4.2.13)$$

All of the unknown quantities have now been packaged together in the exchange-correlation potential, which is the functional derivative of the exchange-correlation functional (with respect to the electron density):

$$V_{\text{xc}}[n(\mathbf{r})] = \frac{\delta E_{\text{xc}}[n]}{\delta n(\mathbf{r})}. \quad (4.2.14)$$

To calculate the total energy of the system, we note that one cannot simply sum together the Kohn-Sham eigenvalues,  $\varepsilon_i$ , as this leads to a double counting of the

Hartree term, and an incorrect accounting of the exchange-correlation energy. Instead, the total energy is given by

$$E = \sum_{i=1}^N \varepsilon_i - \frac{1}{2} \int \int n(\mathbf{r}') \frac{1}{|\mathbf{r} - \mathbf{r}'|} n(\mathbf{r}) d^3r d^3r' + E_{\text{xc}}[n] - \int V_{\text{xc}}[n(\mathbf{r})] n(\mathbf{r}) d^3r. \quad (4.2.15)$$

We note that the application of the Kohn-Sham equations requires both the electron density, as well as the fictitious Kohn-Sham orbitals in order to be able to calculate the energy. This requirement on both objects means that the Kohn-Sham equations must be solved self-consistently. The Kohn-Sham orbitals must correspond to the electron density which minimizes the energy functional. The requirement of self-consistency gives rise to additional complications when applying the method, though discussion of these complications is beyond the scope of this thesis (for details, see, e.g. Martin (2008)).

#### 4.2.6 Exchange-Correlation functionals

As previously mentioned, the functional form of the exact exchange-correlation functional is unknown, and must be approximated. If the exact form of the exchange-correlation functional were known, Hohenberg-Kohn theorem states that this would be a universal functional which is equally valid for all systems. Unfortunately, since we are required to approximate the functional, there will inevitably be systems for which a given approximation may be better than another. The approximation of the exchange-correlation functional is the largest source of error in density functional theory calculations.

Commonly used approximations for the exchange-correlation functional are the *local density approximation* and the *generalized gradient approximation* (although other approximations do exist).

Under the local density approximation (LDA), it is assumed that the electron density may be treated locally as a homogeneous electron gas, and the exchange-correlation potential depends only on the local electron density at a point (rather than including any non-local terms or spatial derivatives of the electron density). The generalized gradient approximation (GGA), is motivated by the fact that the electron density, in general, may be inhomogeneous, and therefore subject to spatial variations. Under the GGA, the exchange-correlation potential can be expanded (through the Taylor series) into terms representing the local electron density and its gradients as a function of space. (i.e:  $V_{\text{xc}} = V_{\text{xc}}[n(\mathbf{r}), \nabla n(\mathbf{r}), \nabla^2 n(\mathbf{r}), \dots]$ ). While the GGAs include terms involving the first derivative of the electron density, the related Meta-GGAs also include second order derivatives of the density. It is the presence of these gradients of the electron

density which makes the computation of exchange-correlation energies using GGAs more demanding than with the LDA.

The choice of the optimal (approximate) exchange-correlation functional is system dependent, and no single exchange-correlation functional performs universally better for all materials. The LDA is particularly suited to situations where the electron density is relatively uniform, whereas GGAs tend to perform better where the electron density is subject to more rapid spatial variations (such as the treatment of surfaces) (Thijssen, 2007).

Throughout this work, a GGA exchange-correlation functional, known as the rPBE functional (Hammer et al., 1999) has been used. The rPBE functional is a revision of the widely used PBE functional (Perdew et al., 1996), which has been adapted for the study of adsorption energies and surfaces, and so is a natural choice for this work.

### 4.2.7 Periodicity and Bloch's theorem

The combination of the Born-Oppenheimer approximation and density functional theory has allowed for the ab initio calculation of the properties of materials to become routine. When the system of interest is that of the bulk, the periodicity of the lattice may be exploited, by making use of periodic boundary conditions. Periodic boundary conditions allow for the accurate treatment of bulk systems, without requiring the large number of atoms that would be necessary to reduce surface effects.

Under periodic boundary conditions, we now only need to calculate the properties of a small repeating unit cell, while applying periodic boundary conditions to the electron density/wavefunctions. This reduces the computational effort required to calculate the properties of macroscopic solids tremendously.

Periodic boundary conditions can be achieved by making use of Bloch's theorem (Kittel, 2005). The theorem states that: for a periodically repeating potential (as is the case of a crystal (where  $V(\mathbf{r}) = V(\mathbf{r} + \mathbf{R})$ )), the magnitude of the wavefunction must also share the same periodicity as the potential:  $|\psi(\mathbf{r})|^2 = |\psi(\mathbf{r} + \mathbf{R})|^2$ , where  $\mathbf{R}$  represents a translation vector for the lattice.

This leads to wavefunctions which can be expressed as Bloch waves,

$$\psi_{i,\mathbf{k}}(\mathbf{r}) = e^{i\mathbf{k}\cdot\mathbf{r}} u_{i,\mathbf{k}}(\mathbf{r}), \quad (4.2.16)$$

where  $e^{i\mathbf{k}\cdot\mathbf{r}}$  is a phase factor, and  $u_{i,\mathbf{k}}(\mathbf{r})$  is a periodically repeating function, which has the same periodicity as the crystal, i.e:  $u_{i,\mathbf{k}}(\mathbf{r} + \mathbf{R}) = u_{i,\mathbf{k}}(\mathbf{r})$ . Here,  $i$  is the orbital index and  $\mathbf{k}$  is a point in the first Brillouin zone of the crystal (the uniquely defined primitive cell in reciprocal space).

The electron density also shares the same periodicity as the potential:

$$n(\mathbf{r}) = \int \sum_i |\psi_{i,\mathbf{k}}(\mathbf{r})|^2 d^3k = n(\mathbf{r} + \mathbf{R}).$$

### 4.2.8 The Pseudopotential Approximation

In addition to the various approximations and methods mentioned in this chapter so far, there is another approximation which is commonly used in electronic structure calculations, known as the pseudopotential approximation.

We begin by explaining the problem of an “all electron” approach: close to the nucleus, where the Coulomb potential is strong, the condition of orthogonality between the single electron wavefunctions results in rapid oscillations of the valence electron wavefunctions (Springborg, 2000). This means that, in order to accurately describe the valence electron wavefunctions, a large number of basis functions are required. In the case of a plane-wave basis set, this means that higher kinetic energy plane-waves must be included, as these are the ones which have a greater number of nodes.

Since valence electrons are the only ones which take place in chemical bonding, it is the valence region, rather than the core region, which is of the most importance to many of the properties of materials. For this reason, it is advantageous to replace the Coulomb potential with a modified potential — a pseudopotential — which does not seek to accurately describe the valence electron wavefunctions in the core region, but instead is chosen to match exactly the wavefunctions in the more smoothly varying valence region (resulting in smoother wavefunctions overall).

The use of a pseudopotential provides us with additional computational savings: they not only allow for a reduction in basis set size due to more smoothly varying wavefunctions, but also allow for the effect of the core electrons to be built into the potential (eliminating the need for their explicit treatment) — these two effects work to reduce the computational effort required, without a significant cost in accuracy.

### 4.2.9 Calculating forces: The Hellmann-Feynman theorem

The solution of the Schrödinger equation (or in DFT, the Kohn-Sham equations) allows for the calculation for the total energy of the system. While this is an incredibly useful property to be able to calculate, for many methods, such as geometry optimization and molecular dynamics, the ionic forces are often also required. Fortunately, the force acting on the ions of the system can be calculated by the application of the Hellmann-Feynman theorem (Hellmann, 1937; Feynman, 1939).

The Hellmann-Feynman theorem is a general theorem which states that the derivative of energy with respect to any parameter,  $\lambda$ , is equal to the expectation value of the derivative of the Hamiltonian:

$$\frac{dE}{d\lambda} = \int \psi^* \frac{d\hat{H}}{d\lambda} \psi dV = \left\langle \psi \left| \frac{d\hat{H}}{d\lambda} \right| \psi \right\rangle. \quad (4.2.17)$$

From Equation 4.2.17, we see that forces on the ions may be calculated from the expectation value of the derivative of the Hamiltonian with respect to the ionic positions. Conceptually, this makes sense, as in classical mechanics,  $\mathbf{F} = -\nabla V$ , therefore in quantum mechanics:  $\mathbf{F} = -\nabla \langle E \rangle = -\langle \psi | \nabla \hat{H} | \psi \rangle$ .

Although the Hellmann-Feynman theorem is commonly used to calculate the ionic forces, its use is not restricted to only this case. For example, it may also be applied to calculate the stress on the simulation cell. In this case,  $\lambda$  is the component of strain tensor of the cell, rather than the ionic positions. The stress tensor can then be reduced to zero in order to calculate the optimum lattice constant for the material (see Appendix A for details).

#### 4.2.10 The CASTEP software package

All density functional theory calculations presented in this thesis were carried out using the CASTEP software package (Clark et al., 2005). CASTEP is a periodic DFT code, which uses a plane-wave basis set and pseudopotentials (as a means of reducing the need for high frequency plane-waves required to describe the (chemically inert) core electrons). All DFT calculations in this work made use of the “on the fly” pseudopotentials which are generated at runtime when performing calculations with CASTEP — these have been shown to have excellent agreement to the “all-electron” treatment, where the core electrons are explicitly treated, rather than through pseudization (Lejaeghere et al., 2016).

### 4.3 The Ni (111) surface

Before we move on to calculate the properties of nickel, we must first understand its structure. Because nickel is a face centred cubic material, this means that the (111) surface has ABCA.. stacking. This can be seen in Figure 4.3.1

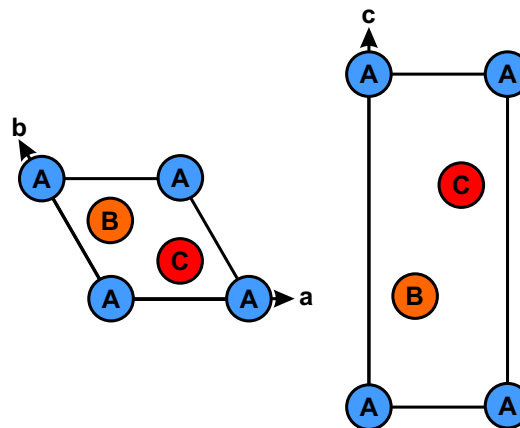


Figure 4.3.1: The simulation cell for nickel, which exposes the (111) surface to the vacuum. Because Ni is an FCC material, it has ABCA stacking.

The lattice vectors for the simulation unit cell are defined such that  $\mathbf{a}$  is aligned along the  $x$  axis, the  $\mathbf{ab}$  plane lies in the  $xy$  plane, and  $\mathbf{c}$  lies along the  $z$  axis, i.e:

$$\mathbf{a} = \left( \frac{a}{\sqrt{2}}, 0, 0 \right) \quad (4.3.1)$$

$$\mathbf{b} = \left( -\frac{a}{2\sqrt{2}}, \frac{a\sqrt{3}}{2\sqrt{2}}, 0 \right) \quad (4.3.2)$$

$$\mathbf{c} = (0, 0, a\sqrt{3}). \quad (4.3.3)$$

The various layers are then defined such that they are evenly spaced along  $\mathbf{c}$ . In fractional space, the layers are defined as:

$$A = (0, 0, 0) \quad (4.3.4)$$

$$B = \left( \frac{1}{3}, \frac{2}{3}, \frac{1}{3} \right) \quad (4.3.5)$$

$$C = \left( \frac{2}{3}, \frac{1}{3}, \frac{2}{3} \right). \quad (4.3.6)$$

We note that a point in fractional space,  $\mathbf{s}$ , may be expressed in Cartesian space, through

$$\mathbf{x} = \underline{\underline{h}}\mathbf{s}, \quad (4.3.7)$$

where  $\underline{\underline{h}}$  is a matrix of the cell vectors,

$$\underline{\underline{h}} = \begin{pmatrix} a_x & b_x & c_x \\ a_y & b_y & c_y \\ a_z & b_z & c_z \end{pmatrix}, \quad (4.3.8)$$

i.e: the columns of the  $\underline{\underline{h}}$  matrix are the cell vectors.

Throughout a simulation, there are often times when it is advantageous to work in either fractional or Cartesian coordinates. In the interest of completeness, we note that the fractional coordinates may be calculated from the Cartesian coordinates through

$$\mathbf{s} = \underline{\underline{h}}^{-1}\mathbf{x}, \quad (4.3.9)$$

where the inverse of the cell vector matrix,  $\underline{\underline{h}}^{-1}$ , has as its rows, the reciprocal lattice vectors (divided by  $2\pi$ ):

$$\mathbf{a}^* = \frac{2\pi}{\Omega} \mathbf{b} \times \mathbf{c} \quad (4.3.10)$$

$$\mathbf{b}^* = \frac{2\pi}{\Omega} \mathbf{c} \times \mathbf{a} \quad (4.3.11)$$

$$\mathbf{c}^* = \frac{2\pi}{\Omega} \mathbf{a} \times \mathbf{b} \quad (4.3.12)$$

where  $\Omega$  is the volume of the cell, which may be calculated from the determinant of the cell vector matrix.

### 4.3.1 Convergence testing

To ensure the accuracy of DFT calculations, there are a number of parameters which must be adjusted until the calculations are suitably converged (that is, some quantity of interest does not change by an appreciable amount when the convergence parameter is changed). In practice no calculation is every *fully* converged (and some quantities may converge faster than others) — though adjusting the various convergence parameters does allow for the quality of a calculation to be improved on balance with the resources available at the time. It should be noted that, because every convergence parameter generally increases the computational cost of the calculations, systematic convergence testing allows us to not only quantify the magnitude of errors in our calculations, but also carry them out as efficiently as possible. When performing convergence calculations, it is advantageous (for efficiency reasons), if these calculations are carried out on a small representative sample of the system of interest.

In CASTEP, the two primary convergence parameters which affect all results are the basis set size (plane wave cut-off energy) and sampling of the Brillouin zone ( $\mathbf{k}$ -point sampling density).

In addition to this, because our system of interest is a surface, and CASTEP makes use of periodic boundary conditions, we also need to converge: the interslab spacing (vacuum gap size), the number of layers that make up the nickel surface, and the concentration of hydrogen on the surface (to determine the dilute limit).

The DFT calculations are ultimately used to calculate a potential energy surface (discussed in Chapter 5), along which the hydrogen dynamics can take place. For this reason, the quantity of interest that is computed during convergence testing is the binding energy:

$$E_{\text{bind}} = E(\text{Ni} + \text{H}) - [E(\text{Ni}) + E(\text{H})]. \quad (4.3.13)$$

When calculating the binding energy,  $E(\text{Ni} + \text{H})$  is the total energy of the nickel system (bulk or surface, depending on the calculation) with a hydrogen atom placed  $1.5\text{\AA}$

above the topmost layer,  $E(\text{Ni})$  is the total energy of the same system, but without the hydrogen, and  $E(\text{H})$  is total energy of the same simulation cell, but with only the hydrogen atom. We note that, through translational invariance, the energy of the system should not change if all atoms are translated throughout a simulation cell by an equal amount.

#### 4.3.1.1 Convergence of basis set size

Computationally, the wavefunction in DFT calculations is represented as a linear combination of basis functions. From the variational principle, it is known that as the basis set size increases, the upper bound for the estimate of the ground state energy tends towards the true ground state energy. Therefore the basis set size should be increased until the number of basis functions included is sufficiently large to accurately represent the true (Kohn-Sham) wavefunction, and reproduce the correct ground state energy.

As previously stated, CASTEP uses plane-waves as its underlying representation of the wavefunction, i.e:

$$\psi_{i,\mathbf{k}}(\mathbf{r}) = \sum_{\mathbf{G}} c_{\mathbf{G}+\mathbf{k}} \exp [i(\mathbf{G} + \mathbf{k}) \cdot \mathbf{r}], \quad (4.3.14)$$

where the  $i$  in the exponent is the imaginary number, and is not the orbital index,  $c_{\mathbf{G}+\mathbf{k}}$  are complex expansion coefficients, and  $\mathbf{k}$  is a point within the Brillouin zone of the crystal.

In the plane-wave basis set, the  $\mathbf{G}$ -vectors are reciprocal lattice vectors, these form a discrete set with a particular maximum wavelength, commensurate with the size of the simulation cell (smallest  $\mathbf{G}$ ). The maximum  $\mathbf{G}$  (smallest wavelength) then defines the size of the basis set (number of plane waves) for the cell. A convenient measure of basis set quality is the cut-off energy:  $E_{\text{cut}} = \frac{1}{2} |\mathbf{G}_{\text{max}} + \mathbf{k}|^2$ . This is the maximum kinetic energy plane wave, beyond which the basis set is truncated. (By defining a maximum cut-off energy, rather than number of plane waves directly, a transferrable measure of basis set quality is defined, rather than something which is dependent on the size of the cell.)

In order to determine convergence, the binding energy for a hydrogen atom placed in a bulk nickel system was calculated as a function of cut-off energy. These calculations were carried out using a relatively coarse 3x3x3 k-point grid and in all cases, the geometry of the structure was kept constant. It was found that the change in the binding energy reduces to 0.6 meV at a cut-off energy of 725 eV (relative to a cut-off energy of 750 eV). A graph of convergence behaviour is presented in Figure 4.3.2.

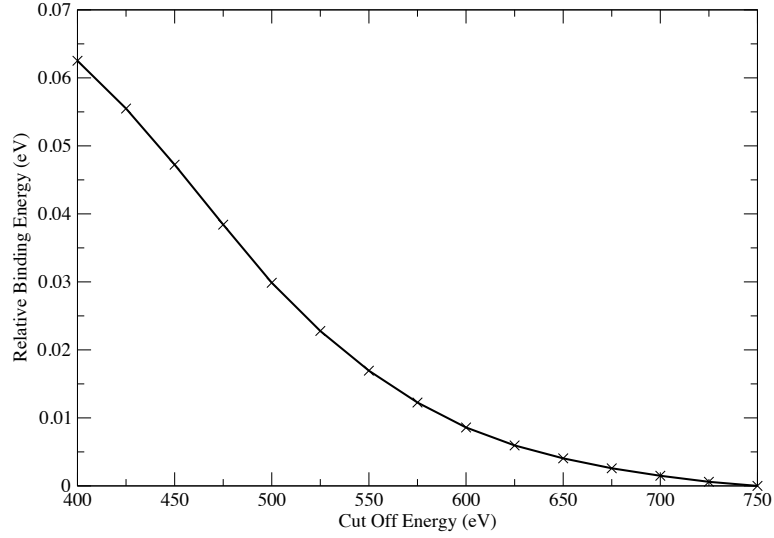


Figure 4.3.2: Change in binding energy for a hydrogen atom placed in a bulk nickel system (with a  $3 \times 3 \times 3$  k-point grid) as a function of cut-off energy. The energy change drops to 0.6 meV at a cut-off energy of 725 eV with all energies presented relative to the 750 eV result.

#### 4.3.1.2 Convergence of Brillouin zone sampling

As can be seen from Bloch's theorem, when performing electronic structure calculations of periodic systems, the wavefunction contains a reciprocal space dependent phase factor. Therefore, in order to accurately calculate material properties, integration must be performed over the Brillouin zone of the structure.

Brillouin zone sampling can be achieved in CASTEP by the widely used method of Monkhorst and Pack (Monkhorst and Pack, 1976). Under the Monkhorst-Pack scheme, the so-called  $\mathbf{k}$ -points form a discrete grid of points which are evenly distributed throughout the Brillouin zone. The density of grid points/number of grid points introduces another convergence parameter.

Following the Monkhorst-Pack scheme, the points in the Brillouin zone are given by

$$\mathbf{k}_{prs} = u_p \mathbf{a}^* + u_r \mathbf{b}^* + u_s \mathbf{c}^*, \quad (4.3.15)$$

where  $\mathbf{a}^*, \mathbf{b}^*, \mathbf{c}^*$  are the reciprocal lattice vectors, and the position of the points are given by the numbers  $u_p, u_r, u_s$ , which are defined as

$$u_r = (2r - q - 1)/2q, \quad (r = 1, 2, 3, \dots, q) \quad (4.3.16)$$

where  $q$  is an integer which determines the number of points along a particular (reciprocal) direction.

Unlike the convergence of energies, which decrease monotonically with respect to cut-off energy (as per the variational principle), the convergence of energy with respect to  $\mathbf{k}$ -point density is not smoothly varying, and does exhibit oscillations as the dimensions of the  $\mathbf{k}$ -point grid are increased. The convergence behaviour of the binding energy with respect to Brillouin zone sampling (fixed cut-off energy of 400 eV) for the same bulk system as was used for the cut-off energy convergence is presented in Figure 4.3.3.

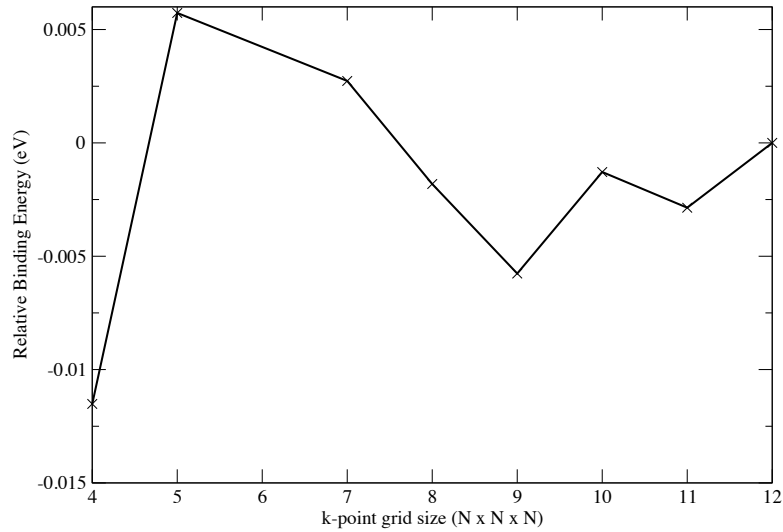


Figure 4.3.3: Change in binding energy for a hydrogen atom placed in a bulk nickel system (with a 400 eV cut-off energy) as a function of  $\mathbf{k}$ -point grid size. The convergence of binding energy is not monotonic as  $\mathbf{k}$ -point grid dimensions are increased: the zero of energy is defined for 12x12x12  $\mathbf{k}$ -point grid. For a 7x7x7 grid, the energy difference is 2.7 meV.

#### 4.3.1.3 Preparing surface calculations: Bulk geometry optimization

The calculations used to determine the cut-off energy and  $\mathbf{k}$ -point sampling grid were carried out on bulk systems. When performing the surface convergence calculations, in order to determine the number of nickel layers, vacuum gap size, and concentration of hydrogen on the surface, it is important that we begin with an accurate estimate for the nickel lattice parameter (to ensure that all distances, such as interlayer spacings of the surface, are reasonable estimates).

With the cut-off energy and  $\mathbf{k}$ -point grid dimensions determined (725 eV and 7x7x7 grid, respectively), a variable cell geometry optimization (see Appendix A for details) was then performed on the bulk nickel system to determine the lattice constant. The lattice

constant was found to be  $3.5549\text{\AA}$ . For this lattice constant, the maximum component of the stress tensor was reduced to  $3.43 \times 10^{-6}$  GPa. (By symmetry, the force on each of the ions was zero).

This bulk structure used in all calculations was composed of 3 atoms (forming 3 layers), and was oriented such that, as a vacuum gap is introduced above the topmost layer, the (111) surface is exposed (ensuring the same k-point sampling in the surface plane as the subsequent surface calculations).

#### 4.3.1.4 Surface calculations: Convergence of vacuum gap size

The treatment of surfaces/non-periodic systems introduces additional complications into the calculation of the electronic structure when using periodic boundary conditions. When calculating the properties of systems which are not periodic in 3D space, the systems must be separated by a suitable vacuum gap, in order to minimize interactions between the periodic images of the system.

As the separation between periodic images is increased, the corresponding Brillouin zone becomes compressed along the (reciprocal) direction. This means that, in order to minimize the unwanted effect that periodic images have on the surface, sampling should be carried out with k-point grids that contain only a single grid point along the reciprocal direction normal to the surface. For this reason, a k-point grid of size  $7 \times 7 \times 1$  was chosen for the following convergence calculations. It should be noted that, as the vacuum gap/number of layers of the surface is varied, the size of the Brillouin zone also varies along the reciprocal direction normal to the surface. The variation in the size of the Brillouin zone acts to change the equilibrium interlayer spacing of the nickel surface as these parameters are varied.

As we have seen previously, when using a plane wave basis set, the number of basis functions is dependent on the size of the cell. Hence, increasing the size of the cell (even along one dimension), will act to increase the computational cost of the calculations in plane wave DFT. Therefore, in the interest of efficiency, the vacuum gap between neighbouring cells should be increased until the property of interest (binding energies in our case), does not change to within some suitable tolerance.

The change in binding energy for a hydrogen atom placed  $1.5\text{\AA}$  above a 4 layer thick (111) nickel surface, as a function of vacuum gap size/interlayer spacing is presented in Figure 4.3.4 (725 eV cut-off energy and  $7 \times 7 \times 1$  k-point grid). In all cases, the interlayer spacing of the nickel surface is kept constant (we do not perform geometry optimizations as the size of the vacuum gap is varied).

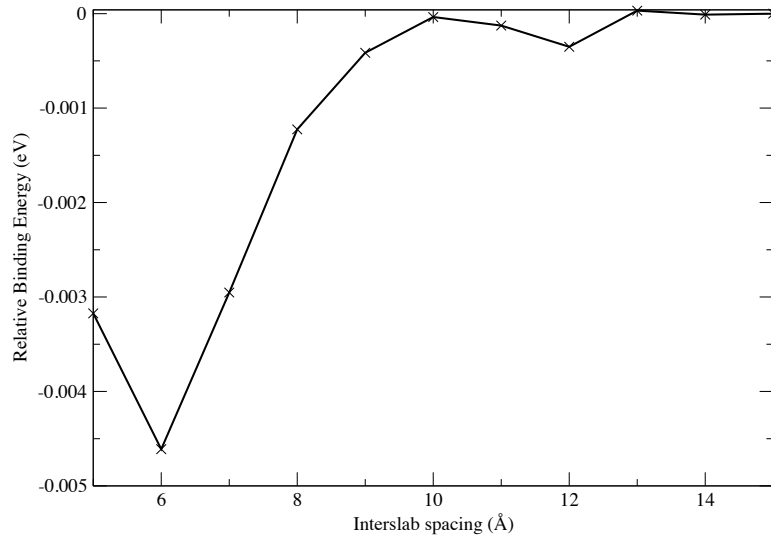


Figure 4.3.4: Convergence of binding energy for a hydrogen atom placed  $1.5\text{\AA}$  above a 4 layer thick (111) nickel surface as a function of interslab spacing. The zero of energy is defined for a  $15\text{\AA}$  spacing between neighbouring slabs. At  $10\text{\AA}$ , the change in energy is less than  $0.04\text{ meV}$  - this corresponds to a vacuum gap of  $8.5\text{\AA}$  above the H atom.

#### 4.3.1.5 Surface calculations: Convergence of slab thickness

Breaking the periodicity of our system, through the introduction of a vacuum gap, in order to treat surfaces, creates an additional parameter that must also be converged. Since we necessarily lose the bulk-like behaviour that periodic boundary conditions provides us (along one of the dimensions of our system), we must now ensure that we include a suitable number of layers, in order to reproduce bulk-like behaviour in the middle of our slab-like system.

When increasing the number of layers of our nickel surface, it should be noted that the total energy will vary depending on which of the two surface layers are exposed to the vacuum. The labelling of the surface layers is arbitrary (as the layers may be relabelled and a translation performed within the simulation cell), but it must be ensured that differences of energies are always calculated by comparing like with like.

The convergence of the binding energy with respect to the number of layers forming the surface is given in Figure 4.3.5. These calculations were again performed by placing a hydrogen atom  $1.5\text{\AA}$  above the topmost layer of the surface, with an interslab spacing of  $6\text{\AA}$ , a  $725\text{ eV}$  cut-off energy, and a  $7\times 7\times 1$  k-point grid. In these calculations “Layer A” was always placed on the bottom layer, and the slab always preserved ABCA stacking that is characteristic of the (111) surface of an FCC material (there was no centre of inversion symmetry present) (Kittel, 2005). Again, the interlayer spacing of the nickel surface was kept constant as the number of layers were increased.

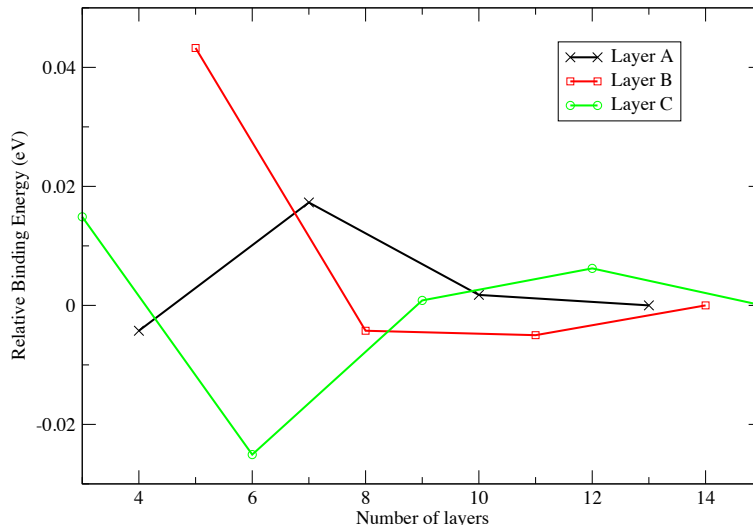


Figure 4.3.5: Convergence of binding energy as a function of number of layers, for a hydrogen atom placed  $1.5\text{\AA}$  above a nickel (111) surface, with an interslab spacing of  $6\text{\AA}$  ( $4.5\text{\AA}$  of vacuum above the H). The cut-off energy was  $725\text{ eV}$ , and the k-point grid was  $7\times 7\times 1$ . For 10 layers, the change in binding energy reduces to  $1.8\text{ meV}$ .

#### 4.3.1.6 Surface calculations: Concentration of H on surface

Our study of diffusion takes place in the dilute limit — where the surface hydrogen does not interact with any hydrogen ions in nearby (image) cells. While the system must still be treated in a periodic manner, we are able to determine the convergence of binding energy as a function of hydrogen concentration by increasing the number of repeats of the nickel surface (in the  $\mathbf{a}$  and  $\mathbf{b}$  directions), while keeping the number of hydrogen ions fixed. For cases where the hydrogen concentration is higher, extra care must be taken to ensure that the hydrogen-hydrogen interactions are correctly accounted for.

Due to the discrete nature of  $\mathbf{k}$ -point sampling, and the oscillatory behaviour of energy convergence with respect to this parameter, the  $1\times 1$  surface calculation was repeated several times with different  $\mathbf{k}$ -point sampling densities, such that binding energy differences are calculated between the  $1\times 1$  supercell and larger supercells with equivalent  $\mathbf{k}$ -point sampling.

All calculations are carried out with a  $10\text{\AA}$  interslab spacing, 10 layers of nickel forming the (111) surface (preserving ABCA stacking), and a  $725\text{ eV}$  cut-off energy.

In order to ensure a fair comparison between the true binding energies, constrained variable cell geometry optimizations were first carried out on the nickel-only systems. The constraints acted to fix the position of the middle layer of the nickel surface, and

ensured that the cell vector (normal to the surface) did not compress to a more bulk-like state. This process ensured that the effect of the different k-point sampling densities were always fully accounted for, with the surface lattice constants, and interlayer spacing of the nickel slab able to vary. In all instances, the geometry optimizations were performed until the maximum force was reduced to less than  $2.5 \times 10^{-2}$  eV/Å and the maximum component of the stress tensor was less than  $1 \times 10^{-2}$  GPa.

With the optimal geometry of the nickel surfaces determined, a single hydrogen atom was placed 1.5Å above the surface (above the same site of each supercell surface, such that the binding energies were comparable), and a further geometry optimization was performed with all cell vectors fixed, and the hydrogen atom constrained to move only along a direction normal to the surface. For this geometry optimization, the hydrogen position was varied until the force on the atom was reduced to  $2.5 \times 10^{-2}$  eV/Å.

Table 4.3.1 shows the binding energies as a function of the concentration for hydrogen above the surface. For equivalent k-point sampling densities, we see that the change in binding energy between the 1.0ML (1x1) coverage system and the 0.25ML (2x2) coverage is 25.7 meV, but the difference between the 0.25ML (2x2) coverage and the 0.0625ML (4x4) coverage is 0.2 meV. Therefore the 0.25ML coverage system can be considered to be a suitable approximation to the dilute limit.

Supercell size (k-point sampling)	Equivalent k-point sampling on 1x1 cell	Binding energy (eV)	$\Delta E_{\text{bind}}$ (meV) (compared with supercell size)
1x1 (k: 8x8x1)	8x8x1	-2.1681	-25.7 (2x2), -25.9 (4x4)
1x1 (k: 9x9x1)	9x9x1	-2.1839	-17.7 (3x3)
1x1 (k:10x10x1)	10x10x1	-2.1652	-20.0 (5x5)
2x2 (k: 4x4x1)	8x8x1	-2.1424	-0.2 (4x4)
3x3 (k: 3x3x1)	9x9x1	-2.1662	-
4x4 (k: 2x2x1)	8x8x1	-2.1422	-
5x5 (k: 2x2x1)	10x10x1	-2.1452	-

Table 4.3.1: Binding energies for a hydrogen atom placed above a 10 layer thick (111) nickel surface (with a 10Å interslab spacing), as a function of the supercell size (concentration of hydrogen).

#### 4.3.1.7 Summary of CASTEP calculation parameters

When determining the potential energy surface using CASTEP, the nickel surface was composed of 10 layers (resulting in a binding energy difference of 1.8 meV between 10 and 13 layers). The interslab spacing was chosen to be 10Å (giving a change in binding energy of 0.04 meV when compared to a 15Å spacing). It was shown that a concentration of 0.25ML coverage of hydrogen turns out to be a reasonable approximation to the dilute limit. This concentration corresponds to a single hydrogen atom for every 2x2 supercell of the nickel surface. The difference in binding energy between a hydrogen atom placed on a 2x2 surface and a one placed at an equivalent site on a 4x4 surface was found to be 0.2 meV.

A cut-off energy of 725 eV was chosen to reduce the difference in binding energy to 0.6 meV (compared with a 750 eV cut-off), and a Monkhorst-Pack k-point sampling grid of dimensions 4x4x1 on a 2x2 supercell of the nickel surface was also chosen. This k-point grid corresponds to an 8x8x1 grid on the 1x1 surface supercell, which has a difference in binding energy of 2.9 meV when compared with the 10x10x1 sampling on the same size supercell.

## 4.4 Embedded Atom Method

The embedded atom method (EAM) is a widely used, semi-empirical potential, designed for the study of metal systems. The original EAM was created by Daw and Baskes (1983; 1984), and is based on earlier “Effective Medium Theory” (Nørskov and Lang, 1980) and “quasi-atom” approaches (Stott and Zaremba, 1980), all of which take inspiration from the work of Hohenberg and Kohn (1964) which underpins density functional theory. The EAM family of potentials has since been extended and reparameterized by others for the study of a wide variety of systems (Daw et al., 1993).

The embedded atom method was designed to overcome the shortcomings of the pair potentials which were available at the time. The use of volume dependent energies in these pair potentials, which was required for the accurate modelling of elastic properties, caused particular concern in the treatment of surfaces and systems involving defects. Furthermore, it had been shown that the energy of a hydrogen atom in a transition metal cluster could not be accurately represented using pairwise interactions, and so necessitated the development of a many-body potential (Daw and Baskes, 1984).

In the embedded atom method, all atoms of the system are viewed as “impurities embedded in a host comprising all the other atoms”. The total energy of the system includes a sum over all of the “embedding energies”,  $F_i$ , and an additional (pairwise) term which accounts for the core-core repulsion,  $\phi_{ij}$ :

$$V = \sum_i F_i(\bar{\rho}_i) + \frac{1}{2} \sum_i \sum_{j \neq i} \phi_{ij}(r_{ij}). \quad (4.4.1)$$

The embedding energy,  $F_i$ , is the energy required to place an atom  $i$  in the host electron density,  $\bar{\rho}_i$ . This host electron density is given by the sum of all of the other atomic densities,  $\rho_j^a$ :

$$\bar{\rho}_i = \sum_{j \neq i} \rho_j^a(r_{ij}). \quad (4.4.2)$$

The particular form of the embedding energy functions,  $F(\bar{\rho})$ , pairwise interactions,  $\phi(r)$  and atomic densities depend on the particular form of the EAM potential used.

Early parameterizations of EAM, suitable for H/Ni systems (such as: Daw and Baskes (1984); Rice et al. (1990)), did not include analytic forms for the embedding energy functions, and instead defined these functions numerically. Here we make use of the “EAM5” potential, developed by Wonchoba, Hu and Truhlar (1995), which *does* provide analytic forms for all of the various functions. EAM5 is an improvement on an earlier (EAM4) parameterization of the potential (Truong and Truhlar, 1990), and is particularly well suited for the study of the (100) Ni surface.

The individual atomic densities,  $\rho^a$ , terms for Ni atoms are given by

$$\rho_j^a(r_{ij}) = N_s \rho_s^a(r_{ij}) + (N - N_s) \rho_d^a(r_{ij}), \quad j = \text{Ni atom} \quad (4.4.3)$$

where  $N$  and  $N_s$  refer to the total number of occupied orbitals, and number of occupied s- orbitals, respectively.

Similarly, for H, the individual atomic densities are

$$\rho_j^a(r_{ij}) = \frac{\exp(-2r_{ij}/a_0)}{\pi a_0^3}, \quad j = \text{H atom} \quad (4.4.4)$$

where  $a_0$  is the Bohr radius.

The Ni atomic densities of Equation 4.4.3 include spherically averaged s- and d- like densities, which are based on calculations by Clementi and Roetti (1974):

$$\rho_{s/d}^a(r_{ij}) = \left| \sum_{\alpha} C_{\alpha} R_{\alpha}(r_{ij}) \right|^2 / 4\pi, \quad (4.4.5)$$

and

$$R_{\alpha}(r_{ij}) = \frac{(2\zeta_{\alpha})^{(n_{\alpha}+1/2)}}{\sqrt{(2n_{\alpha})!}} r_{ij}^{n_{\alpha}-1} \exp(-\zeta_{\alpha} r_{ij}). \quad (4.4.6)$$

The values used for the calculation of the s- and d- like densities,  $n_{\alpha}$ ,  $\zeta_{\alpha}$  and  $C_{\alpha}$ , are reproduced in Table 4.4.1.

$\alpha$	$n_\alpha$	$\zeta_\alpha \left( \text{\AA}^{-1} \right)$	$C_\alpha$
4s			
1	1	54.88885	-0.00389
2	1	38.48431	-0.02991
3	2	27.42703	-0.03189
4	2	20.88204	0.15289
5	3	10.95707	-0.20048
6	3	7.31958	-0.05423
7	4	3.92650	0.49292
8	4	2.15289	0.61875
3d			
1	3	12.67582	0.42120
2	3	5.43253	0.70658

Table 4.4.1: Parameters used for calculation of the atomic density of Ni atoms, reproduced from Clementi and Roetti (1974)

The embedding energy function for Ni is given by

$$F_{Ni}(\bar{\rho}) = \begin{cases} A\bar{\rho} \exp(-\alpha\bar{\rho}) + B\bar{\rho}^3 \exp(-\beta\bar{\rho}) + C\bar{\rho} \exp(-\gamma\bar{\rho}) & 0 \leq \bar{\rho} \leq \rho_c - \Delta \\ A_s(\bar{\rho} - \rho_c)^5 + B_s(\bar{\rho} - \rho_c)^4 + C_s(\bar{\rho} - \rho_c)^3 + D_s & \rho_c - \Delta < \bar{\rho} \leq \rho_c \\ D_s & \rho_c < \bar{\rho} \end{cases} \quad (4.4.7)$$

and for H:

$$F_H(\bar{\rho}) = \alpha_H \bar{\rho} \exp(-\beta_H \bar{\rho}). \quad (4.4.8)$$

The repulsive pair potential is a simple Coulomb interaction,

$$\phi_{ij}(r_{ij}) = \frac{C_\phi Z_i(r_{ij}) Z_j(r_{ij})}{r_{ij}}, \quad (4.4.9)$$

where  $Z_i$  is the effective charge for atom  $i$ :

$$Z(r_{ij}) = Z_0 \left( 1 + br_{ij}^c \right) \exp(-ar_{ij}). \quad (4.4.10)$$

In addition, the atomic electron-density contributions,  $\rho_i^a$ , and the effective charges,  $Z_i$ , are multiplied by a smoothing function,  $s$ , which gives a smooth potential cutoff

$$s(r_{ij}) = \begin{cases} 1 & r_{ij} \leq r_c \\ \frac{r_{ij} - (r_c + \Delta)}{-\Delta} - \frac{1}{2\pi} \left[ \pi \left( \frac{2r_{ij} - 2r_c - \Delta}{\Delta} \right) \right] & r_c < r_{ij} < r_c + \Delta \\ 0 & r_c + \Delta \leq r_{ij} \end{cases} \quad (4.4.11)$$

All of the remaining parameters which define the EAM5 potential are given in Table 4.4.2.

$\rho_{Ni}^a$	$N_s = 2$	$N = 10$
$F_H$	$\alpha_H = -70.5461 \text{ eV}\text{\AA}^3$	$\beta_H = 6.9507 \text{ \AA}^3$
$F_{Ni}$	$A = -126.5009308 \text{ eV}\text{\AA}^3$	$\alpha = 0.3362141252 \text{ \AA}^3$
	$B = 6033.287109 \text{ eV}\text{\AA}^9$	$\beta = 11.02211666 \text{ \AA}^3$
	$C = -209.7682800 \text{ eV}\text{\AA}^3$	$\gamma = 51.76818085 \text{ \AA}^3$
	$A_s = -1.657208422 \times 10^{10} \text{ eV}\text{\AA}^{15}$	$B_s = -5.13226816 \times 10^8 \text{ eV}\text{\AA}^{12}$
	$C_s = -4.377938 \times 10^6 \text{ eV}\text{\AA}^9$	$D_s = -19.23463058 \text{ eV}$
	$\rho_c = 0.21 \text{ \AA}^{-3}$	$\Delta = 0.01 \text{ \AA}^{-3}$
$\phi$	$C_\phi = 14.3888 \text{ eV}\text{\AA}$	
$Z_H$	$Z_0 = 0.1959$	$a = 1.7957 \text{ \AA}^{-1}$
	$b = 3.2108 \text{ \AA}^{-1}$	$c = 1.0$
$Z_{Ni}$	$Z_0 = 10.0$	$a = 1.8633 \text{ \AA}^{-1}$
	$b = 0.8957 \text{ \AA}^{-1}$	$c = 1.0$
$s$	$r_c = 5.0 \text{ \AA}$	$\Delta = 5.0 \text{ \AA}$

Table 4.4.2: EAM5 parameter set, reproduced from Wonchoba et al. (1995)

With knowledge of the potential now fully defined, the force on atom  $i$  can now be calculated with

$$\mathbf{F}_i = - \left( \sum_{j \neq i} F'_i \rho'_j + \sum_{j \neq i} F'_j \rho'_i + \sum_{j \neq i} \phi'_{ij} \right) \hat{\mathbf{r}}_{ij}. \quad (4.4.12)$$

For the EAM5 potential, Wonchoba et al. (1995) give the lattice constant of nickel as  $3.5211\text{\AA}$  (though as we shall show, this is sensitive to the size of the simulation cell).

#### 4.4.1 Notes on EAM5

The original motivation behind using the EAM potential was to investigate the effects of the surface phonons of the nickel on the diffusion of hydrogen/deuterium along the surface, within the potential energy surface (PES) approach (discussed in the following chapter).

The EAM5 potential was designed for the study of hydrogen diffusion on the (100) nickel surface, which exhibits a different diffusion profile than the (111) surface, which is the focus of this study. Unfortunately, Wonchoba, et al. state that the EAM5 potential proves to be inaccurate for the study of the (111) nickel surface, as well as the bulk system. Two further parameterizations of the EAM potential, known as EAM6 and EAM7 (Wonchoba and Truhlar, 1996, 1998) were designed to correct some of the flaws of the EAM5 potential, through the modification of the embedding functions (Equations 4.4.7 and 4.4.8), in order to create a more general purpose potential energy

function. The most significant change of the later potentials was to include a non-local contribution to the embedding function of the hydrogen.

Unfortunately, the implementation of the more recent potential energy functions (EAM6 and 7) exhibited characteristics which did not inspire confidence in their suitability for this project. Serious issues arose when considering the adsorbate dynamics: in particular, there was a high preference for the adsorbate to move into the subsurface layers of the nickel surface, making the calculation of surface diffusion particularly challenging. While the author does not rule out errors in the implementation, a substantial amount of time and effort went into attempting to validate the implementation, and after finding a number of errors in the original papers, the author was left with no alternative but to abandon this path of inquiry.

Therefore, while it is known that the EAM5 potential may be less than ideal for the study of diffusion of hydrogen along the (111) nickel surface, its inclusion in this work is justified by virtue of the EAM family of methods being commonly used for the study of hydrogen-metal interactions, and because many of the functional forms shown above are unchanged in the later EAM6/7 potentials. Furthermore, while the EAM5 potential may perform poorly for the calculation of hydrogen diffusion rates on the (111) surface, it may still be used as a relatively inexpensive model for extending the PES approach at a later date. Finally, it is hoped that by comparing the PES calculated using EAM5 with that of DFT, some of the shortcomings of the potential may be more clearly quantified, hopefully leading to the possibility of improved potential energy functions in the future.

#### 4.4.2 Finite size effects

As with any finite ranged potential, it is important to ensure that the simulation system is large enough to contain a sufficient number of atoms to correctly reproduce the physical properties of the potential. When calculating the distance between pairs of atoms within the EAM5 potential, periodic boundary conditions and the minimum image convention (Section 6.9.1) were used. Fortunately, since the EAM potential contains sums over all *other* atoms in the system, there are no H-H interactions across neighbouring cells (unlike with DFT). Therefore, the size of the simulation cell should be increased until it is large enough to contain all of the H-Ni and Ni-Ni interactions accounted for within the range of the potential.

In what follows, the lattice parameter is initially chosen to be to be  $3.5211\text{\AA}$ , as given in the EAM5 paper. Because including a vacuum gap is of no additional cost in an EAM calculation (unlike with plane wave DFT), a large interslab spacing of  $15\text{\AA}$  is chosen, in order to guarantee that there are no interactions between the surface and its images.

#### 4.4.2.1 Converging supercell size/number of layers

A series of energy and force calculations, as a function of both supercell size (number of repeats in the **a** and **b** directions) and number of layers, were carried out. For these calculations, the nickel atoms were all placed at their crystallographic sites, aside from one atom (in the bottom layer), which was perturbed by 0.1Å along **a**, **b** and **c**, in order to break the symmetry of the system (and avoid cancellation of terms in the potential). The perturbed atom was always chosen such that it represented the same defect in each of the simulation cells (the only thing that varied was the defect concentration).

In order to ensure that the system is large enough to contain all potential terms arising from both the H and Ni interactions, the change in the binding energy was calculated for a H atom placed 1.5Å above the nickel surface (at the same site), as well as the change in the maximum force components in both the Ni-only system, and the Ni-H system. For reference, the maximum force in the Ni-only system acts on the perturbed atom, and on the H atom in the Ni-H system. The results of these calculations (with 7 layers of nickel) are presented in Table 4.4.3

Repeats along <b>a/b</b>	$\Delta E_{\text{Binding}}$ (eV)	$\Delta F_{\text{max}}^{\text{Ni+H}}$ (eV/Å)	$\Delta F_{\text{max}}^{\text{Ni}}$ (eV/Å)
1x1	$-5.69 \times 10^{-1}$	2.76	1.71
2x2	$1.03 \times 10^{-1}$	$3.16 \times 10^{-1}$	$-1.62 \times 10^{-1}$
3x3	$2.54 \times 10^{-3}$	$4.46 \times 10^{-3}$	$-4.28 \times 10^{-2}$
4x4	$2.19 \times 10^{-4}$	$3.94 \times 10^{-4}$	$-4.02 \times 10^{-3}$
5x5	$2.16 \times 10^{-6}$	$3.86 \times 10^{-6}$	$-5.37 \times 10^{-5}$
6x6	$2.97 \times 10^{-8}$	$5.27 \times 10^{-8}$	$-7.32 \times 10^{-7}$

Table 4.4.3: Convergence of change in binding energy and maximum force components (for Ni-only and Ni-H systems), relative to an 8x8 supercell, as a function of supercell size (number of repeats along the **a** and **b** directions). The results shown are for 7 layers, with an interslab spacing of 15Å, and with a H atom placed 1.5Å above the surface (for the Ni-H systems). All results are presented to 3 significant figures.

The results presented in Table 4.4.3 are identical (to the precision given) for any number of layers ranging from 4 to 28 (provided the same surface is exposed). If instead the energy/force differences are calculated as a function of the number of layers (with a fixed supercell size), relative to a 28 layer calculation, the only significant difference occurs with the 1x1 system with 4 layers, where  $\Delta F_{\text{max}}^{\text{Ni}}$  is  $-3.58 \times 10^{-3}$  eV/Å. (At 7 layers, this change reduces to  $\sim 10^{-10}$  eV/Å). This change has reduced significantly for systems larger than the 1x1: for the 5x5 system, with 4 layers,  $\Delta F_{\text{max}}^{\text{Ni}}$  is  $\sim 10^{-10}$  eV/Å.

It is desirable for the nickel slab to reproduce bulk-like behaviour as we penetrate into the slab. For this reason, as an additional test, the variation of energy per atom for a 5x5 bulk system was also calculated, with varying numbers of layers (multiples of 3 to produce the correct layer stacking). For 3 layers, the energy change per atom, relative to 27 layers, is  $\sim 20$  meV, but this reduces to  $\sim 0.02$  meV for 6 layers. Therefore, to be

completely sure of producing the bulk-like behaviour in the slab system, 7 layers were used.

#### 4.4.2.2 Minimizing image interactions

In order to confirm the size of the vacuum gap/interslab spacing necessary to reduce interactions between the nickel surface and its images under periodic boundary conditions, the variation in energy as a function of vacuum gap size was calculated. In this case, a  $5 \times 5$  nickel supercell with 7 layers, and the same system also containing a H atom ( $1.5 \text{ \AA}$  above the surface, as before) were used. It was found that  $\Delta E_{\text{Tot}}$  (relative to a system containing a  $25 \text{ \AA}$  vacuum gap) decays to  $< 0.1 \text{ meV}$  for interslab spacings of  $7 \text{ \AA}$  in both systems — therefore the simulation cell should be made large enough that the H atom never gets closer than this distance.

#### 4.4.2.3 Bulk nickel lattice constant using EAM5

With the knowledge of the supercell size and number of layers necessary to take account of the finite range of the potential, the correct lattice parameter within the EAM5 method may be found by calculating the variation in the energy per atom/total energy as a function of the lattice constant (see Figure 4.4.1). This calculation was carried out with a  $5 \times 5$  supercell and 6 layers (to produce the correct stacking order). The final lattice parameter for bulk nickel was found to be  $3.5208 \text{ \AA}$  (to the same precision as was given in the EAM5 paper).

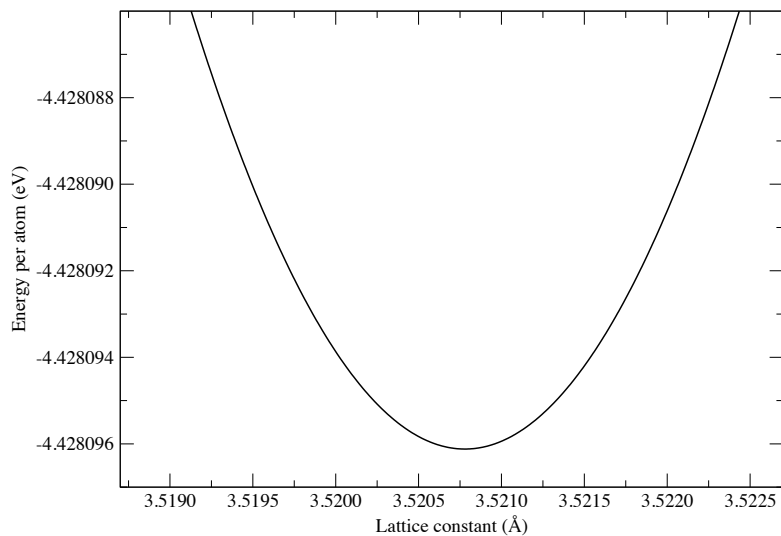


Figure 4.4.1: Variation of energy per atom as a function of lattice constant for the EAM5 potential ( $5 \times 5$  supercell with 6 layers). The lattice parameter is shown to be  $3.5208 \text{ \AA}$ .

#### 4.4.2.4 Determination of the (111) surface

In order to carry out a potential energy surface scan, and perform molecular dynamics simulations of the surface, a geometry optimization was performed on the nickel surface, composed of 7 layers, 5x5 repeats along the **a** and **b** directions, and a 15Å vacuum gap. It is not strictly necessary to apply constraints to the system (as the presence of a large vacuum gap will not cause the cell to compress with the EAM5 potential), although these can be included without adversely affecting the final structure.

The geometry optimization acted to reduce the maximum force to less than  $5 \times 10^{-6}$  eV/Å, and reduced the maximum component of the stress tensor to less than  $1 \times 10^{-5}$  GPa.

Following the geometry optimization, it was found that the presence of the extra layer acted to change the interlayer spacing as well as the lattice constant. The new lattice constant (along the directions **a** and **b**) was found to be 3.5261Å (to the same precision as in the EAM5 paper).

## 4.5 Summary

In this chapter we have seen how the interactions between hydrogen and nickel surfaces may be calculated through the use of density functional theory, or the semi-empirical embedded atom method. We have seen that density functional theory allows for the ab initio calculation of the properties of materials, which would otherwise be infeasible through the direct solution of the Schrödinger equation. This is achieved through a recasting of quantum mechanics, designed specifically for the ground state, which treats the electron density as the fundamental object, rather than the many-body wavefunction.

While density functional theory is a powerful scheme, its expense still limits the time and length scales which are accessible in the study of dynamics. The embedded atom method allows for the approximate treatment of hydrogen-metal interactions with a significantly reduced cost when compared with density functional theory. The success and efficiency of the embedded atom method can be attributed to its many-body interaction, which places the (approximate) atomic charge density in a central role, through the inclusion of embedding energy functions. These embedding energy functions are designed to capture the effects of placing an atom within a charge density that is generated by all of the other atoms, leading to an accurate description of the mechanical properties of metals.

While we shall see (in the following chapter) that the EAM5 potential is unsuitable for the study of hydrogen diffusion along the (111) nickel surface, this should not detract from the overall successes of the general method, or its suitability for the (100) surface in which it was designed.

Given the computational expense of long time (path integral) molecular dynamics studies, and the desire to model hydrogen-nickel interactions as accurately as possible, the methods detailed in this section were used to generate approximate potential energy surfaces (discussed in the following chapter), which may then be used to study the adsorbate dynamics. To this end, the various convergence parameters for both density functional theory and embedded atom method calculations have also been presented.

## Chapter 5

# Potential Energy Surfaces

### 5.1 Introduction

The concept of a potential energy surface (PES) plays an important role in condensed matter physics and the study of chemical reactions. In theoretical chemistry, all chemical reactions can be considered to take place on the potential energy surface which is defined by the configuration of the atoms. For a particular reaction, there is a reaction co-ordinate which defines a low energy pathway along the potential energy surface. The study of reaction rates through transition state theory requires knowledge of the energy minima along this reaction coordinate (describing the reactants and products), as well as the transition state, which represents the highest energy state along the reaction coordinate (Atkins and de Paula, 2006). The transition states of a chemical reaction represent saddle points on the PES.

In this chapter, we present a method for approximating the potential energy surface of hydrogen interactions with a static (111) nickel surface. By considering the dynamics of an adsorbate moving along the potential energy surface, one is able to carry out efficient molecular dynamics studies which would otherwise be prohibitively expensive when using the standard ab initio molecular dynamics method.

### 5.2 The adiabatic approximation

By exploiting the large difference in mass between the nickel ions and a hydrogen adsorbate, we are able to bridge the gap in computational effort and accuracy between first principles methods (such as DFT), and semi-empirical potential (such as EAM). This mass difference allows us to make an approximation which brings us close to DFT accuracy, but with a significantly reduced cost.

The rationale proceeds along the same lines as the Born-Oppenheimer approximation: since hydrogen is relatively light when compared to the ions in the nickel surface, we

may postulate that, for short periods of time, the nickel surface is static from the point of view of the hydrogen adsorbate — there is an adiabatic separation between the dynamics of the nickel surface and the hydrogen. If we are able to accept this approximation, we realise that in the *ab initio* molecular dynamics approach, most of the time would be spent calculating the density for a surface which is relatively stationary. Therefore, if we could somehow cache the energy/forces associated with the adsorbate-surface interaction, as a function of the adsorbate position above the surface, we could do away with many of the expensive electronic minimization procedures inherent in DFT.

The associated storage of the energy as a function of the adsorbate position above the fixed surface allows us to construct a potential energy surface, along which the adsorbate moves. If the constructed PES is an accurate representation of the true, adsorbate-surface interaction, then the dynamics of an adsorbate moving along the calculated PES should agree with the dynamics generated using *ab initio* molecular dynamics (under the same conditions, i.e. with constrained surface ions).

### 5.3 Determining the potential energy surface

Determination of the PES requires knowledge of the ground state nickel surface configuration, which can be calculated by minimizing the enthalpy of the system, by the process of geometry optimization (see Appendix A for details). When performing the surface geometry optimization, it is important to ensure that the cell vector normal to the surface is constrained, ensuring that the cell does not compress to a more bulk-like state. After the optimal geometry of the nickel surface has been determined, we have a suitable starting point for the calculation of the PES. (See Figure 5.3.1 for the surface used in the DFT calculations).

We argue that the dynamics of the nickel-hydrogen system can be approximated by an adiabatic separation of the nickel and hydrogen dynamics: i.e: the nickel surface remains stationary over the timescales of the faster hydrogen dynamics. This adiabatic separation implies that nickel ions does not have sufficient time to reconstruct at the surface (local to the hydrogen position), and so we choose to constrain all of the nickel ions to their minimum enthalpy configuration (in the absence of hydrogen) during the PES determination procedure. At finite temperatures (less than the melting point), the nickel ions should oscillate around their equilibrium positions, and constraining the nickel ions to their equilibrium position allows us to calculate the average (ground state) PES of any (small) thermal fluctuations of the nickel ions (neglecting any thermal expansion, which would act to change the lattice constant, but not the fractional positions of the ions). Of course, the energy of the constrained system will be greater than that of the optimized unconstrained system, since the presence of the hydrogen atom above the surface will exert a force on the nearby surface atoms, acting to change their local configuration.

Of course, it would be impractical to calculate the energy of the hydrogen-nickel system with the hydrogen at all possible positions in 3D space above the surface. Instead, we direct our attention to accurately defining the PES in regions where the adsorbate will spend most of its time — where it is bound to the surface — and approximate the lesser visited regions of configuration space (in the vacuum region far above the surface).

In order to accurately define the PES, we place the hydrogen adsorbate at discrete points in the surface plane (the **ab** plane) at a fixed height above the surface (along **c**), and perform a series of constrained geometry optimizations, moving the hydrogen normal to the surface (parallel to **c**), until we find the minimum energy. The result of this procedure is to define the energies of the hydrogen over a grid of points which span the surface plane. With the energies defined over a discrete grid, we are then able to interpolate between the grid points in order to provide an estimate of the PES at all positions in the surface plane.

In the case where surface contains several repeats of the unit cell, the number of equivalent data points can be reduced by placing the grid points along a subset of the surface, corresponding to the area of the unit cell. It is possible to increase the efficiency further by restricting the data points to span the irreducible wedge of the surface, although this process is more involved as it requires knowledge of the symmetry of the surface.

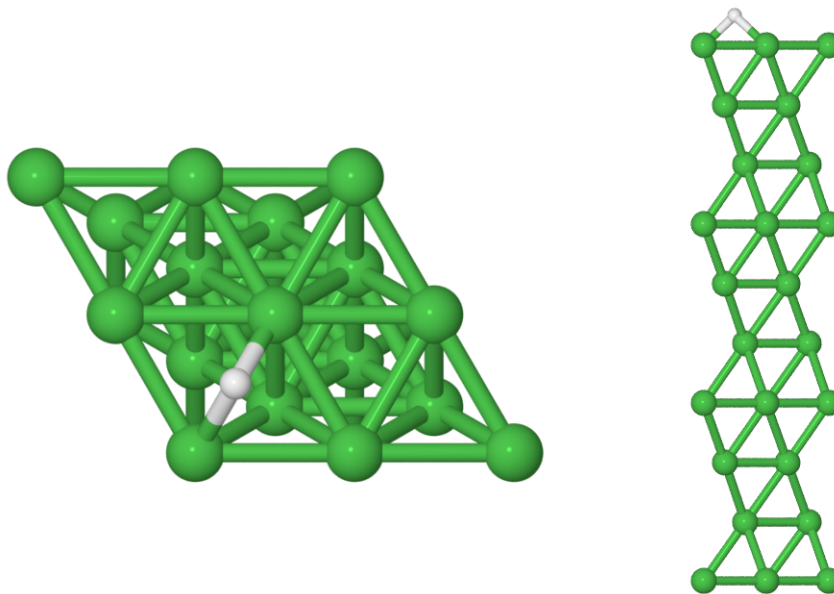


Figure 5.3.1: Top (left) and side (right) view of the nickel slab used for the DFT PES calculations. Due to the symmetry of the slab, the H atom is only scanned along sites in the bottom left quadrant of the (111) surface.

## 5.4 Fourier interpolation

Given a collection of values which are discretely sampled over the domain of a function (such as energies over a grid of positions), there are a number of methods which can be

used to interpolate between the sample points. When our target function (the unknown function we seek to determine) is periodic in nature, as is the case for our PES, a particularly natural choice is the method of Fourier (trigonometric) interpolation.

Fourier interpolation is centred around the application of the discrete Fourier transform (see Press et al. (1986) for details). Physically, the Fourier transform acts to transform a function/data set from the time domain into the frequency domain (although we do not have to restrict ourselves strictly to these units). This transformation process allows us to decompose a function into its fundamental frequencies, in order to perform spectral analysis, or (in our case) construct an approximation to our target function based on knowledge of the underlying frequencies.

$$H_n = \sum_{k=0}^{N-1} h_k \exp(2\pi i k n / N) \quad (5.4.1)$$

Algorithmically, the discrete Fourier transform takes a series of  $N$  (complex) input values ( $h_k$ ,  $k = 0, \dots, N-1$ ), which are evenly sampled across the (time) domain of the target function, and transforms them into  $N$  complex coefficients, ( $H_n$ ,  $n = 0, \dots, N-1$ ) (in the frequency domain), which represent the amplitude and phase of a particular frequency. The transformations mapping  $k$  to time, and  $n$  to frequency are:  $t_k = k(\delta t)$  and  $f_n = \frac{n}{N(\delta t)}$ .

The discrete Fourier transform is calculated across a discrete range of frequencies ranging from  $f = -\frac{1}{2(\delta t)}$  to  $f = \frac{1}{2(\delta t)}$  (the Nyquist frequency). When  $n$  runs over a positive range, the periodicity of the Fourier transform ensures that  $n = 0$  corresponds to the zeroth frequency,  $n = 1, \dots, \frac{N}{2} - 1$  correspond to positive frequencies,  $n = \frac{N}{2}$  corresponds to both the positive and negative Nyquist frequencies, and  $n = \frac{N}{2} + 1, \dots, N-1$  correspond to negative frequencies.

By making the symmetries of the Fourier transform explicit, we arrive at the following equation for the inverse Fourier transform:

$$h_k = \frac{1}{N} \left[ \sum_{n=0}^{N/2} H_n \exp(-2\pi i k n / N) + \sum_{n=N/2+1}^{N-1} H_n \exp(-2\pi i k (n - N) / N) \right]. \quad (5.4.2)$$

If the  $h_k$  are taken to be our energies at a series of grid points (evenly spaced along one dimension of the unit cell), we can use the discrete Fourier transform to calculate the Fourier coefficients of the energies, which allows us to estimate the energy at any point along this dimension, known as the *Fourier interpolation potential*:

$$h(x) \simeq \frac{1}{N} \left[ \sum_{n=0}^{N/2} H_n \exp(-2\pi i n x) + \sum_{n=N/2+1}^{N-1} H_n \exp(-2\pi i (n - N) x) \right]. \quad (5.4.3)$$

We note that by choosing the domain of  $x$  to be  $0 \leq x \leq 1$ , it is straightforward to calculate our PES in fractional coordinates, which ensures that a non-orthogonal PES does not require any special treatment.

The gradient of the Fourier interpolation potential can also be calculated, which allows for the determination of forces which are consistent with the interpolated potential:

$$\frac{dh(x)}{dx} \simeq \frac{-2\pi i}{N} \left[ \sum_{n=0}^{N/2} H_n n \exp(-2\pi i n x) + \sum_{n=N/2+1}^{N-1} H_n (n - N) \exp(-2\pi i (n - N) x) \right]. \quad (5.4.4)$$

This process can straightforwardly be extended to multiple dimensions, allowing for Fourier interpolation potential to be calculated at all points along our 2D surface ( $0 \leq x, y \leq 1$ ).

We note that, because the gradient (and therefore forces) are given in fractional coordinates, these must be transformed into Cartesian forces in order to perform molecular dynamics. The mapping of fractional forces to Cartesian forces is given by (Pfrommer et al., 1997),

$$\mathbf{F}_{\text{cart}} = \underline{\underline{h}} \left( \underline{\underline{g}}^{-1} \mathbf{F}_{\text{frac}} \right), \quad (5.4.5)$$

where we make use of the metric:  $\underline{\underline{g}} = \underline{\underline{h}}^T \underline{\underline{h}}$ , and  $\underline{\underline{h}}$  is the matrix of the cell vectors (where the lattice vectors are placed along the columns of the matrix).

## 5.5 Fourier interpolation potential energy surfaces

The method of Fourier interpolation is a general purpose one, and can be used for more than simply interpolating over the minimum energies. When choosing to interpolate over a surface of energies only, the calculated energies will be independent of the height ( $\mathbf{c}$  position) of the adsorbate — in a sense, we would have “flattened” our system onto 2 dimensions, and would be enforcing that the adsorbate is always bound to the nickel surface (at the height of minimum energy). By including additional levels of interpolation (over spring constants and equilibrium heights), we are able to undo this “flattening”, and create a PES which is more representative of the true adsorbate-surface interaction.

Clearly, in the real system, we expect there to be some motion of the adsorbate away from its minimum energy position. In order to include this motion in our calculations, we choose to approximate the  $\mathbf{c}$  dependence of the interaction with a harmonic potential which acts to confine the adsorbate to the minimum energy surface. The reason for this

choice is its simplicity and wide applicability — by the Taylor expansion, many functional forms are able to be approximated by a quadratic form (for small displacements). Rather than choose an arbitrary confining potential across the whole surface, and risk over/underdamping the motion normal to the surface in some regions, we make use of the output of the geometry optimization part of the PES determination to calculate approximate spring constants at each point along the surface. Fourier interpolation can then be used over these spring constants to introduce a smoothly varying, position dependent, harmonic contribution to the potential.

In choosing the  $\mathbf{c}$  dependence of the potential to be based on a harmonic interaction, we must also define an equilibrium height for the minimum of energy at this particular point. If we were to choose the same equilibrium height above the entirety of the surface, this would lead to an artificial suppression of the motion along the direction normal to the surface— again, introducing a “flattening” along one of the dimensions of the system. Since the output of a geometry optimization provides us with a final height of the adsorbate above the surface, we are able to repeat the interpolation process over these values to introduce a position dependence on the height of minimum energy for the harmonic contribution to our potential.

We now have a complete description of our Fourier interpolation PES. There is an interpolation over energies, which represents the minimum energy (at a point  $(\mathbf{a}, \mathbf{b})$ ) of a harmonic potential along  $\mathbf{c}$ , and provides the force on the adsorbate in the  $(\mathbf{a}, \mathbf{b})$  directions, and then there are two further levels of interpolation: over equilibrium heights and spring constants, which allow for the determination of the harmonic contribution to the final potential energy, and give rise to the  $\mathbf{c}$  components of the force.

By construction, the Fourier interpolation potential is designed to approximate the adsorbate-surface interaction at instances where the adsorbate is close to a static surface. There is no attenuation of the force components in the surface plane as the adsorbate rises above the surface, which is clearly unphysical. Furthermore, the approximation of the  $\mathbf{c}$  dependence on the potential to be a harmonic interaction is likely to be accurate for only small displacements away from the minimum of energy. There will also exist a particular height (or range of heights) at which the interaction between the adsorbate and the surface decays — this “roll-off” is not included in our model. Finally, we note that the PES is constructed under complete adiabatic separation between the dynamics of the adsorbate and the surface — as the mass of the adsorbate increases, or the simulation length increases, this separation is likely to break down and this approximation will become worse (for a description of possible extensions to the method, see Section 9.1).

### 5.5.1 Calculating spring constants

The geometry optimization along  $\mathbf{c}$  (fixed  $(\mathbf{a}, \mathbf{b})$  position) seeks to minimize the energy along this direction, and provides us with not only the minimum energy and equilibrium

height above the surface, but also the energy as a function of height  $E = E(x - x_0)$ . By choosing the functional form:  $|E - E_0| = \frac{1}{2}k|x - x_0|^2$ , approximating this relationship as a harmonic interaction, we are able to estimate an effective spring constant at this position.

The spring constant may be estimated by first linearizing the data, then performing a least squares fit on the equation:  $\sqrt{|E|} = m|x|$ . Where, for simplicity, we have chosen to shift our energies and spring constants such that  $E_0 = 0$  eV and  $x_0 = 0$  Å. After performing the least squares fit on the linearized data set, the spring constant is determined by the gradient of the fitted function:  $m = \sqrt{\frac{1}{2}k} \Rightarrow k = 2m^2$ . We make reference to the explanation of least squares fitting given in Giordano et al. (2009).

The least squares fit, for a function  $y = mx + c$ , is that which minimizes the sum of the squared residuals:

$$S = \sum_{i=1}^N [y_i - (mx_i + c)]^2. \quad (5.5.1)$$

The optimum fit can be found by setting  $\frac{\partial S}{\partial m} = \frac{\partial S}{\partial c} = 0$ , and solving the so-called normal equations which result. This leads to the following equations for the gradient,  $m$ , and intercept,  $c$ :

$$m = \frac{N \sum x_i y_i - \sum x_i \sum y_i}{N \sum x_i^2 - (\sum x_i)^2}, \quad (5.5.2)$$

$$c = \frac{\sum x_i^2 \sum y_i - \sum x_i y_i \sum x_i}{N \sum x_i^2 - (\sum x_i)^2}. \quad (5.5.3)$$

In our case, where  $c = 0$ , the equation for  $m$ , the gradient, reduces to

$$m = \frac{\sum x_i y_i}{\sum x_i^2}. \quad (5.5.4)$$

Note that it is also possible to use the least squares method to fit a parabola to the data directly, though this method requires more care due to the sensitivity of the spring constant (curvature) to residuals far from the minimum of the curve.

### 5.5.1.1 Determining the quality of a least squares fit

The least squares method used to estimate the spring constant introduces an additional source of error into the PES. To ensure the quality of the interpolated surface of spring constants, it is important to verify that each of the lines of best fit represent good approximations to a harmonic interaction.

The coefficient of determination,  $R^2$ , is a measure of the quality of a line of best fit. Its value represents the proportion of the total variation in the  $y$  variable of the data set (when compared with the variation from the mean) that is accounted for by the line of best fit (and therefore  $0 \leq R^2 \leq 1$ ):

$$R^2 = 1 - \frac{\text{SSE}}{\text{SST}}. \quad (5.5.5)$$

In the above, SSE is the value which is minimized when performing a least squares fit is the error sum of squares. This represents a measure of the variation about the line of best fit:

$$\text{SSE} = \sum_{i=1}^N [y_i - (mx_i + c)]^2. \quad (5.5.6)$$

SST is the total correlated sum of squares, which represents the variation of the  $y$  values about their mean:

$$\text{SST} = \sum_{i=1}^N (y_i - \bar{y})^2. \quad (5.5.7)$$

## 5.6 Results: Calculated potential energy surfaces

The determination of the PES is a computationally demanding procedure, and the number of data points used to fit the PES must be increased until convergence is reached. In order to determine at which point convergence is reached, the minimum energies, spring constants and equilibrium heights were calculated for validation set of 16 data points (for both the DFT and the EAM calculations). The points which make up the validation set were randomly generated points along the surface, and were not used in any of the fitting procedures. To determine whether PES had converged with respect to the number of data points, the difference between the results of the interpolation process and the actual values at the validation points were computed.

For efficiency reasons, the number of grid points along each dimension was chosen to be a power of 2. There are no restrictions on the number of data points along each dimension, but defining the grid points in this way meant data could be reused as the number of grid points were increased.

## 5.6.1 DFT (CASTEP) determined PES

### 5.6.1.1 Computational details

For convenience, the DFT calculation parameters, summarised in section 4.3.1.7, are reproduced below.

All calculations were carried out with a 2x2 (111) surface of nickel (corresponding to 0.25 ML coverage when the hydrogen atom was added). The nickel surface was made up of 10 layers, with an interslab spacing between neighbouring nickel surfaces of 10 Å. A cut-off energy of 725 eV, and a 4x4x1 k-point sampling grid were chosen. The calculations also used the rPBE exchange-correlation functional (Hammer et al., 1999), as well as the runtime generated “on the fly” ultrasoft pseudopotentials.

For the initial geometry optimization that was used to determine the static surface, the interlayer spacing of the nickel slab was able to vary, as were the cell vectors in the surface plane (where  $|\mathbf{a}| = |\mathbf{b}|$ ), but the cell vector normal to the surface was fixed. The geometry optimization proceeded until the maximum force was reduced to  $1.28 \times 10^{-2}$  eV/Å, and the maximum component of the stress tensor was smaller than  $5.82 \times 10^{-3}$  GPa. This calculation resulted in  $|\mathbf{a}| = |\mathbf{b}| = 4.9975$  Å, which corresponds to a nickel lattice constant of 3.5337 Å.

For the determination of the PES, the constrained geometry optimizations started with the hydrogen atom placed 1.5 Å above the surface. The associated geometry tolerances were: changes in the energy per atom must be less than  $1 \times 10^{-6}$  eV, the force reduced to less than  $2 \times 10^{-2}$  eV/Å, and position change of less than  $1 \times 10^{-4}$  Å. The requirement of such small changes in the height of the adsorbate meant that forces were actually reduced to be of the order  $\sim 10^{-5}$  eV/Å.

### 5.6.1.2 Interpolation of energies

The interpolated surface of (relative) energies, calculated using a 16x16 grid is presented in Figure 5.6.1, along with the statistics showing the quality of the interpolation (when compared to the validation set) as a function of the size of the interpolation grid is given in Table 5.6.1.

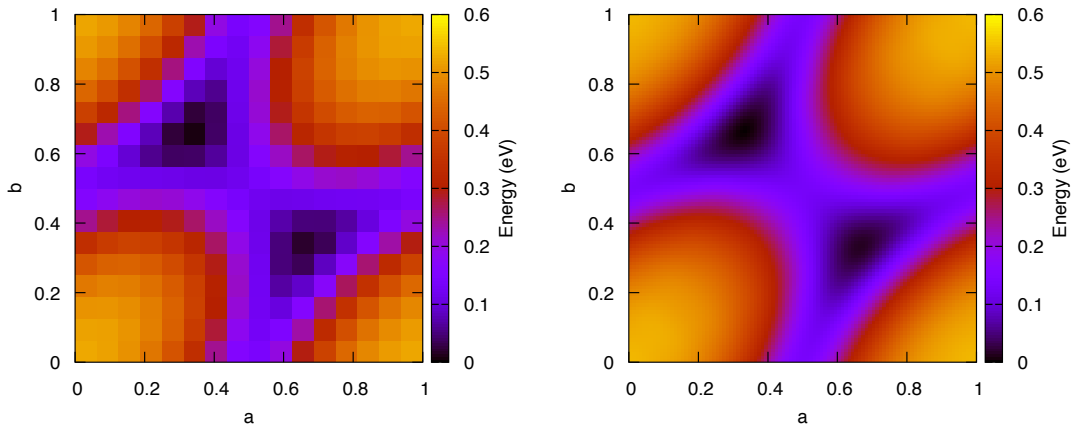


Figure 5.6.1: Relative potential energies of a single H atom, interacting with a 2x2 (111) Ni surface, calculated using DFT. The raw data (left), along with the interpolated surface (right), for a 16x16 grid are presented. All energies are shown relative to the global minimum.

Grid Size	$\overline{\Delta E}$ (eV)	$\Delta E_{\min}$ (eV)	$\Delta E_{\max}$ (eV)	$\sigma(\Delta E)$ (eV)
1x1	$-2.54 \times 10^{-1}$	$-5.96 \times 10^{-3}$	$-4.88 \times 10^{-1}$	$1.49 \times 10^{-1}$
2x2	$8.73 \times 10^{-2}$	$-1.03 \times 10^{-3}$	$3.14 \times 10^{-1}$	$1.28 \times 10^{-1}$
4x4	$3.14 \times 10^{-3}$	$-1.23 \times 10^{-3}$	$-7.79 \times 10^{-2}$	$3.03 \times 10^{-2}$
8x8	$-1.05 \times 10^{-3}$	$2.13 \times 10^{-5}$	$-4.19 \times 10^{-3}$	$2.27 \times 10^{-3}$
16x16	$-3.09 \times 10^{-4}$	$1.94 \times 10^{-5}$	$-1.84 \times 10^{-3}$	$6.83 \times 10^{-4}$

Table 5.6.1: The statistics of the energy difference between the interpolated values and the validation set, calculated using DFT. The mean energy difference reduces to meV level for the 8x8 grid, and is reduced to the sub-meV level for the 16x16 grid (with a sub-meV standard deviation).

### 5.6.1.3 Interpolation of heights

The interpolated surface of (relative) heights, calculated using a 16x16 grid is presented in Figure 5.6.2, along with the statistics showing the quality of the interpolation (when compared to the validation set) as a function of the size of the interpolation grid is given in Table 5.6.2. As would be expected, there is a direct relationship between the potential energy and the binding height, which arises due to the atomic structure of the surface (with lowest energy sites above the hollow sites of the surface).

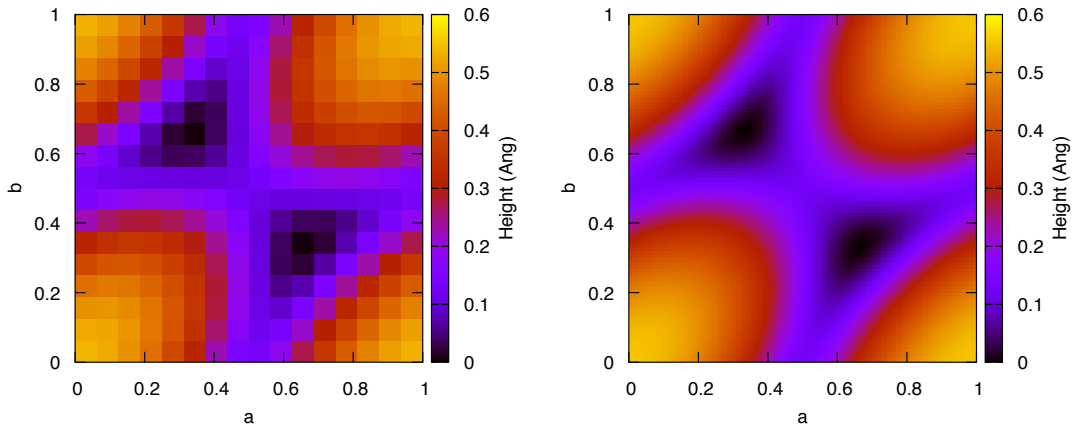


Figure 5.6.2: Relative binding heights of a single H atom, interacting with a 2x2 (111) Ni surface, calculated using DFT. The raw data (left), along with the interpolated surface (right), for a 16x16 grid are presented. All heights are shown relative to the global minimum.

Grid Size	$\overline{\Delta x_0}$ (Å)	$\Delta x_{0\min}$ (Å)	$\Delta x_{0\max}$ (Å)	$\sigma(\Delta x_0)$ (Å)
1x1	$-2.80 \times 10^{-1}$	$-4.84 \times 10^{-3}$	$-5.11 \times 10^{-1}$	$1.51 \times 10^{-1}$
2x2	$7.86 \times 10^{-2}$	$3.26 \times 10^{-4}$	$3.02 \times 10^{-1}$	$1.25 \times 10^{-1}$
4x4	$4.06 \times 10^{-3}$	$1.90 \times 10^{-3}$	$-6.67 \times 10^{-2}$	$2.60 \times 10^{-2}$
8x8	$1.85 \times 10^{-4}$	$2.34 \times 10^{-4}$	$4.30 \times 10^{-3}$	$2.11 \times 10^{-3}$
16x16	$1.07 \times 10^{-4}$	$7.37 \times 10^{-6}$	$6.91 \times 10^{-4}$	$3.12 \times 10^{-4}$

Table 5.6.2: The statistics of the difference in equilibrium hydrogen height between the interpolated values and the validation set, calculated using DFT.

#### 5.6.1.4 Interpolation of spring constants

The interpolated surface of spring constants, calculated using a 16x16 grid is presented in Figure 5.6.3, along with the statistics showing the quality of the interpolation (when compared to the validation set) as a function of the size of the interpolation grid is given in Table 5.6.3.

The interpolated spring constant surface is less smooth than the corresponding energy and height surfaces, especially in the regions above the low energy sites (corresponding to the hollow sites of the surface). It is possible that these fine details are spurious effects which emerge from the fitting procedure used to estimate the spring constants. Since the variation in the spring constant is not significant in these areas, and the coefficient of determination is still relatively high, it is not expected that these details adversely affect the dynamics of the adsorbate in a meaningful way. (The 16x16 grid remains the preferred choice, over the more coarse grids, due to the improved statistics when compared with the validation set).

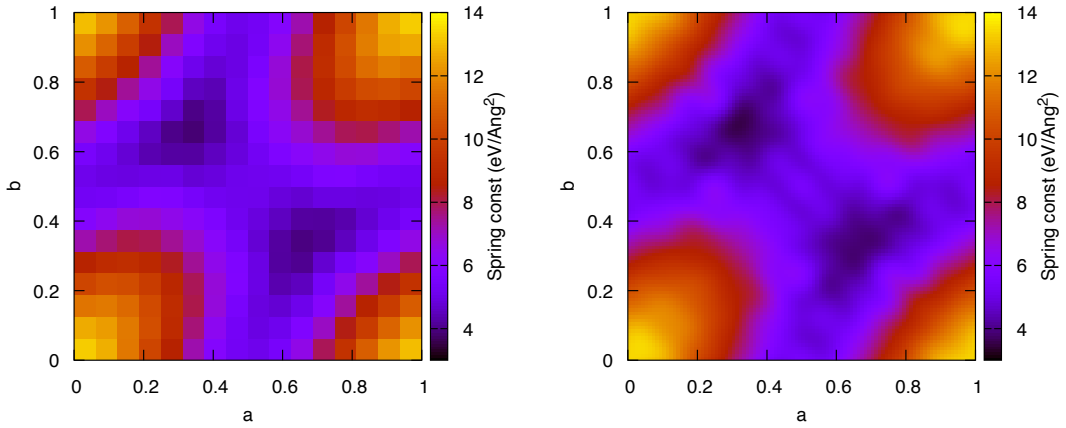


Figure 5.6.3: Effective spring constants approximating the  $\mathbf{c}$  dependent harmonic interaction for a single H atom, interacting with a  $2 \times 2$  (111) Ni surface, calculated using DFT. The raw data (left), along with the interpolated surface (right), for a  $16 \times 16$  grid are presented.

Grid Size	$\overline{\Delta k}$ (eV/Å <sup>2</sup> )	$\Delta k_{\min}$ (eV/Å <sup>2</sup> )	$\Delta k_{\max}$ (eV/Å <sup>2</sup> )	$\sigma(\Delta k)$ (eV/Å <sup>2</sup> )
1x1	-6.36	$-1.20 \times 10^{-1}$	-9.20	2.69
2x2	$3.39 \times 10^{-1}$	$-2.33 \times 10^{-2}$	3.68	1.74
4x4	$-4.33 \times 10^{-1}$	$-5.19 \times 10^{-2}$	-1.15	$3.75 \times 10^{-1}$
8x8	$-1.60 \times 10^{-1}$	$3.00 \times 10^{-2}$	$-6.74 \times 10^{-1}$	$2.82 \times 10^{-1}$
16x16	$4.64 \times 10^{-3}$	$-7.95 \times 10^{-3}$	$4.55 \times 10^{-1}$	$1.76 \times 10^{-1}$

Table 5.6.3: The statistics of the difference in spring constant between the interpolated values and the validation set, calculated using DFT. The mean difference in spring constant drops by two orders of magnitude as the grid dimensions increase from  $8 \times 8$  to  $16 \times 16$ . Note the large standard deviations and maximum differences for grid sizes smaller than the  $8 \times 8$ .

As a means of justifying the validity of the harmonic approximation used to estimate the spring constants, the statistics of the  $R^2$  values are presented in Table 5.6.4, with the position dependence of  $R^2$  shown in Figure 5.6.4. Note that the coefficient of determination is consistently above 0.977, regardless of the number of grid points for which the spring constant is estimated.

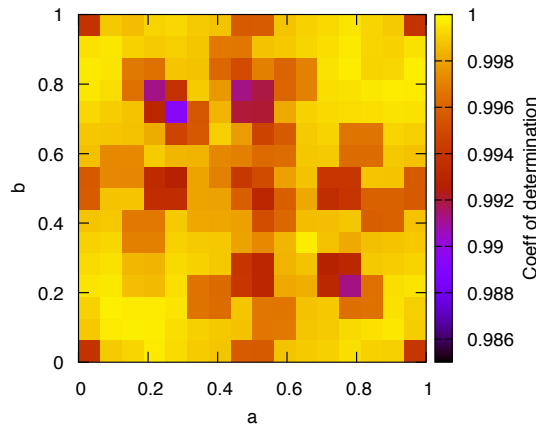


Figure 5.6.4: The position dependence of the coefficient of determination, which was used as a measure of quantifying the quality of the  $\mathbf{c}$  dependent harmonic interaction. Calculations modelled a single H atom interacting with a 2x2 (111) Ni surface using DFT. (A 16x16 grid of points was used).

Grid Size	$\overline{R^2}$	$R_{\min}^2$	$R_{\max}^2$	$\sigma(R^2)$
1x1	0.977	-	-	-
2x2	0.984	0.977	0.987	0.00403
4x4	0.988	0.977	0.999	0.00934
8x8	0.996	0.977	1.000	0.00668
16x16	0.998	0.977	1.000	0.00418

Table 5.6.4: The statistics associated with the coefficient of determination (a measure of the quality of the harmonic approximation used for the  $\mathbf{c}$  dependence of the potential) as a function of the number of grid points. These calculations were based on a least squares fit to the results of geometry optimizations carried out using DFT.

## 5.6.2 EAM5 determined PES

### 5.6.2.1 Computational details

Again, we reproduce the EAM5 calculation parameters (summarised in section 4.4.2.4), for convenience.

These calculations were carried out with a 5x5 surface of nickel (corresponding to 0.04 ML coverage when the hydrogen atom was added) — although it should be noted that the EAM potential does not include a H-H interaction across neighbouring cells. The nickel surface was made up of 7 layers, with an interslab spacing between neighbouring nickel surfaces of 15 Å.

An initial geometry optimization was performed on the static nickel surface (in the absence of hydrogen) in the same manner as the DFT calculations. Following the geometry optimization, the maximum force was reduced to  $4.18 \times 10^{-6}$  eV/Å, and

the maximum component of the stress tensor was  $8.78 \times 10^{-8}$  GPa. This calculation resulted in  $|\mathbf{a}| = |\mathbf{b}| = 12.4668 \text{ \AA}$ , corresponding to a nickel lattice constant of  $3.5261 \text{ \AA}$ .

As with the DFT calculations, the constrained geometry optimizations used to determine the PES started with the hydrogen atom placed  $1.5 \text{ \AA}$  above the surface. The associated geometry tolerances were: changes in the energy per atom must be less than  $1 \times 10^{-6}$  eV, the force reduced to less than  $5 \times 10^{-6}$  eV/ $\text{\AA}$ , and a position change of less than  $1 \times 10^{-6}$   $\text{\AA}$ .

### 5.6.2.2 Interpolation of energies

The interpolated surface of (relative) energies, calculated using an  $8 \times 8$  grid is presented in Figure 5.6.5, along with the statistics showing the quality of the interpolation (when compared to the validation set) as a function of the size of the interpolation grid is given in Table 5.6.5. While the EAM5 PES shows better agreement to the validation set than the DFT PES (using equivalently sized grids), there is little need to go beyond the  $8 \times 8$  grid in this case, as the changes in relative energies are well below the sub-meV level by this point.

While the surface is qualitatively similar to the one calculated using DFT, it is observed that the relative binding energies are much smaller in this case. (A maximum barrier height of  $\sim 0.16$  eV in EAM5, compared with  $\sim 0.6$  eV using DFT).

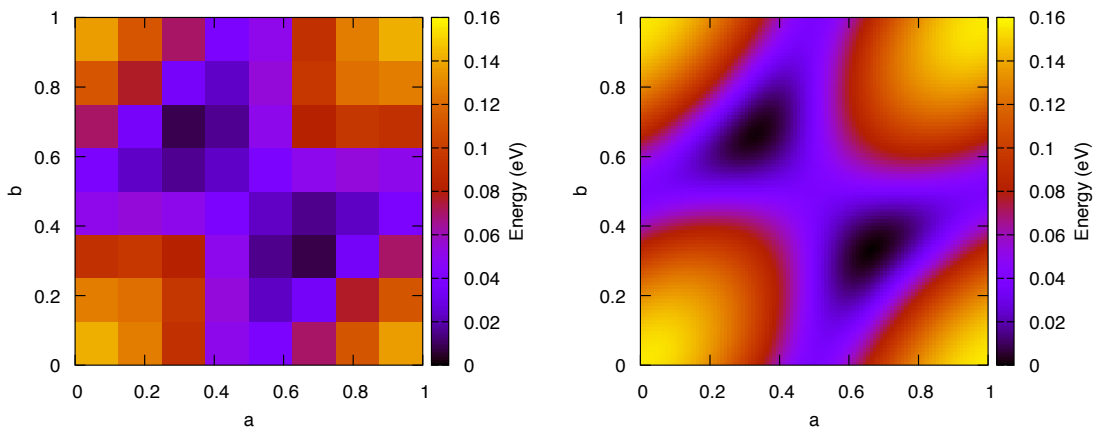


Figure 5.6.5: Relative potential energies of a single H atom, interacting with a  $5 \times 5$  (111) Ni surface, calculated using the EAM5 potential. The raw data (left), along with the interpolated surface (right), for an  $8 \times 8$  grid are presented. All energies are shown relative to the global minimum.

Grid Size	$\overline{\Delta E}$ (eV)	$\Delta E_{\min}$ (eV)	$\Delta E_{\max}$ (eV)	$\sigma(\Delta E)$ (eV)
1x1	$-7.85 \times 10^{-2}$	$-4.01 \times 10^{-3}$	$-1.34 \times 10^{-1}$	$4.33 \times 10^{-2}$
2x2	$7.39 \times 10^{-3}$	$-1.52 \times 10^{-4}$	$7.75 \times 10^{-2}$	$3.61 \times 10^{-2}$
4x4	$6.74 \times 10^{-4}$	$-5.95 \times 10^{-5}$	$-8.85 \times 10^{-3}$	$5.34 \times 10^{-3}$
8x8	$-2.74 \times 10^{-5}$	$1.04 \times 10^{-5}$	$-4.96 \times 10^{-4}$	$2.21 \times 10^{-4}$
16x16	$-5.30 \times 10^{-8}$	$2.48 \times 10^{-9}$	$-1.90 \times 10^{-6}$	$6.57 \times 10^{-7}$

Table 5.6.5: The statistics of the energy difference between the interpolated values and the validation set, calculated using the EAM5 potential. By the 4x4 grid, the mean energy difference is at the sub-meV level, but the maximum energy difference does not decrease to the sub-meV level until the 8x8 grid.

### 5.6.2.3 Interpolation of heights

The interpolated surface of (relative) heights, calculated using an 8x8 grid is presented in Figure 5.6.6, along with the statistics showing the quality of the interpolation (when compared to the validation set) as a function of the size of the interpolation grid is given in Table 5.6.6.

Again, the EAM5 surface is qualitatively the same as the DFT surface, but the relative binding heights are not as large as those calculated using DFT. (A maximum height of  $\sim 0.4$  Å with EAM5, compared with  $\sim 0.6$  Å with DFT).

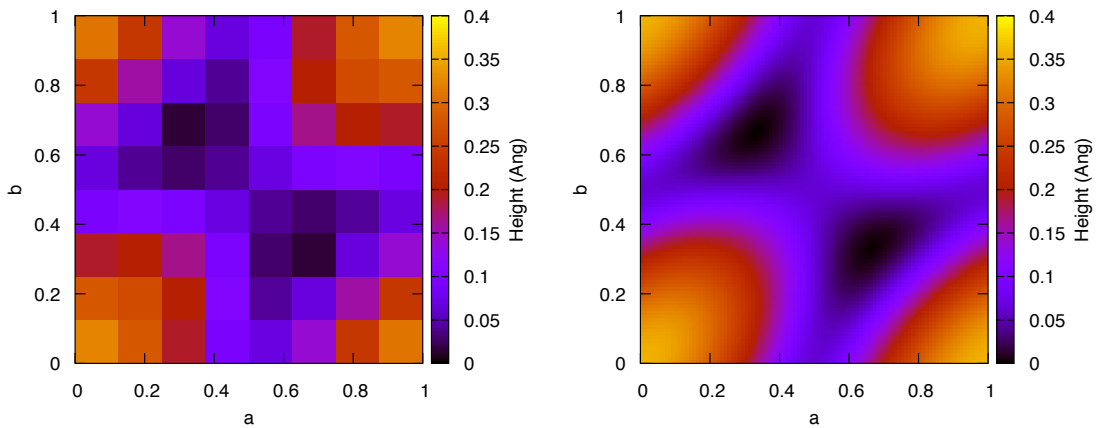


Figure 5.6.6: Relative binding heights of a single H atom, interacting with a 5x5 (111) Ni surface, calculated using the EAM5 potential. The raw data (left), along with the interpolated surface (right), for an 8x8 grid are presented. All heights are shown relative to the global minimum.

Grid Size	$\overline{\Delta x_0}$ (Å)	$\Delta x_{0\min}$ (Å)	$\Delta x_{0\max}$ (Å)	$\sigma(\Delta x_0)$ (Å)
1x1	$-1.99 \times 10^{-1}$	$-1.23 \times 10^{-2}$	$-3.20 \times 10^{-1}$	$1.00 \times 10^{-1}$
2x2	$1.43 \times 10^{-2}$	$-3.69 \times 10^{-4}$	$1.78 \times 10^{-1}$	$8.24 \times 10^{-2}$
4x4	$7.52 \times 10^{-4}$	$-1.09 \times 10^{-4}$	$-1.43 \times 10^{-2}$	$8.11 \times 10^{-3}$
8x8	$-4.17 \times 10^{-5}$	$-1.63 \times 10^{-5}$	$-7.01 \times 10^{-4}$	$3.11 \times 10^{-4}$
16x16	$-1.03 \times 10^{-7}$	$-1.44 \times 10^{-10}$	$-4.02 \times 10^{-6}$	$1.49 \times 10^{-6}$

Table 5.6.6: The statistics of the difference in equilibrium hydrogen height between the interpolated values and the validation set, calculated using the EAM5 potential. The 8x8 grid calculated using EAM5 shows similar agreement its validation set as the 16x16 grid calculated using DFT.

#### 5.6.2.4 Interpolation of spring constants

The interpolated surface of spring constants, calculated using an 8x8 grid is presented in Figure 5.6.7, along with the statistics showing the quality of the interpolation (when compared to the validation set) as a function of the size of the interpolation grid is given in Table 5.6.7.

The interpolated spring constant surface is much smoother than the one calculated using DFT (even when comparing grids with equivalent numbers of grid points). As demonstrated in tables 5.6.3 and 5.6.7, the agreement with the validation set is similar for the 8x8 fit using EAM5, as the 16x16 grid calculated with DFT. Therefore, like with the energies and heights, there is little need to go beyond the 8x8 grid in this case.

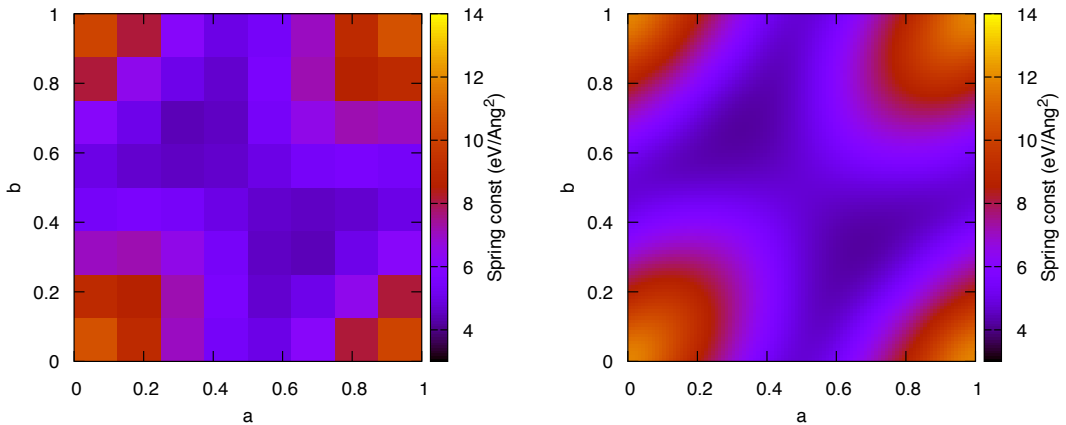


Figure 5.6.7: Effective spring constants approximating the  $\mathbf{c}$  dependent harmonic interaction for a single H atom, interacting with a 5x5 (111) Ni surface, calculated using the EAM5 potential. The raw data (left), along with the interpolated surface (right), for an 8x8 grid are presented.

Grid Size	$\overline{\Delta k}$ (eV/Å <sup>2</sup> )	$\Delta k_{\min}$ (eV/Å <sup>2</sup> )	$\Delta k_{\max}$ (eV/Å <sup>2</sup> )	$\sigma(\Delta k)$ (eV/Å <sup>2</sup> )
1x1	-5.41	-0.945	-7.37	1.92
2x2	$-2.38 \times 10^{-1}$	$-6.46 \times 10^{-3}$	-3.37	1.71
4x4	$-3.94 \times 10^{-2}$	$8.88 \times 10^{-5}$	$-5.18 \times 10^{-1}$	$1.89 \times 10^{-1}$
8x8	$5.84 \times 10^{-3}$	$1.08 \times 10^{-3}$	$1.65 \times 10^{-1}$	$5.13 \times 10^{-2}$
16x16	$2.00 \times 10^{-3}$	$1.83 \times 10^{-4}$	$1.63 \times 10^{-1}$	$4.90 \times 10^{-2}$

Table 5.6.7: The statistics of the difference in spring constant between the interpolated values and the validation set, calculated using the EAM5 potential. There is very little to gain in going from the 8x8 to the 16x16 grid. The 8x8 grid calculated with the EAM5 potential has a similar mean, and a better minimum, maximum and standard deviation than the 16x16 grid generated using DFT.

The statistics of the  $R^2$  values used to determine the quality of the harmonic approximation are presented in Table 5.6.8, with the position dependence of  $R^2$  again shown in Figure 5.6.8. The coefficient of determination is consistently above 0.989 regardless of the number of grid points calculated, and furthermore, the position dependence on  $R^2$  is also relatively smooth.

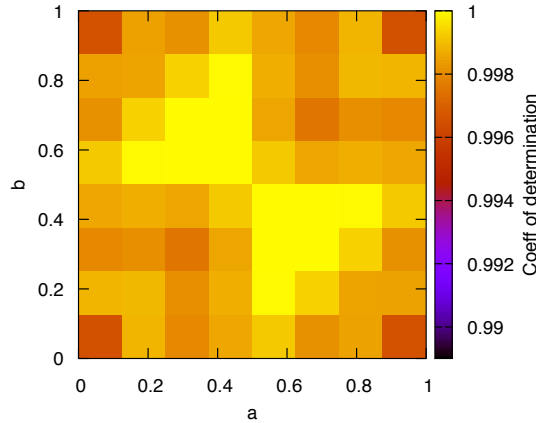


Figure 5.6.8: The position dependence of the coefficient of determination, which was used as a measure of quantifying the quality of the  $\mathbf{c}$  dependent harmonic interaction. Calculations modelled a single H atom interacting with a 5x5 (111) Ni surface using the EAM5 potential. (An 8x8 grid of points was used).

Grid Size	$\overline{R^2}$	$R^2_{\min}$	$R^2_{\max}$	$\sigma(R^2)$
1x1	0.989	-	-	-
2x2	0.997	0.989	1.000	0.00469
4x4	0.999	0.989	1.000	0.00257
8x8	0.999	0.989	1.000	0.00164
16x16	0.999	0.989	1.000	0.00194

Table 5.6.8: The statistics associated with the coefficient of determination (a measure of the quality of the harmonic approximation used for the  $\mathbf{c}$  dependence of the potential) as a function of the number of grid points. These calculations were based on a least squares fit to the results of geometry optimizations carried out using the EAM5 potential.

## 5.7 Summary

The determination of approximate potential energy surfaces allows for the study of the dynamics of light adsorbates on heavy surfaces, which may be prohibitively expensive when using the conventional approaches — this is made possible by the assumption of an adiabatic separation between the motion of the adsorbate and the surface atoms, as well as the small number of degrees of freedom of the system of interest. Such a potential energy surface may be represented using a combination of Fourier interpolation and harmonic approximations, and parameterized in a relatively straightforward manner, through a series of geometry optimization procedures. Of course, the parameterization of a potential energy surface for a system with more degrees of freedom, or one where the adsorbate is not simply bound to the system, is a more involved procedure, and the methods described in this section will require modification.

In addition to describing the parameterization of the potential energy surfaces, methods for analyzing the quality of the PES, through the comparison with a validation set of data points, as well as making use of the statistics related to the least square fitting procedure, were described.

Following the outline of the methods, potential energy surfaces for hydrogen on the (111) nickel surface, calculated using density functional theory, and the EAM5 potential, were presented. It is clear that the EAM5 potential is unsuitable for the study of hydrogen diffusion above the (111) surface, in agreement with the observations of Wonchoba et al. (1995). Given that the EAM5 potential represents a poor model for the interactions with the (111) surface, and because the DFT PES is significantly more efficient than using the EAM5 potential in the conventional manner, the EAM5 potential (and its PES) will not feature in any of the forthcoming results — instead, all following results/calculations will be carried out using the DFT PES.

In the following section, the method of (classical) molecular dynamics is presented. Much of the underlying theory will also form the foundation for path integral based molecular dynamics methods, which are discussed in Chapter 7.

## Chapter 6

# Molecular Dynamics

### 6.1 Introduction

Molecular dynamics (MD) is perhaps the most straightforward method of atomistic simulation. Newton’s laws are used to generate trajectories which sample the phase space of the system. From these trajectories we are able to calculate dynamical properties and/or ensemble averages of statistical mechanics. Its ability to calculate ensemble averages has led to it being described as “statistical mechanics by numbers” by Maddox (1988).

The success of molecular dynamics as a simulation technique can be attributed to its simplicity, the wide number of properties it is able to calculate, and the fact that information about the physical world can be gained which may be inaccessible through experiment alone, due to the difference in time and length scales that simulation and experiment are able to access (although recent advances in technology have allowed for this gap to narrow). This allows, as is typical of computational physics, for molecular dynamics studies to provide additional insight into the world, alongside traditional theory and experiment.

Despite the simplicity of the underlying theory, the field of MD is not stagnant. Work is still ongoing on algorithmic improvements, particularly with regard to the study of rare events and determination of free energy surfaces (e.g. Chen et al. 2015; McCarty et al. 2016; Wu et al. 2016). For example, calculating the properties of rare events represents a particular challenge for simulation, as the short time scales and small number of atoms often means that the process in which we are interested may be unlikely to occur in the duration of a typical simulation. Specialist techniques (which build on the standard molecular dynamics methodology) have been developed to tackle some of these problems (see also: Laio and Parrinello 2002; Miron and Fichthorn 2004; E et al. 2005).

This chapter addresses the underlying theory and methodology behind the molecular dynamics approach. We begin with a review of the Hamiltonian formalism of classical

mechanics, and follow this with a description of the Velocity-Verlet scheme that is used to integrate the resulting equations of motion. The chapter then discusses the ergodic hypothesis, which proves to be of fundamental importance in the calculation of ensemble averages and time correlation functions. This is followed by a description of the constant temperature (NVT, or canonical) ensemble, its properties, and some of the common thermostating methods which are used to sample from this ensemble. We then move on to discuss the details of initializing simulations, and discuss the importance of the equilibration period. This is followed by a description of some of the computational details involved with simulating systems using periodic boundary conditions. Finally, the chapter draws to a close with the details concerning the calculation of correlation functions and their related properties (including the diffusion coefficient).

## 6.2 Classical mechanics: Hamiltonian formalism

The laws of classical mechanics underpin the molecular dynamics method. Throughout an MD simulation, the atoms/nuclei of the system are evolved through time according to the equations of motion which satisfy Newton's laws. For reasons that will become clear in a later section (when we discuss path integral simulations), the Hamiltonian formalism of classical mechanics provides an elegant framework in which to derive these equations of motion.

In Hamiltonian mechanics (see e.g. Goldstein (1980)), the evolution of a classical system is completely determined by the Hamiltonian which describes the system,  $H = H(\{\mathbf{q}_i, \mathbf{p}_i; i = 1, \dots, N\}, t)$  — which is a function of the positions,  $\mathbf{q}_i$  and the momenta,  $\mathbf{p}_i$ .

In order to define the Hamiltonian, we note that it may, most generally, be derived from the Lagrangian,  $L$ , which describes the system (and therefore minimizes the action) through the Legendre transform, which is given in Equation 6.2.1. (Where the  $\mathbf{q}_i$  are the generalized coordinates of Lagrangian mechanics).

$$H = \sum_i \dot{\mathbf{q}}_i \frac{\partial L}{\partial \dot{\mathbf{q}}_i} - L = \sum_i \dot{\mathbf{q}}_i \mathbf{p}_i - L \quad (6.2.1)$$

While it is not always necessary to go through such an involved process in order to determine the Hamiltonian of the system, Equation 6.2.1 is provided to make clear the link between the Lagrangian and Hamiltonian formalisms of classical mechanics. We note that we shall return to Lagrangian mechanics, in the context of the principle of least action, in Section 7.2.1, when we discuss how the path integral formalism of quantum mechanics arises as an extension of classical mechanics.

Often, we find that the Hamiltonian may be written in the following way (which may easily be seen when the Lagrangian is  $L = T - V$ )

$$H = T + V. \quad (6.2.2)$$

Expanding out the kinetic energy, we may also express the Hamiltonian as

$$H = \sum_{i=1}^N \frac{\mathbf{p}_i^2}{2m_i} + V(\mathbf{q}_1, \dots, \mathbf{q}_N). \quad (6.2.3)$$

From the Hamiltonian, we may now make use of Hamilton's equations in order to derive the equations of motion for the system:

$$\frac{d\mathbf{p}_i}{dt} = -\frac{\partial H}{\partial \mathbf{q}_i} \quad (6.2.4)$$

$$\frac{d\mathbf{q}_i}{dt} = \frac{\partial H}{\partial \mathbf{p}_i}. \quad (6.2.5)$$

We see that Equations 6.2.4 and 6.2.5 define the evolution of the positions and momenta coordinates as a function of time. Therefore, the state of the system may be represented by the coordinates,  $(\mathbf{q}, \mathbf{p})$  — these coordinates represent points in what is known as *phase space*.

As the system evolves in time, it may be considered to be exploring a  $6N$ -dimensional phase space, where the explorable volume of phase space is defined by the Hamiltonian (or total energy) of the system. This concept of phase space exploration plays an important role when considering the ergodicity of a molecular dynamics simulation.

### 6.3 Integrating the equations of motion: Velocity Verlet

With the equations of motion now known, we may consider how to evolve the system in time. When performing molecular dynamics, the integration scheme that is employed to evolve the equations of motion must satisfy important criteria. Throughout this section, we make reference to the work of Frenkel and Smit (1996), who provide an excellent description of the subtleties and requirements of integration schemes.

Of crucial importance are the time reversibility and therefore conservation of energy of the integration scheme (since Newton's laws are time reversible). Since any numerical finite difference based integration scheme will suffer from both truncation and rounding errors (with the amount depending on the details of the integration scheme used, as well as the size of the timestep), our definition for energy conservation must simply be that samples taken from a trajectory are sufficiently close to the true constant energy surface in phase space, that ensemble averages calculated are consistent with the microcanonical ensemble.

This final point may be clarified: in order to guarantee that samples from a trajectory following equations of motion arising from Hamilton's equations are consistent with the microcanonical ensemble, we require that our integration scheme is phase space volume preserving: that is, the phase space volume enclosed by the constant energy surface must remain the same during the evolution of the system. This means that the evolution of the system from any point within the region of phase space that is bound by the constant energy surface, must remain confined within this volume.

There is an additional constraint which defines a good integration scheme: in general, the trajectory generated by most integration schemes will not exactly match that of the true Hamiltonian — if the integration scheme is good, the trajectories it generates should approximately follow that of a pseudo-Hamiltonian, which is a small perturbation of the original Hamiltonian. An integration scheme which follows the pseudo-Hamiltonian is referred to as *symplectic*, which is a stronger condition than simply being phase space volume preserving. Symplectic integration schemes are also time reversible, energy conserving and phase space volume preserving.

One of the most widely used integration schemes (and the one used for this work), is the Velocity Verlet algorithm (Swope et al., 1982). Velocity Verlet has the advantages that it is symplectic, volume preserving, time reversible and conserves energy (provided the timestep is reasonable, of course).

We begin with the Verlet algorithm (Verlet, 1967), which can be derived by taking the Taylor expansion of the positions (both forwards and backwards in time):

$$\mathbf{r}(t \pm \Delta t) = \mathbf{r}(t) \pm \mathbf{v}(t) \Delta t + \frac{1}{2} \mathbf{a}(t) \Delta t^2 \pm \frac{1}{3!} \ddot{\mathbf{r}}(t) \Delta t^3 + \mathcal{O}(\Delta t^4). \quad (6.3.1)$$

Addition of the forward and backward expansions, followed by rearranging, leads to the Verlet integrator:

$$\mathbf{r}(t + \Delta t) = 2\mathbf{r}(t) - \mathbf{r}(t - \Delta t) + \mathbf{a}(t) \Delta t^2 + \mathcal{O}(\Delta t^4). \quad (6.3.2)$$

The Verlet integrator (Equation 6.3.2) does not explicitly contain the velocities, these can however be estimated from the centred difference, as

$$\mathbf{v}(t) = \frac{\mathbf{r}(t + \Delta t) - \mathbf{r}(t - \Delta t)}{2\Delta t} + \mathcal{O}(\Delta t^2). \quad (6.3.3)$$

We note two issues with the standard Verlet algorithm (Equations 6.3.2 and 6.3.3): firstly, the algorithm is not self-starting (since we require the positions at the previous timestep to get the new positions). Secondly, the calculation of the velocities are not carried out at the same timestep as the positions, leading to difficulties defining the

kinetic energy (and therefore temperature), as well as the implementation of velocity dependent forces.

The Velocity Verlet algorithm addresses both of these deficiencies and is given:

$$\mathbf{r}(t + \Delta t) = \mathbf{r}(t) + \mathbf{v}(t) \Delta t + \frac{1}{2} \mathbf{a}(t) \Delta t^2, \quad (6.3.4)$$

$$\mathbf{v}(t + \Delta t) = \mathbf{v}(t) + \frac{1}{2} [\mathbf{a}(t) + \mathbf{a}(t + \Delta t)] \Delta t. \quad (6.3.5)$$

This is most commonly carried out in two stages: first, we calculate the new positions and half-timestep velocities:

$$\mathbf{v}\left(t + \frac{\Delta t}{2}\right) = \mathbf{v}(t) + \frac{1}{2} \mathbf{a}(t) \Delta t \quad (6.3.6)$$

$$\mathbf{r}(t + \Delta t) = \mathbf{r}(t) + \mathbf{v}\left(t + \frac{\Delta t}{2}\right) \Delta t. \quad (6.3.7)$$

Finally, we propagate the velocities to the full timestep (after calculating the new forces (and therefore accelerations)) based on the new positions:

$$\mathbf{v}(t + \Delta t) = \mathbf{v}\left(t + \frac{\Delta t}{2}\right) + \frac{1}{2} \mathbf{a}(t + \Delta t) \Delta t. \quad (6.3.8)$$

Therefore, the complete Velocity Verlet algorithm is given by Equations 6.3.6, 6.3.7 and 6.3.8.

We note that in all integration schemes, the timestep required to accurately integrate the equations of motion will be dependent on the highest frequency vibrational mode present in the system. This may be determined by performing (for example), lattice dynamics calculations, or through the (Fourier transformed) velocity autocorrelation function (described in Section 6.12). It is also possible to perform microcanonical (NVE) calculations with a range of different timesteps and monitor the fluctuations of the energy, in order to calculate the optimal timestep — beyond a certain point, the dynamics will become unstable and will conserve energy poorly.

## 6.4 The ergodic hypothesis

With the underlying “mechanics” of the MD methodology specified, we now turn our attention to the ergodic hypothesis, which provides the theoretical underpinning that

allows for the calculation of time correlation functions and ensemble averages from molecular dynamics trajectories.

We begin with ensemble averages: in order for such averages to be calculated from the samples taken from an MD trajectory, we require that such samples are consistent with the laws of statistical mechanics. For a system at thermal equilibrium, an ensemble average may be obtained by averaging over many possible replicas of the system, each of which has an equal probability of existing in one of the available microstates. This means that the ensemble average is invariant to the order in which the averaging is performed (and we do not need to sample from the microstates in any particular order).

While this concept naturally lends itself to a Monte Carlo approach, the ergodic hypothesis states that, for a molecular dynamics trajectory which undergoes a *fair and unbiased sampling* of the accessible phase space configurations, the time average of an observable becomes equivalent to the ensemble average — such a trajectory is said to be *ergodic*. This result can be expressed mathematically as

$$\bar{A} = \langle A \rangle_{\text{ensemble}}, \quad (6.4.1)$$

where  $\bar{A}$  represents a time average of the quantity of interest, and  $\langle A \rangle_{\text{ensemble}}$  is the ensemble average.

The ergodicity of a simulation is also important for the calculation of time correlation functions. As we shall see in Section 6.11, the fair and unbiased sampling which defines an ergodic trajectory means that, because a simulation is able to pass through all possible starting points of a measurement of a dynamical process, a trajectory may be split into multiple “chunks”, and time origin sampling performed in order to determine the equilibrium time correlation function.

## 6.5 Ensemble sampling and the thermodynamic limit

In the absence of any non-conservative forces (i.e. those in which  $\mathbf{F} \neq -\nabla V$ ), the evolution of the system specified by Hamilton’s equations (Equations 6.2.4 and 6.2.5) (and integrated using the Velocity Verlet scheme) will conserve number of particles, the volume of the simulation cell, and total energy (*NVE*). Assuming the trajectory is ergodic, any ensemble averages taken from such a trajectory will be consistent with the microcanonical ensemble of statistical mechanics.

In the thermodynamic limit ( $N \rightarrow \infty$ , with  $N/V = \text{const}$ ), the averages calculated in all statistical ensembles are equal (Tuckerman, 2010). Since our calculations will often be far from the thermodynamic limit, we may instead choose to sample from a different statistical ensemble (often the one which most closely represents the lab conditions) in order to more accurately calculate ensemble averages.

The canonical ensemble is a common choice of statistical ensemble (and the one which is used throughout this work). This ensemble conserves the (average) temperature of the system, rather than energy, as well as the number of particles and volume of the simulation cell, as before ( $NVT$ ). Other choices which are commonly used are the isothermal-isobaric ( $NPT$ ) ensemble, isoenthalpic-isobaric ( $NPH$ ) ensemble and grand canonical ( $\mu PT$ ) ensemble. Other ensemble sampling techniques do exist, but their use is more specialised (such as the isokinetic ensemble).

## 6.6 The canonical ensemble: Thermostatting

Performing molecular dynamics in the canonical ensemble requires the use of a *thermostat*. The thermostat can be thought of as providing a reservoir for the system to exchange energy with, providing a “constant” temperature and ensuring ensemble averages are consistent with the canonical ensemble.

### 6.6.1 Temperature fluctuations in the canonical ensemble

When dealing with the canonical ensemble, it is important to describe exactly what is meant by “constant temperature”, and to distinguish between the canonical and isokinetic ensembles. Following the descriptions in Frenkel and Smit (1996); Glover (2004), we shall attempt to show the magnitude of the temperature fluctuations inherent in an  $NVT$  simulation.

At thermal equilibrium, the temperature of a classical system can be considered proportional to the average amount of kinetic energy per degree of freedom available to the system:

$$\frac{\nu}{2}k_B T = \frac{1}{2} \sum_{i=1}^N m_i \overline{\mathbf{v}_i^2}, \quad (6.6.1)$$

where  $\nu$  is the total number of degrees of freedom available to the system (for our systems, this will be  $3N$ , or  $3N - 3$  when the centre of mass is constrained). This leads to our definition for the instantaneous temperature of the system:

$$T_{\text{inst}}(t) = \frac{\sum_{i=1}^N m_i \mathbf{v}_i^2(t)}{\nu k_B}. \quad (6.6.2)$$

In the isokinetic ensemble, the total kinetic energy for the system ( $\frac{1}{2} \sum_{i=1}^N m_i \mathbf{v}_i^2$ ) is held constant. As such, our measure of the instantaneous temperature is also held constant. This does not correspond to the true canonical ensemble, since, in the canonical ensemble, the Maxwell-Boltzmann distribution (Equation 6.6.3) should hold true for the speed of each of the particles.

$$f(v) dv = 4\pi \left( \frac{m}{2\pi k_B T} \right)^{3/2} v^2 \exp(-mv^2/2k_B T) dv \quad (6.6.3)$$

In order to calculate the fluctuations of the instantaneous temperature which are consistent with the Maxwell-Boltzmann distribution/canonical ensemble, we should calculate the mean squared deviation of the speeds squared (which are the only varying quantity in the kinetic energy):

$$\Delta (v_i^2)^2 = \left\langle (v_i^2)^2 \right\rangle - \langle v_i^2 \rangle^2, \quad (6.6.4)$$

where the averages ( $\langle \dots \rangle$ ) are taken over an MD trajectory, i.e: simulation time (or due to the ergodic hypothesis, these may also be ensemble averages).

This may be calculated as

$$\Delta (v_i^2)^2 = \left\langle (v_i^2)^2 \right\rangle - \langle v_i^2 \rangle^2 = \frac{\int_0^\infty (v^2)^2 f(v) dv}{\int_0^\infty f(v) dv} - \left( \frac{\int_0^\infty v^2 f(v) dv}{\int_0^\infty f(v) dv} \right)^2. \quad (6.6.5)$$

These take the form of standard integrals, for which the solution can be found in Gradshteyn and Ryzhik (2007):

$$\int_0^\infty x^{2n} e^{-px^2} dx = \frac{(2n-1)!!}{2(2p)^n} \sqrt{\frac{\pi}{p}}. \quad (6.6.6)$$

The mean squared deviation of the speeds squared is then found to be

$$\left\langle (v_i^2)^2 \right\rangle - \langle v_i^2 \rangle^2 = 15 \left( \frac{k_B T}{m_i} \right)^2 - 3^2 \left( \frac{k_B T}{m_i} \right)^2 = 6 \left( \frac{k_B T}{m_i} \right)^2. \quad (6.6.7)$$

This result may then be used to calculate the mean squared deviation of the temperature (using the chain rule):

$$\Delta T^2 = \sum_{i=1}^N \left[ \frac{\partial T}{\partial (v_i^2)} \right]^2 \Delta (v_i^2)^2, \quad (6.6.8)$$

leading to:

$$\Delta T^2 = \sum_{i=1}^N \left[ \frac{m_i}{\nu k_B} \right]^2 6 \left( \frac{k_B T}{m_i} \right)^2 = 6N \left( \frac{T}{\nu} \right)^2. \quad (6.6.9)$$

Hence we see that the temperature fluctuation is

$$\frac{\Delta T}{T} = \frac{\sqrt{6N}}{\nu} \sim \frac{1}{\sqrt{N}}. \quad (6.6.10)$$

It can similarly be shown that the Hamiltonian energy of the system varies as  $\sim 1/\sqrt{N}$  (Tuckerman, 2010).

## 6.7 Thermostatting methods

Many different thermostatting methods have been produced over the years, each with their own strengths and weaknesses. Detailed discussion of the subtleties arising from each method are beyond the scope of this thesis, but a brief summary of two different thermostats are presented: the deterministic Nosé-Hoover thermostat (Nosé, 1984; Hoover, 1985), and the stochastic Langevin thermostat (Chandrasekhar, 1943).

The general idea for each thermostatting method is the same: to couple the system of interest to a bath, with which it is able to exchange energy (in accordance with the canonical ensemble), in order to preserve the *average* temperature of the system. The bath can be thought of as a number of additional degrees of freedom, for which we do not care about their explicit dynamics, only their effect on the system of interest. As we are not interested in the dynamics of the bath degrees of freedom, in the interest of computational efficiency, the bath is often reduced to an average effect, or the minimal number of additional degrees of freedom which are required to produce the correct distribution functions.

### 6.7.1 The Nosé-Hoover thermostat

The Nosé-Hoover thermostat (Hoover, 1985) is a commonly used deterministic thermostat, which is a reformulation of a thermostat originally proposed by Nosé (1984), which allows a molecular dynamics trajectory to sample the canonical ensemble.

The general idea behind the thermostat was to introduce an additional degree of freedom into the simulation of the physical system, such that the microcanonical ensemble sampling on the extended system are equivalent to sampling the canonical ensemble of the physical system. In this way, the additional degree of freedom is viewed as the heat bath which exchanges energy with the physical system.

Nosé began by proposing an extended Lagrangian, which introduces the additional degree of freedom,  $s$ , and its associated “mass”,  $Q$ , which controls the coupling of the physical system to this additional degree of freedom. This extended Lagrangian (through the Legendre transform) can be transformed into the following Hamiltonian:

$$H = \sum_i \frac{\mathbf{p}_i^2}{2m_i s^2} + V(\mathbf{q}) + \frac{p_s^2}{2Q} + gk_B T \ln s. \quad (6.7.1)$$

The Hamiltonian of Equation 6.7.1 introduces momentum conjugate to the additional degree of freedom ( $p_s$ ), and is defined in terms of the so-called *virtual variables* ( $\mathbf{q}_i$ ,  $\mathbf{p}_i$ ,  $t$ ) which are related to the physical variables ( $\mathbf{q}'_i$ ,  $\mathbf{p}'_i$ ,  $t'$ ) through the transformations listed in Equations 6.7.2, 6.7.3 and 6.7.4. In the above Hamiltonian,  $g$  denotes the number of degrees of freedom, which are either  $3N$  or  $3N + 1$  depending on whether are dealing with the virtual or physical variables.

$$\mathbf{q}'_i = \mathbf{q}_i \quad (6.7.2)$$

$$\mathbf{p}'_i = \frac{\mathbf{p}_i}{s} \quad (6.7.3)$$

$$t' = \int^t \frac{dt}{s}. \quad (6.7.4)$$

It is straightforward to determine the equations of motion of the virtual variables using Hamilton's equations (noting that this also leads to equations of motion for  $s$  and  $p_s$ ). From these equations of motion, and the transformations given above, we are able to derive equations of motion for the physical variables as well.

Unfortunately, the transformation of the virtual Hamiltonian into one in terms of the physical values does not produce a true Hamiltonian, as equations of motion cannot be derived from it. Instead, this "Hamiltonian" only exists as a conserved quantity during the course of the simulation (which may be used to monitor the suitability of the timestep). The form of this "Hamiltonian" is not included in the interest of brevity.

The original Nosé thermostat had an unfortunate side effect: since it can be shown that  $dt' = dt/s$ , we have a time scaling effect — there is a fluctuation of the real timestep during the simulation, when we choose to work with the equations of motion for the virtual variables. If we instead use the physical variables, then our dynamics are non-Hamiltonian (though we do still have a conserved quantity which can be monitored).

The Hoover reformulation, which is referred to as the Nosé-Hoover thermostat is the most commonly used form of the thermostat used today. The Nosé-Hoover thermostat does not contain the unfortunate time scaling effect of the original Nosé thermostat. By rescaling the equations of motion of Nosé's virtual variables, and rewriting them in a slightly different form, Hoover was able to arrive at the following equations of motion:

$$\dot{\mathbf{q}}_i = \frac{\mathbf{p}_i}{m_i} \quad (6.7.5)$$

$$\dot{\mathbf{p}}_i = -\nabla_i V(\mathbf{q}) - \zeta \mathbf{p}_i \quad (6.7.6)$$

$$\dot{\zeta} = \left[ \sum_i \frac{p_i^2}{m} - g k_B T \right] / Q. \quad (6.7.7)$$

The Nosé-Hoover equations of motion no longer require us to differentiate between physical and virtual variables, hence we are able to drop the prime notation. Hoover introduced the so-called friction coefficient,  $\zeta$ , which is defined as  $\zeta = p_s/Q$ . In the Hoover reformulation,  $g = 3N$  in Equation 6.7.7.

### 6.7.1.1 Non-ergodic behaviour and Nosé-Hoover chains

Unfortunately, while the Nosé-Hoover is an elegant mathematical result, and has many desirable properties as a thermostat, it can be shown to have non-ergodic behaviour (meaning that it does not sample the canonical ensemble) for the harmonic oscillator, or for systems which are dominated by harmonic interactions. This behaviour was first shown by Hoover (1985), who states that the non-ergodic behaviour arises from the presence of additional conservation laws for the simulated system. This can clearly be demonstrated by the presence of “holes” in phase space which are not sampled during long time trajectories. This non-ergodic behaviour for strongly harmonic systems is particularly a problem when we wish to include quantum nuclear effects using path integral molecular dynamics based methods (for reasons which will become clear in Section 7.4).

An extension to the Nosé-Hoover thermostat, known as Nosé-Hoover chains (NHC) was later developed by Martyna et al. (1992). The NHC thermostat was designed to fix the non-ergodicity problems of the original thermostat, and is commonly used for path integral based simulations. The algorithm works by coupling the physical system to a 1D chain of thermostats, rather than only a single additional degree of freedom (as with the original algorithm).

Unfortunately, while the NHC algorithm often fixes the ergodicity problems, it is in general difficult to show that it *rigorously* produces the correct distribution functions/ergodic trajectories, and its use therefore requires particular care. In addition, the length of the chain required to sample the canonical ensemble introduces an additional parameter into the simulations.

### 6.7.2 The Langevin thermostat

The Langevin thermostat (Chandrasekhar, 1943) is a stochastic thermostat, based on the Langevin equation (Langevin, 1908; Lemons and Gythiel, 1997). The Langevin

thermostat represents the balance of a frictional drift term ( $-\gamma m_i \mathbf{v}_i$ ) and a stochastic diffusion term ( $\mathbf{R}_i$ ). The net effect of these two terms is to buffet the system, allowing it to either gain or lose energy, ensuring the system is kept at a constant average temperature, without explicitly needing to model the behaviour of the bath dynamics through an addition degree of freedom.

The Langevin thermostat can be straightforwardly implemented in molecular dynamics by modifying the force felt on each particle (at every timestep) in the following way:

$$\mathbf{F}_i(t) = -\nabla_i V(t) - \gamma m_i \mathbf{v}_i(t) + \mathbf{R}_i(t). \quad (6.7.8)$$

The force which arises from the thermostating procedure is a non-conservative force, hence the dynamics will be non-Hamiltonian.

In Equation 6.7.8, there is a damping rate:  $\gamma = 1/\tau$ , which is defined in terms of the damping time,  $\tau$ . The damping time controls the coupling of the system to the bath (and therefore the strength of the thermostat). As  $\tau \rightarrow 0$ , the stochastic term in the thermostat dominates, and the dynamics produced are effectively Monte Carlo. Therefore, when we seek to describe the short term dynamics, care must be taken not to thermostat the system too strongly, else we risk destroying them. The damping time,  $\tau$ , should ideally be chosen to be longer than the dominant vibrational period of the system, in order to minimize any negative effects. The effect of  $\tau$  on the diffusion coefficient was demonstrated, for a Lennard-Jones liquid (Lennard-Jones, 1924, 1931), by Bussi and Parrinello (2008).

As we can determine from the Maxwell-Boltzmann distribution, each component of the random force,  $\mathbf{R}_i$ , in Equation 6.7.8 is given by:

$$R_i^\alpha(t) = \sqrt{\frac{2\gamma m_i k_B T}{\Delta t}} N(0, 1) = N\left(0, \frac{2\gamma m_i k_B T}{\Delta t}\right), \quad (6.7.9)$$

where  $\alpha$  represents one of the Cartesian directions, and  $N(\mu, \sigma^2)$  is random number drawn from a Gaussian distribution, with a mean of  $\mu$  and a variance of  $\sigma^2$ .

We note that, because the Langevin thermostat is applied to each degree of freedom separately, this thermostat is known as a *local thermostat*, which is compared to the Nosé-Hoover thermostat which is a *global thermostat*, because it couples the entire system's kinetic energy to the auxiliary degree of freedom. Generally, global thermostats are able to provide a much more gentle thermostating procedure, but it is the author's opinion that this leads to an increase in the possibility of non-ergodic behaviour. An interesting global version of the Langevin thermostat has been developed in recent years (Bussi et al., 2007), although this version was not used for this work.

Applying the Langevin thermostat in conjunction with the Velocity Verlet integration scheme presents us with a problem, however. The Langevin force at time  $t$  (Equation

6.7.8) requires the particle velocity at time  $t$ , but in order to calculate the velocity at time  $t + \Delta t$  (in Velocity Verlet; Equation 6.3.8), we require the force at time  $t + \Delta t$ !

Fortunately, substituting the velocity propagator (Equation 6.3.8) of the Velocity Verlet algorithm into Equation 6.7.8 allows us to overcome this difficulty:

$$\mathbf{F}_i(t + \Delta t) = \left[ \frac{1}{1 + \frac{\gamma \Delta t}{2}} \right] \left[ -\nabla_i V(t + \Delta t) - \gamma m_i \mathbf{v}_i \left( t + \frac{\Delta t}{2} \right) + \mathbf{R}_i(t + \Delta t) \right]. \quad (6.7.10)$$

Finally, a note on the ergodicity of the Langevin thermostat: given a sufficiently long trajectory, the random force term in the Langevin thermostat will almost certainly be large enough to ensure that the system does not get trapped in a particular region of phase space. For this reason, the Langevin thermostat will guarantee that the system is ergodic. This proves to be a particular advantage when considering systems with a large number of harmonic interactions (which is particularly true when using path integral molecular dynamics based methods).

Because of the algorithmic simplicity of the Langevin thermostat, and its guarantee of ergodicity, it was this thermostat which was chosen for the calculations carried out as part of this work.

## 6.8 Initialization and equilibration

In general, we cannot ensure that our system will be initialized in a state of thermal equilibrium (though, by choosing the initial positions and momenta carefully, we hope that it is not sufficiently far from it). Therefore, before any observables are calculated, it is crucial that the system has been given time to reach equilibrium, this is known as the *equilibration period*.

For an NVT simulation, during the equilibration period, depending on initial conditions of the system and thermostating method used, there is likely to be an initial period of thermal shock to the system, where the instantaneous temperature fluctuates wildly as the thermostat acts to bring the system to the desired temperature. Once the system has reached thermal equilibrium, we may expect temperature fluctuations  $\propto 1/\sqrt{N}$ , as was demonstrated in Section 6.6.1.

Once our system has reached equilibrium, the initial conditions in which we prepared our system should not affect the calculation of any ensemble averages — provided that the trajectory is ergodic, of course. This arises out of the requirement that an ergodic trajectory give a fair sampling of phase space configurations — hence, for such a trajectory, the probability of reaching a particular point in phase space should not depend on the starting point. When calculating dynamical properties, the initial state will of

course affect the precise trajectory through phase space, and therefore the measurement of time correlation functions, but provided that a trajectory is sufficiently long, the presence of a decorrelation time associated with the trajectory allows for a sampling over many time origins, and hence we should be able to produce the equilibrium time correlation function.

Because MD simulations often require significant amounts of computing time, it is advantageous to prepare the system as close to the equilibrium state as possible — preparing the system in a state which is far from equilibrium will lead to an increased equilibration time, acting to increase the cost of the calculation.

For simulations involving multiple atoms, the initial atomic positions are often chosen to be at their crystallographic positions. In our case, because the simulations covered in this work contain only a single H atom on a PES, we are free to place the adsorbate at any position along the surface — although we note that the initial height should always be chosen to be at, or close to, the minimum of the harmonic confining potential along  $\mathbf{c}$ , as the PES was constructed with the assumption that the adsorbate stay close to this height throughout the simulation.

Finally, we choose to initialize any velocities/momenta from a Gaussian distribution — for systems including more than a single particle, these should also be rescaled such that the instantaneous temperature matches the target temperature, and that there is no overall linear centre of mass momentum:

$$\mathbf{p}_i^\alpha(t=0) = N(0, m_i k_B T), \quad (6.8.1)$$

where, in Equation 6.8.1 we use the notation  $N(\mu, \sigma^2)$  to refer to a Gaussian distribution with mean  $\mu$  and variance  $\sigma^2$ . i.e. the standard deviation of the momenta should be:  $\sqrt{m_i k_B T}$ .

## 6.9 Periodic boundary conditions

As we have already seen in Section 4.2.7, the use of periodic boundary conditions (PBCs) allows us to vastly reduce the computational requirements necessary to calculate bulk properties. While the calculations used in this work focus on surface interactions, it was felt appropriate to design the software with the inclusion of periodic boundary conditions. Not only does this make the software more general purpose, but it allows for the efficient treatment of other potentials, e.g. EAM, which will hopefully play a role in future work.

When performing molecular dynamics simulations under periodic boundary conditions, the simulation cell is considered to be surrounded by neighbouring identical cells in all 3 dimensions. The particles in the neighbouring cells are images of those in the simulation

cell; they move in lockstep with the simulation particles. (We do not actually need to explicitly include these particles, only infer their effects).

Throughout a simulation, as a particle moves through one boundary of the simulation cell, it should return through the opposite side of the cell. Equivalently, we can consider that, as the particle leaves the cell, it is replaced by an image of the same particle, which enters through the opposite face. (In the implementation of PBCs, we make use of fractional coordinates,  $\mathbf{s}$ , where  $0 \leq s_i < 1$ , and map back to the unit cell with:  $s_i \leftarrow s_i - \text{floor}(s_i)$ ).

We note that, while the so-called “wrapped” coordinates are helpful for determining a particle’s position *within* the simulation cell, for certain quantities, such as the mean squared displacement (Section 6.12), we require that the “unwrapped” coordinates are used. Failure to use these unwrapped coordinates when calculating the MSD effectively means that the particle is only ever able to move as far away as the edge of the simulation cell, before its position was remapped — leading to unphysical correlation functions.

We finish with a note of caution on the use of the PES with periodic boundary conditions: while the PES method does not include interactions between atoms on the surface, or their images, when we come to treat the atoms quantum mechanically, we do have to ensure that the simulation cell is not too small. This is because, as we shall see in 7.4, there *is* an interaction between the multiple replicas of the adsorbate. This means that the simulation cell must be sufficiently large that the cyclic chain of replicas is able to fully expand, without being artificially constrained by its images. In practice, this means that, when the quantum mechanical delocalization of a particle is thought to be large, we should ensure that our simulation cell is large enough to contain repeats of the PES (this is of no additional cost to the calculation). In addition, the presence of periodic boundary conditions means that, dependent on the size of the box, there will be a maximum height that the adsorbate is able to displace away from the surface, before it is attracted towards the other surface (causing the simulation to become unstable) — again, the vacuum gap should be made large enough that this will not cause issue.

### 6.9.1 Minimum image convention

The second component of our implementation of periodic boundary conditions involves the calculation of distances between pairs of atoms (or points) within the periodic system.

When calculating the distance/vector between pairs of particles (for example, when calculating interactions), we make use of the *minimum image convention*. Under the minimum image convention, the distance between two particles is always chosen such that it is the smallest in the periodic system. That is, to calculate the distance between

particles  $i$  and  $j$ , we choose the minimum distance between  $i$  (in the simulation cell) and all of the possible replicas of  $j$  (including, of course, the one in the simulation cell).

For sufficiently inexpensive interatomic potentials, with large numbers of atoms, enforcing the minimum image convention proves to be a relatively time consuming part of the calculation — we make use of the efficient algorithm described by Mezei (1992) to carry out this procedure.

## 6.10 Centre of mass constraint

Although not relevant to molecular dynamics simulations carried out as part of this work, for completeness it should be mentioned that, for systems involving multiple particles, in order to ensure that there is no net drift for the system as a whole within the simulation cell, the centre of mass constraint must be applied at every timestep.

In order to enforce this constraint, between each step of the Velocity Verlet algorithm we rescale the forces such that there is no net force on the centre of mass of the system:

$$\mathbf{F}_i \leftarrow \mathbf{F}_i - \frac{1}{N} \sum_{i=1}^N \mathbf{F}_i. \quad (6.10.1)$$

This process must be carried out after any additional (non-conservative) forces are introduced into the system (such as additional forces due to thermostating, e.g. Equation 6.7.8). The forces due to the interatomic potential should naturally sum to zero (which, when using empirical potentials, means that the system should be sufficiently large to ensure that all of the relevant interactions are included).

## 6.11 Correlation functions

We now move on from the consideration of simple ensemble averages, to the calculation of dynamical properties, which are the focus of this work. In order to describe the time dependent properties of a system, in molecular simulation, we often make use of *correlation functions*. These are functions which allow us to determine the possible cause and effect relationships which exist between properties of the system.

Although our use of correlation functions are in the context of *time correlation functions*, the functions themselves may be used as a general purpose tool to determine other types of correlation (e.g. spatial correlation), not only correlations in time.

Statistically, the correlation coefficient between two properties,  $A$  and  $B$ , is defined as (Allen and Tildesley, 1987)

$$c_{AB} = \frac{\langle \delta A \delta B \rangle}{\sigma(A) \sigma(B)}. \quad (6.11.1)$$

This may equivalently be written in terms of an unnormalized correlation coefficient,  $C_{AB} = \langle \delta A \delta B \rangle$ . In Equation 6.11.1,  $\delta A = A - \langle A \rangle$ , and the RMS deviation is the usual:  $\sigma^2(A) = \langle \delta A^2 \rangle = \langle A^2 \rangle - \langle A \rangle^2$ . The normalized correlation coefficient,  $c_{AB}$ , varies between +1 and -1, with 0 representing no correlation.

In the case where the properties of interest are functions of time, i.e:  $A(t)$  and  $B(t)$ , the correlation coefficient becomes a function of time;  $c_{AB}(t)$ , which can be produced by calculating the correlation coefficient of the two properties at different times. What the resulting correlation function tells us, is the effect that property  $A$  will have on property  $B$  at some later time (the time lag between cause and effect).

Although the correlation function may be calculated in a number of different ways, if a molecular dynamics trajectory is both ergodic and significantly longer than the correlation time of interest, we may use a single trajectory to determine the correlation function — otherwise we should determine the correlation function from several trajectories. (We note that it may still be beneficial to average over several correlation functions, if the resources are available).

The ability to generate a correlation function from a single trajectory is possible because, for times longer than the correlation time, by definition, the system loses memory of its initial conditions — for this reason, a sufficiently long trajectory may be broken into several segments, each of which can be used to sample the correlation function. The time origin of the correlation function can be therefore be shifted, and a number of correlation functions can be averaged over, in order to improve the accuracy of the calculated function. Here we make reference to Frenkel and Smit (1996); Tuckerman (2010), for the method of calculating correlation functions from a single trajectory.

For a trajectory of length  $M$  timesteps, the trajectory may be broken into chunks of length  $N$ , where  $N \ll M$ , and  $(N - 1) \Delta t$  represents the length of the correlation function. The calculation of the unnormalized correlation function is then given by Equation 6.11.2:

$$C_{AB}(t = n\Delta t) = \frac{1}{M - n} \sum_{m=0}^{M-n-1} A(m\Delta t) B(m\Delta t + n\Delta t). \quad n = 0, \dots, N - 1 \quad (6.11.2)$$

It should be observed that, as the value of  $n$  increases, the number of sample points used to compute the correlation function for the time interval  $n\Delta t$  decreases, and the correlation function becomes less accurate — this is the reason why we require a significantly longer trajectory than the correlation time.

In the case where  $A$  and  $B$  represent the same property, the correlation function which is produced is known as an *autocorrelation function*. For autocorrelation functions, the normalization condition reduces to:  $c_{AA}(t) = C_{AA}(t)/C_{AA}(0)$  — hence, the maximum correlation of a property with itself occurs at the same time. Two particular autocorrelation functions: the velocity autocorrelation function, and the mean squared displacement, are commonly computed, and allow for the calculation of diffusion coefficients from time correlation functions.

The velocity autocorrelation function is given by:

$$C_{vv}(t) = \langle \mathbf{v}(0) \cdot \mathbf{v}(t) \rangle. \quad (6.11.3)$$

We may also, if we choose to, modify Equation 6.11.3 to calculate the velocity autocorrelation function as an average over all of the atoms (usually within a particular species). The average denoted by  $\langle \dots \rangle$  represents an averaging over trajectories, or equivalently, time origin averaging from a long trajectory (calculated using Equation 6.11.2).

The velocity autocorrelation function is commonly measured in molecular simulation, and it gives a measure of the effect that the interatomic forces have on the motion of atoms in the system — for this reason, it can be used to determine the average timescales between atomic collisions in the system, or alternatively the vibrational modes of the system (through the Fourier transform) (Allen and Tildesley, 1987).

Finally, the mean squared displacement is given by:

$$C_{xx}(t) = \langle |\mathbf{r}(0) - \mathbf{r}(t)|^2 \rangle. \quad (6.11.4)$$

This tells us, on average, how far a particle moves from its initial point during the length of the correlation function, with the rate proportional to the diffusion coefficient.

## 6.12 Calculation of the diffusion coefficient

As mentioned in the previous section, the diffusion coefficient may be calculated from either the velocity autocorrelation function, or the mean squared displacement. The relationship between these two correlation functions, and their theoretical equivalence in the determination of the diffusion coefficient is explained in Allen and Tildesley (1987).

Allen and Tildesley state that there exist a number of transport coefficients (such as the diffusion coefficient), which may be calculated from equilibrium time correlation

functions. When the transport coefficient can be calculated in this way, we have a choice between two equivalent methods.

For a general transport coefficient,  $\gamma$ , there is the Green-Kubo relation, which is based on the integration of an autocorrelation function:

$$\gamma = \int_0^\infty \langle \dot{A}(0) \dot{A}(t) \rangle dt, \quad (6.12.1)$$

or there is the equivalent Einstein relation, which may be calculated by taking the gradient of the mean squared difference of the time integral of the relevant observable:

$$2t\gamma = \langle (A(0) - A(t))^2 \rangle. \quad (6.12.2)$$

We have already seen that Einstein showed that the diffusion coefficient may be calculated from the mean squared displacement (Equation 3.3.1), we now see that it may also be calculated from the integral of the velocity autocorrelation function:

$$D = \frac{1}{3} \int_0^\infty \langle \mathbf{v}(0) \cdot \mathbf{v}(t) \rangle dt = \frac{1}{6t} \langle |\mathbf{r}(0) - \mathbf{r}(t)|^2 \rangle. \quad (6.12.3)$$

Typically, the velocity autocorrelation function shows that velocities are in a highly correlated state for short periods of time, with this correlation decaying as a function of time, leading to complete decorrelation in the long time limit. It is this long time decorrelation behaviour which allows for the calculation of the diffusion coefficient.

Unfortunately, both Allen and Tildesley (1987); Tuckerman (2010) state that the decay of the tail of the velocity autocorrelation is slow (oscillating around the axis) with the noise in this part of the autocorrelation function making the accurate determination of the diffusion coefficient numerically challenging. Furthermore, it is expected that, when using long trajectories to calculate the autocorrelation function (rather than explicitly performing the average over an ensemble of trajectories), because the statistics of the autocorrelation become worse in the long time limit (due to the reduced number of sample points), this problem will be exacerbated.

Instead, we choose to calculate the diffusion coefficient from the mean squared displacement, which appears to be a much more numerically well-behaved quantity than the velocity autocorrelation function.

### 6.13 Summary

This chapter explained the theoretical background behind the (classical) molecular dynamics methodology. To summarise, trajectories may be generated from the integration

of the equations of motion arising from Hamilton's equations. These trajectories can then be used to calculate ensemble averages or time correlation functions, provided that the system is ergodic. In the absence of any external influences, the equations of motions generated from the Hamiltonian will conserve energy — sampling the microcanonical ensemble, and so, in order to fix the average temperature of the system (sampling from the canonical ensemble), the system should be coupled to a thermostat.

Throughout this work, the Langevin thermostat was used as the thermostat of choice — its relatively straightforward implementation, as well as its guarantee of ergodicity (provided the trajectory is long enough) make it an appealing method. Furthermore, the direct link between the Langevin thermostat, and the Langevin equation describing diffusion make it a particularly natural choice when studying diffusive processes. We do note that particular care needs to be taken when choosing the Langevin damping time, as short time values are expected to adversely affect the dynamics of the adsorbate.

Sections 6.11 and 6.12 showed how equilibrium time correlation functions (and therefore the diffusion coefficient) can be calculated from molecular dynamics trajectories.

In the following chapter we shall build on these concepts by extending the classical molecular dynamics method to one in which the nuclei are treated as quantum particles.

## Chapter 7

# Path Integrals in Molecular Dynamics

### 7.1 Introduction

The path integral formulation of quantum mechanics, developed by Feynman (1948; 2010), provides an alternative method of describing the motion of a quantum system which is mathematically equivalent to the approaches of Schrödinger and Heisenberg. The utility of the method lies in its intuitive picture of the motion of objects, which makes clear the link between the classical laws of motion and the newer quantum laws. Furthermore, the path integral method provides a useful utility in that it can be employed as a means of extending the classical molecular dynamics method to include many of the key quantum mechanical properties associated with the nuclei (including zero point motion and tunnelling).

This chapter begins with a review of the principle of least action and its relationship to both classical and quantum mechanics. This is followed by a brief description of the properties of the path integral and the relationship between the imaginary time propagator and the density matrix — leading to the classical isomorphism which allows quantum nuclear effects to be straightforwardly added to molecular dynamics simulations. We then move on to discuss the conventional path integral molecular dynamics (PIMD) method, which allows for the calculation of quantum ensemble averages. This is then followed by the details of an extension to PIMD, known as centroid molecular dynamics (CMD), which allows for the calculation of approximate quantum time correlation functions. Finally, we end with the details of a some commonly calculated properties in path integral based molecular dynamics simulations.

## 7.2 From classical to quantum mechanics

### 7.2.1 The principle of least action and classical mechanics

The principle of least action plays a fundamental role in the development of the path integral method of quantum mechanics, and additionally makes clear the link between classical and quantum mechanics (as described by Feynman). In order to illustrate this link, let us first begin by reviewing the motion of a classical object, as described by Lagrange (summarised in many books, e.g. Goldstein (1980)).

The laws of classical mechanics can be derived from the statement that the trajectory which a classical object follows, is that which minimizes some quantity, known as the action — this is known as the *principle of least action*.

In order to determine the path of least action, we must first define the action, which is the time integral of the Lagrangian functional:

$$S = \int_{t_a}^{t_b} L(x, \dot{x}, t) dt, \quad (7.2.1)$$

where the Lagrangian is (most commonly) defined as the difference between the kinetic energy and the potential energy,  $L = T - V$ .

The action (Equation 7.2.1) is functional of the position (which itself is a function of time), and therefore evaluates to a constant (single number) for a given path. The notation  $S[x(t)]$  is henceforth used to make it completely clear that the value for the action depends on the chosen path, which itself is a function of time – not that the action itself has *explicit* time dependence.

Following the definition of the action, the classical trajectory,  $\bar{x}(t)$ , can therefore be found by determining the path for which the action does not change (to first order) for small variations in the path. i.e:

$$\delta S = S[\bar{x}(t) + \delta x(t)] - S[\bar{x}(t)] = 0. \quad (7.2.2)$$

The effect on the action due to a small change in the path (at a particular time) is then given as:

$$S[x(t) + \delta x(t)] = \int_{t_a}^{t_b} L(x + \delta x, \dot{x} + \delta \dot{x}, t) dt \quad (7.2.3)$$

$$= \int_{t_a}^{t_b} \left[ L(x, \dot{x}, t) + \delta x \frac{\partial L}{\partial x} + \delta \dot{x} \frac{\partial L}{\partial \dot{x}} \right] dt \quad (7.2.4)$$

$$= S[x(t)] + \int_{t_a}^{t_b} \left[ \delta x \frac{\partial L}{\partial x} + \delta \dot{x} \frac{\partial L}{\partial \dot{x}} \right] dt. \quad (7.2.5)$$

By using integration by parts on the final term, we arrive at the following expression for the variation in the action:

$$\delta S = \left[ \delta x \frac{\partial L}{\partial \dot{x}} \right]_{t_a}^{t_b} - \int_{t_a}^{t_b} \delta x \left[ \frac{d}{dt} \left( \frac{\partial L}{\partial \dot{x}} \right) - \frac{\partial L}{\partial x} \right] dt = 0. \quad (7.2.6)$$

If the end points of the path are fixed, i.e:  $\delta x(t_a) = \delta x(t_b) = 0$ , then the first term disappears, and since  $\delta x$  can take any value along the path, we recover the well known Euler-Lagrange equations:

$$\frac{d}{dt} \left( \frac{\partial L}{\partial \dot{x}} \right) - \frac{\partial L}{\partial x} = 0. \quad (7.2.7)$$

Thus, application of the principle of least action leads to the equation of motion describing classical objects.

### 7.2.2 Extension to quantum mechanics

While in classical mechanics there is a single physically meaningful path which arises from the principle of least action, in the path integral formulation of quantum mechanics, all possible paths between two fixed end points are important because they all contribute to the total probability of observing a particle (at the end point, given that it was at a particular starting point).

The contribution,  $\phi$ , which is associated with each of the paths, is:

$$\phi[x(t)] \propto e^{iS[x(t)]/\hbar}, \quad (7.2.8)$$

where  $S[x(t)]$  is the classical action for the particle traveling along the path  $x(t)$ . We note that the contribution is a complex number, and therefore has both a phase and an amplitude associated with it. The relative phase of each contribution (for a given path) represents its deviation from the classical path of least action. Where, from the principle of least action, we know that the action will not change significantly for paths close to the classical one.

The total probability amplitude (or wavefunction) of a particle which starts at point  $x(t_a) = x_a$  and ends up at point  $x(t_b) = x_b$ , moving unobserved between these points, is denoted by  $\psi(x_b; x_a)$ . The calculation of this wavefunction requires summing the contributions of all paths (known as the *path integral*), where each path contributes to the total with equal weighting, but differing phase.

It is the differing phases of the path contributions which give rise to the quantum mechanical nature of motion. The presence of a phase associated with each contribution

allows for constructive interference between paths which are close to the classical path of least action, and destructive interference of paths which are far from the classical path.

Loosely speaking, under the path integral picture of quantum mechanics, a particle moving *unobserved* between two points can be considered as following all possible paths simultaneously. If the particle is observed at the intermediate positions, then of course, the quantum mechanical effects are no longer apparent (corresponding to the collapse of the wavefunction).

### 7.3 The path integral

Before we consider how the path integral may be formed, we take a moment to consider how it may be motivated. If we consider the well known double slit experiment, it is known that there are contributions to the wavefunction (and therefore the probability of finding a particle) from each of the two slits. In the path integral picture, if the paths from the source to the screen are constructed by straight lines, the probability of finding a particle at any point along the screen will be found by considering the contribution to the total wavefunction from only two paths. Mathematically, if there are wavefunctions  $\psi(1; x)$  and  $\psi(2; x)$  for the particles traveling through holes 1 and 2 (respectively) and being observed at  $x$ , then the total probability of finding the particle at position  $x$  on the screen, is given by  $P(x) = |\psi(1; x) + \psi(2; x)|^2$ .

As described by Zee (2010), we can see that what Feynman did in constructing the path integral was to essentially generalize the double slit experiment to a problem involving an infinite number of screens with an infinite number of holes. Rather than having a single screen with two alternate paths, one could imagine first having a single screen with  $N$  holes, then adding  $M$  intermediate screens between the source and the detector (summing the wavefunctions of a particle traveling through every possible combination of the holes separately to get the total wavefunction) and finally letting both the number of holes and the number of screens tend to infinity. In this case, the approximation of only allowing paths constructed of straight lines becomes exact and the discrete sum becomes a path integral.

Mathematically, Feynman defines the wavefunction via the path integrals as

$$\psi(x_b; x_a) = \lim_{N \rightarrow \infty} \mathcal{N} \int \dots \int \phi[x_b; x_a] dx_1 dx_2 \dots dx_{N-1}, \quad (7.3.1)$$

where Equation 7.3.1 corresponds to a path integral which is a multidimensional integral over the paths, where time has been divided into  $N$  sections. (We do not integrate over the beginning and end points,  $x_0$  and  $x_N$ , because they are fixed in position). Here,  $\mathcal{N}$  is a normalization constant which depends on the number of time slices.

If we absorb the constant of proportionality in Equation 7.2.8 into the normalization constant,  $\mathcal{N}$ , then we can consider the contribution of a path to be:  $\phi[x_b; x_a] = \exp\{iS[x_b; x_a]/\hbar\}$ , where the action is the classical action (Equation 7.2.1) of the particle passing through all possible points from  $x_a$  to  $x_b$ , which connected by straight lines. As the number of time slices tends to infinity, the path integral in Equation 7.3.1 reproduces the exact wavefunction.

A more elegant way of writing this same path integral is shown in Equation 7.3.2, where the normalization constant has absorbed into the new notation (i.e:  $\mathcal{D}x(t) = \mathcal{N}dx_1dx_2\dots dx_{N-1}$ ):

$$\psi(x_b; x_a) = \int_{x(t_a)=x_a}^{x(t_b)=x_b} \phi[x_b, x_a] \mathcal{D}x(t) = \int_{x(t_a)=x_a}^{x(t_b)=x_b} \exp\left\{\frac{i}{\hbar}S[x_b; x_a]\right\} \mathcal{D}x(t). \quad (7.3.2)$$

Finally, we note that the property  $\psi(x_b; x_a)$  is a wavefunction (or probability amplitude), but is often referred to as either a kernel or a propagator for reasons which will become clear in the next section. This propagator represents the evolution of a particle moving from point  $x_a$  to point  $x_b$  (given that it moves unobserved between these two points).

### 7.3.1 Path integrals with variable starting points

In the previous section we described how the path integral may be used to determine the wavefunction associated with a particle whose initial and final positions were well defined. In order to determine the wavefunction associated with finding a particle at a particular position (and time) when we don't necessarily know where the particle was to begin with, we may extend the path integral approach:

$$\psi(x, t) = \int K(x, t; x', t') \psi(x', t') dx'. \quad (7.3.3)$$

Equation 7.3.3 shows that the wavefunction associated with finding a particle at position  $(x, t)$  is given by the summation (over all starting points) of some propagator,  $K(x, t; x', t')$ , operating on a wavefunction,  $\psi(x', t')$ . In this equation,  $K(x, t; x', t')$  represents the probability of a particle being located at point  $(x, t)$ , on the assumption that it was originally at point  $(x', t')$ . In this case, we note that the integral is performed exactly as it was for a single time slice in the previous subsection: there is no explicit integration over  $t'$ , but instead a sum over all possible starting positions,  $x'$ , which could occur at time  $t'$ .

Equation 7.3.2 already tells us how we can find the probability associated with such a trajectory; the kernel,  $K(x, t; x', t')$  is simply the same as the wavefunction described in the last section:

$$K(x, t; x', t') = \int_{x'=x(t')}^{x=x(t)} \exp \left\{ \frac{i}{\hbar} S[x(t'')] \right\} \mathcal{D}x(t''). \quad (7.3.4)$$

Therefore, we see that the determination of the wavefunction associated with finding a particle at a particular point  $(x, t)$  can be found by extending the previous approach (defining the wavefunction between two fixed end points) to the case where we have a variable starting point — this is the reason that the wavefunction is sometimes known as the propagator or kernel.

### 7.3.2 Imaginary time propagators and statistical mechanics

The quantum density matrix,  $\rho$ , proves to be a useful property in the path integral formalism of quantum mechanics. It makes clear the link between quantum and statistical mechanics, and the utility of the imaginary time propagator in the calculation of ensemble averages.

For a system in thermal equilibrium, the elements of the density matrix (in the position representation), may be written as (Feynman, 1998)

$$\rho(x, x') = \sum_n \phi_n(x) \phi_n^*(x') e^{-\beta E_n}. \quad (7.3.5)$$

In this case, we note that the underlying states of the system, the  $\phi_n(x)$  are eigenfunctions of the Hamiltonian, and have energy eigenvalues,  $E_n$  — where  $\beta = 1/k_B T$ . (In representation free notation, the density matrix is often given by  $\rho = e^{-\beta \hat{H}}$ ).

As with the wavefunction, knowledge of the density matrix provides a complete description of the properties of the system. For example, the partition function of statistical mechanics,  $Z$ , may be found by summing the elements along the main diagonal of the density matrix (known as the trace):

$$Z = \text{Tr}[\rho] = \int \rho(x, x) dx. \quad (7.3.6)$$

Furthermore, the expectation value of an observable,  $A$ , at thermal equilibrium, is given by:

$$\langle A \rangle = \frac{1}{Z} \text{Tr}[A\rho]. \quad (7.3.7)$$

The density matrix may also be related to the propagator in the path integral formalism, through what is known as the Wick rotation (where, to show this, we follow the approach taken by Glover (2004)).

We begin with an initial wavefunction which is expanded in terms of basis functions:

$$|\psi(x, 0)\rangle = \sum_n c_n |\phi_n(x)\rangle. \quad (7.3.8)$$

By applying the time evolution operator,  $e^{-iE_n t/\hbar}$ , to the initial wavefunction, we arrive at an expression for the wavefunction at a later time:

$$|\psi(x, t)\rangle = \sum_n c_n e^{-iE_n t/\hbar} |\phi_n(x)\rangle. \quad (7.3.9)$$

Substituting in for the complex coefficients,  $c_n = \langle \phi_n(x') | \psi(x', 0) \rangle$ , we find:

$$|\psi(x, t)\rangle = \sum_n |\phi_n(x)\rangle \langle \phi_n(x') | \psi(x', 0) \rangle e^{-iE_n t/\hbar}. \quad (7.3.10)$$

If we perform a Wick rotation (letting  $it = \hbar\beta$ , where dimensional analysis shows  $\hbar\beta$  to have units of time), we are left with our rotated wavefunction in imaginary time:

$$|\psi(x, -i\beta\hbar)\rangle = \sum_n |\phi_n(x)\rangle \langle \phi_n(x') | \psi(x', 0) \rangle e^{-\beta E_n}. \quad (7.3.11)$$

Dropping out of Dirac notation, we can rewrite this as:

$$\psi(x, -i\beta\hbar) = \int \underbrace{\sum_n \phi_n(x) \phi_n^*(x')}_{\rho(x, x')} e^{-\beta E_n} \psi(x', 0) dx'. \quad (7.3.12)$$

It is clear that Equation 7.3.12 has the same form as that involving the propagator (Equation 7.3.3). Therefore, we can see that the density matrix,  $\rho(x, x')$  (Equation 7.3.5) is equivalent to the imaginary time propagator  $K(x, -i\beta\hbar; x', 0)$ .

In other words, the elements of the density matrix may be written as:

$$\rho(x, x') = \int_{x'=x(0)}^{x=x(-i\beta\hbar)} \exp\left\{\frac{i}{\hbar} S[x(t)]\right\} \mathcal{D}x(t) = \int_{x'=x(0)}^{x=x(\beta\hbar)} \exp\left\{-\frac{1}{\hbar} S[x(\tau)]\right\} \mathcal{D}x(\tau), \quad (7.3.13)$$

where, in Equation 7.3.13, we denote imaginary time,  $\tau = it$ , which runs from 0 to  $\hbar\beta$  (because  $t = -i\hbar\beta$  when  $\tau = \hbar\beta$ ).

Hence, by propagating a particle through imaginary time, we are able to calculate the quantum density matrix, and therefore calculate ensemble averages using statistical mechanics.

We note that because  $Z = \int \rho(x, x) dx$ , and  $\rho(x, x) = K(x, -i\beta\hbar; x, 0)$ , in order to calculate the partition function, we may simply integrate over all imaginary time paths where the particle begins and ends *at the same point*. This imaginary time propagation proves to be the underlying principle in the path integral molecular dynamics method.

To make this explicit, by switching to imaginary time, the partition function in terms of the path integral, is given by:

$$\begin{aligned} Z &= \int \dots \int \exp \left\{ -\frac{1}{\hbar} S[x(\tau)] \right\} \mathcal{D}x(\tau) \\ &= \int \dots \int \mathcal{D}x(\tau) \exp \left\{ -\frac{1}{\hbar} \int_0^{\hbar\beta} \left[ \frac{1}{2} m \dot{x}(\tau)^2 + V(x(\tau)) \right] d\tau \right\}. \end{aligned} \quad (7.3.14)$$

### 7.3.3 The free particle density matrix

Before focussing on the method of path integral molecular dynamics, it is helpful to consider the calculation of the density matrix for a free particle. This proves to be an important system which demonstrates how the form of the partition function, which is fundamental to the path integral molecular dynamics method, arises.

Firstly, we consider the solutions of the Schrödinger equation for a particle of mass  $m$  in a 1D box. In this case the Hamiltonian is simply

$$\hat{H} = -\frac{\hbar^2}{2m} \frac{d^2}{dx^2}. \quad (7.3.15)$$

Outside of the box, the wavefunction must vanish to zero since there is no probability of finding the particle in this region. Inside the box, the wavefunction is given by the plane wave solution:

$$\psi_n(x) = \frac{1}{\sqrt{L}} e^{ik_n x}, \quad (7.3.16)$$

where the wavenumber,  $k_n = 2\pi n/L$  and the eigenenergies corresponding to these solutions are  $E_n = \hbar^2 k_n^2 / 2m$ . The normalization constant,  $1/\sqrt{L}$  is defined such that  $\int \psi^* \psi dx = 1$ , where  $L$  is the width of the box (that is centred on  $x = 0$ ).

If we substitute these wavefunctions into the definition of the density matrix (in the position representation) we find that:

$$\rho(x, x') = \sum_n \frac{1}{L} e^{-k_n(x-x')} e^{-\beta \hbar^2 k_n^2 / 2m}. \quad (7.3.17)$$

In order to make the particle “free”, we take the limit as  $L \rightarrow \infty$ . In this limit  $k_n$  becomes continuous ( $k_n \rightarrow k$ ) and the discrete summation becomes an integral over this continuum of  $k$  (where  $dk \approx \Delta k = k_{n+1} - k_n = \frac{2\pi}{L}$ ). The density matrix for a free particle can now be represented by the following integral:

$$\rho(x, x') = \frac{1}{2\pi} \int_{-\infty}^{+\infty} e^{-ik(x-x')} e^{-\beta\hbar^2 k^2/2m} dk. \quad (7.3.18)$$

This integral can be computed by completing the square and performing a transformation to polar coordinates. The density matrix for a free particle is then found to be:

$$\rho(x, x') = \left(\frac{m}{2\pi\beta\hbar^2}\right)^{1/2} \exp\left[-\frac{m}{2\beta\hbar^2}(x-x')^2\right]. \quad (7.3.19)$$

## 7.4 A classical isomorphism – beads and springs

At the end of the previous subsection, we arrived at an expression for the density matrix of a free particle (Equation 7.3.19). The extension of this idea to particles in arbitrary potentials, to calculate a discretized form of the partition function proves to be a particularly powerful tool for including quantum nuclear effects in molecular dynamics simulations. This is because, as we shall see, the Hamiltonian which can be used to sample from the quantum partition function has the same form as a classical system of “beads” connected by springs — allowing for quantum nuclear effects to be included in MD simulations by simply replacing the classical particles with these bead-spring systems. While the method of PIMD has been detailed by many people in the field, here we make reference to work of Gillan (1988).

For reasons which will become clear shortly, we begin by rewriting the partition function as  $Z = \text{Tr} \left[ e^{-\beta\hat{H}/P} \right]^P$ . This corresponds to a division of the density matrix, and therefore imaginary time propagator, into a discrete number of imaginary timesteps,  $P$  (which is referred to as the Trotter number).

With the density matrix divided out in this way, the elements of the matrix can for a free particle can then be written as follows:

$$\rho_P(x, x') = \sum_n \phi_n(x) \phi_n^*(x') e^{-\beta E_n/P} = \left(\frac{mP}{2\pi\beta\hbar^2}\right)^{1/2} \exp\left[-\frac{mP}{2\beta\hbar^2}(x-x')^2\right]. \quad (7.4.1)$$

We see that Equation 7.4.1 shares the same form as that given in Equation 7.3.19, aside from presence of a factor of  $P$  in the prefactor and exponent.

In order to calculate the properties of real systems, we must include the effect of a spatially varying (external) potential,  $V(x)$ , in the density matrix. Gillan states that, while the elements of the density matrix elements may not be written down exactly, they are, to a good approximation:

$$\rho_P(x, x') \simeq \left( \frac{mP}{2\pi\beta\hbar^2} \right)^{1/2} \exp \left[ -\frac{mP}{2\beta\hbar^2} (x - x')^2 - \frac{\beta}{2P} (V(x) + V(x')) \right]. \quad (7.4.2)$$

This expression for the density matrix elements may be found by making use of the second order Trotter expansion, which applies for non-commuting operators (Tuckerman, 2010):

$$e^{\hat{T}+\hat{V}} = \lim_{P \rightarrow \infty} \left[ e^{\hat{V}/2P} e^{\hat{T}/P} e^{\hat{V}/2P} \right]^P. \quad (7.4.3)$$

Taking the trace of such a density matrix, we arrive at the discretized partition function:

$$Z \simeq Z_P = \left( \frac{mP}{2\pi\hbar^2} \right)^{P/2} \int dx_1 \dots dx_P \exp \left\{ -\beta \sum_{s=1}^P \left[ \frac{mP}{2\beta^2\hbar^2} (x_{s+1} - x_s)^2 + \frac{1}{P} V(x_s) \right] \right\}. \quad (7.4.4)$$

As the number of discrete imaginary timesteps  $P \rightarrow \infty$ , the partition function  $Z_P = Z$  and is exact. In this limit, we recover the full path integral form of the partition function (Equation 7.3.14). As stated previously, the calculation of the partition function represents a trace over elements of the density matrix where the start and end points of the imaginary time propagation are equivalent. Therefore, upon discretizing the partition function (as in Equation 7.4.4), the imaginary time values have a periodicity such that  $x_{s+P} = x_s$ .

In order to turn the results so far into a computational scheme compatible with the molecular dynamics method, the prefactor in the discretized partition function (Equation 7.4.4) is replaced by a set of Gaussian integrals over the momentum variables, leading to the following partition function (Tuckerman, 2010):

$$Z_P = Z \simeq \int dp_1 \dots dp_P \int dx_1 \dots dx_P \exp \left\{ -\beta \sum_{s=1}^P \left[ \frac{p_s^2}{2m'} + \frac{1}{2} m\omega_P^2 (x_{s+1} - x_s)^2 + \frac{1}{P} V(x_s) \right] \right\}, \quad (7.4.5)$$

where the chain frequency has been introduced, which is defined as  $\omega_P = \sqrt{P}/(\beta\hbar)$ , and the mass associated with the momentum variables ( $p_s$ ) is defined as  $m' = mP/(2\pi\hbar)^2$  (where  $m$  is the physical particle mass).

Finally, because the partition function may be expressed in terms of the Hamiltonian ( $Z = \text{Tr} [e^{-\beta\hat{H}}]$ ), we are able to express the classical Hamiltonian for this system as:

$$H = \sum_{s=1}^P \left[ \frac{p_s^2}{2m'} + \frac{1}{2}m\omega_P^2 (x_{s+1} - x_s)^2 + \frac{1}{P}V(x_s) \right]. \quad (7.4.6)$$

The classical Hamiltonian given in Equation 7.4.6 has the form of a cyclic chain of quasiparticles (often referred to as beads) in an external potential, which are connected by harmonic springs. We note that each bead feels only a fraction of the external potential (which is calculated separately for each of the beads, and does not depend on the position of the other beads), and the inter-bead interaction is nearest-neighbour harmonic. Furthermore, the number of beads in the cyclic chain corresponds to the number of imaginary time slices in the path integral propagator (where the start and end positions of the quantum particle are equivalent, i.e:  $x_s = x_{s+P}$ ). This cyclic chain of quasiparticles is often referred to as a “necklace” or “ring polymer”.

The isomorphism between a quantum particle and a classical system of particles connected by springs provides an intuitive picture for many quantum effects (such as delocalization, zero point motion and tunnelling). Furthermore, the classical isomorphism allows for a relatively straightforward modification of the classical molecular dynamics methodology, in order to include the quantum effects of the nuclei.

Finally, we note that, as the form of the quantum partition becomes exact as  $P \rightarrow \infty$  — we should treat this value as a convergence parameter and increase the number of beads until we reach the convergence of our observable of interest. (In practice, when the observable is expensive to calculate, such as the diffusion coefficient, we can use another measure, such as the radius of gyration (seen in Section 7.8.1), to determine approximate convergence behaviour).

### 7.4.1 Capturing quantum effects with ring polymers

Throughout a path integral simulation, the ring polymer used to represent a quantum particle will vary in shape and size. This changing size represents the delocalization, or “spreading” of a quantum particle (arising from the contribution of a particular imaginary time path). It is the distribution of the chain throughout space which allows for quantum effects to be included in path integral simulations.

For example, as the extent of the ring polymer varies throughout a simulation, the mean position of the chain (known as the centroid — explained in Section 7.7) may also vary (on a slower timescale). Because the centroid represents an averaging of position over an imaginary time path, the centroid can be considered to correspond to the most likely position of our quantum particle along a particular path, therefore, the motion of the centroid which arises out of the fluctuations of the chain acts to include

the effect of zero point motion of the particle. In reality, it is the time average of the centroid which corresponds to the expectation value of the particle's position, and the concept of zero point motion (of the centroid) relates to the uncertainty in the position. (More attention will be paid to the centroid when we consider quantum dynamics in Section 7.7).

The ring polymer also allows for the effect of tunnelling to be included in simulations. As the chain moves along a potential surface, it is possible that part of the chain will, at some point, be in an area of higher or lower potential than its centroid, meaning that the quantum particle will be able to “feel” a fraction of the potential that its classical counterpart would not. The presence of beads in a region of the potential which the classical particle would ordinary not experience shows that there must be a non-zero probability that the particle can be found in this region —when considering dynamics, this gives rise to a probability that the particle may tunnel through an energy barrier. This concept plays an important role in the study of quantum diffusion, as it gives rise to an increase in the diffusion rate.

## 7.5 Path integral molecular dynamics

Up until this point, our attention has been focused on describing the underlying principles behind the path integral formalism — in particular, how the ring polymer concept can be used to include quantum nuclear effects in a simulation. In order to simplify the concepts, up until this point, we have considered the motion of a single particle moving in 1-dimension. We now shift our attention to describing how this approach may be implemented as a practical computational scheme, in the context of molecular dynamics, in order to calculate quantum *ensemble averages*. To this end, it is helpful to extend the ring polymer approach to many particles moving in 3-dimensions.

The isomorphic classical Hamiltonian of Equation 7.4.6, when written for  $N$  particles in 3-dimensions (where  $i$  is the atom index, and  $s$  is the bead index), takes the form:

$$H = \sum_{i=1}^N \sum_{s=1}^P \left[ \frac{\mathbf{p}_{i,s}^2}{2m_i'} + \frac{1}{2} m_i \omega_P^2 (\mathbf{r}_{i,s+1} - \mathbf{r}_{i,s})^2 \right] + \frac{1}{P} \sum_{s=1}^P V(\mathbf{r}_{1,s}, \dots, \mathbf{r}_{N,s}). \quad (7.5.1)$$

Conceptually, the ring polymer picture of each particle still holds true. However, in order to clarify the details of the implementation, it may be more helpful to think of the quantum system as being built up of  $P$  replicas of the classical system, where each replica represents a particular value of imaginary time (bead). For each of the replicas, there are still  $N$  atoms in the system (corresponding to beads with the same index,  $s$ ), and the interatomic potential that is felt by each of the atoms (within that replica) is produced only by atoms within the same replica, as in the classical system (though its strength is only  $\frac{1}{P}$ th of the classical system). The inter-bead interaction is the only point

at which knowledge of the positions of an atom's imaginary time (replica) neighbours need be known, otherwise, each of the replicas of the system evolve independently of one another. We note that, for a given atom at a particular value of imaginary time, only the knowledge of that atom's imaginary time neighbours is known — there is no “communication” between different atoms at different values of imaginary time.

Application of Hamilton's equations to Equation 7.5.1 leads to the following equations of motion:

$$\dot{\mathbf{r}}_{i,s} = \frac{\mathbf{p}_{i,s}}{m'_i} \quad (7.5.2)$$

$$\dot{\mathbf{p}}_{i,s} = -m_i\omega_P^2 (2\mathbf{r}_{i,s} - \mathbf{r}_{i,s+1} - \mathbf{r}_{i,s-1}) - \frac{1}{P} \frac{\partial}{\partial \mathbf{r}_{i,s}} V(\mathbf{r}_{1,s}, \dots, \mathbf{r}_{N,s}). \quad (7.5.3)$$

Aside from a mass rescaling (which we shall discuss in a moment), Equation 7.5.2 is no different than the classical system. The key difference between the classical and path integral system comes about in the calculation of the force on each atom/bead. As Equation 7.5.3 shows, the force on each atom/bead is  $\frac{1}{P}$ th of the original force (due to the interatomic potential of all atoms with the same value of  $s$ ), as well as the addition of the harmonic interactions between the beads to the side of the bead of interest on the ring polymer — to make this clear, the force on each bead may be rewritten as:

$$\mathbf{F}_{i,s} = \frac{1}{P} \mathbf{F}_{i,s}^{\text{int}} - m_i\omega_P^2 (2\mathbf{r}_{i,s} - \mathbf{r}_{i,s+1} - \mathbf{r}_{i,s-1}). \quad (7.5.4)$$

It should be noted that the masses associated with the momenta of the beads, the  $m'_i$ , are defined as  $m'_i = m_i P / (2\pi\hbar)^2$ , only so that the prefactor in Equation 7.4.4 is reproduced by the integrals over the Gaussian distribution of the momenta. Tuckerman (2010) states that these masses are fictional, and their choice does not affect the results of ensemble averages or equilibrium properties. The freedom of choice associated with the mass of the beads (without affecting ensemble averages) proves to be a key feature when developing a scheme to efficiently calculate time correlation functions using path integrals (partially adiabatic centroid molecular dynamics — Section 7.7.3). We note that the mass associated with the bead-bead interactions (in Equations 7.5.3 and 7.5.4) *must* always be the physical particle mass (this is unchanged by rescaling the  $m'_i$ ).

In order to calculate ensemble averages consistent with the canonical ensemble, the equations of motions (Equations 7.5.2 and 7.5.3) should be coupled to a suitable thermostat (such as the Langevin thermostat). The method of calculating ensemble averages using the equations of motion defined in Equations 7.5.2 and 7.5.3 result in the method known as *path integral molecular dynamics* (PIMD).

An important point must be made concerning the PIMD method as it has been described so far: when performing dynamics using the so-called primitive variables (the

$\{\mathbf{r}_s; s = 1, \dots, P\}$ ), because there are harmonic nearest neighbour interactions between beads, even for moderate numbers of beads, there exists a large number of normal mode frequencies in the ring polymer system (which Tuckerman states range densely from 0 to  $4P/(\beta\hbar)$ ). The presence of such high frequency modes acts to reduce the timestep required to accurately integrate the equations of motion, and the low frequency modes (such as the motion of the centroid) will also require that long MD trajectories are required in order to adequately sample thermodynamic ensembles. It is the presence of these harmonic interactions which cause the standard Nosé-Hoover thermostat to become non-ergodic, requiring the use of Nosé-Hoover chains, or another thermostat (e.g. Langevin).

### 7.5.1 Computational details

When using path integral molecular dynamics, while most of the underlying methodology is identical to classical molecular dynamics, there are a few extra details which we must pay attention to.

In order to initialize a path integral simulation, we choose to distribute the beads evenly around a ring, with the radius equal to the radius of gyration (Section 7.8.1) of a free particle (Gillan, 1988):

$$r = \sqrt{\frac{\beta\hbar^2}{12m}}. \quad (7.5.5)$$

This ring is then rotated by random angles so that, although the ring polymer for a given particle will initially lie in a plane, all of the ring polymers within the simulation do not lie within the same plane.

The initial momenta of each of centroids are drawn from a Maxwell-Boltzmann distribution (and rescaled to match the desired temperature) — following this, the same process is repeated for each of the beads, but these are rescaled such that the momentum of the centroid gives the same as the previously determined value.

## 7.6 Quantum dynamics

While the conventional path integral molecular dynamics method can be used to incorporate quantum nuclear effects into the calculation of *ensemble averages*, it does *not* permit the calculation of quantum *time correlation functions*. The reason for this is simple; when calculating ensemble averages, we only require that a representative portion of phase space is sampled — not that it is sampled in any particular order (which is why Monte Carlo methods are successful). The conventional PIMD method makes use of this fact, and, despite producing believable looking dynamics, its time

evolution is purely used as a phase space sampling device, rather than producing true quantum dynamics. When used in the conventional manner, the beads of the ring polymer represent the imaginary time positions of a particle along a *single* Feynman path, and the trajectory produces the sum over all such paths (provided that the trajectory is ergodic, of course), but no restriction is placed on the order of this integration.

In order to produce true quantum dynamics, if the centroid is to be identified with the observed position of the particle, each of the paths in the sum must correspond to having the centroid located at a particular position. Therefore, in order to calculate the true quantum dynamics, the fluctuations of the ring polymer (constrained about the centroid) can be used to generate a quantum correction to the force that is felt by the particle, whose position can then be evolved in the usual manner. Conceptually, this is the foundation of the method of centroid molecular dynamics (CMD).

## 7.7 Centroid molecular dynamics

### 7.7.1 Fundamentals

Introduced by Cao and Voth (1993, 1994a,b,c,d), centroid molecular dynamics provides a means of calculating approximate quantum time correlation functions within a path integral molecular dynamics framework. Their work was based on reformulating the imaginary time correlation function in terms of the path centroid variable, which, once known, may then (in principle) be related to the real time correlation function by an inverse Wick rotation, i.e:  $\tau \rightarrow it$ . This method was inspired by the earlier work of Feynman and Kleinert (1986), who recognized the utility of the path centroid in providing a means of defining a semi-classical partition as an approximation to the true quantum partition function.

In terms of the imaginary time path integral, the path centroid,  $x_0$ , is given by:

$$x_0 = \frac{1}{\hbar\beta} \int_0^{\hbar\beta} x(\tau) d\tau. \quad (7.7.1)$$

This represents the average position of a particle along closed path in imaginary time,  $x(\tau)$ ; where  $x(0) = x(\hbar\beta)$ , due to the imaginary time path periodicity conditions (see Section 7.3.2).

For a discretized path integral (as is used in the PIMD based methods), the path centroid variable is the centre of mass of the ring polymer:

$$x_0 = \frac{1}{P} \sum_{s=1}^P x_s. \quad (7.7.2)$$

In order to define the imaginary time correlation function, Cao and Voth made use of a property known as the centroid density,  $\rho_c$ , which is defined as the sum over all paths with their centroids located at a point in space,  $x_c$ :

$$\rho_c(x_c) = \int \dots \int \mathcal{D}x(\tau) \delta(x_c - x_0) \exp \left\{ -\frac{1}{\hbar} S[x(\tau)] \right\}. \quad (7.7.3)$$

It is clear that the centroid density in Equation 7.7.3 is equivalent to the imaginary time propagator (Equation 7.3.4), with the additional constraint (courtesy of the  $\delta$ -function), that the centroid  $x_0$  is placed at position  $x_c$ . We note that the centroid density is different to the usual position density (Equation 7.3.13), because the centroid does not generally (except in the case where  $P = 1$ ) lie along the ring polymer.

Following the definition of the centroid density, the following centroid-constrained imaginary time propagator ( $C_c$ ) was then introduced (Equation 7.7.4). This propagator is the correlation function of the path fluctuations with respect to position of the centroid variable (constrained such that  $x_0 = x_c$ ):

$$C_c(\tau, x_c) = \frac{\int \dots \int \mathcal{D}x(\tau) \delta(x_c - x_0) [x(\tau) - x_0] [x(0) - x_0] \exp \{-S[x(\tau)]/\hbar\}}{\int \dots \int \mathcal{D}x(\tau) \delta(x_c - x_0) \exp \{-S[x(\tau)]/\hbar\}}. \quad (7.7.4)$$

We note that Cao and Voth (1994a) (in addition to Feynman and Kleinert (1986); Feynman (1998)) showed that ensemble averages can be calculated using the centroid density (where the partition function is:  $Z = \int \rho_c(x_c) dx_c$ ), though because the chief advantage in the centroid molecular dynamics method is in calculating time correlation functions, we shall not dwell on this.

Unfortunately, the form of Equation 7.7.4 does not readily lend itself to a straightforward computational scheme. In order to progress, Cao and Voth chose to approximate the action functional of the centroid-constrained correlation function as:

$$S_{\text{approx}}[x(\tau)] = \int_0^{\hbar\beta} \left\{ \frac{1}{2} m \dot{x}(\tau)^2 + \frac{1}{2} m \bar{\omega}^2 [x(\tau) - x_c]^2 \right\} d\tau, \quad (7.7.5)$$

i.e: that the potential along the imaginary time path may be represented by a harmonic interaction with the centroid (where  $\bar{\omega}$  is some centroid-dependent effective frequency).

They then showed (Cao and Voth, 1994b) how this action functional leads to an approximate imaginary time correlation function, which, following an inverse Wick rotation, gives rise to a real-time correlation function of the form:

$$C_{\text{approx}}(t) = \frac{1}{Z} \int dx_c \rho_c(x_c) \frac{\hbar}{2m\bar{\omega}} \left[ \frac{1}{\tanh(\hbar\beta\bar{\omega}/2)} \cos(\bar{\omega}t) - i \sin(\bar{\omega}t) \right] + \langle x_c \rangle_{\rho_c}^2, \quad (7.7.6)$$

which they state is a superposition of centroid correlation functions of effective harmonic oscillators at each centroid position, with each such correlation function being weighted by the appropriate centroid density.

Making use of the following Fourier relationship allows the form of Equation 7.7.6 to be simplified greatly:

$$\tilde{C}(\omega) = \frac{\hbar\beta\omega}{2} \left[ 1 + \coth\left(\frac{\hbar\beta\omega}{2}\right) \right] \tilde{C}^*(\omega). \quad (7.7.7)$$

In Equation 7.7.7,  $C^*$  is known as the Kubo transformed correlation function. This is related to the original correlation function through their Fourier transforms (denoted by  $\tilde{C}$ ). It turns out to be the Kubo transformed correlation function that we calculate when performing centroid molecular dynamics, and so Equation 7.7.7 becomes important when we wish perform the inverse transform to arrive at the real time correlation function.

By making use of Kubo transform relationship, Equation 7.7.6 may now be expressed as:

$$C_{\text{approx}}^*(t) = \frac{1}{Z} \int dx_c \rho_c(x_c) \frac{1}{m\bar{\omega}^2\beta} \cos(\bar{\omega}t) + \langle x_c \rangle_{\rho_c}^2. \quad (7.7.8)$$

Where we now focus our simulation on calculating the *Kubo transformed correlation function*.

Cao and Voth noticed that the first term in Equation 7.7.8 represents the correlation of fluctuations about the mean value, meaning that the Kubo transformed correlation function may be written as:

$$C_{\text{approx}}^*(t) = \frac{1}{Z} \int dx_c \rho_c(x_c) \langle x_c(t) x_c(0) \rangle_{\rho_c(x_c, p_c)}, \quad (7.7.9)$$

where  $\langle \dots \rangle_{\rho_c(x_c, p_c)}$  denotes an *initial condition averaging* of the correlation function over the phase space centroid density, which is given by:

$$\rho_c(x_c, p_c) = \int \dots \int \mathcal{D}x(\tau) \mathcal{D}p(\tau) \delta(x_c - x_0) \delta(p_c - p_0) \exp\left\{-\frac{1}{\hbar} S[x(\tau), p(\tau)]\right\}, \quad (7.7.10)$$

where the action (in Equation 7.7.10) is taken to be:

$$S[x(\tau), p(\tau)] = \int_0^{\hbar\beta} \left\{ \frac{p(\tau)^2}{2m} + V[x(\tau)] - ip(\tau) \dot{x}(\tau) \right\} d\tau. \quad (7.7.11)$$

Based on the harmonic approximation used in the action functional that was used to derive the approximate Kubo transformed correlation function, Equation 7.7.9 can be considered to be the short time approximation to the actual quantum correlation function. In order to determine a more accurate form of the true quantum correlation function, Cao and Voth make the ad-hoc argument that the quantum position time correlation function is related to the centroid position correlation function:

$$C^*(t) = \langle x_c(t) x_c(0) \rangle_{\rho_c(x_c, p_c)}. \quad (7.7.12)$$

While this approximation may be ad-hoc in nature, it is physically motivated through the justification that the centroid position corresponds to the expectation value of the position along a closed path — it makes physical sense that the true quantum correlation function can be approximated by the correlation of the centroid positions, when an averaging is taken over the initial conditions of the phase space centroid density. (That is, averaging over all paths whose initial centroid positions and momenta are constrained to be  $x_c$  and  $p_c$  respectively). It should be noted that the centroid molecular dynamics method was later placed on a firmer footing by Jang and Voth (1999b,a), although their results do not affect the arguments in this thesis.

With the final form of the approximate real time (Kubo transformed) correlation function now known (Equation 7.7.12), we now turn our attention to the generation of the trajectories of the centroid, and the foundations of the practical scheme used to calculate approximate quantum time correlation functions.

## 7.7.2 Centroid constrained molecular dynamics

Following the result that the real time quantum correlation function may be related to the Kubo transformed centroid correlation function, we now state how the centroid may be evolved through a path integral molecular dynamics calculation.

The centroid trajectories follow the classical equations of motion:

$$\dot{x}_c(t) = \frac{p_c(t)}{m} \quad (7.7.13)$$

$$\dot{p}_c(t) = F_c(t) = -\frac{dV_c(x_c)}{dx_c}. \quad (7.7.14)$$

Where the centroid moves along the potential of mean force generated by the non-centroid modes (the other beads) — the centroid potential,  $V_c$ , is stated by Cao and Voth to be the excess quantum free energy of the centroid, which is given by:

$$V_c(x_c) = -\frac{1}{\beta} \ln \left[ \frac{\rho_c(x_c)}{\sqrt{\frac{m}{2\pi\beta\hbar^2}}} \right], \quad (7.7.15)$$

corresponding to a centroid force:

$$F_c(x_c) = \frac{\int \dots \int \mathcal{D}x(\tau) \delta(x_c - x_0) \left[ \frac{dV[x(\tau)]}{dx} \right] \exp \{-S[x(\tau)]/\hbar\}}{\int \dots \int \mathcal{D}x(\tau) \delta(x_c - x_0) \exp \{-S[x(\tau)]/\hbar\}}. \quad (7.7.16)$$

In the discretized form (as is typical in computer simulation), the centroid force is instead given as:

$$F_c(x_c) = \frac{\int \dots \int \prod_{s=1}^P dx_s \delta(x_c - x_0) \left[ \frac{1}{P} \sum_{s=1}^P \frac{dV(x_s)}{dx_s} \right] \exp \{-S_P(x_1, \dots, x_P)/\hbar\}}{\int \dots \int \prod_{s=1}^P dx_s \delta(x_c - x_0) \exp \{-S_P(x_1, \dots, x_P)/\hbar\}}, \quad (7.7.17)$$

with the discretized action:

$$S_P(x_1, \dots, x_P) = \sum_{s=1}^P \left[ \frac{mP}{2\hbar\beta} (x_{s+1} - x_s)^2 + \frac{\hbar\beta}{P} V(x_s) \right]. \quad (7.7.18)$$

If fictional momenta are reintroduced, this leads to the Hamiltonian:

$$H = \sum_{s=1}^P \left[ \frac{p_s^2}{2m'} + \frac{1}{2} m\omega_P^2 (x_{s+1} - x_s)^2 + \frac{1}{P} V(x_s) \right]. \quad (7.7.19)$$

This is the same form as the Hamiltonian given in Equation 7.4.6, although Cao and Voth note that  $m' = m/P$  in this case, so that the centroid has the physical particle mass (although we shall discuss the bead masses in more detail when discussing the normal mode transformation).

Therefore, by performing a constrained-centroid PIMD trajectory (using RATTLE (Andersen, 1983) or similar schemes to enforce the constraints), the centroid force,  $F_c(x_c)$ , may be calculated, provided that the trajectory is ergodic and samples the canonical ensemble, from

$$F_c(x_c) = -\lim_{T \rightarrow \infty} \frac{1}{T} \int_0^T dt \frac{1}{P} \sum_{s=1}^P \frac{dV(x_s)}{dx_s} \Big|_{x_c=x_0}, \quad (7.7.20)$$

i.e. The force on the centroid can be calculated by performing a PIMD trajectory where the centroid is constrained to a particular initial position, and time averaging the force

on the centroid from that trajectory. While this method of calculating the centroid force will ultimately prove correct, it does require a full centroid-constrained PIMD trajectory at every position of the centroid, which would be prohibitively expensive for most practical uses.

Fortunately, Cao and Voth (1994d) provided suggestions for improving the efficiency of calculation of the centroid force, which was later expanded on by Martyna (1996); Cao and Martyna (1996) — these methods do not require a full PIMD trajectory at each position of the centroid in order to calculate the centroid force.

### 7.7.3 Partially adiabatic centroid molecular dynamics

The efficient schemes used to sample centroid force all centre around the concept of enforcing a degree of adiabatic separation between the motion of the centroid, and that of the non-centroid modes. As mentioned in Section 7.5, while the physical particle mass must be used when calculating the harmonic bead-bead interaction, there is a degree of freedom in choosing the masses associated with the momentum degrees of freedom (without affecting the ensemble averages).

By making the masses associated with the momentum degrees of freedom significantly lighter for the non-centroid modes when compared with the centroid, they will experience rapid oscillations around the centroid variable, when compared with the slower time evolution of the centroid itself. This means that, by choosing these masses in a suitable way, and strongly thermostating the system (including the non-centroid modes), the phase space sampling of the non-centroid modes should be ergodic on the timescales of the slower centroid mode, and the centroid force (the potential of mean force generated by the non-centroid modes) will be generated “on the fly” — without requiring that we explicitly constrain the centroid position.

Before we discuss the imposition of the adiabatic separation, we first describe a coordinate transformation, known as the normal mode transformation, which allows for a more efficient means of evolving the ring polymer. As we have already seen in Section 7.5, the wide range of normal mode frequencies present in the ring polymer means that the integration timestep must be made smaller when using the primitive modes (which gets increasingly worse as the number of beads increases). By transforming into the normal modes, the frequency of all modes becomes identical (and equal to  $\sqrt{P}/\hbar\beta$ ) (Hone et al., 2006) and we recover some of this loss of efficiency.

Furthermore, the coordinate transformation to the normal modes of the free ring polymer leads to a natural identification of the centroid modes, which are the zero frequency normal modes of the ring polymer, and makes enforcing the adiabatic separation trivial.

### 7.7.3.1 Normal mode transformation

The forward transformation, to normal mode variables,  $u_k$ , (from primitive mode variables,  $x_s$ ) is defined as (Tuckerman, 2010)

$$u_k = \frac{1}{\sqrt{P}} \sum_{s=1}^P O_{ks}^T x_s, \quad (7.7.21)$$

with the inverse transform:

$$x_s = \sqrt{P} \sum_{k=1}^P O_{sk} u_k. \quad (7.7.22)$$

Under such a transformation, the position of the centroid becomes equal to  $u_1$ , which is equivalently

$$u_1 = \frac{1}{P} \sum_{s=1}^P x_s. \quad (7.7.23)$$

In order to evolve the normal mode coordinates, we also require the forces acting on them. These can be calculated from the knowledge of the forces acting on the primitive variables:

$$\frac{1}{P} \frac{\partial V}{\partial u_1} = \frac{1}{P} \sum_{s=1}^P \frac{\partial V}{\partial x_s} \quad (7.7.24)$$

$$\frac{1}{P} \frac{\partial V}{\partial u_k} = \frac{1}{\sqrt{P}} \sum_{s=1}^P \frac{\partial V}{\partial x_s} O_{sk}. \quad (7.7.25)$$

The transformation matrix, mapping the primitive variables to the normal mode variables,  $O$ , is an orthogonal matrix which can be constructed from diagonalization of the monodromy matrix ( $A$ ), which is defined as:

$$A_{ij} = 2\delta_{ij} - \delta_{i,j-1} - \delta_{i,j+1}, \quad ; \quad i, j = 1, \dots, P \quad (7.7.26)$$

which has path periodicity: i.e. for  $j+1$  and  $j-1$ ,  $0 \rightarrow P$  and  $P+1 \rightarrow 1$ , as expected from the periodicity of the ring polymer.

After constructing and diagonalizing the monodromy matrix, the eigenvalues,  $\lambda$ , are:

$$\lambda_{2k-1} = \lambda_{2k-2} = 2 \left[ 1 - \cos \left( \frac{2\pi(k-1)}{P} \right) \right], \quad (7.7.27)$$

where  $k$  is simply the index of the mode.

After a transformation into normal modes, the inter-bead coupling in the isomorphic Hamiltonian becomes (where we note that  $\lambda_1 = 0$ )

$$\sum_{s=1}^P (x_{s+1} - x_s)^2 = \sum_{k=1}^P \lambda_k u_k^2. \quad (7.7.28)$$

Meaning that the isomorphic Hamiltonian may be written in terms of the normal modes as

$$H = \sum_{k=1}^P \left[ \frac{p_k^2}{2m'_k} + \frac{1}{2} m_k \omega_P^2 u_k^2 + \frac{1}{P} V(u_k) \right].$$

We note that, because the momenta sample from the Maxwell-Boltzmann distribution, they can simply be redefined, and do not require a transformation — the thermostating procedure will guarantee that these sample the correct distribution. Under the normal mode transformation, we assign different masses to each of the non-centroid modes: where:  $m_k = m\lambda_k$ ,  $m'_1 = m$ , and  $m'_k = m_k$  — i.e. all non-centroid modes are rescaled by the eigenvalues of the transformation matrix.

After the transformation to normal variables, the equations of motion of the normal mode variables are:

$$\dot{u}_k = \frac{p_k}{m'_k}, \quad (7.7.29)$$

$$\dot{p}_s = -m_k \omega_P^2 u_k - \frac{1}{P} \frac{\partial V}{\partial u_k}. \quad (7.7.30)$$

In addition to the normal mode transformation, there is another widely used (in PIMD, but not CMD) coordinate transformation, known as the staging transformation, which acts to compress the frequency spectrum, allowing for efficient integration (Tuckerman et al., 1993). While the staging transformation is different than the normal modes, the form of the isomorphic Hamiltonian is equivalent, leading to the same equations of motion for the staging coordinates.

Finally, we note that the normal mode transformation can equivalently be carried out using the fast Fourier transform, with the precise details given in the appendix of Cao and Martyna (1996).

### 7.7.3.2 Enforcing the adiabatic separation

The normal mode transformation listed in the previous section does not enforce the adiabatic separation between the centroid and non-centroid modes — it is merely another method of propagating the isomorphic Hamiltonian in another coordinate system (we note that, although this will lead to the same calculation of ensemble averages using the PIMD method, it does not produce the same trajectories).

It turns out that enforcing the adiabatic separation is relatively straightforward — we simply rescale the masses of the non-centroid modes. This leads to the introduction of an additional parameter,  $\gamma$ , known as the *adiabaticity parameter* (Cao and Martyna, 1996; Hone et al., 2006).

The rescaling of the masses is follows:  $m_k = \gamma^2 m \lambda_k$ ,  $m'_1 = m$ , and  $m'_k = m_k$ .

Although early CMD papers advocated a complete adiabatic separation between the centroid and non-centroid modes, it was later shown by Hone et al. (2006) that a partial adiabatic separation can lead to accurate time correlation functions with large gains in computational efficiency. In effect,  $\gamma$  becomes another convergence parameter (along with  $P$ ). This method is known as *partially adiabatic centroid molecular dynamics* (PACMD).

We note that, as the amount of adiabaticity increases, i.e. as  $\gamma \rightarrow 0$ , the normal mode frequencies oscillate more quickly, and we require a smaller timestep to accurately integrate the equations of motion.

## 7.8 Common path integral measurements

### 7.8.1 Measuring delocalization: the gyration tensor and radius of gyration

As previously mentioned, throughout the course of a path integral simulation, the size and shape of the ring polymer varies, where the extent of the variation is dependent on the amount of delocalization of the quantum particle (which depends on the local environment, as well as the number of beads). The average amount of variation in the ring polymer can therefore be used as a measure of the amount of quantum delocalization that the particle experiences.

The gyration tensor,  $R^2$ , can be used in order to quantify the variation of a ring polymer:

$$R_{\alpha\beta}^2 = \frac{1}{P} \left\langle \sum_{s=1}^P (r_s^\alpha - r_c^\alpha) (r_s^\beta - r_c^\beta) \right\rangle, \quad (7.8.1)$$

where  $\alpha$  and  $\beta$  are Cartesian components of a vector, and the average is conducted over the length of a trajectory.

While the gyration tensor is particularly useful when it is desirable to determine whether the delocalization favours a particular orientation, a more simplistic measure, which gives a single number representing the spread of the ring polymer is the radius of gyration:

$$r = \sqrt{\frac{1}{P} \left\langle \sum_{s=1}^P (\mathbf{r}_s - \mathbf{r}_c)^2 \right\rangle}, \quad (7.8.2)$$

where  $\mathbf{r}_c$  which is used in Equations 7.8.1 and 7.8.2 is the position of the centroid, which is the centre of mass of the ring polymer:  $\mathbf{r}_c = \frac{1}{P} \sum_{s=1}^P \mathbf{r}_s$

(It should be noted that the radius of gyration may also be calculated through the diagonalization of the gyration tensor. Upon diagonalizing the gyration tensor, the principle moments of the gyration tensor are found, which may be summed to give the radius of gyration: i.e. taking the trace.)

## 7.8.2 Thermodynamic energy estimators

While calculating the total energy of a classical molecular dynamics system is relatively straightforward (the sum of the kinetic and potential energies of the system), calculating the total energy of a path integral simulation is a more involved process.

Because dynamics calculated using the Hamiltonian of a path integral simulation acts to sample the partition function of the quantum system, the energy estimator can be calculated using the approach of statistical mechanics:

$$E = -\frac{\partial}{\partial \beta} \ln Z = \frac{1}{Z} \frac{\partial Z}{\partial \beta}. \quad (7.8.3)$$

For  $N$  particles in 3-dimensions, the resulting estimator, known as the *primitive energy estimator*,  $\varepsilon_P$ , becomes:

$$\varepsilon_P = \frac{3NP}{2\beta} - \sum_{i=1}^N \sum_{s=1}^P \frac{1}{2} m_i \omega_P^2 (\mathbf{r}_{i,s} - \mathbf{r}_{i,s+1})^2 + \frac{1}{P} \sum_{s=1}^P V(\mathbf{r}_{1,s}, \dots, \mathbf{r}_{N,s}). \quad (7.8.4)$$

In the limit that  $P \rightarrow \infty$ , the average  $\langle \varepsilon_P \rangle$  corresponds to the average Hamiltonian energy.

Unfortunately, the kinetic energy terms of the primitive estimator grow linearly with  $P$  — furthermore, as  $P$  increases, the nearest neighbour harmonic interactions become

more stiff for systems involving large numbers of beads, meaning fluctuations of the ring polymer become pronounced — this makes it difficult to converge the average of the primitive energy estimator.

An improved energy estimator, known as the *virial energy estimator*,  $\varepsilon_V$ , was derived by Herman et al. (1982), who used a path integral form of the virial theorem to produce an energy estimator which do not suffer from the same large fluctuations that the primitive energy estimator suffers from. This is given by

$$\varepsilon_V = \frac{3N}{2\beta} + \frac{1}{2P} \sum_{i=1}^N \sum_{s=1}^P (\mathbf{r}_{i,s} - \mathbf{r}_{i,c}) \cdot \frac{\partial V}{\partial \mathbf{r}_{i,s}} + \frac{1}{P} \sum_{s=1}^P V(\mathbf{r}_{1,s}, \dots, \mathbf{r}_{N,s}), \quad (7.8.5)$$

where  $\mathbf{r}_{i,c}$  is the centroid of atom  $i$ .

When calculating the average energy of a path integral simulation, the virial energy estimator should be preferentially used.

## 7.9 Summary

In this chapter we have seen how Feynman’s sum over paths leads to an intuitive picture of quantum mechanics, which shows us that the wavefunction may be obtained by considering contributions arising from a particle travelling over all possible paths to arrive at a point. The resulting propagator may be cast in terms of an imaginary time path integral, through the Wick rotation, which allows for the partition function of statistical mechanics to be obtained through the sum over all imaginary time paths which begin and end at the same point. Through a discretization of this imaginary time path integral, we arrive at a classical isomorphism where quantum particle may be represented by a cyclic chain of quasiparticles, connected by springs. This “ring polymer” may be simulated with molecular dynamics in order to calculate quantum mechanical ensemble averages in a relatively straightforward manner — known as path integral molecular dynamics.

We then showed how Cao and Voth’s approach of reformulating the imaginary time path integral, this time with the centroid playing a central role, may be used to extend the path integral molecular dynamics method to calculate approximate real time quantum correlation functions — the resulting method known as centroid molecular dynamics.

While the original formulation of centroid molecular dynamics did not lend itself to an efficient computational scheme, by performing a transformation to the normal modes of the free ring polymer, and reassigning the masses associated with the non-centroid modes, an adiabatic separation could be introduced between the centroid and non-centroid modes, allowing for improved efficiency when calculating quantum time correlation functions. Under the resulting scheme, the centroid is evolved classically, and

moves along the potential of mean force which is generated “on the fly” by the non-centroid modes.

In later work, Hone et al. showed that the method could be made more efficient still: by adjusting the degree of adiabaticity between the modes, they showed that accurate quantum time correlation functions were still able to be calculated, even without complete adiabatic separation — this final algorithm is known as partially adiabatic centroid molecular dynamics, and forms the basis of the quantum mechanical results in the following chapter. These results were generated using software which was solely developed by the author, specifically for this work.

## Chapter 8

# Diffusion of H/D on the (111) Ni surface

### 8.1 Introduction

This chapter presents the key observations relating to the diffusion of both hydrogen and deuterium on the (111) nickel surface, as approximated by the potential energy surface which was parameterized to the density functional theory calculations. Unless otherwise stated, the molecular dynamics results presented in this section were all carried out in the NVT ensemble, using the Langevin thermostat as a way of fixing the temperature of the system.

### 8.2 Classical simulations

#### 8.2.1 Determination of the timestep

When performing molecular dynamics simulations, it is important to ensure that the timestep used for the integration scheme is suitable — this means that the integration of the equations of motion must be numerically stable, and that there is no long-time energy drift associated with a trajectory.

The choice of timestep is determined by the highest vibrational frequency of the system — it must be sufficiently small to accurately describe vibrational modes with the smallest period, while not being too small to introduce additional errors due to numerical rounding, or to adversely affect the efficiency of the simulations by unnecessarily increasing the computational time associated with a fixed amount of simulation time. In the case of the simulations carried out for this work, this means that the most appropriate timestep can be determined by considering the quality of the integration of the hydrogen adsorbate at the highest temperature under observation (250 K).

In order to determine the most suitable timestep, a series of simulations of hydrogen on the PES, under the microcanonical (NVE) ensemble, with initial momentum corresponding to a temperature of 250 K, were carried out with varying timesteps ( $\Delta t = 0.1 \dots 2$  fs) for the same total simulation time of 1 ns. For each of these simulations, the H atom was placed at the same point on the PES (corresponding to the global minimum of potential energy), and the random seed was fixed, thereby ensuring that the same initial momentum was applied to the adsorbate for each of the simulations. In addition, the total energy was written out to disk every 50 fs for each of the trajectories, corresponding to the same number of total sample points as  $\Delta t$  varied. (i.e: the total number of MD steps and number of steps between writing the data to disk were varied as  $\Delta t$  changed). The root mean squared fluctuations of the total energy (standard deviation of the total energy) for these simulations, as a function of timestep are presented in Figure 8.2.1.

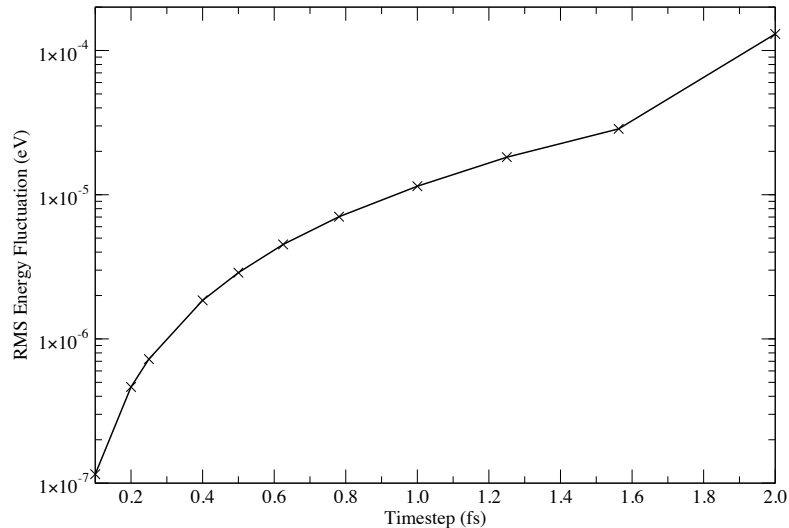


Figure 8.2.1: RMS fluctuations of the total energy for H on the (111) Ni PES under the NVE ensemble (with an initial temperature of 250 K), from (1 ns) classical MD trajectories as a function of timestep size.

As can be seen in Figure 8.2.1, for timesteps of 1 fs or smaller, the RMS energy fluctuation is found to be 0.01 meV or smaller. We note that there is a sharp jump in the energy fluctuations as  $\Delta t$  increases from 1.5625 fs to 2 fs, indicating that the dynamics begin to become unstable for large values of the timestep. The unsuitability of large timesteps is further illustrated in Figure 8.2.2, which shows a long time drift in the total energy for a 4 ns trajectory with a timestep of 2 fs. (In addition, the behaviour shown in Figure 8.2.1 is qualitatively the same for a higher initial temperature of 500 K).

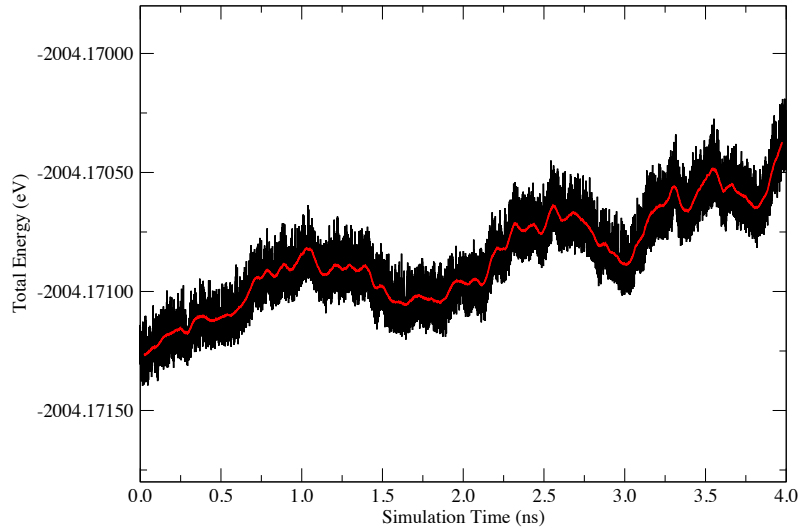


Figure 8.2.2: Long time total energy drift of H on the (111) Ni PES under the NVE ensemble (with an initial temperature of 250 K) when the timestep is 2 fs. The red line is a running average taken over a 50 ps interval.

It should be noted that the dissipative nature of the Langevin thermostat can also act to stabilize the dynamics of the system, meaning that potentially larger timesteps may produce observables which are invariant to small increases in the timestep, but this should not be relied upon — the dynamics should be stable under NVE dynamics for the timestep chosen, as large Langevin damping times are likely to decrease the stabilizing nature of the thermostat. Thus, the timestep chosen for the classical MD simulations is 1 fs, as this provides a reasonable compromise between numerical accuracy and computational efficiency.

### 8.2.2 Determination of Langevin damping time

As mentioned in section 6.7.2, when using the Langevin thermostat, there is a damping time,  $\tau$ , which couples the system to the bath — fixing the average temperature of the system. As the damping time;  $\tau \rightarrow 0$ , the stochastic influence of the thermostat becomes more pronounced, and dominates the dynamics. While this will not affect the calculation of ensemble averages (provided the trajectory is ergodic), when calculating time correlation functions (or properties relating to them, such as the diffusion coefficient), care must be taken that the trajectories being sampled are not adversely affected by the thermostat.

Although the Langevin thermostat is applied at every timestep of a molecular dynamics simulation, the damping time may loosely be considered to be the average time between Brownian “kicks” to the system (which exchange thermal energy).

This means that, in order to accurately model the diffusive behaviour of an adsorbate moving along the *static* potential energy surface, the Langevin time must be sufficiently long so as to provide only gentle thermostating — the dynamics should be approximately NVE-like on timescales of the diffusive dynamics. In effect, the Langevin damping time can be treated as a convergence parameter — it should be increased until there is no *significant* change in the dynamics. While we know that there will be kinetic energy exchange between the surface metal ions and the adsorbate in the real system, the thermostating procedure here exists to generate the *average* diffusion rate of the adsorbate between kinetic energy exchange events (collisions) with the surface atoms.

We note that, when we come to the quantum mechanical simulations, the normal modes of the system must be thermostatted in order to ensure canonical sampling of the non-centroid modes on the timescale of the slower centroid mode — this means that we *require* a thermostat in order to carry out these simulations. Therefore, it is in our interest to determine the optimal Langevin damping time for the classical system, and apply this to both types of calculation, in the interest of generating comparable results.

In general, it is expected that for extremely large damping times, the phase space sampling may be worse, requiring longer trajectories for a simulation to be considered ergodic, in addition to requiring longer time for the simulation to equilibrate — therefore it is not wise to increase the damping time arbitrarily. Of course, for the systems described in this thesis, the limited number of degrees of freedom means that the equilibration period is almost always vanishingly small, and so we do not need to concern ourselves too much with these details. Still, we make use of the equilibration period as a means of allowing the particle to lose “memory” of its initial conditions, allowing us calculate averages of an ensemble of trajectories.

Finally, we note that we may find that particular values of  $\tau$  will give better agreement to experimental results than those which leave the diffusion coefficient (approximately) invariant to a change in  $\tau$  (in effect, treating  $\tau$  as a physical parameter, as was done in work of Aarons (2013)). We argue that the reason that some values may give better agreement with experiment, are because the Langevin thermostat is then adding in the non-adiabatic effects which are not captured with the static PES. Bussi and Parrinello (2008) showed that, for a free particle and an LJ liquid (Lennard-Jones, 1924, 1931), small values of  $\tau$  act to reduce the diffusion coefficient — therefore, if the diffusion coefficient is over-estimated, we may expect that reducing  $\tau$  can bring it closer to the experimental value, and we know that the motion of the surface atoms acts to retard the adsorbate, and therefore the adiabatic approximation breaks down.

The aim of this work is therefore to calculate the diffusion of the adsorbate from first principles, rather than to provide interpretation of experimental results. If the long  $\tau$  limit does not correctly predict the diffusion coefficient, we know that something needs to be added to our model in order to improve agreement with experiment. The focus of this work is, in part, to identify how well the approximations used throughout this work are able to predict the diffusion.

### 8.2.2.1 Computational details

A series of classical molecular dynamics simulations were carried out on the static PES, for both hydrogen and deuterium, with a range of Langevin damping times, from 5 fs to 25000 fs, at both high and low temperatures (250 K and 75 K). At each temperature, and for each of the Langevin times, 10 independent trajectories were carried out for both hydrogen and deuterium, in order to, not only determine the Langevin damping time which leaves the diffusion coefficients approximately invariant to an increase in the damping time, but also quantify the error in the diffusion coefficient associated with each set of calculations.

In order to ensure that changes in the diffusion rate can be attributed *only* to a change in the damping time, the calculations presented in this section were all run with identical parameters, aside from those mentioned above: each of the simulations took place over a total simulation time of 10 ns, with a timestep of 1 fs (corresponding to 10M MD steps), with the data output to disk every 50 fs (50 MD steps). When calculating the autocorrelation functions, and therefore diffusion coefficients, the starting time was chosen to be 0.5 ns (500K MD steps), as this ensured more than sufficient time for the system to reach thermal equilibrium (which is vanishingly small due to the number of degrees of freedom), but also to lose “memory” of its initial configuration. The correlation function was calculated over a time period of 0.95 ns, allowing for time origin averaging of the autocorrelation functions — improving the quality of these functions.

Furthermore, because a series of 10 independent trajectories was carried out (at each temperature and value of Langevin damping time), the diffusion rates obtained from a line of best fit to the time origin averaged MSD autocorrelation functions can also be averaged over, allowing for improved estimates of the diffusion rates, in addition to providing an estimate of the error associated in the mean of the diffusion coefficients (taken from the standard error in the mean of the diffusion coefficients).

We note that, while it may not be necessary to carry out simulations of the length presented in this work; as Section 6.11 explains, longer simulations allow for a better estimate of the correlation function (due to time origin averaging) — the methods used throughout this work are sufficiently inexpensive that we are able to perform long-time simulations with relatively low computational requirements. This is particularly important for the low temperature simulations, where the diffusion rate will be slower, and longer runs may be necessary to produce well converged diffusion rates.

Following confirmation that the diffusion behaviour of the adsorbate was not dependent on its initial position (i.e. the trajectories are ergodic), all calculations presented in this chapter begin with the adsorbate initially placed at the saddle point in the centre of the simulation cell (fractional coordinates  $(\frac{1}{2}, \frac{1}{2})$ ) (with the height of the adsorbate corresponding to the minimum of the harmonic well along  $\mathbf{c}$  at this point).

### 8.2.2.2 Diffusion coefficients as a function of damping time

The diffusion coefficients, as calculated from averaging over the gradients of the lines of best fit to the time origin averaged MSDs, for both hydrogen and deuterium at 75 K are presented in Figure 8.2.3. We notice that, at 75 K, for small values of the Langevin damping time ( $\lesssim 1000$  fs), the diffusion coefficient does not change significantly — after this point, the diffusion coefficient does increase, but so too does the error associated with the diffusion coefficients. It is expected that the rapid increase in the error associated with the diffusion coefficients for very long Langevin times is an artefact of the thermostating procedure, as the thermostat must periodically provide large thermal “kicks” in order to bring the temperature back within the desired range to compensate for its reduced efficacy when the damping time is long, thereby adversely affecting the diffusion rate (and, in addition, requiring a long time to get the temperature of the system back under control). It is expected that the minimal number of degrees of freedom, coupled with the relatively slow diffusion rate at low temperatures means that the associated diffusion rates will be more sensitive to thermostating effects than those encountered either during a more typical MD simulation, or for the same type of simulation but at higher temperatures. For these reasons, it is not expected that extremely long damping times would be suitable for this study, if that means that the diffusion rates are subject to large errors.

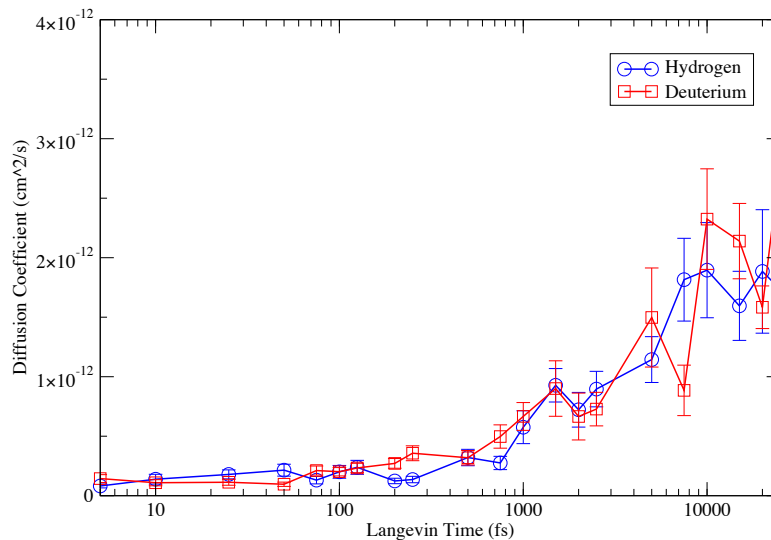


Figure 8.2.3: Diffusion coefficients of classical H and D on the (111) Ni surface, as a function of the Langevin damping time, at a temperature of 75 K.

Finally, it should be noted that for the 75 K results presented in Figure 8.2.3, there appears to be very little difference between the diffusion rates of hydrogen and deuterium — it is not obvious that there is a convergence to the expected behaviour of hydrogen

being more mobile than deuterium (owing to its smaller mass). It is highly likely that the diffusion of both H and D at low temperatures is sufficiently slow that very long/a large number of trajectories is required to fully distinguish between the isotopes on the basis of diffusion rates alone. Therefore, any observations where D is found to be more mobile than H as the damping time increases in Figure 8.2.3 is unlikely to be significant, and more likely to be an indication of the error associated with the calculation of the diffusion coefficient based on the length of the trajectory, number of trajectories and/or fitting procedure to the MSD.

When considering the effect of the Langevin damping time on the diffusion coefficient at a high temperature (250 K), Figure 8.2.4 presents results which are much more in line with the expected affect of the thermostat on the diffusion rates. Hydrogen is consistently more mobile than deuterium, with a diffusion rate which appears to increase with respect to the damping time (from 5 fs to 100 fs), which then stabilizes after around 200 fs. As before, the error in the diffusion coefficient does tend to increase as the damping time increases, but the convergence behaviour is much more obvious in the high temperature results than the low temperature results.

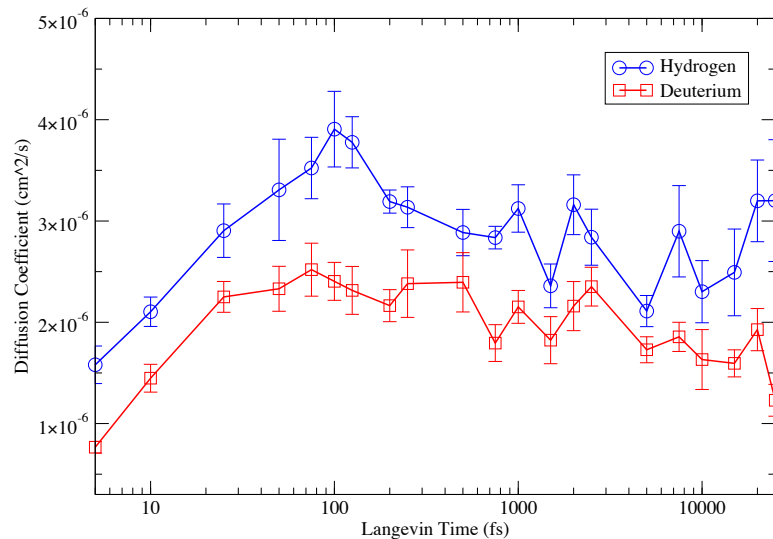


Figure 8.2.4: Diffusion coefficients of classical H and D on the (111) Ni surface, as a function of the Langevin damping time, at a temperature of 250 K.

In order to give an appreciation for how the damping time affects the diffusion rate relative to a change in the temperature, Figure 8.2.5 shows both the high and low temperature results on the same set of axes. It is clear that, while there does tend to be a slight upward drift in the diffusion coefficient as the damping time increases at 75 K, relative to the increased diffusion rates at 250 K, these small changes are not significant.

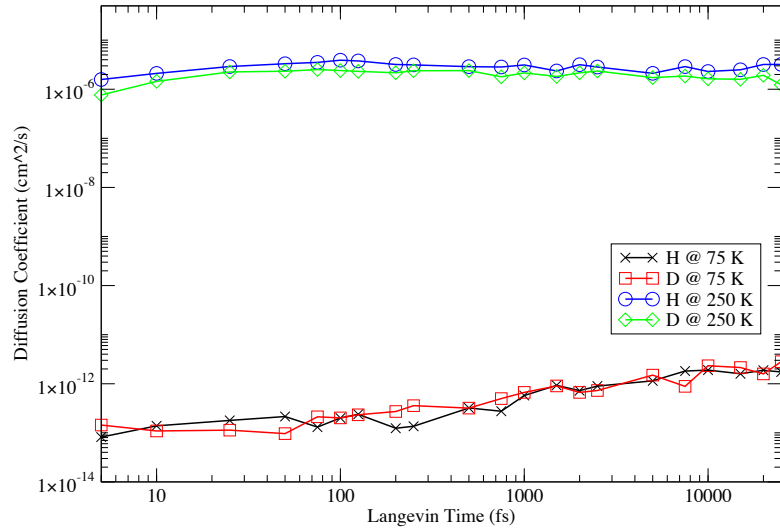


Figure 8.2.5: Diffusion coefficients of classical H and D on the (111) Ni surface, as a function of the Langevin damping time, at temperatures of 75 K and 250 K.

It was therefore decided that a compromise should be sought between seeking the long damping time diffusion behaviour and the reproducibility (small errors) of the diffusion coefficients. Because the plateau region in the low temperature results lies at low damping times, and this region falls at higher damping times in the high temperature results, in order to choose a single damping time which is suitable across the whole temperature range, a Langevin damping time of 500 fs was chosen for all subsequent calculations, it is not expected that an increase beyond this point would lead to significant changes in the diffusion behaviour at the temperatures being studied in this work. This does however indicate that a wide variety of diffusion rates may be produced by simply varying the damping time (at the cost of increasing the error, for large damping times), and that the optimal damping time required to produce invariant diffusive behaviour may also have a temperature dependence.

### 8.2.3 Temperature dependence of the diffusion rate

Following the determination of the Langevin damping time, the temperature dependence of the diffusion rate of both H and D on the Ni PES, was then calculated. This was determined by performing a series of 20 independent trajectories (for each isotope) at 8 different temperatures, ranging from 75 K to 250 K, in steps of 25 K, using the same parameters as the previous calculations ( $\Delta t$  of 1 fs, total time of 10 ns, writing to disk every 50 fs and a Langevin damping time of 500 fs). Following the completed trajectories, the mean squared displacements for each of the trajectories was produced, starting 0.5 ns into the trajectory, for a total length of 0.95 ns — allowing for time

origin averaging to produce a single MSD from the remaining 9.5 ns trajectory. By selecting the start time for the MSD in this way, the system is given 1000 Langevin damping times to reach equilibration and lose memory of its initial position.

Figure 8.2.6 shows the result of averaging over each of the 20 MSDs, in order to produce a single MSD, at each temperature. It is immediately obvious (before calculating the diffusion coefficient), that the expected behaviour of H being more mobile than D is observed.

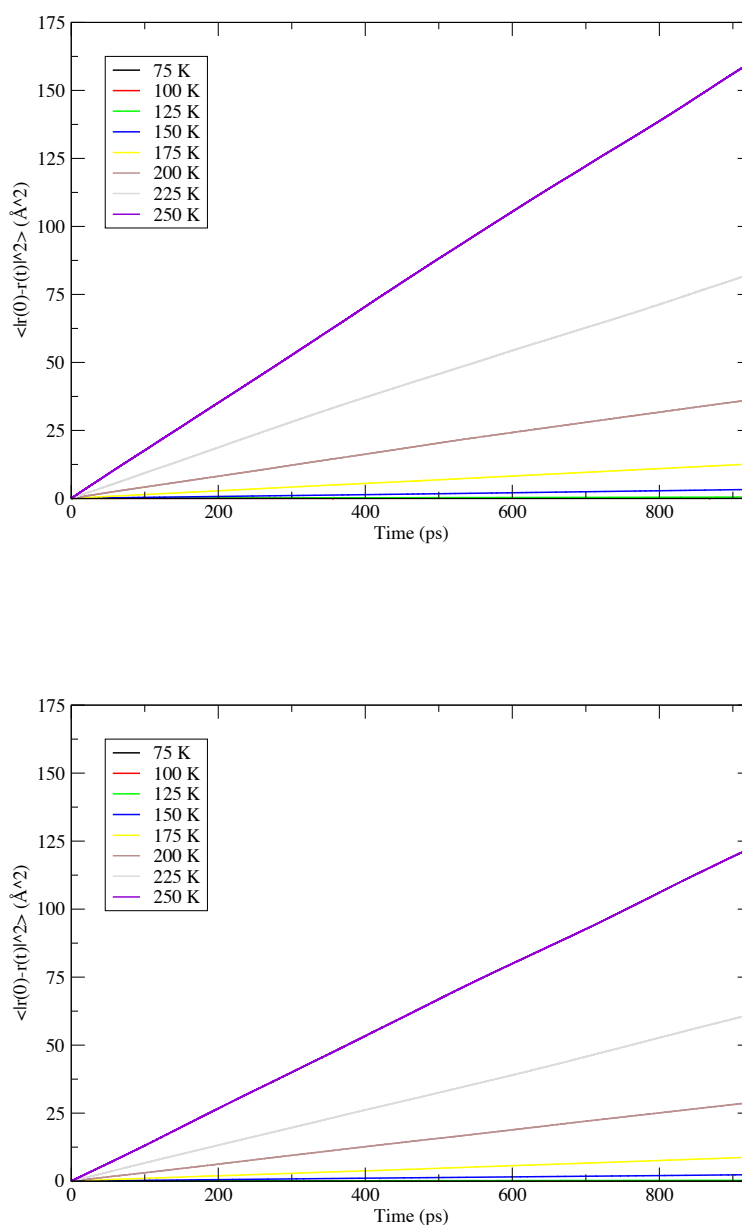


Figure 8.2.6: Mean squared displacements from the classical simulations of H (top) and D (bottom) on (111) Ni, at a range of temperatures. The MSDs pictured were obtained through averaging over MSDs resulting from 20 independent trajectories at each temperature.

Following the determination of the mean squared displacements associated with each trajectory, the diffusion coefficients at each temperature were then calculated by performing a least squares fit to each of the 20 correlation functions (rather than just the average MSD), taking the gradient of each resulting line, and averaging over them in order to produce a single diffusion coefficient at each temperature, as well as an estimate of the associated error. The resulting diffusion coefficients are presented as a function of the temperature in Figure 8.2.7.

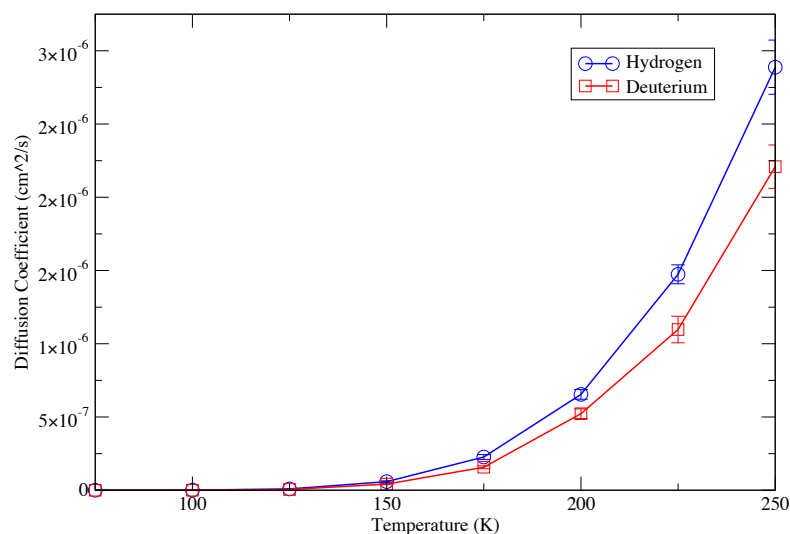


Figure 8.2.7: Diffusion coefficients as a function of temperature for classical simulations of H and D on the (111) Ni surface.

In order to determine whether the temperature dependence of the diffusion rates agrees with the Arrhenius relationship, it is helpful to plot the logarithm of the diffusion coefficient (or the diffusion coefficient on a logarithmic scale) against the inverse temperature — the result of this procedure is shown in Figure 8.2.8.

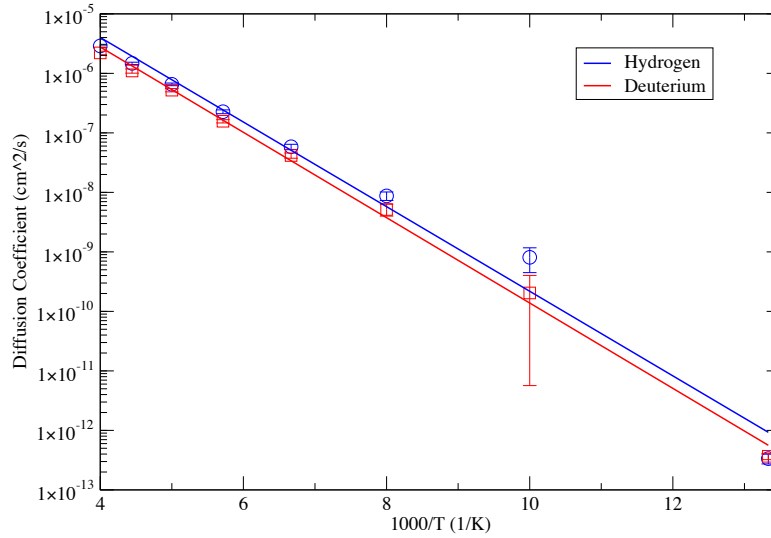


Figure 8.2.8: Arrhenius plot of the diffusion coefficient as a function of inverse temperature, for classical simulations of H and D on the (111) Ni surface (shown with lines of best fit).

As demonstrated in Figure 8.2.8, it is observed that classically the diffusion rate varies by 6 orders of magnitude over the temperature range 75 K to 250 K. Furthermore, we see that the classical results tend to follow the Arrhenius relationship quite closely, especially in the high temperature regime. Although the H results do not track the straight line quite as nicely as the D results, especially at low temperatures, it is expected that performing more simulations/longer simulations may bring any outlying points closer to this line. Due of the method used to calculate the diffusion coefficients and estimate the associated error, it may also be reasonable to assume that, for the slowest diffusion rates (temperatures of 75 K and possibly 100 K), the true errors may actually be larger than as illustrated on the graph, but that an unfortunate collection of trajectories, or insufficient length runs/numbers of trajectories have conspired to decrease the error estimate, and/or shift the mean in an unfortunate way.

The activation energies and frequency factors associated with the adsorbate diffusion were then calculated by substituting the gradients and intercepts of the lines of best fit (in Figure 8.2.8) into the Arrhenius relationship, leading to the results given in Table 8.2.1.

	Frequency factor (Hz)	$E_a$ (meV)
H	$2.80 \times 10^{-3}$	-141.1
D	$2.05 \times 10^{-3}$	-142.3

Table 8.2.1: Frequency factors and activation energies from the Arrhenius law, for classical H and D on the (111) Ni surface.

In the purely classical regime, because diffusion occurs via thermally activated hopping over energy barriers, it is the barrier height which determines the activation energy, rather than the shape of the energy barrier (as in quantum tunnelling), this means that, because the potential energy surface is identical for H and D, that the lines on the Arrhenius plot should lie parallel, and the activation energies should be the same. Instead, we find a slight (1.2 meV) difference between the two activation energies, which is attributed to the undesirable low temperature behaviour of hydrogen in the classical simulations. It is hoped that more trajectories would act to reduce this difference in the activation energies.

Ignoring for a moment the small discrepancy in the activation energy, the classical difference in diffusion rates for H and D, arising from the change in mass enter into the Arrhenius equation in the form of the pre-exponential frequency factor. Here we find that the ratio between the frequency factors, H/D, is found to be 1.37 (to 3 significant figures), slightly smaller than the expected  $\sqrt{m_D/m_H} \simeq 1.41$ .

#### 8.2.4 Classical trajectories

Before moving on to the quantum calculations, it is worthwhile to plot the trajectories of H and D, at both low (75 K) and high (250 K) temperatures, as a means of determining the diffusion pathways, as well as ensuring that the adsorbate motion is plausible.

Figure 8.2.9 shows the trajectories at 75 K. As one might expect, these trajectories are rather uninteresting, owing to the incredibly slow diffusion rate at this temperature. There appears to be little difference between the motion of H and D in these trajectories, and both are shown to be confined to a single potential well for the length of the trajectory plotted. While there is still a non-zero diffusion rate, it is sufficiently slow that we would have to run the trajectory for a long time in order for the adsorbate to thermally jump from one site to another (through a “kick” from the Langevin thermostat).

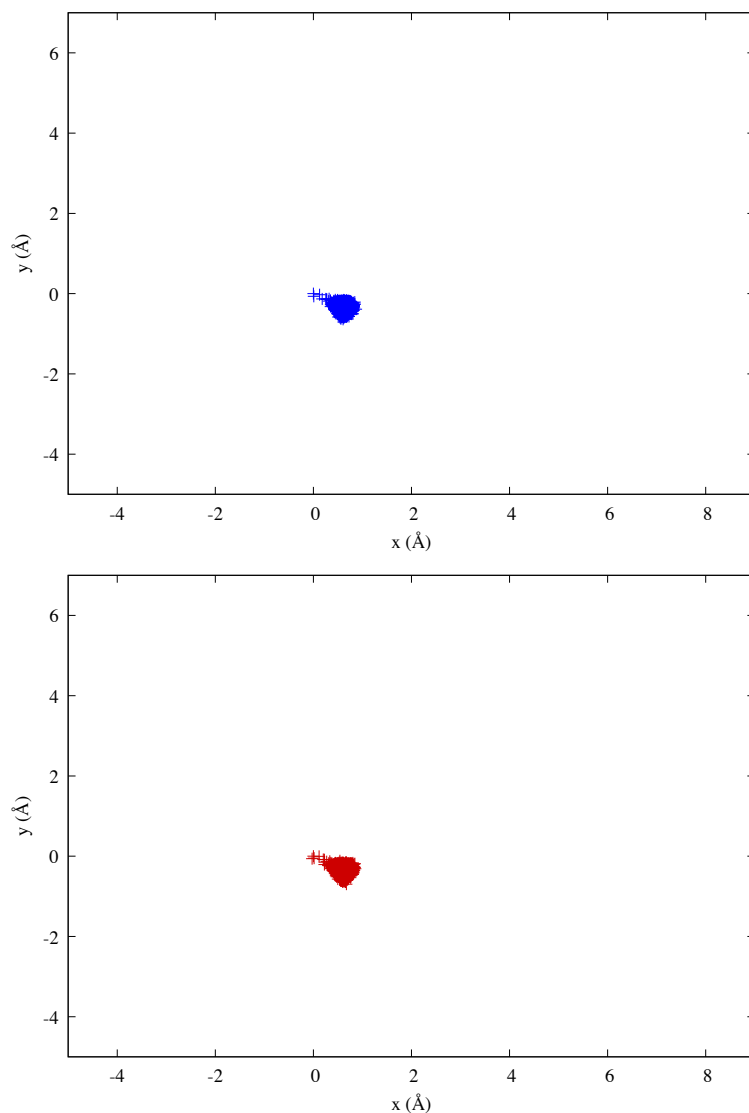


Figure 8.2.9: The trajectories of H (top, blue) and D (bottom, red) along the Ni (111) PES at a temperature of 75 K. For visualization purposes, these trajectories were plotted from a short 500 ps simulation, with the adsorbate position written out to disk every 10 fs. All other simulation parameters were kept the same as in the calculations which were used to calculate the diffusion coefficients (i.e: a Langevin damping time of 500 fs, and a timestep of 1 fs).

Figure 8.2.10 shows the motion of H and D along the surface at a temperature of 250 K. Due to the faster diffusion rate, these trajectories give us more insight into the diffusive process than the previous trajectories. Here, we see that (for the length of the trajectory visualized) the adsorbate appears to spend a large amount of time in the two minima of the PES (because of the large number of data points in these regions), before thermally hopping to another of the minima, via the bridge site — this gives rise to a trajectory which appears to have a characteristic hexagonal pattern, which arises out of the structure of the (111)-surface of a nickel (which is an FCC material).

To expand on the previous point: the sites above the surface atoms are energetically unfavourable, and are unlikely to be explored by the adsorbate during a comparatively

short MD trajectory. It would however be expected that, given enough time, and a suitable (ergodic) thermostat, these sites should also be occasionally visited.

Finally, we see that the hydrogen atom appears to travel further than the deuterium during the length of the trajectory — this is unsurprising as the smaller mass of hydrogen should mean that it is more mobile than the comparatively heavier deuterium.

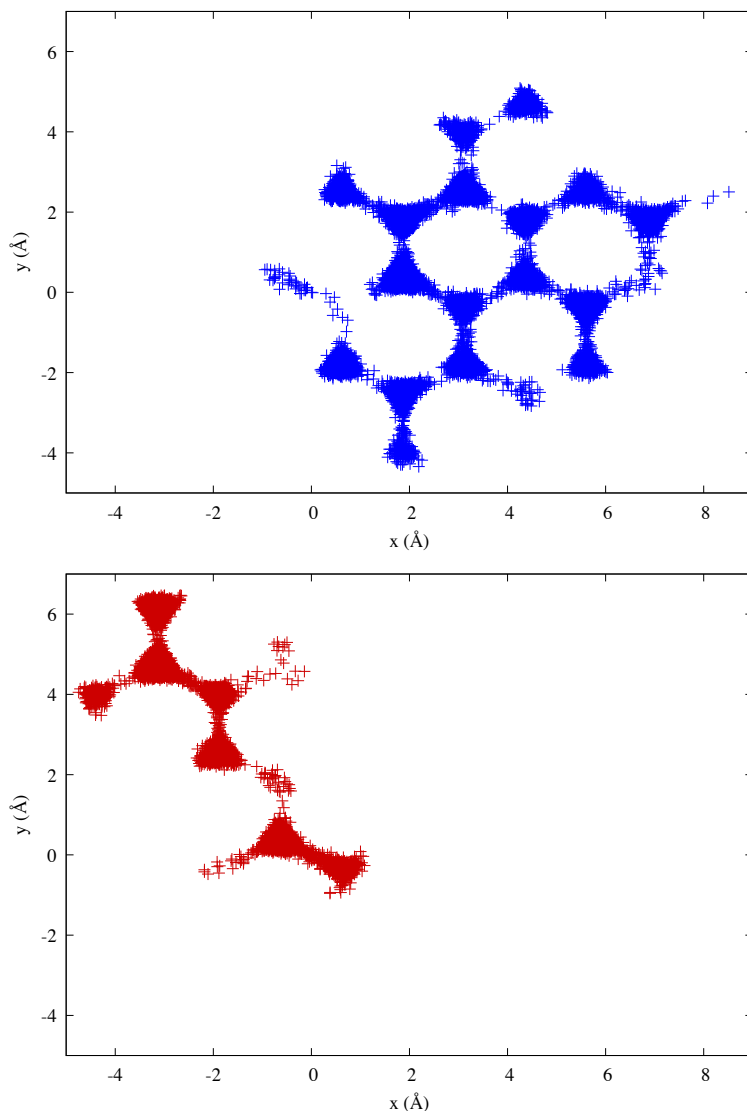


Figure 8.2.10: The trajectories of H (top, blue) and D (bottom, red) along the Ni (111) PES at a temperature of 250 K. For visualization purposes, these trajectories were plotted from a short 500 ps simulation, with the adsorbate position written out to disk every 10 fs. All other simulation parameters were kept the same as in the calculations which were used to calculate the diffusion coefficients (i.e: a Langevin damping time of 500 fs, and a timestep of 1 fs).

### 8.3 Quantum diffusion

We now present the results of the partially adiabatic centroid molecular dynamics simulations which were carried out using the DFT PES, in order to determine the

quantum mechanical effects on the temperature dependence of the diffusion rates.

### 8.3.1 Convergence of number of beads

When performing path integral based molecular dynamics simulations, it is important that we converge with respect to the number of beads (noting that the expense of the calculation increases approximately linearly as the number of beads is increased). Unfortunately, before first determining the number of beads that are required, we must note that, as the number of beads increases, the strength of the harmonic interaction between the nearest neighbour beads also increases. Therefore, it is likely that, as the number of beads increases, the timestep required to accurately integrate the equations of motion may also decrease (this is why the increase in computational cost is only approximately linear in beads).

We begin by taking a slight detour into the determination of the timestep required to perform PIMD simulations, noting that this process needs repeating again when performing PACMD simulations, as the introduction of an adiabatic separation between the centroid and non-centroid modes means that the timestep may also need to be reduced further as the higher order modes become lighter.

#### 8.3.1.1 Determining the timestep in PIMD simulations

In order to determine the optimum timestep for the bead convergence test, we must first decide on an upper bound on the number of beads that we desire to use (as this will require the smallest timestep) — previous experience suggests that it is rare for production PIMD calculations to use more than 64 beads — hence we shall fix the number of beads, initially, at 64. Next, a series of short PIMD simulations is carried out for both H and D at 75 K and 250 K, for a range of timesteps from 0.1 fs to 1 fs. The parameters of these simulations are as follows: a Langevin damping time of 500 fs, the total simulation time fixed at 250 ps, and the data output to disk every 50 fs, with the total number of MD steps, and the output interval (number of steps between writing data to disk) varied to preserve these values as the timestep was varied. As with classical molecular dynamics, it is expected that the timestep will be determined by the lightest mass isotope (hydrogen) and the highest temperature (250 K).

We note that the PIMD simulations presented in this thesis are carried out using the normal mode transformation, as this is required for the PACMD method (meaning results are transferrable between PIMD and PACMD), and because it also acts to compress the frequency spectrum, meaning that the timestep requirement should not change significantly as the number of beads is increased.

Figure 8.3.1 shows the mean and root mean squared fluctuations of the virial total energy estimator for the aforementioned calculations. Noting that the virial total energy

is subject to fluctuations, and is always less well converged (larger fluctuations) than the total energy in classical MD simulations, we note that the results in Figure 8.3.1 suggest that there is no significant reduction in accuracy when using a similar timestep as the classical simulations (1 fs). As previously mentioned, PIMD calculations must always use a thermostat, which can compensate (to some degree) for a slightly larger timestep than would be required if the thermostat were not present.

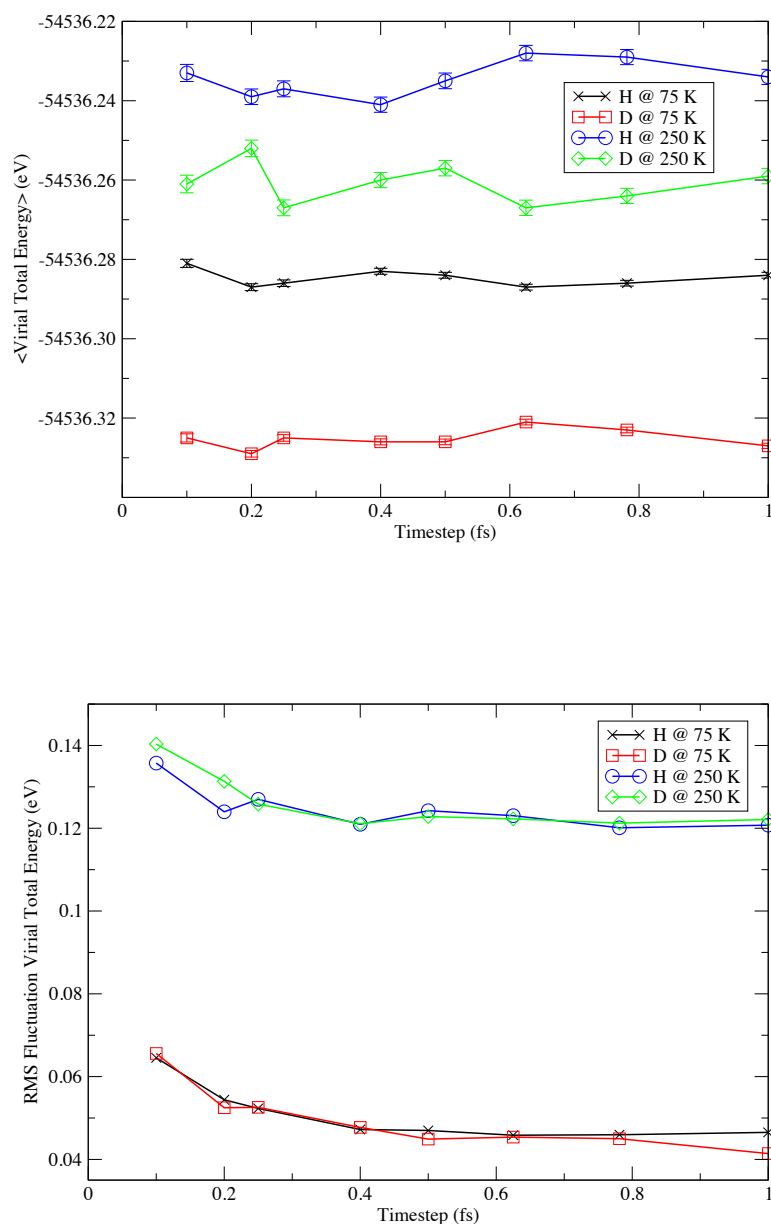


Figure 8.3.1: The mean (top) and RMS fluctuation/standard deviation (bottom) of the virial total energy for H/D on (111) Ni at 75/250 K as a function of timestep size. The PIMD calculations were carried under the normal mode transformation, with 64 beads.

In addition to monitoring the mean of the virial total energy, Figure 8.3.1 suggests

that a small timestep actually acts to increase the fluctuations about the mean of the estimator, indicating that too small a timestep can actually have a detrimental effect on the behaviour of the energy estimator. Therefore, there is nothing to suggest that a 1 fs timestep is not sufficient, at least, for the determination of the number of beads (for our purposes, it does not matter if the virial total energies are not completely converged, as the convergence with respect to the number of beads is likely to have a much more significant effect on the quality of the calculations).

While the increase in the fluctuations of the virial total energy is unexpected (especially when the timestep is still sufficiently large that numerical rounding error should not have an effect), we note that the mean virial total energy is still reasonably well converged (for all but a single data point in the 250 K deuterium results). Unfortunately, there is no obvious reason for this behaviour, especially since there is no explicit dependence on the timestep for the virial energy estimator. It is thought that this issue possibly arises due to the thermostating procedure: as the timestep decreases, the random noise term of the thermostat increases, and since each bead is thermostatted independently but also exerts a force on its neighbouring beads, it is likely that there is a negative impact on the virial total energy — thus, as we seek to increase the accuracy of the integration scheme, the thermostat appears to be working against us to increase the phase space sampling and there is a competition between these two effects.

### 8.3.1.2 Bead convergence

Because convergence tests of the diffusion coefficient with respect to the number of beads can prove to be computationally expensive, due to the number and length of the simulations required, it was decided that the radius of gyration and virial total energy could instead be used as a proxy for determining the convergence of the simulations with respect to the number of beads.

For the following convergence calculations, PIMD simulations of H and D at 75 K and 250 K were carried out for a varying number of beads (from 2 to 64), each for a total run time of 2.5 ns, with a timestep of 1 fs, a Langevin damping time of 500 fs, and with the data written out to disk every 50 fs.

Figure 8.3.2 shows the mean radius of gyration and virial total energies as a function of the number of beads. We see the expected behaviour: at convergence, H is more delocalized (has a larger radius of gyration) than D at the same temperature, and the radius of gyration for both particles is larger at lower temperatures — indicating that delocalization will play more of a role at lower temperatures. In addition, the virial total energies are also what we would expect — larger for H than D at the same temperature (increased zero point energy), and both increase as the temperature increases. For our calculations, 16 beads were chosen to represent the quantum particle — although it may be argued that 32 beads may be required for H at 75 K, it was not felt that this warranted a doubling in the computational cost for such a small apparent gain.

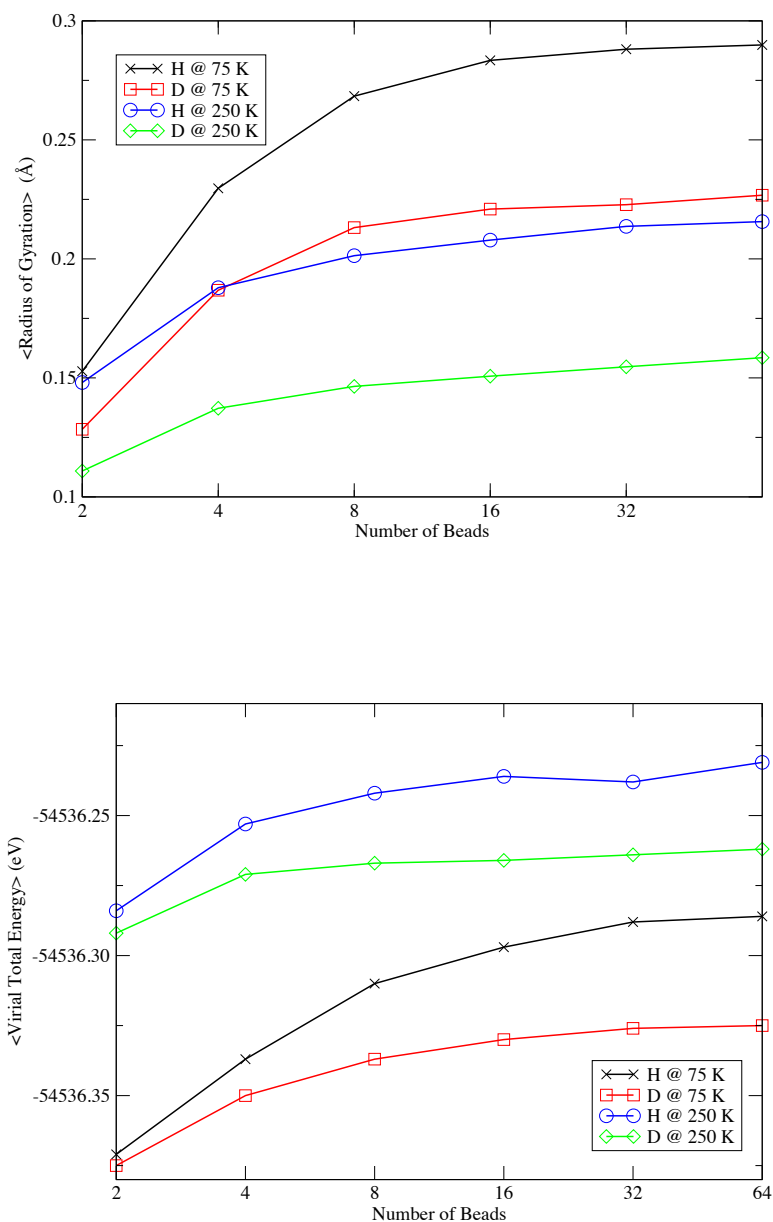


Figure 8.3.2: Convergence behaviour of the mean radius of gyration (top) and virial total energy (bottom) as a function of the number of beads, for H/D on (111) Ni at 75/250 K.

Finally, while it is only through monitoring the behaviour of the diffusion coefficient as a function of the number of beads that we are able to confirm complete convergence of our property of interest, it is hoped that the results presented Figure 8.3.2 are at least able to convince us that we have, at the very least, included a large part of the quantum correction.

### 8.3.2 Convergence of the adiabaticity parameter

In order to rigorously determine the convergence of the diffusion coefficient with respect to the adiabaticity parameter,  $\gamma$ , a series of PACMD trajectories should be carried out, reducing the value of  $\gamma$  until the diffusion coefficient does not change by an appreciable amount. Unfortunately, as  $\gamma$  decreases, the computational cost associated with these simulations tends to increase (as we shall see). Because the accurate determination of diffusion coefficients often requires long time/multiple trajectories, this makes directly measuring the convergence of this property with respect to  $\gamma$  an expensive procedure. Instead, we must consider whether other quantities may instead be used as a proxy of measuring the convergence with respect to  $\gamma$ .

As previously stated, the effect of reducing  $\gamma$  acts to increase the adiabatic separation between the motion of the centroid and non-centroid modes of the ring polymer, by reducing the masses associated with the momentum variables of the non-centroid modes. This adiabatic separation acts to introduce an adiabatic averaging of the mean centroid force due to the relatively quick motion of the non-centroid modes with respect to the centroid. It is important to reduce this parameter until the potential of mean force on the centroid is well converged, but reducing this parameter tends to lead to an increase in computational cost: as  $\gamma \rightarrow 0$ , the non-centroid modes become lighter and the timestep used for the simulations must be reduced accordingly in order to accurately integrate the equations of motion. Values of  $\gamma$  which are smaller than necessary should not adversely affect the diffusion rates, but they will mean that the computational cost may be increased.

Therefore, the determination of  $\gamma$  must, like the number of beads, be preceded by a further determination of the timestep required for the highest degree of adiabatic separation (smallest  $\gamma$ ), in order to ensure that the integration remains stable for all values of adiabatic separation (of course, it is possible to re-converge  $\Delta t$  for each value of  $\gamma$ , but this would be time consuming and potentially more computationally expensive). Skipping over the details (which are the same as in Section 8.3.1.1, but with different values of  $\Delta t$ ), the largest timestep which could be used for our lower bound of  $\gamma = 0.0025$  was found to be  $\Delta t = 0.005$  fs — even a timestep as small as 0.01 fs was found to produce unstable dynamics at 250 K for H (although D at 250 K was stable with this timestep) — as is evident by a discontinuous jump in the radius of gyration during a simulation.

Following the determination of the optimal timestep, a series of PACMD calculations were carried out to determine which degree of adiabatic separation was required to accurately generate the centroid force, and therefore correctly calculate the quantum diffusion coefficients. These calculations were carried out for a range  $\gamma$  (from 0.0025 to 0.75), for both H and D at high (250 K) and low (75 K) temperatures, for a total simulation time of 250 ps (corresponding to 50M MD steps), again with a Langevin damping time of 500 fs, and with the data written out to disk every 50 fs.

First, we begin by considering the variation of the diffusion coefficient, as calculated from the gradient of the line of best fit to the MSD. The MSDs are calculated, beginning 50 ps into the trajectory, for a total length of 50 ps (1/4 of the remaining simulation time), allowing for some small amount of time origin averaging. Because we are not only averaging over a single trajectory, but also using a very short trajectory to estimate the diffusion coefficient (with a small amount of time origin averaging), the diffusion coefficients calculated in this instance were not expected to be quantitatively correct, but it was hoped that we might be able to gain some insight into the qualitative behaviour of the convergence behaviour of the diffusion coefficient — these results are presented in Figure 8.3.3.

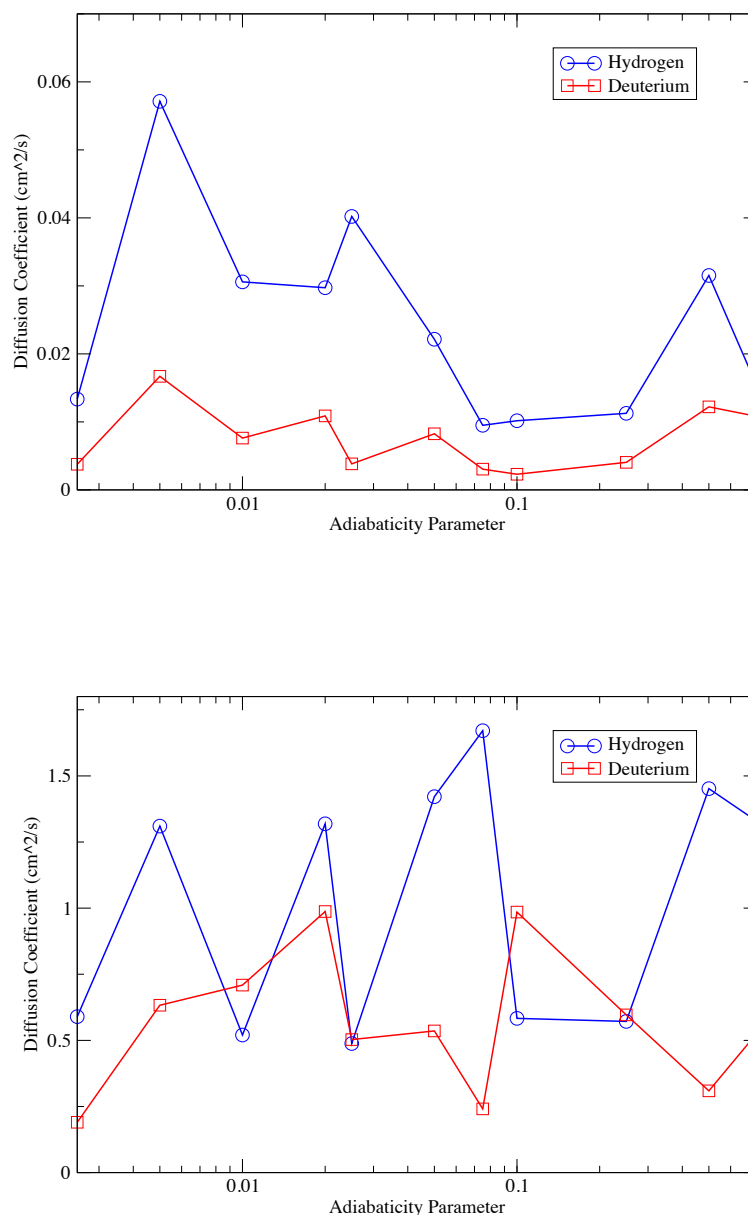


Figure 8.3.3: Effect of the adiabaticity parameter on the diffusion coefficients for H/D (16 beads) on the (111) Ni surface, at 75 K (top) and 250 K (bottom). Note that only a single short run for each value of adiabatic separation was carried out, and so diffusion coefficients will be a poor estimate to the true value.

As we can see in Figure 8.3.3, not only are the diffusion coefficients orders of magnitude faster than the true diffusion coefficient (owing to insufficient number of data points, due to the short trajectory), but there is also no clear convergence of the diffusion rate as  $\gamma$  is reduced. If we wish to measure the convergence of the diffusion coefficient with respect to  $\gamma$ , it appears we must do so properly, and perform (a series of) long trajectories. Instead, we turn our attention to the mean radius of gyration calculated from these PACMD runs, to determine whether this quantity provides any indication

as to which values of  $\gamma$  are required.

Figures 8.3.4 and 8.3.5 show the mean radius of gyration for H and D at 75 K and 250 K respectively. For H at 75 K, there appears to be oscillatory behaviour in the radius of gyration, but we may consider that at least some of the data points to be the same within error — still, the behaviour is not clear. In the case of D at 75 K, aside from the smallest value of  $\gamma = 0.0025$ , there appears to be some degree of convergence for small values of  $\gamma$  (from  $\gamma = 0.025$  to  $\gamma = 0.005$ ).

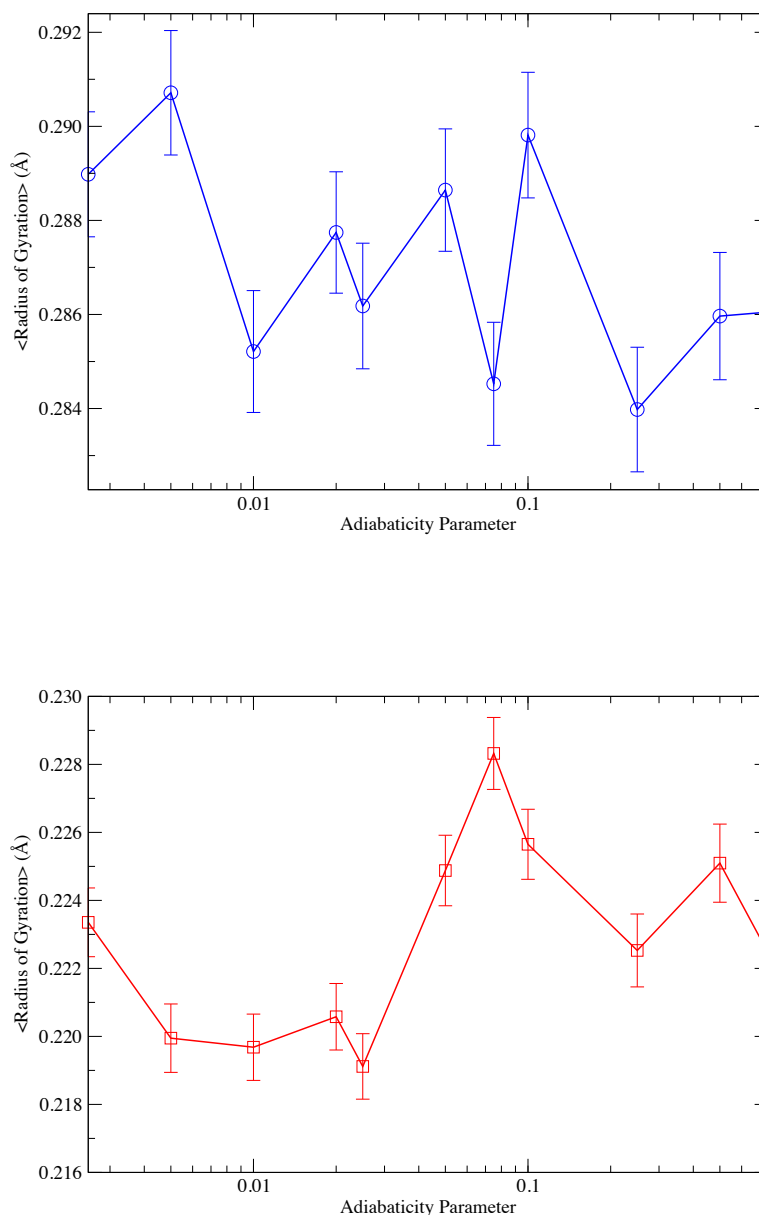


Figure 8.3.4: The mean radius of gyration of H (top) and D (bottom) on the (111) Ni surface (at 75 K) at varying degrees of adiabatic separation between the centroid and non-centroid modes (16 beads).

When considering the 250 K results (Figure 8.3.5), the roles are reversed — hydrogen (top) appears to show much clearer convergence behaviour than deuterium (bottom). The hydrogen results suggest that values of  $\gamma \leq 0.02$  are sufficient, although it is unclear whether the radius of gyration has fully decayed in the deuterium results, or whether smaller values of  $\gamma$  will reduce this further still.

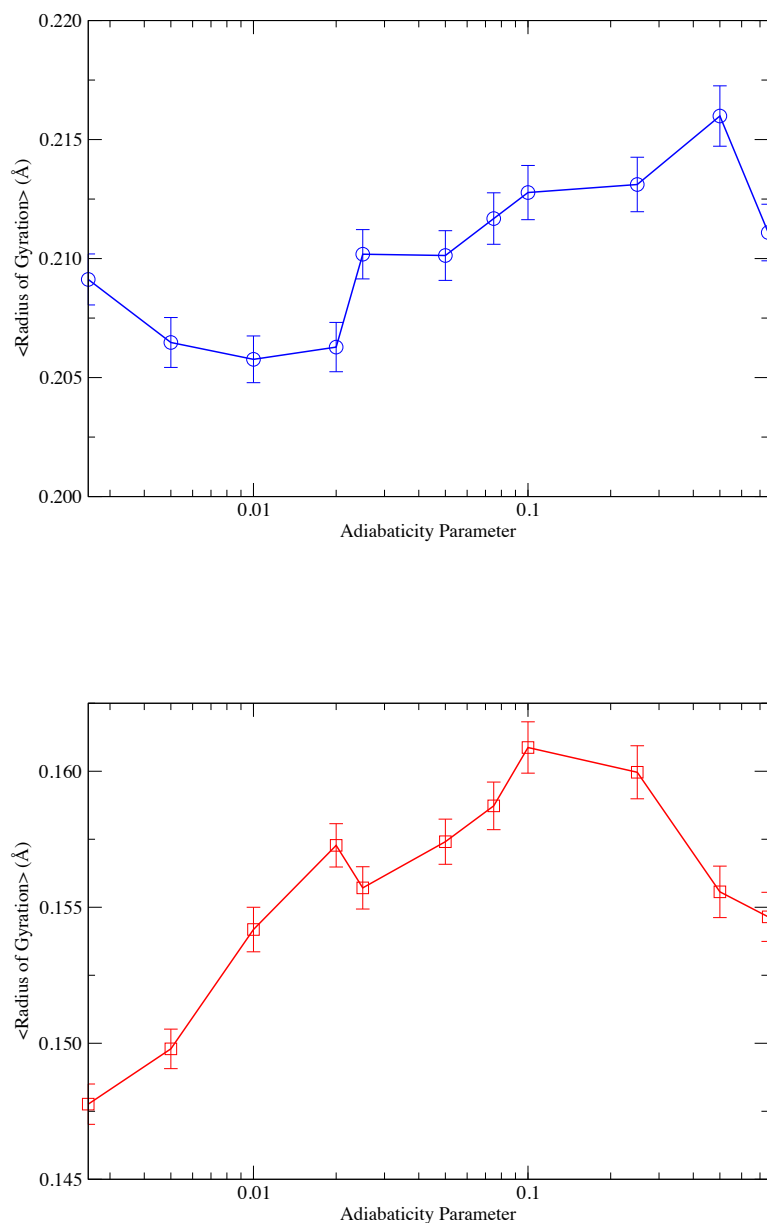


Figure 8.3.5: The mean radius of gyration of H (top) and D (bottom) on the (111) Ni surface (at 250 K) at varying degrees of adiabatic separation between the centroid and non-centroid modes (16 beads).

It may simply be the case that the results presented in Figures 8.3.4 and 8.3.5 are indicative of trajectories which are insufficiently long as to provide a full unbiased

exploration of phase space.

If we instead consider the root mean squared fluctuations about the mean of the radius of gyration (Figure 8.3.6), we begin to see a clearer pattern of convergence. In all cases there is a clear tendency of RMS fluctuation to decay as the adiabaticity parameter decreases (corresponding to lighter non-centroid modes) — this could suggest that there becomes a point when the masses of the non-centroid modes are sufficiently small to give rise to oscillations about the centroid which are relatively unaffected by a change in their position along the PES, rather than exhibiting larger fluctuations when the non-centroid masses are high, because the extent of their fluctuations about the centroid are more dependent on their position on the PES. The results of Figure 8.3.6 seem to suggest that the required value of  $\gamma$  might be between 0.025 and 0.0025 (with only the 250 K deuterium results casting doubt on these numbers).

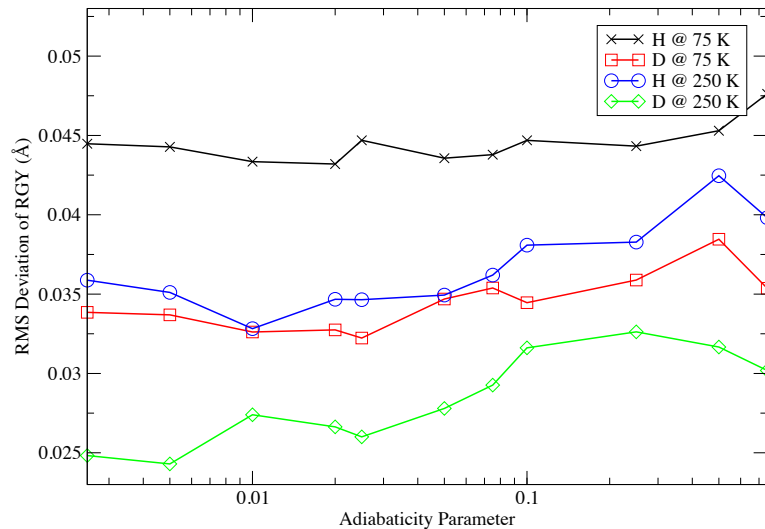


Figure 8.3.6: The root mean squared fluctuation of the radius of gyration of H (top) and D (bottom) on the (111) Ni surface, at 75 K and 250 K, for varying amounts of adiabatic separation between the centroid and non-centroid modes (16 beads).

Turning our attention now to the mean virial total energy, Figure 8.3.7 shows the convergence of this value with respect to the adiabaticity parameter, at 75 K (top) and 250 K (bottom). In both cases, the virial total energy is much more well behaved for smaller values of  $\gamma$  in the deuterium results, but the hydrogen results are less clear (especially at 250 K). There seems to be an upward trend in the virial total energy for hydrogen at 75 K, but it is unclear whether we have yet reached full convergence, or whether the short trajectory is adversely affecting the measurement of this property. At 250 K, the hydrogen results are much more variable, with a few data points which may in fact be anomalous — if these high energy points were discarded, then the behaviour is much more smooth, with an indication that there is a slight upward trend in the

virial total energy at either extreme of high or low values of  $\gamma$ .

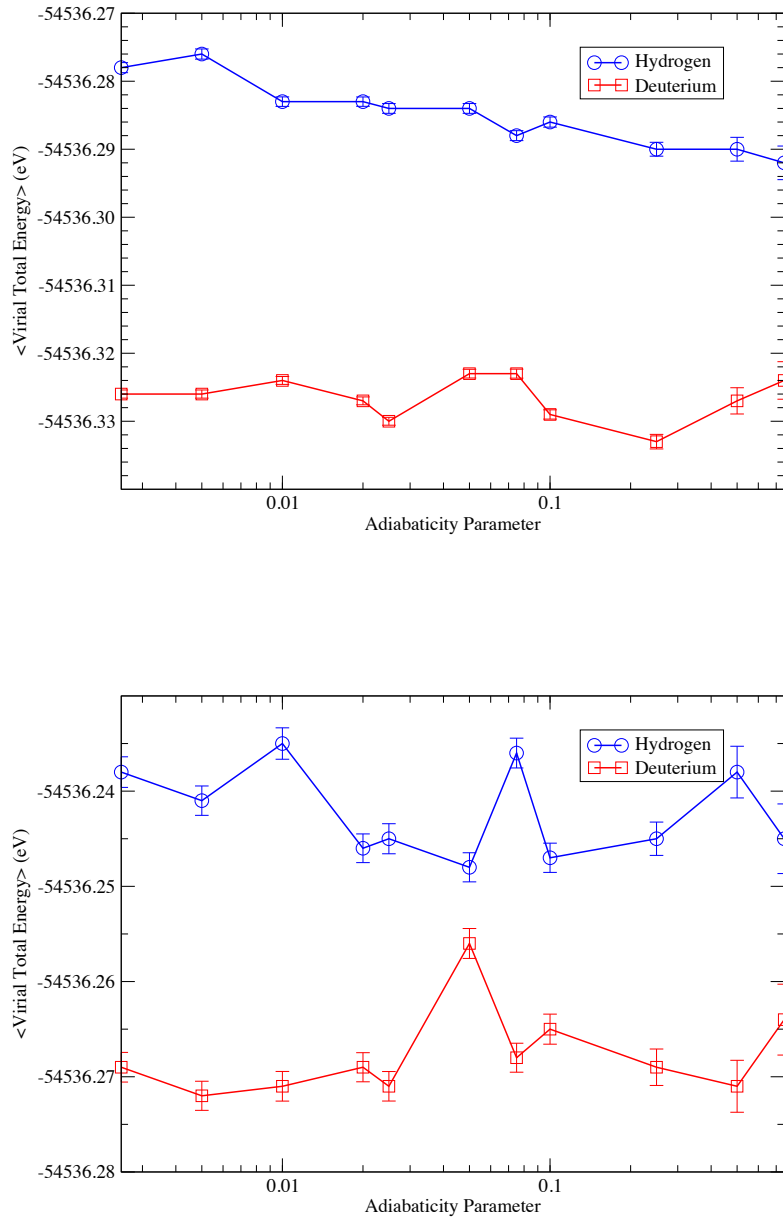


Figure 8.3.7: Mean virial total energies of H and D on the (111) Ni surface, at 75 K (top) and 250 K (bottom), as a function of the adiabaticity parameter (16 beads).

Finally, we turn our attention to the root mean squared fluctuation of the virial total energy (see Figure 8.3.8). In the classical MD simulations, we used the fluctuations of the total energy as a measure of the quality of the numerical integration due to a particular size of timestep. If we were to consider the virial total energy as the closest equivalent in PACMD simulations to the total energy in classical MD, then we might also feel justified in using the RMS fluctuations of the virial total energy to describing the quality of the underlying integration in PACMD. In this case, the fluctuations of

the virial total energy can be thought of as representing the quality of the integration of the adiabatically averaged equations of motion of the centroid in our simulation. If the fluctuation of the virial total energy were to decrease, then we can consider the integration of the centroid equations of motion of good quality, which implies that there is at least some degree of convergence in the calculation of the centroid mean force. Figure 8.3.8 seems to suggest that all values of  $\gamma \leq 0.1$  are suitable for accurate integration of the centroid equations of motion.

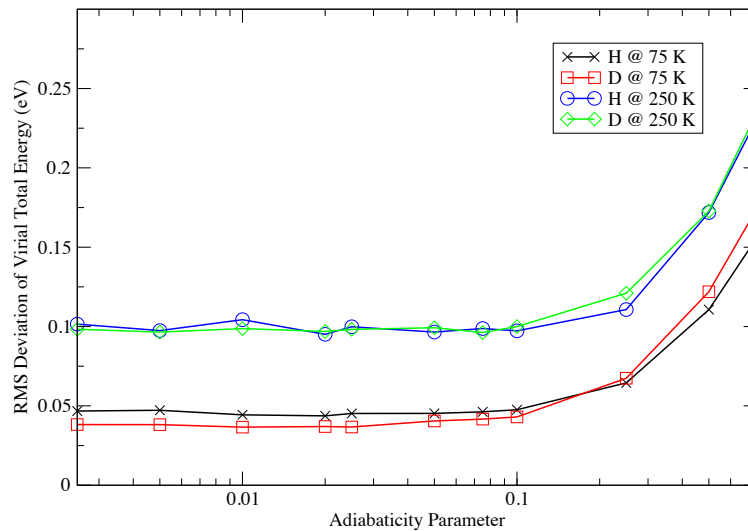


Figure 8.3.8: The root mean squared fluctuation of the virial total energy estimator for H and D on the (111) Ni surface, at 75 K and 250 K, as a function of the adiabaticity parameter (16 beads).

On the basis of the results presented in Figures 8.3.8 and 8.3.6, we settle on an adiabaticity parameter of  $\gamma = 0.01$ . While the only way of determining for certain whether the diffusion coefficient is invariant to further reductions in the adiabaticity parameter is to perform the computationally expensive systematic studies, it is hoped that this degree of adiabatic separation is sufficiently small to be able to suitably converge the average centroid force at all positions along the surface, and therefore produce the correct quantum diffusion coefficients. To the end, the results of Hone et al. (2006) are encouraging, as they showed that it is not completely necessary to guarantee a *complete* adiabatic separation between the centroid and non-centroid modes in order to accurately determine time correlation functions — in fact, it is precisely this result which allows for the PACMD method to be more efficient than fully adiabatic centroid MD.

### 8.3.3 Temperature dependence of diffusion rate

Following the determination of the relevant computational parameters (Langevin damping time, number of beads and adiabaticity parameter), we now turn our attention to the calculation of quantum diffusion rates using the PACMD method.

Before carrying out the calculation of the diffusion coefficients, we must first attempt to make the PACMD simulations more efficient if possible. We have already determined that a timestep of  $\Delta t = 0.005$  fs is required for PACMD simulations where  $\gamma = 0.0025$ . Now that we have increased the adiabaticity parameter to  $\gamma = 0.01$ , we also find that the timestep may also be increased. By tracking the stability of the numerical integration (as was done when determining the timestep for  $\gamma = 0.0025$ ), we find that we are able to increase the timestep to  $\Delta t = 0.05$  fs (for timesteps larger than this, the radius of gyration again exhibits a discontinuous jump in the output for H at 250 K).

As with the classical calculations, the diffusion rate was calculated from the mean squared displacement, for both H and D on the (111) Ni surface (as approximated by the DFT PES) at the same 8 temperatures (from 75 K to 250 K), with a Langevin damping time of 500 fs. For each of these calculations, we ran for a total simulation time of 2.5 ns, with a timestep of 0.05 fs, outputting the data to disk every 50 fs. This time, at each value of the temperature (for each isotope), a set of 12 independent trajectories was computed, in order to allow for an averaging over several diffusion coefficients to improve the quality of the final diffusion coefficients, as well as allowing an estimate of the error.

When calculating the mean squared displacements, the start time was adjusted to be 100 ps, and the total length of the MSDs changed to 240 ps (allowing for time origin averaging over the remaining 2.4 ns trajectory, after the equilibration period is taken into account). Figure 8.3.9 shows the MSDs which result from averaging each of the individual 12 MSDs at each temperature. Immediately we see that the diffusion rate is higher for H than D (at the same temperature), as expected — in addition, the quantum diffusion rates appear significantly faster than those calculated from the classical simulations.

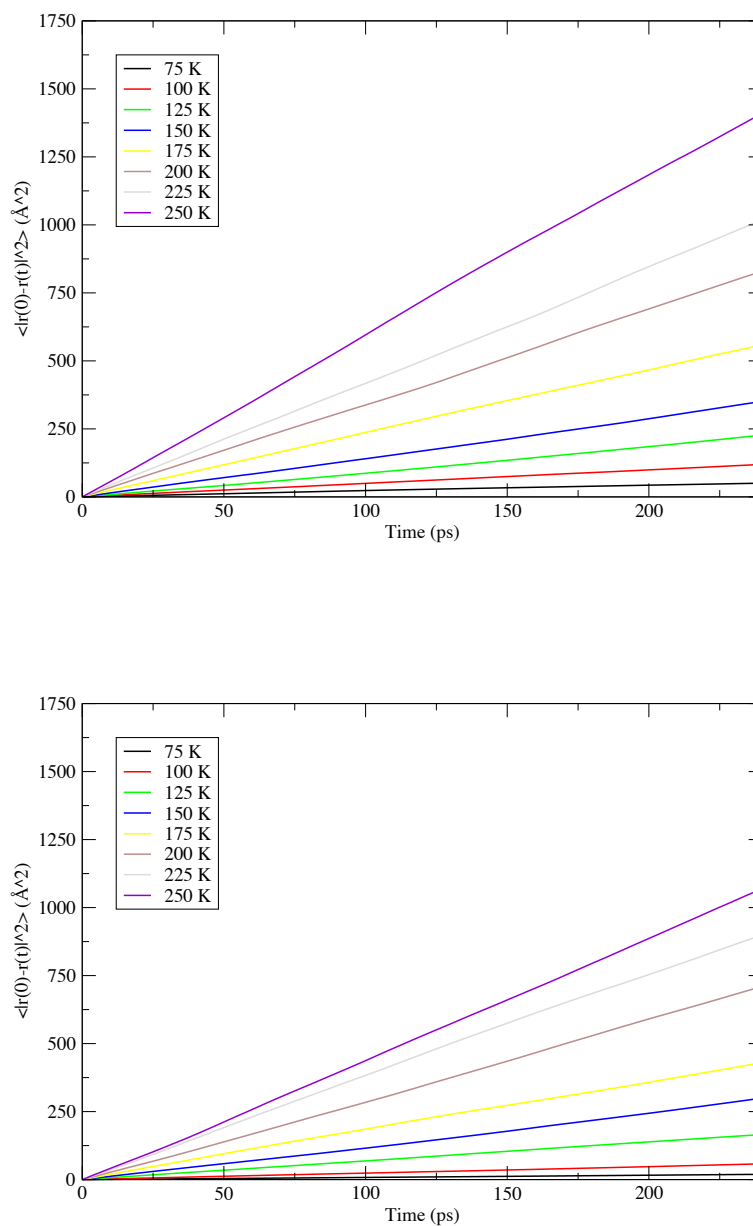


Figure 8.3.9: Mean squared displacements obtained through quantum (PACMD) simulations of H (top) and D (bottom) on (111) Ni (using 16 beads). These MSDs were taken by averaging over the resulting MSDs from 12 independent trajectories at each temperature.

Figure 8.3.10 shows the diffusion coefficient as a function of temperature, resulting from an averaging over each of the 12 independent diffusion coefficients at each temperature. We see that, although the curve is less smooth than the classical calculations, the diffusion rates span fewer orders of magnitude across the temperature range being studied than in the classical simulations. In addition, even at the highest temperature studied throughout this work (250 K), quantum effects act to increase the diffusion rate significantly for both hydrogen and deuterium — this is not surprising, as it has

been observed that quantum nuclear effects are significant for protons even at room temperature (Berne and Thirumalai, 1986).

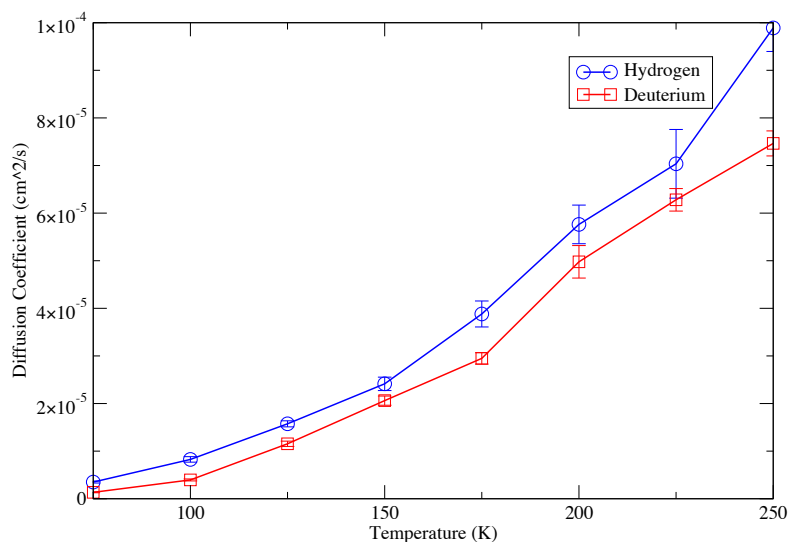


Figure 8.3.10: Diffusion coefficients as a function of temperature for quantum (PACMD) simulations of H and D on the (111) Ni surface (using 16 beads).

In order to determine whether the adsorbate diffusion still follows the Arrhenius relationship, with only a single activation energy, we again calculate the line of best fit on an Arrhenius plot, across the whole temperature range, which is given in Figure 8.3.11. In this case, we observe is that a single line does not appear to produce a good fit to the data points — while the fit tends to be better for D than H, it does generally get worse as the temperature decreases, possibly indicating a transition from thermally activated classical hopping between sites to quantum tunnelling mediated diffusion at lower temperatures. If we are seeing a transition to quantum diffusion, it is not entirely unexpected that a classical Arrhenius relationship tends to fit the deuterium data better than the hydrogen data (as the radius of gyration indicates that deuterium is less delocalized than hydrogen at the same temperature, as expected).

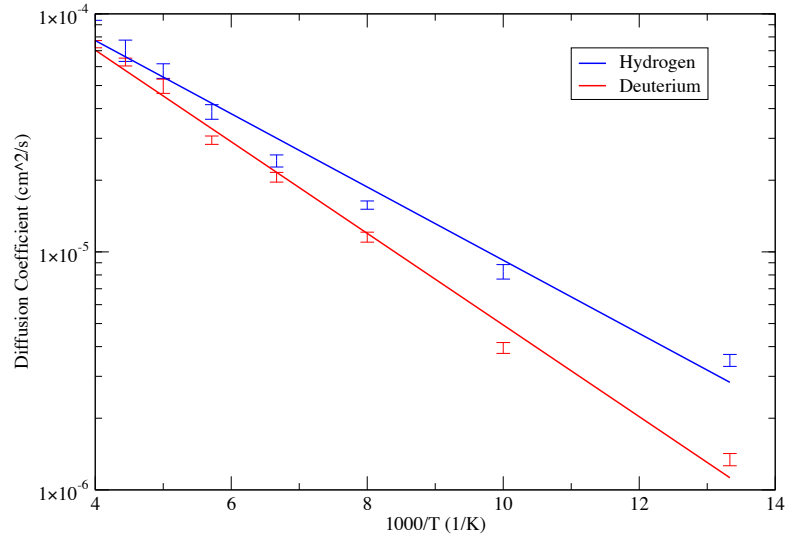


Figure 8.3.11: Arrhenius plot of diffusion rates against inverse temperature from quantum (PACMD) simulations of H and D on the (111) Ni surface (using 16 beads). Presented with a single line of best fit across the whole temperature range.

From the line of best fit, a single activation energy and frequency factor describing the diffusion across the whole temperature range was calculated. These are expressed in Table 8.3.1. What we now see is a larger discrepancy in the activation energies (which are both significantly reduced) when compared with the classical simulations, indicating that the shape of the energy barriers plays a role, not only the height — and that hydrogen and deuterium effectively “see” different barriers, which can be attributed to the effect of tunnelling (the difference in activation energies is now: 7.7 meV). In addition, the ratio of the frequency factors is now found to be 0.77, rather than the 1.37 as was found with the classical simulations.

250 K - 75 K		
	Frequency factor (Hz)	$E_a$ (meV)
H	$3.19 \times 10^{-4}$	-30.5
D	$4.15 \times 10^{-4}$	-38.2

Table 8.3.1: Frequency factors and activation energies (given to 3 significant figures) from the Arrhenius law fitted across the entire temperature range, for quantum H and D (16 beads) on the (111) Ni surface.

A deviation from classical Arrhenius behaviour can be investigated by dividing the temperature range into two regions: a high temperature region (250 K to 100 K), and a low temperature region (100 K to 75 K). When fitting lines of best fit to each of these regions separately, the resulting Arrhenius plot is given in Figure 8.3.12. Here we see that (unsurprisingly), by virtue of fitting each of the lines to a reduced number of

points, the fit is much better than in Figure 8.3.11. Almost all of the data points now fall along the lines of best fit, with the 150 K hydrogen diffusion rate being the biggest outlier.

The most interesting feature of Figure 8.3.12 is that there does appear to be some breaking in the Arrhenius slope at low temperatures, indicating a possible transition from thermally activated (classical) tunnelling at high temperatures, and the more temperature independent diffusion through quantum tunnelling at lower temperatures. While we do not observe a sharp transition into temperature independent tunnelling, as we might expect, and we must be careful to draw conclusions on the basis of two data points, the quantum diffusion profile in Figure 8.3.12 presents a vastly different picture to that obtained with classical simulations (Figure 8.2.8). Of course, including more data points, not only within the existing temperature range, but also going out to lower temperatures is the only way of verifying that there is indeed a transition to temperature independent diffusion — still, the results presented are promising.

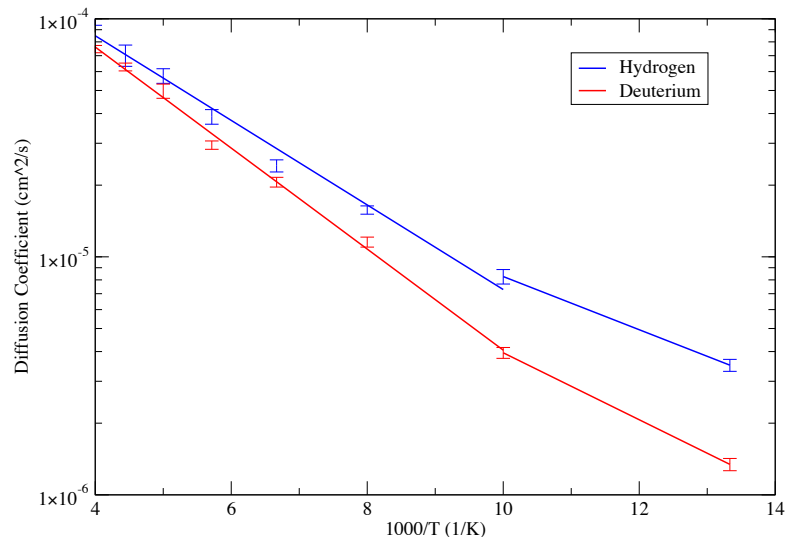


Figure 8.3.12: Arrhenius plot of diffusion rates against inverse temperature from quantum (PACMD) simulations of H and D on the (111) Ni surface (using 16 beads). Presented with a two lines of best fit, this time with one line fitted at high temperatures (from 250 K to 100 K), and another at low temperatures (100 K to 75 K). A sharp break in the gradient between the two lines indicates a possible transition from thermally activated (classical) diffusion to diffusion mediated by tunnelling (quantum diffusion).

Repeating the process of calculating the activation energies and frequency factors associated with the lines of best fit in the above Arrhenius plot, leads to the results presented in Table 8.3.2. We now find that, in the high temperature region, the difference in the activation energies is found to be 6.8 meV, which reduces to 5.7 meV in the low temperature region. In addition, the ratio of the frequency factors is now found to

be 0.81 and 1.07 in the high and low temperature regions respectively. These results are a further indication that the diffusion rate is significantly different for the quantum results when compared with the classical results.

250 K - 100 K			100 K - 75 K	
	Frequency factor (Hz)	$E_a$ (meV)	Frequency factor (Hz)	$E_a$ (meV)
H	$4.36 \times 10^{-4}$	-35.3	$1.08 \times 10^{-4}$	-22.2
D	$5.37 \times 10^{-4}$	-42.1	$1.01 \times 10^{-4}$	-27.9

Table 8.3.2: Frequency factors and activation energies (given to 3 significant figures) from the Arrhenius law, for quantum H and D (16 beads) on the (111) Ni surface. In this case, these values are calculated separately for the high and low temperature regions.

### 8.3.4 Radius of gyration as a function of temperature

The radius of gyration has been used throughout this work as a measure of the quantum delocalization of the adsorbate as it moves across the static surface. Figure 8.3.13 shows how the mean radius of gyration, and the fluctuations of the radius of gyration vary as a function of temperature, for both H and D. We see that the mean radius of gyration for hydrogen seems to increase more or less linearly as the temperature decreases (with the sharpest increase arising between 75 K and 100 K), whereas the deuterium results seem to suggest a gradual increase from 100 K to 75 K, and again from 250 K to 125K, but there does appear to be a sharp increase between 125 K and 100 K, suggesting that the adsorbate suddenly becomes “more quantum” at these temperatures.

By considering the fluctuations about the mean of the radius of gyration, we are also able to gain an appreciation of how much the delocalization of the adsorbate varies as it moves across the surface. We note that while these fluctuations seem to be fairly constant across the whole temperature range for hydrogen, there appears to be the general trend for the fluctuations to become more pronounced as the temperature decreases for the deuterium. This may indicate that, as the temperature decreases, the hydrogen delocalization tends to unaffected by the position along the surface, whereas the deuterium tends to be more easily affected by these changes in position. At this stage, it is uncertain whether the jump in the fluctuations for D at 100 K are a physical feature (possibly indicating the point at which there is a transition in the diffusive behaviour), or an artefact of the data.

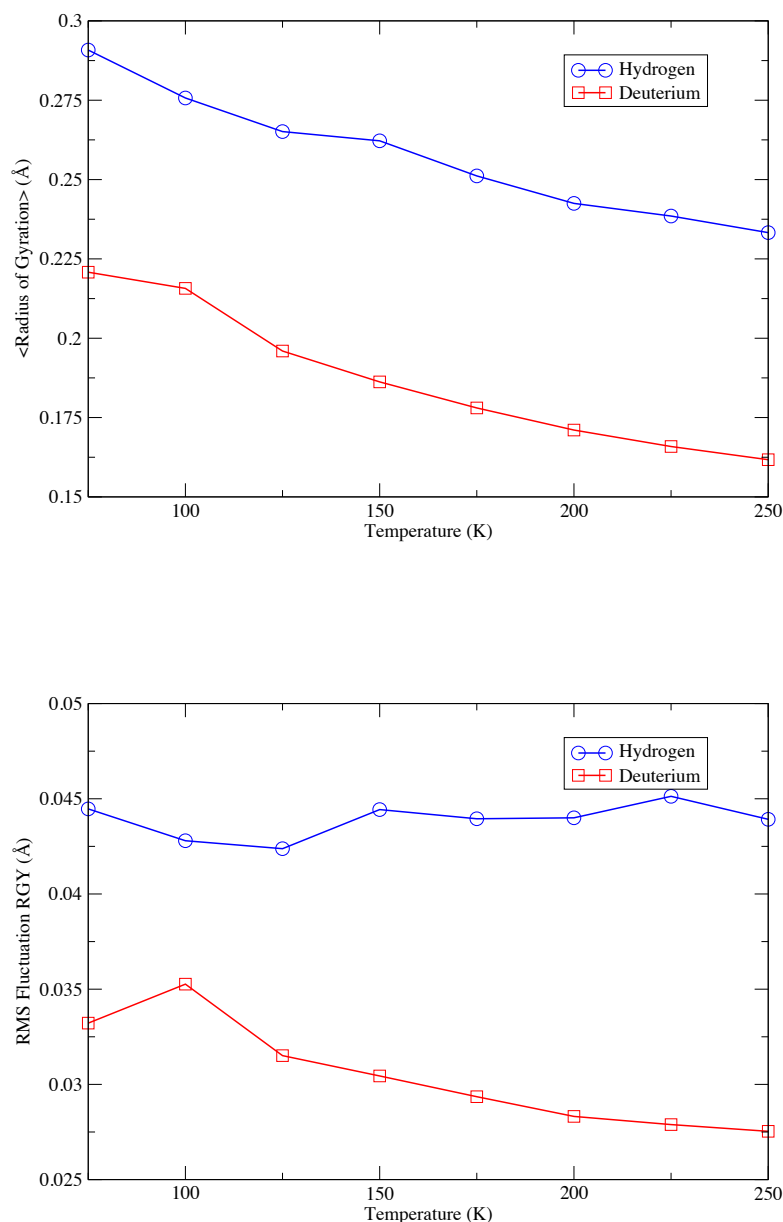


Figure 8.3.13: The temperature dependence of the mean (top) and RMS fluctuations (bottom) of the radius of gyration for H and D on the (111) Ni surface (using 16 beads).

Figure 8.3.14 shows the ratio of the mean radius of gyration of H to D varies as function of the temperature. We see that, at high temperatures, the ratio between the two measures of delocalization is more or less constant, with there being a large change in as the temperature reduces from 150 K to 100 K, as the delocalization of the deuterium increases relative to the hydrogen. As the temperature decreases further from 100 K to 75 K, the relative amount of hydrogen delocalization increases, indicating that the deuterium becomes more quantum mechanical as the temperature decreases from 150 K, but with the hydrogen becoming more relatively more quantum mechanical at the

lower temperature of 75 K.

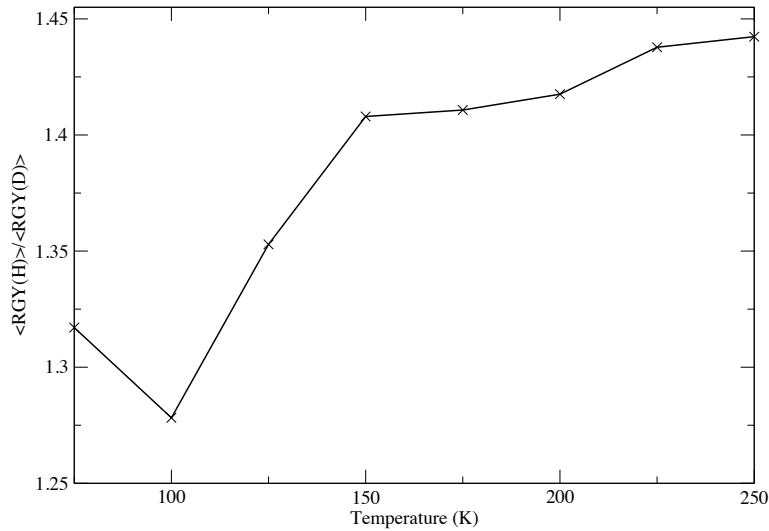


Figure 8.3.14: The ratio of the H to D mean radius of gyration from quantum (PACMD, 16 beads) simulations on the (111) Ni surface as a function of temperature.

### 8.3.5 Quantum trajectories

As with the classical simulations, it is instructive to plot the trajectories of the adsorbate as it moves across the surface. This is particularly useful for the quantum simulations, which give us additional information that was not available to us in the classical simulations: from the properties of the ring polymer, we are able to know not only where the adsorbate was located (or at least, its position expectation value along a closed Feynman path), but also how delocalized it was at any point along the surface. By plotting the centroid position superimposed onto a circle representing the radius of gyration, we are able to visualize which regions of the surface the quantum adsorbate “feels” as it moves on its journey across the surface. In the figures that follow, the circles representing the delocalized quantum particles are plotted with a small amount of transparency, such that darker regions represent overlapping delocalized positions (and therefore more probable positions of the quantum particle).

Figure 8.3.15 shows the quantum trajectories of H and D along the surface at a temperature of 75 K. Here, even though the visualized trajectory is shorter than the corresponding classical trajectories (Figure 8.2.9), the adsorbates are shown to explore more of the surface than in the classical simulations. In addition, we see the same characteristic hexagonal structure emerging as in the 250 K classical simulations (Figure 8.2.10), except this time there is a degree of “smearing” due to the delocalized nature of the adsorbates.

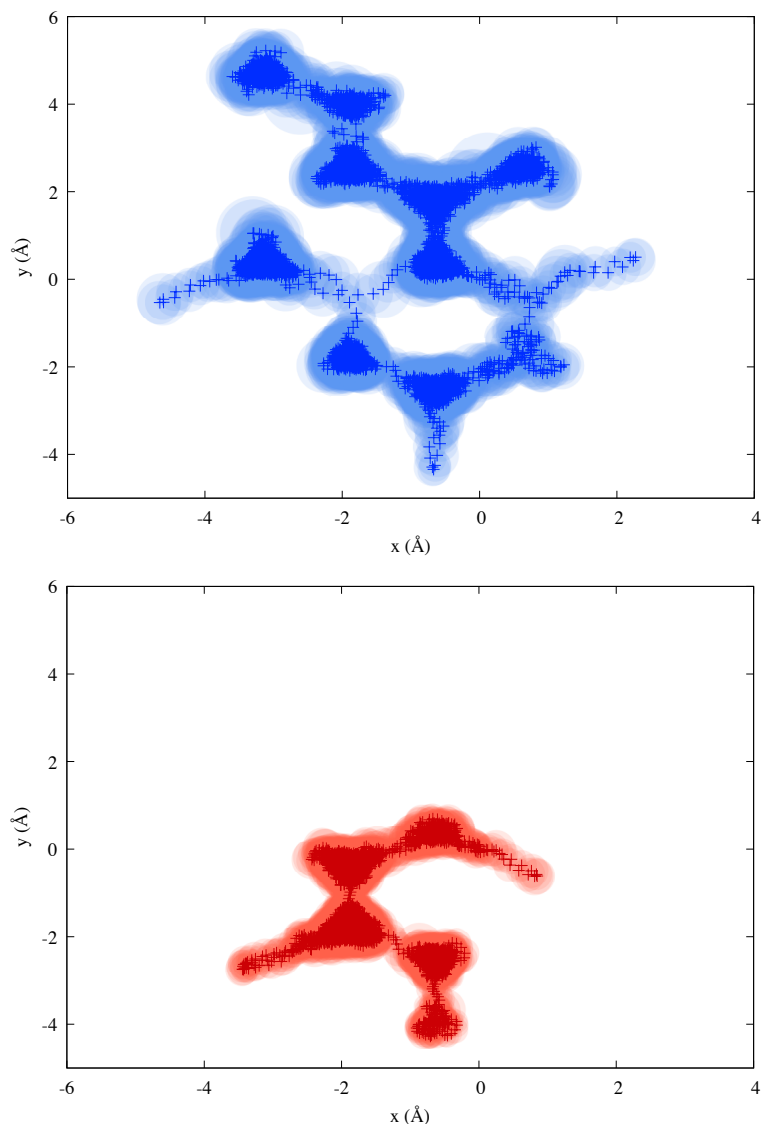


Figure 8.3.15: Quantum trajectories of the H (top, blue) and D (bottom, red), both represented by a ring polymer (of 16 beads), along the Ni (111) PES at a temperature of 75 K. These plots were generated from a short PACMD trajectory of 200 ps, with the centroid position and radius of gyration outputted to disk every 10 fs. All other simulation parameters were kept identical to those used for the calculation of the diffusion coefficients (16 beads, Langevin damping time of 500 fs and an adiabaticity parameter of 0.01). Here the (darker) points represent the centroid position, with the (lighter) circles representing the radius of gyration of the ring polymer at that point.

When comparing hydrogen to deuterium, we see that the hydrogen is not only more mobile than the deuterium, but it is also more delocalized as well — in line with the other results presented in this chapter. In addition, there is also an indication that the adsorbate becomes more delocalized in the minima of the potential than across the bridge site — this is to be expected, as the PES curvature is smaller at the minima than along the bridge site (due to the position of the topmost nickel atoms). In these calculations, although there does not appear to be any indication of the ring polymer extending directly over the sites above the topmost nickel atoms, there is a significant amount of delocalization extending into this region, where the classical particle would

be unlikely to explore.

Moving on to the 250 K results, in Figure 8.3.16 we again see the emergence of the hexagonal structure of the surface, but this time there are some regions where the adsorbate deviates slightly from this path (passing over a site above one of the topmost nickel surface atoms) — this is most obvious in the deuterium trajectory, highlighted in Figure 8.3.17. The deviation away from this path is not unexpected — given a sufficiently long trajectory, the Langevin thermostat would almost certainly force the adsorbate over this barrier at some point, with the quantum delocalization giving additional energy to increase the likelihood of such motion.

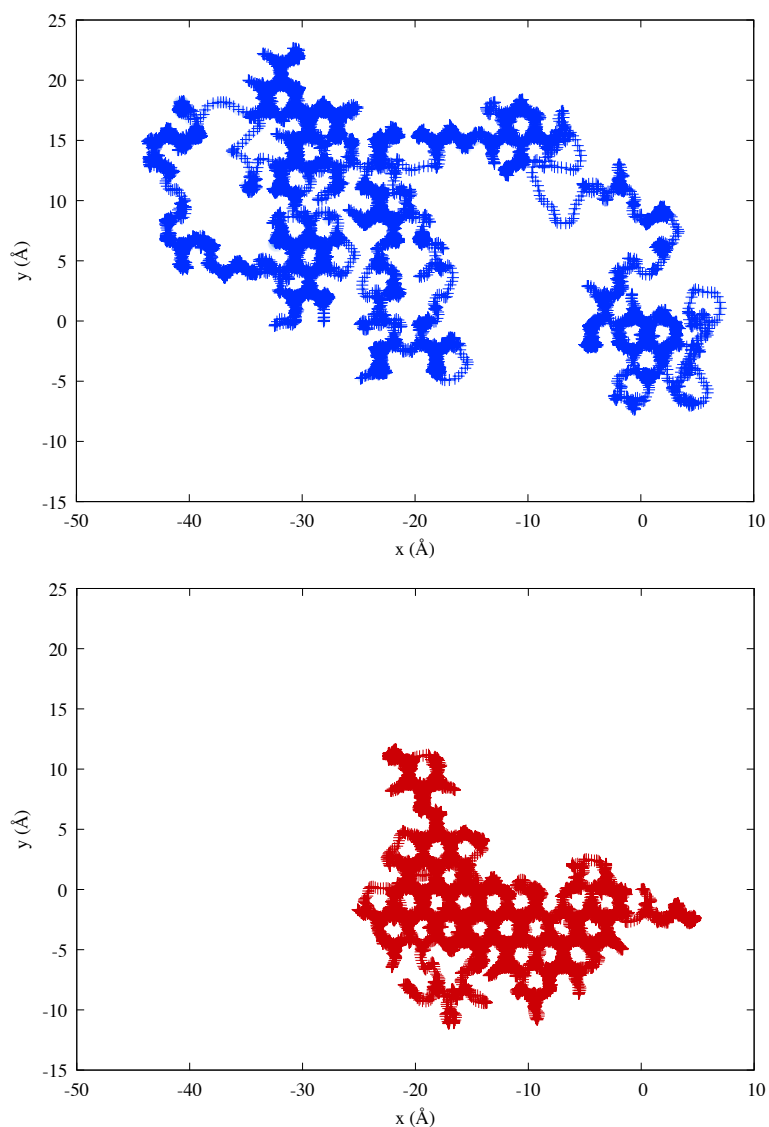


Figure 8.3.16: Quantum trajectories of the H (top, blue) and D (bottom, red), both represented by a ring polymer (of 16 beads), along the Ni (111) PES at a temperature of 250 K. These plots were generated from a short PACMD trajectory of 200 ps, with the centroid position and radius of gyration outputted to disk every 10 fs. All other simulation parameters were kept identical to those used for the calculation of the diffusion coefficients (16 beads, Langevin damping time of 500 fs and an adiabaticity parameter of 0.01). Here the (darker) points represent the centroid position, with the (lighter) circles representing the radius of gyration of the ring polymer at that point.

When comparing the hydrogen and deuterium results, we see again the expected behaviour: hydrogen is more mobile and more delocalized than deuterium, giving rise to a greater mean displacement and a larger radius of gyration. In both cases, the adsorbate is more mobile but less delocalized than the corresponding 75 K trajectories shown in Figure 8.3.15.

Due to the large distances shown in Figure 8.3.16, it is difficult to see the extent of the delocalization of the adsorbate on this scale. This effect is made worse by the fact that the amount of delocalization decreases at higher temperatures. In order to show the extent of the delocalization as a function of adsorbate position along the surface, Figure 8.3.17 shows zoomed in regions of a subset of the two trajectories. Note that because these two trajectories took different pathways, the absolute positions shown are different for both particles, but due to the periodicity of the underlying potential energy surface, the adsorbate would be subject to the same potential energy derived forces in these regions.

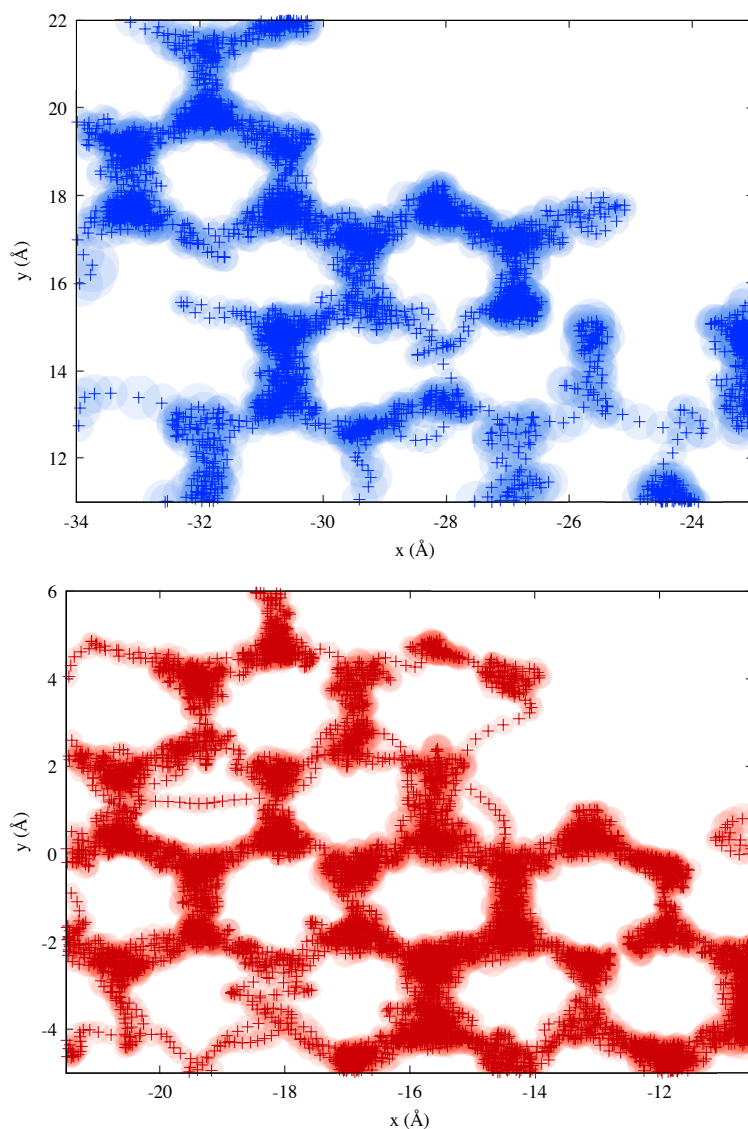


Figure 8.3.17: A subset of the quantum trajectories shown in Figure 8.3.16 for H (top, blue) and D (bottom, red) moving along the Ni PES at 250 K.

### 8.3.6 Ratio of classical and quantum diffusion coefficients

Given that deuterium has twice the mass of hydrogen, it would be instructive to see how the ratio of the two diffusion coefficients compare as a function of temperature, for both the classical and the quantum results. The results of this can be seen in Figure 8.3.18. We can see that while the ratio of the two diffusion coefficients is similar both classically and quantum mechanically at higher temperatures (150 K to 250 K), as the temperature reduces, there appears to be a widening between the ratios of the classical and quantum results.

We note the previous comments about the difficulties in generating accurate diffusion coefficients for the low temperature classical results, and suggest that more trajectories may need to be generated in order to accurately determine the ratio of the diffusion rates at low temperatures. At 75 K, it should still be expected that H is more mobile than D (and so  $D(H)/D(D)$  should be  $> 1$ ). It is natural to assume that, for well converged diffusion coefficients, the ratio of the two diffusion coefficients should remain more or less constant across the whole temperature range in the classical simulations, because there is only a single mechanism by which diffusion can occur.

In the quantum results, as the temperature decreases, because there are two mechanisms by which the adsorbate can diffuse across the surface, it is expected that there should be some change in the ratios as the temperature decreases. In this case, we expect the observed behaviour: that the hydrogen diffusion rate will increase more rapidly than the deuterium rate, owing to its larger amount of delocalization.

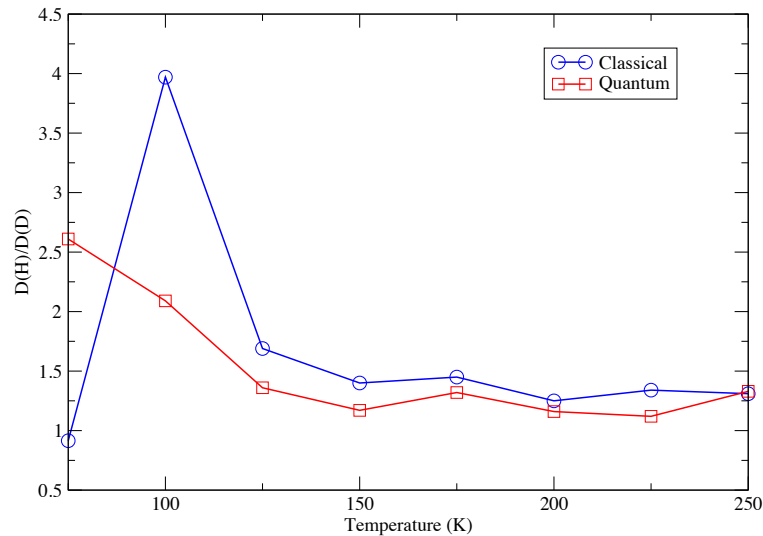


Figure 8.3.18: The ratio of H to D diffusion coefficients for classical and quantum (PACMD, 16 beads) simulations on the (111) Ni surface as a function of temperature.

It is also helpful to plot the ratio of the classical diffusion rate to the quantum one for the same isotope. The results of such a graph are presented in Figure 8.3.19. Down to 150 K, we observe that the hydrogen and deuterium diffusion ratios tend to track each other quite nicely, with the deuterium rate being affected more by the QM effects than the hydrogen results at high temperatures. This can be attributed to the fact that, in the high temperature regime, because the hydrogen is already moving quite quickly, the addition of extra energy from the quantum “correction” does not have a significant impact on the results, whereas because the deuterium is moving relatively more slowly, the addition of any extra energy contributions from the QM effects are likely to affect its diffusion rate more significantly — of course, the decreased amount of delocalization of D is likely to offset this extra increase, so we are still expecting for the two curves to track each other reasonably closely.

As the temperature decreases, the gap between the ratios of the hydrogen and deuterium results does tend to widen (for the aforementioned reasons). It is not yet known whether the transition at 75 K, with the hydrogen results being quantum mechanically corrected more than the deuterium is because the deuterium has already reached its maximum amount of quantum delocalization, and the hydrogen still has further to go, or because the low temperature classical results at 75 K underestimated the hydrogen diffusion rate.

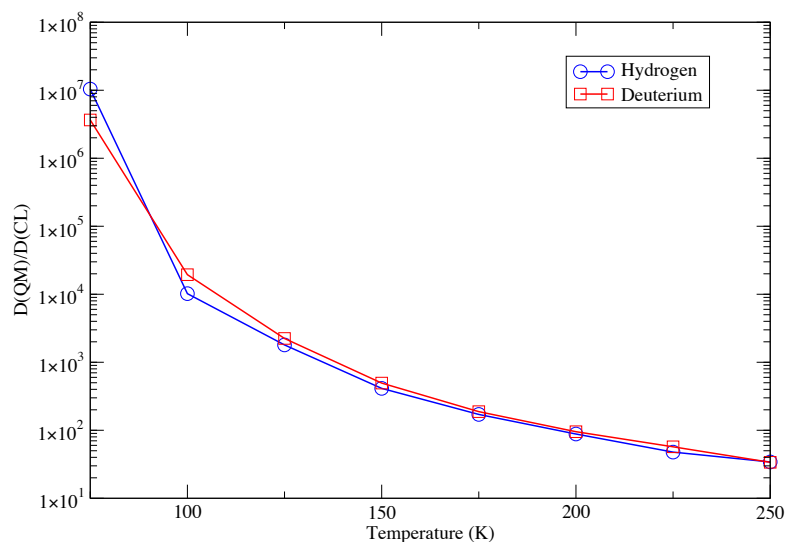


Figure 8.3.19: The ratio of quantum (PACMD, 16 beads) to classical diffusion coefficients for H and D on the (111) Ni surface as a function of temperature.

## 8.4 Summary

We have seen that quantum nuclear effects are essential in the treatment of the diffusion of hydrogen/deuterium along the nickel (111) surface. At all temperatures studied, the quantum results exhibited significantly larger diffusion coefficients than the classical results. Figure 8.4.1 shows the diffusion rates for both H and D, from the classical and quantum simulations on the same set of axes.

It is observed that the quantum diffusion rates span many fewer orders of magnitude than the classical results, and also that there is an indication of non-Arrhenius behaviour as the temperature decreases in the quantum simulations. This indicates that, not only are the classical results quantitatively wrong, but that they also show qualitative differences at low temperatures, when compared with the quantum simulations.

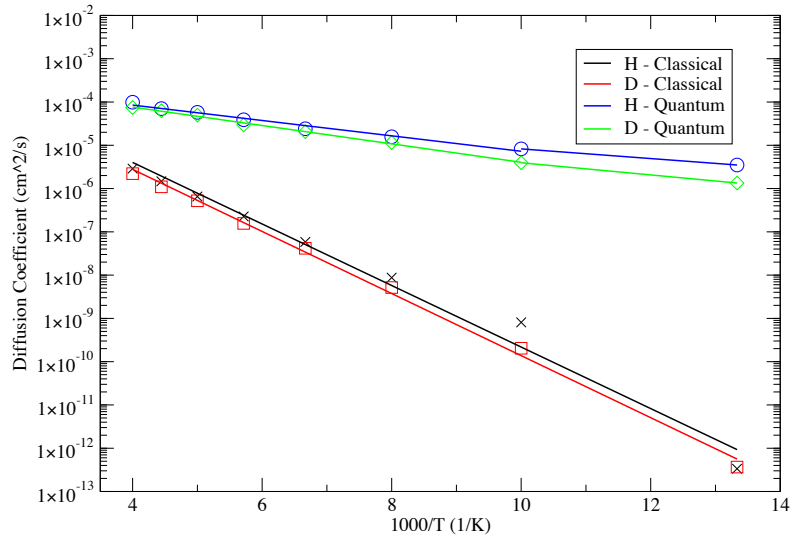


Figure 8.4.1: Arrhenius plots of the diffusion coefficient as a function of inverse temperature for classical and quantum (PACMD, 16 beads) of H and D on the (111) Ni surface. Presented with lines of best fit (1 line for classical results, 2 lines for quantum results).

Referring back to the experimental results which motivated this work, we find that the classical diffusion rates are consistently faster than diffusion rates reported by Lin and Gomer (1991), Lee et al. (1993) and Cao et al. (1997) (see Figures 2.3.1, 2.3.2 and 2.3.3) (often by  $\sim 2$ -3 orders of magnitude), and unsurprisingly do not describe the temperature independent diffusive regime. When comparing with the newer (preliminary) results of Zhu and Ward (2013) (whose results suggest diffusion rates of  $\sim 10^{-6}$  to  $10^{-7}$  cm<sup>2</sup>/s across a temperature range of 250 K to 125 K, and a transition temperature of approximately 170 K), we find that the diffusion rates are very similar at 250 K, but differ by around an order of magnitude as the temperature decreases to 125 K, with

the classical simulations being the slower of the two — this is encouraging, because we should naturally expect that the system behaves classically at higher temperatures, but should report slower diffusion rates than the physical system as the temperature decreases due to quantum effects being neglected in these calculations.

When turning to the quantum simulations, we have already stated that the effect of including the quantum nuclear effects acts to increase the diffusion rate across the whole temperature range — unfortunately this has a negative effect on the comparison with all of the experimental results previously mentioned (with the difference between all experimental results increasing by a few more orders of magnitude). With particular reference to the results of Zhu and Ward (2013), we now find that our diffusion coefficients are typically larger than the experimental results by 2 orders of magnitude, and in addition we find a less sharply defined transition temperature, which is  $\sim 70$  K lower than the experimental result.

We do however note a few positive points from comparison of the quantum simulations to experiment: firstly, the diffusion coefficient now spans a reduced number of orders of magnitude when compared with the classical results (more closely in line with the results of Lin and Gomer (1991), Lee et al. (1993) and Zhu and Ward (2013), even though the absolute rates are different). In addition, there appears to be a transition from classical to quantum diffusion at a temperature of approximately 100 K (in agreement with Lin and Gomer (1991)), although the transition is not as sharp as given by all experimental data sets except Cao et al. (1997) (who report a much more gradual change in the gradient of the Arrhenius plot — with a transition temperature of 110 K).

Regarding the transition from classical to quantum diffusion, we note that almost all of the experimental results do actually show continuous change in the gradient of the Arrhenius plot, before finally transitioning to relatively temperature independent diffusion (with the exception of Cao et al. (1997), whose diffusion coefficients still vary significantly beyond this transition), it is simply the case that the transition appears to occur over a much smaller temperature range than is shown in the simulation results. In this work, the results presented in this thesis do not appear to go down to a low enough temperature for the Arrhenius plot to level off, and so it is hoped that, by continuing down to lower temperatures, we should see this plateau region as well. In addition to this, a greater number of simulations carried out close to the transition temperature would also aid to see how sharp this transition is, in addition to determining precisely at what temperature this transition occurs.

Finally, we remind ourselves that the simulations carried out in this work were done so under the approximation that the nickel surface could be treated as a static surface. It is hoped (although not guaranteed) that including the effects of the nickel surface phonons might act to slow the adsorbate, hopefully by a sufficient amount to bring the simulation results more closely aligned to experiment (particularly the results of Zhu and Ward (2013), which motivated this study).

## Chapter 9

# Conclusions

While there may be lingering doubts which exist about the precise quantitative nature of the quantum diffusion coefficients, arising out of the sensitivities to the thermostating procedure and the convergence behaviour of the adiabaticity parameter, this project has been broadly successful in that it has shown that quantum nuclear effects do have a substantial effect on the diffusion rates of both hydrogen and deuterium. The results presented in this thesis have shown that quantum effects are essential in the treatment of this system, as there is a qualitative difference between the diffusion profiles as generated with classical and quantum simulations.

If time allowed, it would have been beneficial to further improve the quality of the low temperature classical diffusion results, and in addition, generate more low temperature quantum mechanical diffusion rates, in order to more accurately determine the transition temperature from classical to quantum diffusion. The generation of more data points would allow for a greater certainty in the low temperature regime, and would clarify if there does exist a temperature at which we can predict quantum diffusion coefficients which are approximately independent of temperature.

Perhaps, the largest outstanding question though, is whether an improved agreement to experiment can be found by including the vibrational effects of the surface nickel atoms in the simulations, as this seems to be by far the largest approximation made throughout this work.

It is hoped that, with the simulation software now fully developed, it can be put to good use in order to carry out further studies in the context of this work. In addition to moving beyond the static surface approximation, it would also be beneficial to further determine the precise nature of the pathways that lead to higher and lower diffusion rates: in effect, by calculating a single diffusion rate, we have averaged across the entire surface, and lost information about the directional nature of the diffusive pathways. Furthermore, it would be interesting to investigate the calculation of the time between “hops” across various parts of the surface, for both the quantum and classical adsorbates.

## 9.1 Further work: Improving on the adiabatic approximation

Although the calculations carried out in this work make use of an adiabatic separation between the adsorbate and the nickel ions (allowing the use of the PES), in reality, this is only an approximation. It is expected, that, for long time periods, or as the mass ratio between the adsorbate and the metals ions becomes smaller, this approximation will break down. As the adiabatic approximation becomes worse, it will obviously become important to treat the coupling between the adsorbate dynamics and the metal surface dynamics.

Since the use of the PES is motivated by the desire to calculate diffusion coefficients with ab initio accuracy, in the case where conventional ab initio MD approaches are too computationally demanding (considering the explicit dynamics of the metal ions), the obvious approach of including the non-adiabatic effects through explicit dynamics of all atoms using ab initio MD methods is also unfeasible. To this end, it would be advantageous if the PES approach can be modified to take into account these non-adiabatic effects in a computationally efficient manner.

It is expected that, for a system at thermal equilibrium, the dominant non-adiabatic effect on the diffusion coefficient (at long timescales) will arise from interactions between the adsorbate and the phonon modes of the surface atoms (although there may be other effects such as electronic friction effects). If there were a way to modify the PES in order to, at least approximately, capture these interactions, we could eliminate one of the largest approximations in our calculations, and yet still calculate the diffusion coefficients relatively efficiently.

It is precisely this idea which motivated the use of the EAM potential in this work: it was hoped that the reduced cost of the EAM potential would allow for a rapid prototyping of ideas in which to modify the PES to include these surface phonon effects. The desire was to allow for a time dependent modulation of the PES, consistent with the effect of the phonon-adsorbate coupling, in order to include this effect with a similar computational cost as the static PES. Unfortunately, due to the problems previously mentioned with the EAM6/7 potentials, time did not allow for all of the details of this method to be fully determined.

Despite issues with the EAM6/7 potentials, the simulation software written by the author contains a working implementation of the EAM5 potential which, although unsuitable for the study of the (111) Ni surface, claims to be suitable for the (100) Ni surface, and can nevertheless be used as the simple testbed that EAM6/7 was hoped to be. It is hoped that this idea will at some point be carried forward, whether by the author or by another person.

## Appendix A

# Geometry Optimization

The accurate knowledge of the material's structure is a prerequisite for calculating many material properties (such as binding energies, vibrational modes etc). While we expect that the structure that is most commonly observed in nature is the *global* minimum enthalpy structure, it turns out that finding the global minimum is particularly challenging task.

In order to simplify the problem, we can make use of the experimentally observed crystal structure as a starting point in our calculations, and instead restrict our search to the *local* minimum enthalpy structure. The method of minimizing the enthalpy for a particular configuration of atoms is known by several similar names, such as geometry optimization or structure relaxation.

There exist many different methods, and classes of method for finding local minima. In the interest of brevity, only the method which was used for this work (the two-point steepest descent geometry optimization) is discussed.

### Two-point steepest descent geometry optimization

We seek to minimize the enthalpy per unit cell, which is defined as

$$\mathcal{H} = E + p\Omega, \tag{A.0.1}$$

where  $E$  is the ground state energy of the system,  $p$  is the external pressure (1/3 of the trace of the pressure tensor) which is applied to the cell, and  $\Omega$  is the volume of the cell.

Following the method of Pfrommer et al. (1997), the free variables in the optimization procedure are chosen to be the strain tensor,  $\underline{\underline{\epsilon}}$ , and the atomic positions (in fractional

space),  $(\mathbf{s}_1, \dots, \mathbf{s}_N)$ . These variables define a “position” vector,

$$\mathbf{X} = \left( \underline{\underline{\varepsilon}}, \mathbf{s}_1, \mathbf{s}_2, \dots, \mathbf{s}_N \right)^T. \quad (\text{A.0.2})$$

The first 9 components of  $\mathbf{X}$  are mapped to the elements of the strain tensor as:  $X_{3(i-1)+j} = \varepsilon_{ij}$ ;  $i, j = 1, 2, 3$ , and the remaining  $3N$  components are simply the fractional coordinates of the  $N$  atoms in the cell.

The lattice vector matrix is denoted as  $\underline{\underline{h}}$ . This is a 3x3 matrix, which has as its columns the 3 lattice vectors that define the simulation cell. The strain tensor,  $\underline{\underline{\varepsilon}}$ , acts to expand the lattice vectors of the initial configuration to a new configuration by:  $\underline{\underline{h}} = \left( \underline{\underline{1}} + \underline{\underline{\varepsilon}} \right) \underline{\underline{h}}_0$ .

By defining the free variables of the optimization procedure in this way, both the atomic positions and the lattice vectors of the cell are able to be optimized simultaneously.

Pfrommer et al. also define a “force” vector,  $\mathbf{F}$ :

$$\mathbf{F} = - \left. \frac{\partial \mathcal{H}}{\partial \mathbf{X}} \right|_p. \quad (\text{A.0.3})$$

Similar to as was done with the  $\mathbf{X}$  vector, the first 9 components of the  $\mathbf{F}$  vector are the strain components,  $\mathbf{f}^{(\varepsilon)}$ , and the other  $3N$  components are built up from the forces on the atoms:

$$\mathbf{F} = \left( \mathbf{f}^{(\varepsilon)}, \underline{\underline{g}}\mathbf{f}_1, \dots, \underline{\underline{g}}\mathbf{f}_N \right)^T, \quad (\text{A.0.4})$$

where the strain components,  $\mathbf{f}^{(\varepsilon)}$  are calculated from the derivatives of the enthalpy with respect to the strain in the following way:

$$\mathbf{f}^{(\varepsilon)} = - \left( \underline{\underline{\sigma}} + p\Omega \right) \left( \underline{\underline{1}} + \underline{\underline{\varepsilon}}^T \right)^{-1}. \quad (\text{A.0.5})$$

In the above,  $\underline{\underline{\sigma}}$  is the stress tensor for the configuration defined by the vector  $\mathbf{X}$ . This can either be calculated by application of the Hellmann-Feynman theorem in density functional theory, or numerically using finite difference approaches.

Finite difference calculation of the stress tensor involves calculating the derivative of the energy with respect to some perturbation to the the lattice vectors, through the application of some small finite strain tensor,  $\underline{\underline{\varepsilon}}'$ :

$$\underline{\underline{\sigma}} = \frac{1}{\Omega} \left. \frac{\partial E \left( \left( \underline{\underline{1}} + \underline{\underline{\varepsilon}}' \right) \underline{\underline{h}} \right)}{\partial \underline{\underline{\varepsilon}}'} \right|_{\underline{\underline{\varepsilon}}'=0}. \quad (\text{A.0.6})$$

We note that the final  $3N$  components of the  $\mathbf{F}$  vector involve the multiplication of the Cartesian forces by the metric tensor,  $\underline{\underline{g}} = \underline{\underline{h}}^T \underline{\underline{h}}$ , which acts to convert the forces from Cartesian space to the fractional space.

The configuration of the system can then be updated in the following way:

$$\mathbf{X}_{i+1} = \mathbf{X}_i - \lambda \mathbf{G}_i, \quad (\text{A.0.7})$$

$$\mathbf{G}_i = -\underline{\underline{H}}_i \mathbf{F}_i. \quad (\text{A.0.8})$$

Where  $\underline{\underline{H}}$  is an approximation to the inverse Hessian, and  $\lambda$  is a scalar which reduces the enthalpy to a minimum along a particular direction defined by  $\mathbf{G}_i$ . The optimum value of  $\lambda$  can (generally) be found by a line search, although the two-point steepest descent method removes the need for this step of the procedure.

Pfrommer et al. then apply the widely used BFGS algorithm to build up an approximation to the (inverse) Hessian,  $\underline{\underline{H}}$ , which can be used to update the geometries in an efficient way. Anecdotal evidence suggests that the more (algorithmically) simplistic method of two-point steepest descent (Barzilai and Borwein, 1988) is more efficient (requires fewer geometry updates) for systems involving a large number of constraints, and has the aforementioned advantage of not requiring a line search in order to find the value of  $\lambda$ . The two-point steepest descent method does not however provide a straightforward way to iteratively improve the approximation of the Hessian, and so  $\underline{\underline{H}}_0 = \underline{\underline{H}}_i = \underline{\underline{H}}_{i+1}$  when this algorithm is used to provide the value of  $\lambda$ .

The optimal value of  $\lambda$  under the two-point steepest descent method is given by

$$\lambda = \frac{\Delta \mathbf{X}_i \cdot \Delta \mathbf{G}_i}{\Delta \mathbf{G}_i \cdot \Delta \mathbf{G}_i}, \quad (\text{A.0.9})$$

where  $\Delta \mathbf{X}_i = (\mathbf{X}_i - \mathbf{X}_{i-1})$  and  $\Delta \mathbf{G}_i = (\mathbf{G}_i - \mathbf{G}_{i-1}) = -\left(\underline{\underline{H}}_i \mathbf{F}_i - \underline{\underline{H}}_{i-1} \mathbf{F}_{i-1}\right) = -\underline{\underline{H}}_0 (\mathbf{F}_i - \mathbf{F}_{i-1})$ .

Pfrommer et al. also suggest a method for initialization of the inverse Hessian. This initialization is based on estimates of the bulk modulus and the average optical phonon frequencies at the centre of the Brillouin zone of the material, although the method is equally successful when  $\underline{\underline{H}}_0 = \underline{\underline{1}}$  (albeit less efficient).

# Bibliography

- Aarons, J. (2013). Quantum Dynamics of Hydrogen on Ruthenium. Master's thesis, University of York.
- Allen, M. P. and Tildesley, D. J. (1987). *Computer Simulation of Liquids*. Clarendon Press, Oxford.
- Andersen, H. C. (1983). RATTLE: A velocity version of the SHAKE algorithm for molecular dynamics calculations. *J. Comp. Phys.*, 52:24–340.
- Atkins, P. and de Paula, J. (2006). *Atkins' Physical Chemistry*. Oxford University Press, 8th edition.
- Barzilai, J. and Borwein, J. M. (1988). 2-point step size gradient methods. *IMA J. Numer. Anal.*, 8:141–148.
- Berg, H. C. (1993). *Random Walks in Biology*. Princeton University Press, revised edition.
- Berne, B. J. and Thirumalai, D. (1986). On the simulation of quantum systems: Path integral methods. *Ann. Rev. Phys. Chem.*, 37:401–424.
- Bhadeshia, H. K. D. H. (2016). Prevention of Hydrogen Embrittlement in Steels. *ISIJ International*, 56:24–36.
- Binnig, G., Quate, C. F., and Gerber, C. (1986). Atomic Force Microscope. *Phys. Rev. Lett.*, 56(9):930–933.
- Binnig, G., Rohrer, H., Gerber, C., and Weibel, E. (1982). Tunneling through a controllable vacuum gap. *Appl. Phys. Lett.*, 40(2):178–180.
- Born, M. and Oppenheimer, R. (1927). Zur quantentheorie der molekeln. *Ann. Phys.*, 84(20):457–484.
- Brown, R. (1828). XXVII. A brief account of microscopical observations made in the months of June, July and August 1827, on the particles contained in the pollen of plants; and on the general existence of active molecules in organic and inorganic bodies. *Philos. Mag.*, 4(21):161–173.
- Burton, G., Holman, J., Lazonby, J., Pilling, G., and Waddington, D. (2000). *Chemical Ideas*. Heinemann, 2nd edition.

- Bussi, G., Donadio, D., and Parrinello, M. (2007). Canonical sampling through velocity rescaling. *J. Chem. Phys.*, 126:014101.
- Bussi, G. and Parrinello, M. (2008). Stochastic thermostats: comparison of local and global schemes. *Comp. Phys. Comm.*, 127:26–29.
- Cao, G. X., Nabighian, E., and Zhu, X. D. (1997). Diffusion of Hydrogen on Ni(111) over a Wide Range of Temperature: Exploring Quantum Diffusion on Metals. *Phys. Rev. Lett.*, 79(19):3696–3699.
- Cao, J. and Martyna, G. J. (1996). Adiabatic path integral molecular dynamics methods. II. Algorithms. *J. Chem. Phys.*, 104(5):2028–2035.
- Cao, J. and Voth, G. A. (1993). A new perspective on quantum time correlation functions. *J. Chem. Phys.*, 99(12):10070–10073.
- Cao, J. and Voth, G. A. (1994a). The formulation of quantum statistical mechanics based on the Feynman path centroid density. I. Equilibrium properties. *J. Chem. Phys.*, 100(7):5093–5105.
- Cao, J. and Voth, G. A. (1994b). The formulation of quantum statistical mechanics based on the Feynman path centroid density. II. Dynamical properties. *J. Chem. Phys.*, 100(7):5106–5117.
- Cao, J. and Voth, G. A. (1994c). The formulation of quantum statistical mechanics based on the Feynman path centroid density. III. Phase space formalism and analysis of centroid molecular dynamics. *J. Chem. Phys.*, 101(7):6157–6167.
- Cao, J. and Voth, G. A. (1994d). The formulation of quantum statistical mechanics based on the Feynman path centroid density. IV. Algorithms for centroid molecular dynamics. *J. Chem. Phys.*, 101(7):6168–6183.
- Ceperley, M. (1999). Microscopic simulations in physics. *Rev. Mod. Phys.*, 71(2):S438–S443.
- Chandrasekhar, S. (1943). Stochastic problems in physics and astronomy. *Rev. Mod. Phys.*, 15:1–89.
- Chen, M., Yu, T., and Tuckerman, M. E. (2015). Locating landmarks on high-dimensional free energy surfaces. *Proc. Nat. Acad. Sci.*, 112(11):3235–3240.
- Chung, Y. (2014). Validity of Caltrans’ environmental hydrogen embrittlement tests on grade BD anchor rods in the SAS span. Technical report, Toll bridge program oversight committee.
- Clark, S. J., Segall, M. D., Pickard, C. J., Hasnip, P. J., Probert, M. J., Refson, K., and Payne, M. (2005). First principles methods using CASTEP. *Z. Kristall.*, 220:567–570.
- Clementi, E. and Roetti, C. (1974). *Atomic Data and Nuclear Data Tables*, volume Vol. 14, Nos. 3 and 4. Academic, New York.

- Daw, M. S. and Baskes, M. I. (1983). Semiempirical, Quantum Mechanical Calculation of Hydrogen Embrittlement in Metals. *Phys. Rev. Lett.*, 50(17):1285–1288.
- Daw, M. S. and Baskes, M. I. (1984). Embedded-atom method: Derivation and application to impurities, surfaces, and other defects in metals. *Phys. Rev. B*, 29(12):6443–6453.
- Daw, M. S., Foiles, S. M., and Baskes, M. I. (1993). The embedded-atom method: a review of theory and applications. *Mat. Sci. Rep.*, 9(7-8):251–310.
- E, W., Ren, W., and Vanden-Eijnden, E. (2005). Finite Temperature String Method for the Study of Rare Events. *J. Phys. Chem. B*, 109(14):6688–6693.
- Eigler, D. M. and Schweizer, E. K. (1990). Positioning single atoms with a scanning tunnelling microscope. *Nature*, 344:524–526.
- Einstein, A. (1905). Über die von der molekularkinetischen Theorie der wärme geforderte Bewegung von in ruhenden Flüssigkeiten suspendierten Teilchen. *Ann. Phys.*, 322(8):549–560.
- Einstein, A. and Cowper, A. D. (1926). *Investigations on the theory of the Brownian movement*. Dover.
- Feynman, R. P. (1939). Forces in Molecules. *Phys. Rev.*, 56:340–343.
- Feynman, R. P. (1948). Space-time approach to non-relativistic quantum mechanics. *Rev. Mod. Phys.*, 20(2):367–387.
- Feynman, R. P. (1998). *Statistical Mechanics: A Set of Lectures*. Westview Press, revised edition.
- Feynman, R. P., Hibbs, A. R., and Styer, D. F. (2010). *Quantum Mechanics and Path Integrals*. Dover Publications, emended edition.
- Feynman, R. P. and Kleinert, H. (1986). Effective classical partition functions. *Phys. Rev. A*, 34(6):5080–5084.
- Fick, A. (1855). Über diffusion. *Ann. Phys.*, 170:59–86.
- Fick, A. (1995). On liquid diffusion. *J. Membr. Sci.*, 100(1):33–38.
- Foiles, S. M., Baskes, M. I., and Daw, M. S. (1986). Embedded-atom-method functions for the fcc metals Cu, Ag, Au, Ni, Pd, Pt, and their alloys. *Phys. Rev. B*, 33(12):7983–7991.
- Foiles, S. M., Baskes, M. I., and Daw, M. S. (1988). Erratum: embedded-atom-method functions for the fcc metals Cu, Ag, Au, Ni, Pd, Pt, and their alloys [Phys. Rev. B 33, 7983 (1986)]. *Phys. Rev. B*, 37(17):10378.
- Frenkel, D. and Smit, B. (1996). *Understanding Molecular Simulation: From Algorithms to Applications*. Academic Press.

- Germann, G. J., Cohen, S. R., Neubauer, G., McClelland, G. M., and Coulman, H. S. (1993). Atomic scale friction of a diamond tip on diamond (100) and (111) surfaces. *J. Appl. Phys.*, 73(1):163–167.
- Gillan, M. J. (1988). The quantum simulation of hydrogen in metals. *Phil. Mag. A*, 58(1):257–283.
- Giordano, F. R., Fox, W. P., Horton, S. B., and Weir, M. D. (2009). *A First Course in Mathematical Modeling*. Brooks/Cole, Cengage Learning, 4th edition.
- Glover, M. (2004). *Path Integral Computer Simulations of Liquid Water*. PhD thesis, University of York.
- Goldstein, H. (1980). *Classical Mechanics*. Addison-Wesley, 2nd edition.
- Gradshteyn, I. S. and Ryzhik, I. M. (2007). *Table of Integrals, Series, and Products*. Academic Press, 7th edition.
- Graham, T. (1866). On the Absorption and Dialytic Separation of Gases by Colloid Septa. *Phil. Trans. R. Soc. Lond.*, 156:399–439.
- Haile, J. M. (1997). *Molecular Dynamics Simulation: Elementary Methods*. John Wiley & Sons.
- Hammer, B., Hansen, L. B., and Nørskov, J. K. (1999). Improved adsorption energetics within density-functional theory using revised Perdew-Burke-Ernzerhof functionals. *Phys. Rev. B*, 59(11):7413–7421.
- Hellmann, H. (1937). *Einführung in die Quantenchemie*. Deuticke, Leipzig.
- Herman, M. F., Bruskin, E. J., and Berne, B. J. (1982). On path integral Monte Carlo simulations. *J. Chem. Phys.*, 76(10):5150–5155.
- Hirano, M. (2006). Atomistics of friction. *Surf. Sci. Rep.*, 60:160–201.
- Hohenberg, P. and Kohn, W. (1964). Inhomogeneous electron gas. *Phys. Rev.*, 136:B864–B871.
- Hone, T. D., Rossky, P. J., and Voth, G. A. (2006). A comparative study of imaginary time path integral based methods for quantum dynamics. *J. Chem. Phys.*, 124:154103.
- Hoover, W. G. (1985). Canonical dynamics: Equilibrium phase-space distributions. *Phys. Rev. A*, 31(3):1695–1697.
- Jang, S. and Voth, G. A. (1999a). A derivation of centroid molecular dynamics and other approximate time evolution methods for path integral centroid variables. *J. Chem. Phys.*, 111(6):2371–2384.
- Jang, S. and Voth, G. A. (1999b). Path integral centroid variables and the formulation of their exact real time dynamics. *J. Chem. Phys.*, 111(6):2357–2370.

- Jardine, A. P., Alexandrowicz, G., Hedgeland, H., Allison, W., and Ellis, J. (2009a). Studying the microscopic nature of diffusion with helium-3 spin-echo. *Phys. Chem. Chem. Phys.*, 11:3355–3374.
- Jardine, A. P., Hedgeland, H., Alexandrowicz, G., Allison, W., and Ellis, J. (2009b). Helium-3 spin-echo: Principles and application to dynamics at surfaces. *Prog. Surf. Sci.*, 84(1112):323–379.
- Jardine, A. P., Lee, E. Y. M., Ward, D. J., Alexandrowicz, G., Hedgeland, H., Allison, W., Ellis, J., and Pollak, E. (2010). Determination of the Quantum Contribution to the Activated Motion of Hydrogen on a Metal Surface: H/Pt(111). *Phys. Rev. Lett.*, 105(13):136101.
- Johnson, W. H. (1875). On some remarkable Changes produced in Iron and Steel by the Action of Hydrogen and Acids. *Proc. R. Soc. Lond.*, 23:168–179.
- Kittel, C. (2005). *Introduction to Solid State Physics*. John Wiley & Sons, 8th edition.
- Kohn, W. and Sham, L. J. (1965). Self-consistent equations including exchange and correlation effects. *Phys. Rev.*, 140:A1133–A1138.
- Krim, J. (2002). Surface science and the atomic-scale origins of friction: what once was old is new again. *Surf. Sci.*, 500:741–758.
- Laio, A. and Parrinello, M. (2002). Escaping free-energy minima. *Proc. Natl. Acad. Sci. USA*, 99(20):12562–12566.
- Langevin, P. (1908). Sur la théorie du mouvement brownien. *C. R. Acad. Sci. (Paris)*, 146:530–533.
- Lee, A., Zhu, X. D., Wong, A., L., D., and Linke, U. (1993). Observation of diffusion of H and D on Ni(111) from over-barrier hopping to nonactivated tunneling. *Phys. Rev. B*, 48(15):11256–11259.
- Lejaeghere, K., Bihlmayer, G., Björkman, T., Blaha, P., Blügel, S., Blum, V., Caliste, D., Castelli, I. E., Clark, S. J., Corso, A. D., de Gironcoli, S., Deutsch, T., Dewhurst, J. K., Di Marco, I., Draxl, C., Dułak, M., Eriksson, O., Flores-Livas, J. A., Garrity, K. F., Genovese, L., Giannozzi, P., Giantomassi, M., Goedecker, S., Gonze, X., Grånäs, O., Gross, E. K. U., Gulans, A., Gygi, F., Hamann, D. R., Hasnip, P. J., Holzwarth, N. A. W., Iuşan, D., Jochym, D. B., Jollet, F., Jones, D., Kresse, G., Koepf, K., Küçükbenli, E., Kvashnin, Y. O., Loch, I. L. M., Lubeck, S., Marsman, M., Marzari, N., Nitzsche, U., Nordström, L., Ozaki, T., Paulatto, L., Pickard, C. J., Poelmans, P., Probert, M. I. J., Refson, K., Richter, M., Rignanese, G., Saha, S., Scheffler, M., Schlipf, M., Schwarz, K., Sharma, S., Tavazza, F., Thunström, P., Tkatchenko, A., Torrent, M., Vanderbilt, D., van Setten, M. J., Van Speybroeck, V., Wills, J. M., Yates, J. R., Zhang, G., and Cottenier, S. (2016). Reproducibility in density functional theory calculations of solids. *Science*, 351(6280):aad3000.

- Lemons, D. S. and Gythiel, A. (1997). Paul Langevin's 1908 paper "On the Theory of Brownian Motion" ["Sur la théorie du mouvement brownien," C. R. Acad. Sci. (Paris) 146, 530 (1908)]. *Am. J. Phys.*, 65(11):1079–1081.
- Lennard-Jones, J. E. (1924). On the Determination of Molecular Fields. II. From the Equation of State of a Gas. *Proc. R. Soc. London, Ser. A.*, 106:463–477.
- Lennard-Jones, J. E. (1931). Cohesion. *Proc. Phys. Soc.*, 43(240):461–482.
- Lin, T. S. and Gomer, R. (1991). Diffusion of  $^1\text{h}$  and  $^2\text{h}$  on the ni(111) and (100) planes. *Surf. Sci.*, 255:41–60.
- Lindsay, S. M., Nagahara, L. A., Thundat, T., Knipping, U., Rill, R. L., Drake, B., Prater, C. B., Weisenhorn, A. L., Gould, S. A. C., and Hansma, P. K. (1989). STM and AFM Images of Nucleosome DNA Under Water. *J. Biomol. Struct. and Dyn.*, 7(2):279–287.
- Maddox, J. (1988). Statistical mechanics by numbers. *Nature*, 334:561.
- Martin, R. M. (2008). *Electronic Structure: Basic Theory and Practical Methods*. Cambridge University Press.
- Martyna, G. J. (1996). Adiabatic path integral molecular dynamics methods. I. Theory. *J. Chem. Phys.*, 104(5):2018–2027.
- Martyna, G. L., Klein, M. L., and Tuckerman, M. (1992). Nosé-Hoover chains: The canonical ensemble via continuous dynamics. *J. Chem. Phys.*, 97:2635–2645.
- McCarty, J., Valsson, O., and Parrinello, M. (2016). Bespoke Bias for Obtaining Free Energy Differences within Variationally Enhanced Sampling. *J. Chem. Theory Comput.*, 12(5):2162–2169.
- McIntosh, E. M., Wilkfeld, K. T., Ellis, J., Michaelides, A., and Allison, W. (2013). Quantum effects in the diffusion of hydrogen on Ru(0001). *J. Phys. Chem. Lett.*, 4(9):1565–1569.
- Mezei, M. (1992). Determining nearest image in non-orthogonal periodic systems. *Information Quarterly for Computer Simulation of Condensed Matter*, 34.
- Miron, R. A. and Fichthorn, K. A. (2004). Multiple-Time Scale Accelerated Molecular Dynamics: Addressing the Small-Barrier Problem. *Phys. Rev. Lett.*, 93(12):128301.
- Monkhorst, H. J. and Pack, J. D. (1976). Special points for Brillouin-zone integrations. *Phys. Rev. B*, 13:5188–5192.
- Neumann, R. M. (1980). Entropic approach to Brownian movement. *Am. J. Phys.*, 48(5):354–357.
- Nørskov, J. K. and Lang, N. D. (1980). Effective-medium theory of chemical binding: Applications to chemisorption. *Phys. Rev. B*, 21(6):2131–2136.

- Nosé, S. (1984). A unified formulation of the constant temperature molecular dynamics methods. *J. Chem. Phys.*, 81(1):511–519.
- Payne, M. C., Teter, M. P., Allan, D. C., Arias, T., and Joannopoulos, J. D. (1992). Iterative minimization techniques for ab initio total-energy calculations - molecular-dynamics and conjugate gradients. *Rev. Mod. Phys.*, 64:1045–1097.
- Perdew, J. P., Burke, K., and Ernzerhof, M. (1996). Generalized gradient approximation made simple. *Phys. Rev. Lett.*, 77:3865–3868.
- Pfrommer, B. G., Cote, M., Louie, S. G., and Cohen, M. L. (1997). Relaxation of crystals with the quasi-Newton method. *J. Comput. Phys.*, 131:233–240.
- Press, W. H., Flannery, B. P., Teukolsky, S. A., and Vetterling, W. T. (1986). *Numerical Recipes: The Art of Scientific Computing*. Cambridge University Press.
- Rapaport, D. C. (2004). *The Art of Molecular Dynamics Simulation*. Cambridge University Press, 2nd edition.
- Rice, B. M., Garrett, B. C., Koszykowski, M. L., Foiles, S. M., and Daw, M. S. (1990). Kinetic isotope effects for hydrogen diffusion in bulk nickel and on nickel surfaces. *J. Chem. Phys.*, 92(1):775–791.
- Rice, B. M., Garrett, B. C., Koszykowski, M. L., Foiles, S. M., and Daw, M. S. (1994). Erratum: kinetic isotope effects for hydrogen diffusion in bulk nickel and on nickel surfaces [J. Chem. Phys. 92, 775 (1990)]. *J. Chem. Phys.*, 100(11):8556.
- Sherwood, L. (2007). *Human Physiology: From Cells to Systems*. Brooks Cole, 6th edition.
- Springborg, M. (2000). *Methods of Electronic-Structure Calculations: From Molecules to Solids*. John Wiley & Sons.
- Stott, M. J. and Zaremba, E. (1980). Quasiatoms: An approach to atoms in nonuniform electronic systems. *Phys. Rev. B*, 22(4):1564–1583.
- Swope, W. C., Andersen, H. C., Berens, P. H., and Wilson, K. R. (1982). A computer-simulation method for the calculation of equilibrium-constants for the formation of physical clusters of molecules - application to small water clusters. *J. Chem. Phys.*, 76:637–649.
- Thijssen, J. M. (2007). *Computational Physics*. Cambridge University Press, 2nd edition.
- Truong, T. N. and Truhlar, D. G. (1990). Effect of Steps and Surface Coverage on Rate and Kinetic Isotope Effects for Reactions Catalyzed by Metallic Surfaces: Chemisorption of Hydrogen on Ni. *J. Phys. Chem.*, 94(21):8262–8279.
- Tuckerman, M. E. (2010). *Statistical Mechanics: Theory and Molecular Simulation*. Oxford Graduate Texts, Oxford University Press.

- 
- Tuckerman, M. E., Berne, B. J., Martyna, G. J., and Klein, M. L. (1993). Efficient molecular-dynamics and hybrid monte-carlo algorithms for path-integrals. *J. Chem. Phys.*, 99:2796–2808.
- Verlet, L. (1967). Computer "experiments" on Classical Fluids. I. Thermodynamical Properties of Lennard-Jones Molecules. *Phys. Rev.*, 159(1):98–103.
- Wipf, H. (1997). *Diffusion of hydrogen in metals*. Springer Berlin Heidelberg.
- Wonchoba, S. E., Hu, W., and Truhlar, D. G. (1995). Surface diffusion of H on Ni(100): Interpretation of the transition temperature. *Phys. Rev. B*, 51(15):9985–10002.
- Wonchoba, S. E. and Truhlar, D. G. (1996). General potential-energy function for H/Ni and dynamics calculations of surface diffusion, bulk diffusion, subsurface-to-surface transport, and absorption. *Phys. Rev. B*, 53(16):11222–11241.
- Wonchoba, S. E. and Truhlar, D. G. (1998). Embedded Diatomics-in-Molecules Potential Energy Function for Methyl Radical and Methane on Nickel Surfaces. *J. Phys. Chem. B*, 102(35):6842–6860.
- Wu, X., Brooks, B. R., and Vanden-Eijnden, E. (2016). Self-guided Langevin dynamics via generalized Langevin equation. *J. Comput. Chem.*, 37(6):595–601.
- Zee, A. (2010). *Quantum Field Theory in a Nutshell*. Princeton University Press, 2nd edition.
- Zhu, J. and Ward, D. (2013). Private communication.